





# Toward Pure Electronic Spectroscopy

by  
Vladimir S. Petrović

Submitted to the Department of Chemistry  
on December 31 2008, in partial fulfillment of the  
requirements for the degree of  
Doctor of Philosophy.

## Abstract

In this thesis is summarized the progress toward completing our understanding of the Rydberg system of CaF and developing Pure Electronic Spectroscopy. The Rydberg system of CaF possesses a paradigmatic character due to its strongly polar ion-core. The first characterization of the Stark effect in a Rydberg system of this nature is presented here, and a diagnostic application of the Stark effect for making assignments of  $N^+$  and  $\ell$  quantum numbers has been demonstrated. In addition, a general method, which relies on polarization diagnostics and is applicable not only to studies of Rydberg states, for making unambiguous rotational assignments in the absence of rotational combination differences, has been described for the case of unresolved doublet states. New information, obtained using the Stark effect and polarization diagnostics, has furthered our knowledge of the partially core-penetrating character of nominally core-nonpenetrating states. In order to systematically obtain the same information that is contained in a Stark effect spectrum, but with less difficulty, we are developing experimental methods to record same- $n^*$  Rydberg-Rydberg transitions directly, using Time Domain THz and Chirped-Pulse Microwave Spectroscopies. In both of these methods, the spectrum is recorded in the time domain, which results in reliable relative transition intensities. We show that the relative transition intensities in a Rydberg-Rydberg spectrum provide information that permits separation of different interaction mechanisms between the Rydberg electron and the ion-core.

Thesis Supervisor: Robert W. Field

Title: Haslam and Dewey Professor of Chemistry



## Acknowledgments

At the *Institute for World Domination through the Study of Small Molecules*, the name under which Professor Robert Field's group was known at the time when I joined, what is to be conquered is partitioned, then treated perturbatively. Bob is an extreme reductionist, who distills large bodies of experimental data into models that capture the most important physical aspects. His use of semiclassical mental pictures to understand the molecular dynamics on the most fundamental level never ceased to stimulate my curiosity. With my interest in the coherent control of chemical reactions, I could not have hoped for a better teacher. I owe my gratitude to Bob not only for stimulating my scientific development, but also for going beyond what is expected from an academic advisor in his efforts to help my professional growth.

During my six years at MIT, Professor Keith Nelson played a role closest to an angel guardian: I set up our THz spectrometer with help of his students and postdocs, initially with equipment borrowed from his group, on a laser table borrowed from his group. I have benefited from many an advice from Professor Nelson, not only related to THz spectroscopy, but also in directing my research interests and my search for a postdoctoral research position. I am glad to have had the opportunity to work closely with Professor Nelson in designing experiments for the UREICA Spectroscopy Module.

I would like to express my gratitude to all current and former Field group members who patiently answered my many questions. I have learned a lot about various aspects of the Rydberg project, and spectroscopy in general, from Dr. Stephen Coy, during our many discussions. Dr. Serhan Altunata's help was essential in developing my initial understanding of the Rydberg states of CaF, and I was lucky to, as well, have a great friend in him. I enjoyed our regular dinners in Asgard, together with Dr. Ryan Thom and Dr. Steve Pressé. I am grateful to Barratt Park for his help in setting up and operating our chirped-pulse microwave spectrometer. I enjoyed working with Yan Zhou on modeling the pulse propagation through a

sample of Rydberg absorbers. Working with other members of the Rydberg project, past and present, including Dr. Daniel Byun, Dr. Jeffrey Kay, Dr. Bryan Wong, Anthony Colombo, Dr. Kirill Kuyanov, and Dr. Severine Boyé-Péronne during her short visit, was a source of incessant joy and learning for me, and I hope they enjoyed working with me as much as I did with them. I wish Kirill, Tony, Yan, and Barratt best of luck with the chirped-pulse microwave experiments that we launched together. I enjoyed regular squash matches with Dr. Wilton Virgo, whose sangfroid I was always impressed by. I delighted in spending time with Drs. Hans and Kate Bechtel, both on campus and off. Other members of the Field group, including Dr. Adya Mishra, Dr. Kyle Bittinger, Dr. David Oertel, Adam Steeves, Sam Lipoff, Josh Baraban, and Erika Robertson were great people to share the office with. I am particularly grateful to Peter Giunta for his continuous help over the last several years.

Working with several undergraduate students, including Phillip Lichtor, Emily Fenn, Meghan Reedy, and Edwin Guerrero, who helped with various aspects of the THz experiment, was a source of satisfaction, and I hope they enjoyed learning about experimental physical chemistry. I was pleased to see Emily embark on career in spectroscopy, after graduating from MIT.

I am indebted to Dr. Thomas Hornung and Dr. Joshua Vaughan, who helped set up our first time-domain THz spectrometer, and to Dr. Thomas Feurer, Katherine Stone, Ka-Lo Yeh, Dr. Emanuel Péronne, Dr. Matthias Hoffmann, and Dr. Janos Hebling, all of Professor Keith Nelson's research group, for helpful discussions about running, maintaining, and improving the TDTHz spectrometer.

I would like to thank Professor Brooks Pate, our collaborator from University of Virginia, whose group I visited in August 2007, for helping me get acquainted with chirped-pulse microwave technology, and Justin Neill, a graduate student in the Pate group, who visited our lab at MIT and helped us set up and test our initial chirped-pulse microwave spectrometer.

I benefited from the stimulating discussions that I had with Professor Frederic Merkt over several years at various conferences.

I enjoyed the time I spent in Cambridge, in great part due to many friends I have here, and hosting semi-regular dinner parties was a source of great pleasure for me. I have forged many new friendships during my years in Cambridge, but it was interesting to see almost all of my closest friends from the time I was in high school and college pass through the Boston area, as graduate students, postdocs, and visiting scientists. In particular, I am grateful to have had the company of Ivan Vilotijević through most of the time I was at MIT. I am especially thankful to Tom Schmidt, my partner and tireless helper. I thank my parents, grandparents, and sister for their continuous support.





# Contents

<b>1</b>	<b>Introduction</b>	<b>29</b>
1.1	Bibliography . . . . .	33
<b>2</b>	<b>Polarization dependence of transition intensities in double resonance experiments: Unresolved Spin Doublets</b>	<b>35</b>
2.1	Prologue . . . . .	35
2.2	Introduction . . . . .	36
2.3	Calculation . . . . .	44
2.4	Experiment . . . . .	51
2.5	Results and discussion . . . . .	53
2.6	Summary . . . . .	57
2.7	Bibliography . . . . .	58
<b>3</b>	<b>The Stark effect in Rydberg states of a highly polar diatomic molecule: CaF</b>	<b>61</b>
3.1	Prologue . . . . .	61
3.2	Introduction . . . . .	62
3.3	Background . . . . .	67
3.4	Experiment . . . . .	76
3.5	Calculation . . . . .	78
3.6	Results and discussion . . . . .	83

3.6.1	Stages of decoupling . . . . .	83
3.6.2	Effective Hamiltonian matrix diagonalization . . . . .	85
3.6.3	Assignments . . . . .	92
3.6.4	Polarization dependence . . . . .	95
3.7	Summary . . . . .	100
3.8	Bibliography . . . . .	103
<b>4</b>	<b>Time domain terahertz spectroscopy for investigation of Rydberg-Rydberg transitions</b>	<b>107</b>
4.1	Introduction . . . . .	107
4.2	Generation . . . . .	109
4.3	Propagation of THz pulses . . . . .	117
4.4	Detection . . . . .	121
4.5	Conversion to 40 Hz operation . . . . .	128
4.6	Polarization sensitivity . . . . .	130
4.7	Spectral content of the pulse . . . . .	132
4.8	Sample cell . . . . .	133
4.9	Attempt to record rotational spectra of small molecules . . . . .	135
4.10	Extraction of molecular parameters . . . . .	142
4.11	UV-THz double resonance experiment . . . . .	145
4.12	Bibliography . . . . .	149
<b>5</b>	<b>Rydberg-Rydberg chirped-pulse microwave spectroscopy</b>	<b>153</b>
5.1	Introduction . . . . .	153
5.2	32.5 - 39 GHz spectrometer . . . . .	159
5.3	69.6 - 84 GHz spectrometer . . . . .	166
5.4	Rydberg-Rydberg transitions in Ca . . . . .	172
5.5	Rydberg-Rydberg transitions . . . . .	179

5.6	Conclusion . . . . .	184
5.7	Bibliography . . . . .	185
<b>6</b>	<b>Calculated Pure Electronic spectra of <math>\ell</math>-mixed Rydberg states</b>	<b>187</b>
6.1	Prologue . . . . .	187
6.2	Introduction . . . . .	188
6.3	Calculation . . . . .	191
6.4	Results and discussion . . . . .	195
6.5	Summary . . . . .	200
6.6	Bibliography . . . . .	202
<b>7</b>	<b>Appendix</b>	<b>203</b>
7.1	Multipole expansion of the Hamiltonian . . . . .	204
7.2	Matrix elements in the Hund's case (d) basis for the Stark effect arising from Rydberg-Rydberg electric dipole transition moments . . . . .	209
7.3	Matrix elements in the Hund's case (d) basis for the Stark effect due to the permanent dipole moment of the ion-core . . . . .	212
7.4	Hamiltonian expressed in the Hund's case (d) basis set . . . . .	215
7.5	Stark effect matrix elements expressed in the Hund's case (b) basis set . . .	216
7.6	Bibliography . . . . .	218



# List of Figures

- 2.1 Correlation between Hund's case (d) (left and right) and Hund's case (b) (center) states for  $\ell = 3$ , and the allowed transitions into them from an  $N = 7$  level of a  $^2\Sigma^+$  state with predominant d character. States of positive parity are blue (solid line) and the states of negative parity are red (dashed line). Hund's case (b) states are formed by mixing three or four case (d) states of the appropriate parity. Spin components of the doublet are not represented on the diagram. . . . . 40
- 2.2 Calculated polarization dependence of the double resonance transition intensities of the composite  $N \leftarrow N'' + 1 \leftarrow N''$  lines (R pump). The  $N''$ -dependence of  $\mathcal{R}(N, N', N'')_{\perp}$  and  $\mathcal{R}(N, N', N'')_{\parallel}$  is represented on panels (a) and (b) (see the text for the explanation). The values of the ratios are plotted versus the ground state rotational quantum number,  $N''$ . Note that points with  $N < \Lambda$ ,  $N' < \Lambda'$ , and  $N'' < \Lambda''$  will be absent, as well as Q branches for  $\Lambda = 0$ . P branches are red (dashed line), Q branches are black (solid line) and R branches are blue (dotted line). . . . . 49
- 2.3 Experimentally observed polarization dependence of the intensity of a P(1) and R(1) pair of transitions into a  $^2\Sigma^+$  Rydberg state with R(0) pump pulse. The upper trace is for the case of two photons having the opposite helicity, and the lower is for same helicity. The P transition in the lower trace should be absent and its intensity is due to the imperfect polarization selection. . . . 54

3.1 Interference effects in the intensity of P (blue) and R (red) branches between a pure Hund's case (b) lower state,  $N' = 3$ , and an upper state that is mixed in this basis. Plotted is the transition intensity (scaled to 1) as a function of the mixing coefficient,  $\alpha$ . In a) the transition is into the states  $\alpha |f, \Sigma^+\rangle + \sqrt{1 - \alpha^2} |f, \Pi^+\rangle$ , from a lower state,  $|d, \Sigma^+\rangle$ . The plot for the case of the  $\alpha |f, \Sigma^+\rangle - \sqrt{1 - \alpha^2} |f, \Pi^+\rangle$  upper state is a mirror image of the plot in a) with the  $y$  axis as the axis of reflection. Plot a) is a square of the sum of  $\Sigma^+$  and  $\Pi^+$  contribution plotted in b), for both P (blue) and R (red) transitions. Distortion of the pattern in a) by  $\ell$ -mixing is shown in c). Here both states involved in the transition are  $\ell$ -mixed in addition to being  $\Lambda$ -mixed, the lower state is  $\eta |p\rangle - \sqrt{1 - \eta^2} |d\rangle$  and the upper state is  $\theta |d\rangle + \sqrt{1 - \theta^2} |f\rangle$ , with  $\eta = 0.5$  and  $\theta = 0.5$ . Both a) and b) plots were produced using the Eq. (5) from [3], but with a correction that  $(1 + \delta_{\Lambda',0} + \delta_{\Lambda,0} - 2\delta_{\Lambda',0}\delta_{\Lambda,0})$  in that equation should appear with the exponent  $\frac{1}{2}$  instead of  $-\frac{1}{2}$ . It was assumed that  $S = 0$ ,  $J = N$ , and  $M_J = 0$  in the plot. The intensities are scaled in the same manner as in a). Since there are no  $\Sigma^-$  states in the CaF Rydberg supercomplex, there are no interferences in the Q branches excited from a  $\Sigma^+$  intermediate state. . . . . 65

3.2 Stark effect in the Rydberg states of atomic H,  $m_\ell = 1$ . The external electric field removes the degeneracy between the  $n - |m_\ell|$  states with different values of  $\ell$ , and these states tune linearly with the field. When the field increases above  $E_{Stark} = \frac{1}{3n^5}$  (in atomic units), the states belonging to different  $n$ -manifolds cross. Due to the conservation of the Runge-Lenz vector, which is diagonal in the parabolic basis (in which Schrödinger equation for the hydrogen atom in an external electric field is analytically soluble), the states with different values of the  $n_1$  parabolic quantum number ( $n = n_1 + n_2 + |m_\ell| + 1$ ) cross even though they have same value of  $m_\ell$ . Reprinted with permission, Fig. 5 from E. Luc-Koenig and A. Bachelier in J. Phys. B 13, 1743 (1980). Copyright (1980) by the Institute of Physics. . . . . 68

3.3 Stark effect in  $n^* = 15$ ,  $m_\ell = 0$ , Rydberg states of atomic Li. In addition to the Stark manifold centered around integer values of  $n^*$ , states with nonzero quantum defects, which tune quadratically with the field, become apparent. Since core-penetration removes the supersymmetry present in hydrogen, the states that belong to neighboring values of  $n^*$  interact above Inglis-Teller limit and undergo avoided crossings. Reprinted with permission, Fig. 7 from M. L. Zimmerman, M. G. Littman, M. M. Kash, and D. Kleppner, published in Phys. Rev. A 20, 1979, 2251. Copyright (1979) by the American Physical Society. [9]. . . . . 70

3.4 Absolute value of the transition dipole moments in which  $\ell$  of the Rydberg electron changes by  $\pm 1$ , in atomic units. Part a) gives the variation of the absolute value of the  $\langle n' = 13, \ell' = 3 | \mu | n, \ell = 4 \rangle$  transition dipole moment with  $n$ , calculated using hydrogenic wavefunctions (for integer values of  $n$ ). b) displays the dependence of the absolute value of the intracomplex (same- $n^*$ ) transition dipole moments on the quantum defect,  $\delta$ , for the  $\langle n^{*'} = 13, \ell' = 0, 1, 2, 3 | \mu | n^* = n^{*' } + \delta, \ell = \ell' + 1 \rangle$  transition moment, where  $\delta$  varies between -1 and 1. Nonhydrogenic dipole moments were evaluated using the method described in [10]. . . . . 72

3.5 Calculated or experimentally observed (where available) energies of all of the the core-nonpenetrating ( $3 \leq \ell \leq 12$ ) states that belong to the  $N^+ = 3$  cluster in  $n^* = 13$ . Most of the states are located near the center of the cluster, especially at higher values of  $\ell$  and  $N$ . Outliers are found among lower- $\ell$ , lower- $N$  states for which the evolution toward Hund's case (d) is not complete, or where core-penetration effects are non negligible. . . . . 84

3.6 Stark effect in the energy region around the integer value of  $n^* = 13$ , experimentally observed in double resonance spectra from the  $N' = 1$  intermediate state, in the  $pp$  polarization arrangement. A weak electric field causes the Stark manifolds associated with different values of  $N^+$  to appear, but as the field increases, these manifolds merge. The electric field in V/cm is given on the right hand side of the plot. The  $N^+$  values of the dominant zero-field bright features are marked on the plot. . . . . 86



3.7 Interaction among  $f(-3)$ ,  $g(-4)$ , and  $13.19\ ^2\Sigma^+$  states. The  $\ell(\ell_R)$  labels at high  $N$  correspond to the assignments in [6]. Marker sizes approximately represent the experimentally observed intensities of the spectral features. The interactions among these three states become apparent only for  $N \leq 4$  rotational levels, and could remain unnoticed if the lowest- $N$  rotational assignments are not available. . . . . 89

3.8 Calculated (upper traces) and experimentally observed (lower traces) Stark effect in the double resonance spectra of the Rydberg states of CaF in the vicinity of  $n^* = 13$ . Spectra are accessed through the  $N' = 3$  level of the  $F'\ ^2\Sigma^+$  intermediate state (accessed through an R pump transition from the ground state) in the  $pp$  polarization arrangement. The electric field is 0 V/cm (a), 60 V/cm (b), 120 V/cm (c) and 180 V/cm (d). . . . . 91

3.9 Stacked double resonance spectra at 0 V/cm (a) and 70 V/cm (b), recorded from  $N' = 0, 1, 2,$  and  $3$  (bottom to top), in the  $pp$  polarization arrangement. Electric field induced mixing ( $\Delta\ell = \pm 1, \Delta N = 0, \pm 1, \Delta N^+ = 0$ ) results in intensity borrowing and the appearance of new features in the spectrum. Transitions that terminate in different values of  $N^+$  are color-coded according to the value of  $N^+$ , with the corresponding values of  $N^+$  given in the same color on the plot. . . . . 93

3.10 Calculated polarization dependence of the double resonance transition intensities of the composite (transition intensities summed over the transitions among the unresolved spin-rotation components)  $N \leftarrow N' = N'' + 1 \leftarrow N''$  lines (R pump), when both photons are circularly polarized. The plots show the  $N''$ -dependence of the ratio of the transition intensity with two photons of the same helicity to that of two photons with opposite helicity ( $N''$  is the ground state rotational quantum number). Note that points with  $N < \Lambda$ ,  $N' < \Lambda'$ , and  $N'' < \Lambda''$  must be absent, as well as Q branches, for  $\Lambda = 0$ . P, Q, and R branches are plotted in dashed, solid, and dotted line, respectively. For more details see [3]. . . . . 96

3.11 Double resonance spectrum of CaF at 250 V/cm in the vicinity of  $n^* = 13$ , recorded from  $N' = 1$  in RHCP-RHCP-vertical (red) and RHCP-LHCP-vertical (blue) arrangements. The arrow identifies the region in the spectrum where the  $N$ -mixing within a particular  $N^+$  cluster due to the external electric field is incomplete, but memory of the polarization dependence is not yet lost. 98

3.12 Double resonance spectrum of CaF at 250 V/cm in the vicinity of  $n^* = 13$ , recorded from  $N' = 1$  in  $pp$  (red) and  $ps$  (blue) arrangements. The arrow identifies a feature that exhibits a distinct Q-like polarization dependence at 250 V/cm, even though the surrounding features have lost their memory of the polarization dependence due to  $N$ -mixing induced by the field. This polarization behavior, different from other features in the  $N^+ = 3$  cluster at the same electric field amplitude, is explained by an accidental degeneracy between two states that have different values of  $N^+$ . . . . . 98

4.1	Scheme of our 20 Hz THz spectrometer: a $\approx 100$ fs pulse output by the Spitfire laser at 800 nm is split into pump and probe pulses at the beamsplitter BS. The pump pulse is focused onto a MgO-doped LiNbO <sub>3</sub> crystal to generate THz radiation. The THz pulse (thick line) is collimated and focused twice by four parabolic mirrors (PM1, PM2, PM3, and PM4). The sample cell can be located in either the collimated or focused region of the THz beam. The delay between the pump and probe pulses is varied by stepping a delay stage in the probe beam. Both the probe and THz beams are focused onto ZnTe. ZnTe was used for free space electrooptic sampling. The polarization rotation of the probe pulse is measured using a balanced photodiode pair (BPD) after converting its linear polarization into elliptical (using a quarter waveplate, $\lambda/4$ ) and spatially separating the two polarization components (in a Wollaston prism WP). . . . .	110
4.2	Four THz pulses (electric field transients and Fourier transforms), generated under different experimental conditions. Pulse a) was generated in the Cherenkov arrangement, with a $60 \times 15 \times 25$ mm LiNbO <sub>3</sub> crystal, while b), c), and d) were generated in the perpendicular arrangement, with 2.5 mm, 100 $\mu\text{m}$ and 30 $\mu\text{m}$ thick 0.6 % MgO-doped LiNbO <sub>3</sub> . The detection scheme changed between recording these spectra (spectra were taken: a), 06/16/04 b) 06/02/05, c) 11/10/06, and d) 01/03/07), and the absolute intensities cannot be directly compared between them. Water absorption was not removed in a) and b). . . . .	116
4.3	Calculated frequency dependence of the filter frequency function due to the finite aperture of the four parabolic mirrors in the $4f$ arrangement, with $f_{PM_1} = f_{PM_4} = 10$ cm and $f_{PM_2} = f_{PM_3} = 20$ cm (see Fig. 4.1). . . . .	118

4.4	Experimentally recorded absorption spectrum of atmospheric water, before the water vapor was removed from the spectrometer by building an enclosure which was dried with a desiccant and purged with N <sub>2</sub> . . . . .	120
4.5	Free Space Electro-optic Sampling used to measure $E_{THz}$ in our THz spectrometer: both the THz and 800 nm probe pulses are focused onto a 500 $\mu\text{m}$ thick ZnTe crystal that has a large electrooptic coefficient, followed by a quarter waveplate ( $\lambda/4$ ) that converts the linear polarization of the probe pulse into an elliptically polarized pulse. The distortion from circular polarization is a measure of $E_{THz}$ . A Wollaston prism (WP) spatially separates the two polarization components, which are then detected on a balanced photodiode pair (BPD). The signal difference between the two photodiodes, detected in a phase-sensitive scheme using a lock-in amplifier, is proportional to $E_{THz}$ . A boxcar, acting as a sample-and-hold device, precedes the lock-in amplifier in the low pulse repetition-rate modification of the THz spectrometer. . . . .	122
4.6	Phase sensitive detection: alternate probe pulses ( $P'$ ) are modified in the electrooptic crystal by the presence of the THz pulse (unmodified pulses are labeled by P). The signal from the balanced photodiode pair is multiplied by the sinusoidal reference frequency in the lock-in amplifier. The reference frequency has opposite phases between the P and $P'$ pulses. The lock-in amplifier thus effectively subtracts the intensities of two successive pulses, and provides a direct measure of $E_{THz}$ . . . . .	125
4.7	The THz and probe beams propagate collinearly ( $k_{THz}$ and $k_p$ ), impinging on the (110) surface of the ZnTe crystal. The angle that the polarization vectors make relative to the $z$ axis of the crystal are $\alpha$ and $\phi$ for the THz and probe beams, respectively. . . . .	126
4.8	Frequency response of a FSEOS detector with a 500 $\mu\text{m}$ thick ZnTe crystal, calculated using Eq. (4.8). . . . .	128

4.9	Triggering scheme in the 20 Hz THz spectrometer: the Q-switch output signal from the Evolution laser at 1 kHz triggers the Spitfire SDG. The SDG is capable of frequency conversion to 40 Hz. The SDG drives the two Pockels cells in the Spitfire laser at 40 Hz and triggers a Stanford Research Systems Delay Generator, which provides a trigger for the optical chopper and the second Stanford Research Systems Delay Generator. The second SRS DG converts the frequency from 40 Hz to 20 Hz and triggers the Q switch in the Nd:YAG laser. The second SRS DG also provides the trigger for Nd:YAG laser flashlamps, but with almost 50 ms delay, effectively triggering the flashlamps prior to the arrival of the next pulse from the Spitfire laser. Timing jitter associated with long delays is thus transferred to the triggering of the flashlamps, as the experiment is much less sensitive to the timing of the flashlamp firing as it is to that of the Q switch. . . . .	130
4.10	Gas cell for UV-THz double resonance experiments: the THz beam enters and exits the cell through a pair of high-resistivity Si windows (HR Si W). The Si surfaces inside the cell are polished so that the UV beam, entering through a perpendicularly mounted Brewster window (BW), is reflected, propagating collinearly with the THz beam through the cell. The fluorescence is collected through a side window (SW). . . . .	134
4.11	Experimentally recorded CH <sub>3</sub> F TDTHz spectrum at 100 Torr in an 18.5 cm long gas cell. The spectrum was recorded using a 2.5 mm thick, 0.6 % MgO-doped LiNbO <sub>3</sub> crystal at 1 kHz, before removal of water vapor absorption, and before numerous improvements to the spectrometer, described in the text, were made. The duration of the electric field transient used to generate the spectrum was $\approx$ 160 ps, respectively. . . . .	136

4.12	Experimentally recorded spectra of H <sub>2</sub> CO at 5.1 Torr a), and 500 mTorr b). The spectra were recorded at 20 Hz using a 30 μm thick 0.6 % MgO-doped LiNbO <sub>3</sub> crystal. The transient durations used to generate the Fourier transforms were ≈ 160 ps, and ≈ 900 ps in a) and b). . . . .	138
4.13	Calculated frequency dependence of $\alpha L/2$ for rotational transitions of H <sub>2</sub> CO at 500 mTorr and room temperature. . . . .	140
4.14	Calculated frequency dependence of $\Delta kL$ for rotational transitions of H <sub>2</sub> CO at 500 mTorr and room temperature. . . . .	141
4.15	The pulse-averaged bandwidth of a dye laser pulse with no extracavity etalon is approximately 1 GHz. However, in each pulse a mode of the 0.05 GHz width is produced. . . . .	148
5.1	When an external electric field, $E_I$ , which causes ionization, is ramped linearly in time, states with higher energy (and higher $n^*$ ), such as $R_2$ , are ionized earlier than states with lower energy, such as $R_1$ . A time-of-flight mass spectrometer can be used to determine from which state the ionization occurs. The time of flight from the excitation region to the MCP detector is short compared to the time between the two ionization pulses. . . . .	154
5.2	In this experiment, a pulsed ionizing electric field, $E_I$ , has a value sufficient to ionize the higher energy state, $R_2$ , but not sufficient to ionize the lower energy state, $R_1$ . When a microwave pulse, resonant with the $R_2 \leftarrow R_1$ transition, precedes the ionization pulse, ions are detected at laser frequencies resonant with transitions into <i>both</i> $R_2$ and $R_1$ . . . . .	155

5.3	32.5 - 39 GHz chirped pulse microwave spectrometer: AWG is an arbitrary waveform generator, PLDRO is a phase locked dielectric resonator oscillator, M1 is a broadband mixer, IS is an isolator, F1 is a filter, X4 is a frequency quadrupler, X2 is a frequency doubler, H1 and H2 are horn antennas, M2 is a broadband mixer, X3 is a frequency quadrupler, and F3 is a filter. The operation of this spectrometer is discussed in the text. . . . .	159
5.4	$J = 3 \leftarrow J = 2$ transition in OCS, recorded with a 10 MHz sweep in 1 $\mu$ s, with 1000 signal averages. . . . .	162
5.5	$J = 5 \leftarrow J = 4$ (left) and $J = 6 \leftarrow J = 5$ (right) transitions in trifluoropropyne, observed with a 6.6 GHz sweep in 1 $\mu$ s, averaged over 1000 signal pulses. . . . .	163
5.6	Dependence of the CPMW signal intensity on the sweep rate, measured on the $J = 6 \leftarrow J = 5$ transition in trifluoropropyne at 34.535 GHz. . . . .	163
5.7	6.6 GHz acetone sweep in 1 $\mu$ s, averaged over 10000 pulses. Upper and lower sideband frequencies of the downconverted signal are given at the bottom and top of the Figure, respectively. . . . .	164
5.8	69.6 - 84 GHz chirped pulse microwave spectrometer: AWG is an arbitrary waveform generator, PLD, PLDRO 1 and 2 are phase locked dielectric resonator oscillators, M 1-3 are broadband mixers, C 1 and 2 are isolators, A1 is an amplifier, F 1 and 2 are filters, X4 is a frequency quadrupler, X2 is a frequency doubler, T 1-4 are attenuators, H1 and 2 are horn antennas, L1 and 2 are teflon lenses, M 1 and 2 are mirrors, GO is a Gunn oscillator, GPC is a Gunn phase control unit, DP is a diplexer, LNA is a low noise amplifier, and WD is a Wilkinson power divider. The operation of this spectrometer is discussed in the text. . . . .	167

5.9	In order to optimize the free-space microwave transmission between horns H1 and H2, the optimum distances, $l_{H1,L1}$ , $l_{L1,L2}$ , and $l_{L2,H2}$ , have been determined in a table-top experiment. A focus located between H1 and H2 is achieved using two teflon lenses L1 and L2. . . . .	168
5.10	Arrangement of the microwave elements used to focus the microwave beam at the spot where it intersects the molecular beam. An aluminum mirror M1, with a $2 \times 0.5$ " diameter hole in the center, milled at $45^\circ$ to the surface, is used to combine the microwave beam with the two laser pulses. Labels of the microwave components, and distances between them, are the same as in Fig. 5.9. . . . .	169
5.11	Double resonance spectrum of Rydberg states of Ca in the region $84 \geq n^* \geq 33$ , after compensation of stray homogeneous fields and minimization of inhomogeneous fields in the excitation region. The inset shows the region of $84 \geq n^* \geq 60$ . . . . .	173
5.12	Energy level schemes for the three optical-optical-microwave experiments attempted on atomic Ca. The same intermediate state, $4s5p^1P(J = 1)$ was used in all three cases. . . . .	174
5.13	Microwave-assisted ionization: when the ionizing electric field strength is 390 V/cm (uppermost trace), it is strong enough to ionize both $4s32d^1D(J = 2)$ and $4s33s^1S(J = 0)$ states. However, when the field is decreased to 375 V/cm, neither of these two states are ionized (middle trace), but $4s33p^1P(J = 1)$ (not a bright state in this spectrum) is ionized. In the presence of a microwave pulse ionization, ionization happens from both of these states (lowermost trace), probably due to non-resonant and multiphoton processes. . . . .	176



5.14	The line position and linewidth of the $4s36p\ ^1P(J = 1) \leftarrow 4s36s\ ^1S(J = 0)$ Rydberg-Rydberg transition dependence on the nominal voltage of one of the plates between which the excitation occurs. The voltage on the other plate is nominally 1500 V. These spectra are recorded prior to balancing out of the stray homogeneous fields and minimization of the inhomogeneous fields between the plates. . . . .	181
5.15	$4s36p\ ^1P(J = 1) \leftarrow 4s36s\ ^1S(J = 0)$ transition in Ca with 60 dB attenuation after H1 (red line) and after a book has been inserted in the microwave beam in addition to 60 dB attenuation (black line). The transition frequency reported in [4] is indicated by a vertical line. . . . .	183
6.1	Simulated pure electronic Rydberg-Rydberg spectrum of CaF, acquired using time domain THz spectroscopy. The launch state was a strongly $\ell$ -mixed, $N^+$ -mixed, $f(-3)$ , $N = 2$ state. The $N^+$ characters of each feature observed in the spectrum, and those of the launch state, are represented by the color coding of each bar next to the corresponding spectral feature. Even values of $N^+$ are represented by shades of blue and odd values of $N^+$ by shades of red. . . . .	196
6.2	Simulated pure electronic Rydberg-Rydberg spectrum of CaF, acquired using the chirped-pulse microwave spectroscopy. The launch state was $f(3)$ , $N = 9$ . The $N^+$ characters of each feature observed in the spectrum and of the launch state, are represented by the color coding of each bar next to the corresponding spectral feature. Even values of $N^+$ are represented by shades of red and odd values of $N^+$ by shades of blue. . . . .	198



# List of Tables

3.1	Selection rules for interactions discussed in text. Matrix elements for these types of interactions are nonzero when the conditions from the table are satisfied.	63
3.2	Best fit values for the $\ell$ mixing coefficients of rotationless $p, d, f, g,$ and $h$ ${}^2\Sigma^+$ states. The $s$ ${}^2\Sigma^+$ basis state was not included in the fit, as it was not located near an integer value of $n^*$ . Its $\ell$ -decomposition corresponds to that of [5]. Nonunity in the sum of <i>squared</i> mixing coefficients is due to the loss of $v^+ = 1$ basis state character due to coupling with higher- $v^+$ states.	87
3.3	Assignments of lowest- $N$ , low- $\ell_R$ , $f$ -states ( $\text{cm}^{-1}$ ).	94
3.4	Assignments of lowest- $N$ , low- $\ell_R$ , $g$ -states ( $\text{cm}^{-1}$ ).	94
3.5	Assignments of lowest- $N$ , low- $\ell_R$ , $h$ -states ( $\text{cm}^{-1}$ ).	94
4.1	Electro-optic characteristics of ZnTe and LiNbO <sub>3</sub> .	113
4.2	Characteristics of materials often used to generate THz radiation. Values are given for 1 THz, except for DAST, for which values are given for 0.8 THz. $d_{eff}$ is given at 800 nm. All values are for room temperature, except for stoichiometric LiNbO <sub>3</sub> (sLN) at 100 K. The table is reproduced from [15], and for more details refer to this publication.	123
4.3	Rotational constants for molecules studied using TDTS.	137



# Chapter 1

## Introduction

The Rydberg states of CaF permit the study of the interaction of an electron with a strongly anisotropic object, the highly polar ion-core,  $\text{CaF}^+$ .  $\text{CaF}^+$  has one of the largest dipole moments in a diatomic molecular cation  $\approx 9$  D [1] (origin at center of mass of  $\text{CaF}^+$ ). A strongly polar ion-core, together with core-penetration in lower- $\ell$  states ( $\ell \leq 3$ ), result in  $\ell$  not being even an approximately good quantum number for the core-penetrating states<sup>†</sup>. For core-nonpenetrating states,  $\ell$  is an approximately good quantum number. Due to the presence of the polar ion-core,  $\ell$ -mixing is profoundly different from what occurs in other small molecules, such as  $\text{H}_2$  and  $\text{NO}$ , for which the Rydberg systems have been well characterized. This paradigmatic character of the Rydberg system of CaF has resulted in a long-standing Field group research interest in this molecule.

Rice, Martin, and Field proposed a ligand-field model to describe the valence states of alkaline earth fluoride molecules, including CaF [2]. In this model, the electronic structure of  $\text{Ca}^+$  is perturbed by a polarizable point-charge  $\text{F}^-$  ion. Although the energies and mixed- $\ell$  characters of the lowest excited electronic states of CaF are described well, as  $n^*$  increases, the electronic cloud localized on  $\text{Ca}^{2+}$  expands and starts to encompass the  $\text{F}^-$  ion, and the

---

<sup>†</sup>The distinction between core-penetrating and core-nonpenetrating states is made based on whether the location of the inner turning point of the wavefunction of the Rydberg electron is inside or outside of the ion core, respectively. As  $\ell$  increases, the centrifugal barrier increases, and the turning point moves outward from the ion-core.

ligand field model starts to break down.

Harris and Jungen [3] developed a generalized quantum defect theory treatment of intermediate- $n^*$  Rydberg states of CaF. In this framework, the most important aspects of the electronic structure of the singly-excited CaF are derived from the  $\text{Ca}^+$  atomic properties - quantum defects  $\mu_s$ ,  $\mu_p$ , and  $\mu_d$  of  $\text{Ca}^+$ . Murphy et al. [4] characterized the  $s \sim p \sim d$ -mixed supercomplexes of the low- $n^*$  Rydberg states in the  $n^* = 6 - 8$  region using multichannel quantum defect theory, and performed a least-square fit to determine the eigenquantum defects and mixing angles. Due to the larger partial core-penetration at lower- $n^*$ , the investigation of the evolution of the molecular parameters of the ion-core extended to higher- $n^*$ .

An extensive list of assignments of the  $0 \leq \ell \leq 3$  Rydberg states in the region  $12 \leq n^* \leq 18$  is presented in [5]. The effective Hamiltonian approach employed by Gittins et al. [5] was complemented by the MQDT model, based on the same data set, published in [6]. Kay et al. developed a method to make model-free assignments of the  $f$  and  $g$  core-nonpenetrating states, and extended the region of the available assignments to  $17 \leq n^* \leq 20$ . An extended MQDT fit [7], including  $n^* \approx 12 - 18$ ,  $N = 0 - 14$ ,  $v^+ = 1$ ,  $n^* \approx 9 - 10$ ,  $N = 0 - 14$ ,  $v^+ = 2$ , and  $n^* \approx 7$ ,  $N = 3 - 10$ ,  $v^+ = 3$  regions, produced a complete empirical  $0 \leq \ell \leq 3$  quantum defect matrix and its matrix derivatives with respect to internuclear separation,  $R$ . The determination of the quantum defect derivatives with respect to  $R$  was enabled by observation of several higher- $v^+$  interlopers. Based on the predicted Franck-Condon factors, observation of higher- $v^+$  interlopers for  $v^+ > 1$  was unexpected. However, a mixing between two  $v^+$  vibrational states is mediated by the  $\text{Ca}(^1\text{S}) + \text{F}(^2\text{P})$  repulsive curve, thus indirect interaction disrupts the expected transition intensity patterns. Even though our knowledge of the electronic structure of CaF is extensive, the characterization of the interaction of the Rydberg system with the repulsive predissociation curve remains incomplete. An investigation of systematic disruptions of the expected transition intensity patterns will enable us to get information about the repulsive curve.

An augmented long-range model has been developed by Kay et al. [8] to describe the

interaction of the  $f$ ,  $g$ , and  $h$  core-nonpenetrating Rydberg states with the  $\text{CaF}^+$  ion-core. In that model, the electron-core interaction is described in terms of multipole moments and polarizabilities of the ion-core. A broad shape resonance [9] and "stroboscopic" [10] resonances between the electronic and rotational motions [11] have been predicted in  $\text{CaF}$ .

One important contribution of the work presented in this thesis is in developing general methods to make rotational assignments without having to rely on standard spectroscopic methods, which require the identification of *both* P and R branches (combination differences). As will be explained in detail in the text, the interplay between  $\ell$ -mixing and  $\ell$ -uncoupling distorts the expected transition intensity patterns [12], and almost regularly results in one of the rotational branches being weak or absent. The problem is especially severe at low- $N$  rotational levels, which are most important for the determination of the rotationless molecular parameters. A method relying on polarization diagnostics in multiple-resonance experiments, presented in Chapter 2, provides a way to make reliable rotational assignments in the absence of combination differences, even for low- $N$  rotational levels. The expressions derived here for the transition intensities in multiple resonance experiments are given for resolved and unresolved spin-multiplets, and their usefulness extends well beyond the Rydberg states of  $\text{CaF}$ .

The second major contribution of the work presented in this thesis is in the description of the Stark effect in Rydberg states of  $\text{CaF}$ , presented in the Chapter 3. Unlike other small molecules for which the Stark effect in Rydberg states has been characterized, the Rydberg states of  $\text{CaF}$  are strongly  $\ell$ -mixed, even in the absence of an external electric field. Also, as a fundamental difference from atomic Rydberg states, the decoupling of the Rydberg electron from the ion-core in molecular Rydberg states proceeds in several stages. We have characterized this separation of the stages of decoupling, and used it to provide diagnostic insights into the higher- $\ell$  Rydberg states.

The third major contribution of the work presented in this thesis is in developing the experimental methods for recording *pure electronic spectra*. The electric dipole transition

moments among the Rydberg states of the same value of  $n^*$  scale approximately as  $n^2$  [13]. Even at moderate  $n^*$ , these Rydberg-Rydberg transition moments are exceptionally large, and much larger than the permanent dipole moment of the ion-core. As the selection rules for the Rydberg-Rydberg transitions, which rely on these large transition dipole moments, specify that the quantum numbers for the Rydberg electron must change, but the quantum numbers of the ion-core must not change, the result is a spectrum dominated by the electronic transitions, with rotational and vibrational transitions *de facto* forbidden, hence the name "Pure Electronic Spectroscopy". We built a low-repetition rate time-domain THz spectrometer and a chirped-pulse microwave spectrometer in order to record pure electronic spectra. Detailed descriptions of the two experimental methods are presented in Chapters 4 and 5.

The fourth major contribution is in paving the way for the quantitative use of transition intensities in Rydberg-Rydberg spectra to extract information about the different mechanisms of the interaction between the Rydberg electron and the ion-core, and, in particular, to separate the dipole and quadrupole interactions. In multiple resonance frequency-scanning spectroscopic methods, the transition intensities are corrupted by pulse-to-pulse intensity and spectral mode fluctuations. When a Rydberg-Rydberg spectrum is recorded in transmission, in the time domain, relative transition intensities become quantitatively useful. These relative transition intensities in Rydberg-Rydberg spectra can be related to the mixing coefficients among the Rydberg states. Spectra recorded from  $\ell$ -mixed and pure- $\ell$  launch states, provide complementary diagnostic information and give insights into the different multipolar mechanisms of interaction between the Rydberg electron and the ion core. Reduction of spectral congestion that is inherent to the pure electronic spectroscopy provides a way to examine the Rydberg systems vastly more complex than those of CaF.



## 1.1 Bibliography

- [1] S. N. Altunata, S. L. Coy, and R. W. Field. *J. Chem. Phys.*, 123:084318, 2005.
- [2] S. F. Rice, H. Martin, and R. W. Field. *J. Chem. Phys.*, 82:5023, 1985.
- [3] N. A. Harris and Ch. Jungen. *Phys. Rev. Lett.*, 70:2549, 1993.
- [4] J. E. Murphy, E. Friedman-Hill, and R. W. Field. *J. Chem. Phys.*, 103:6459, 1993.
- [5] C. M. Gittins, N. A. Harris, M. Hui, and R. W. Field. *Can. J. Phys.*, 79:247, 2001.
- [6] Ch. Jungen and A. L. Roche. *Can. J. Phys.*, 79:287, 2001.
- [7] R. W. Field, C. M. Gittins, N. A. Harris, and Ch. Jungen. *J. Chem. Phys.*, 122:184314, 2005.
- [8] J. J. Kay, S. L. Coy, V. S. Petrović, B. M. Wong, and R. W. Field. *J. Chem. Phys.*, 128:194301, 2008.
- [9] S. N. Altunata, S. L. Coy, and R. W. Field. *J. Chem. Phys.*, 124:194302, 2006.
- [10] B. Tribollet P. Labastie, M. C. Bordas and M. Broyer. *Phys. Rev. Lett.*, 52:1681, 1984.
- [11] J. J. Kay, S. N. Altunata, S. L. Coy, and R. W. Field. *Mol. Phys.*, 105:1661, 2007.
- [12] Hélène Lefebvre-Brion and Robert W. Field. *The Spectra and Dynamics of Diatomic Molecules*. Elsevier Academic Press, 2004.
- [13] Thomas F. Gallagher. *Rydberg Atoms*. Cambridge University Press, 1994.



## Chapter 2

# Polarization dependence of transition intensities in double resonance experiments: Unresolved Spin Doublets

### 2.1 Prologue

The text of this chapter was published as V. S. Petrović and R. W. Field “Polarization dependence of transition intensities in double resonance experiments: Unresolved spin doublets”, *Journal of Chemical Physics* 128, 014301 (2008). Polarization-based low- $N$  rotational assignments, made using the method described in this chapter, were used in developing the extended long-range model for the description of the  $f$ ,  $g$ , and  $h$  states of CaF, published as J. J. Kay, S. L. Coy, V. S. Petrović, B. M. Wong and R. W. Field “Separation of long-range and short-range interactions in Rydberg states of diatomic molecules”, *Journal of Chemical Physics*, 128, 194301 (2008), and these assignments were necessary to interpret the Stark effect in the Rydberg states of CaF, described in Chapter 3.

## 2.2 Introduction

Information about molecular structure and the mechanism of intramolecular energy flow is encoded in a frequency domain spectrum. At low excitation, the spectrum is sparse, patterns are evident, and a variety of methods suffices to determine, without ambiguity, the quantum numbers of the initial and final eigenstates of the vast majority of observed transitions. Assignments are definitive. At high excitation, or when electron spin and orbital angular momentum quantum numbers are not zero, the spectrum is not sparse, patterns are either multiply overlaid, subtly distorted, or shattered almost beyond recognition. Often, a key dynamical detail is revealed in a tiny distortion of a pattern, a small level splitting, or intensity anomalies. Special methods are required to record and definitively assign complex and congested spectra.

In order to obtain information from a spectrum it is essential to make definitive rotational assignments. The traditional method for making rotational assignments without fitting to *a priori* models is based on rotational combination differences, a method in which two spectral features ending in the same upper eigenstate (i.e.  $P(J+1)$  and  $R(J-1)$ ), or the same lower eigenstate (i.e.  $P(J)$  and  $R(J)$ ) are matched together. Combination differences are never corrupted by intensity or level-shift perturbations, however, they are often unobservable, either owing to rigorous selection rules, or special effects [1].

A tool that provides assignments as reliably as combination differences, but is usable when combination differences are not accessible, is required. In multiple resonance experiments, where photons of more than one frequency are absorbed, it is possible to use polarization to facilitate the assignment procedure. The photons in successive transition steps can have the same or different polarization, and the transition intensity is, in general, expected to be affected by the relative orientation of their polarization directions. Then, instead of searching for matching P and R pairs, the spectrum is recorded twice, in two different polarization arrangements, and the observed changes in relative signal intensities guide the rotational assignment.

Making rotational assignments in multiple resonance spectra is profoundly simplified by limiting the possible second step (probe) transitions by state selection in the first step (pump). By recording the spectrum from different known, or easily assignable, rotational levels of an intermediate state, the spectrum is broken into subsets with limited possible values of rotational quantum numbers. Lower state rotational combination differences, when they exist, are easier to recognize in multiple resonance experiments than in one-step experiments. However, Q branches can *never* be identified using combination differences, and require either the use of a different intermediate state, when access to such a state is parity allowed, or they must be assigned after the assignment of all members of P and R branches has been completed.

Lower state combination differences do not exist for the lowest rotational levels, for which R branch transitions are absent (e.g. only a P(1) transition connects with a  $J = 0$  upper level). For example, if an R branch is used in the first step in a double resonance spectrum, the lowest accessed level in the intermediate electronic state will be  $J' = 1$ , and R branches will be missing in the upper step for  $J = 0$  and  $J = 1$  of the final state, since they would require  $J' = 0$  and  $J' = -1$  (throughout this paper the unprimed quantum numbers are reserved for the last accessed state in the sequence, primed for the intermediate state, and double primed for the ground state).

Combination differences can also be absent due to interference effects [1]. If, for example, the lower state in a transition is  $\Lambda'$  and upper state is a mixture of  $\Lambda'$  and  $\Lambda' + 1$ , then the total transition intensity will result from interference between  $\Delta\Lambda = 0$  and  $\Delta\Lambda = 1$  transition amplitudes. Destructive interference can completely suppress *either* the R or P branch, which renders both upper state and lower state combination differences unusable.

Even when both P and R branches are observed in a spectrum, there are cases when combination differences are difficult to use or give inconclusive results. Since the spacing between P( $J + 1$ ) and R( $J - 1$ ) transitions is  $2B'(2J + 1)$ , at high  $J$  the spectral region that must be scanned in order to observe both features can make the experiment difficult

either because it is rarely possible to maintain the same signal level in long scans, or because the width of the needed scan can exceed the scan range limited by the etalon free spectral range. Also, when the density of lines is comparable to the measurement precision, false combination differences can lead to incorrect assignments. Combination differences alone are not sufficient to assign *both*  $J$  and  $N$  (spin fine structure), or *both*  $N$  and  $N^+$  ( $\ell$  fine structure in near case (d) Rydberg states).

The polarization dependence of rotational lines in multiphoton experiments has been described for many kinds of spectra, for cases when there is only one angular momentum,  $J$ , and all transitions are resolved [2, 3, 4, 5, 6, 7, 8, 9, 10, 11]. Here we discuss methods that are generally applicable in multiple resonance spectra and provide reliable and robust distinctions between P, Q and R transitions, in cases where more than one rotational/fine structure quantum number is necessary for a complete description of a system, even in cases when spin fine structure is unresolved.

In the spectroscopy of Rydberg states the density of spectral features increases as  $n^{*3}$  ( $n^*$  denotes the non-integer principal quantum number corrected for the quantum defect), and spectra are inherently complex and congested due to the large number of close-lying, and interacting via  $\ell$ -uncoupling, electronic states. Because of the tendency toward uncoupling of the orbital angular momentum of the Rydberg electron from the body frame as the rotation of the molecule increases, the appropriate coupling case for the Rydberg state will change as the rotational quantum number increases.

At low rotation, the suitable coupling case will almost always be Hund's case (b). This owes to the fact that for molecules with a closed shell ion core the spin-orbit splitting scales as  $n^{*-3}$ , so as  $n^*$  increases, the spin structure becomes unresolved and the pattern-forming rotational quantum number becomes  $N$  ( $\mathbf{N} = \mathbf{J} - \mathbf{S}$ ). As the rotation increases, the orbital angular momentum of the Rydberg electron decouples from the body frame, and the pattern-forming quantum number becomes the rotational quantum number of the ion core,  $N^+$  ( $N^+ = N - \ell$ ). When this happens, the appropriate coupling case becomes Hund's case (d).

The evolution from Hund's case (b) to case (d) as the rotation increases is faster and more complete for core-nonpenetrating high- $\ell$  states than for core-penetrating low- $\ell$  ones.

Rydberg states are usually experimentally accessed in two or more steps, through low-lying valence states, which are almost always near Hund's case (a) or (b) limit. This means that the observed spectral patterns in the transition from an intermediate state into a Rydberg state will change qualitatively between low and high  $N$ . For example, if the intermediate state is in Hund's case (b), which is typical for  $\Sigma$  states, the patterns evolve from those of (b)  $\leftarrow$  (b) at low  $N$  to those of (d)  $\leftarrow$  (b) at high  $N$ . Insight into spectral patterns can be gained by decomposing both states involved in the transition in the same basis, first in nearly perfect case (b), and then in nearly perfect case (d). Propensity rules appropriate for either of these two limiting cases will get relaxed when the Rydberg state involved in the transition is in an intermediate coupling case between Hund's cases (b) and (d). Figure (2.1) shows the correlation between Hund's case (d) and Hund's case (b) states.

First, we can think of the upper, case (d), states being decomposed in terms of case (b) basis states. If the lower state in the transition is  $\Sigma$ , the allowed transition amplitude will be into the  $\Sigma$  and  $\Pi$  upper basis states. Since the upper state, in general, will have some partial  $\Sigma$  and some partial  $\Pi$  character (see Figure (2.1)), the relative intensities of the transitions will depend on the interference of the two transition moments. This means that the intensity patterns of  $\Pi \leftarrow \Sigma$  and  $\Sigma \leftarrow \Sigma$  transitions, which will be observed at low  $N$ , will evolve into intensity patterns dominated by the interference effects. This can lead to some of the spectral features becoming weak, or completely missing, with the result that combination differences often cannot be relied on to make the assignments.

Alternatively, we can decompose the Hund's case (b) states in terms of case (d) states. The already mentioned  $\Sigma$  intermediate state will be composed of several states with different values of  $N^+$ :

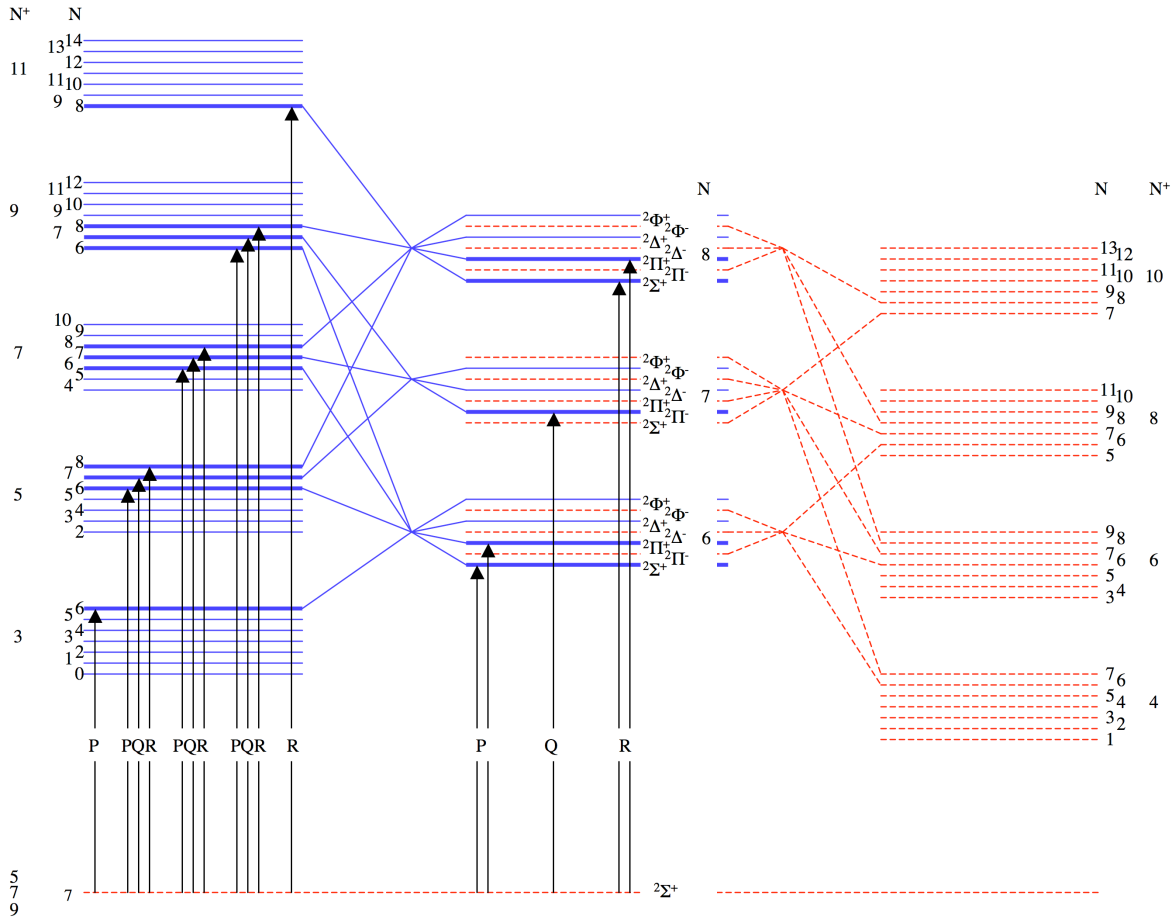


Figure 2.1: Correlation between Hund's case (d) (left and right) and Hund's case (b) (center) states for  $\ell = 3$ , and the allowed transitions into them from an  $N = 7$  level of a  $2\Sigma^+$  state with predominant d character. States of positive parity are blue (solid line) and the states of negative parity are red (dashed line). Hund's case (b) states are formed by mixing three or four case (d) states of the appropriate parity. Spin components of the doublet are not represented on the diagram.



$$|\eta, \ell, \Lambda, N\rangle = \sum_{N^+} (-1)^{N^+ - \ell + \Lambda} (2N^+ + 1)^{1/2} \begin{pmatrix} N & \ell & N^+ \\ \Lambda & -\Lambda & 0 \end{pmatrix} |\eta, \ell, N, N^+\rangle \quad (2.1)$$

Parity will limit the different  $N^+$  basis states that contribute to a case (b) intermediate state, since parity in case (d) goes as  $(-1)^{N^+ + \ell}$ . For example, if we are interested in transitions into an f Rydberg state, from a valence intermediate state with a dominant d character, the intermediate state will be a superposition of three (or four, depending on the parity) different- $N^+$  basis states (see Figure (2.3)). At high rotation, the case (d)  $\Delta N^+ = 0$  transition propensity rule limits the number of accessible  $N^+$  values of the f Rydberg state to three (or four). Within each  $\Delta N^+ = 0$  transition, there are going to be, in general, three close-lying transitions with  $\Delta N = 0, \pm 1$ .  $N$  is a rigorously good quantum number, whereas  $N^+$  is not. The polarization methods discussed here provide a rigorous assignment of  $\Delta N$ . These three  $\Delta N = 0, \pm 1$  transitions into a single  $N^+$  value will be clustered together in the spectrum, and their intensity evolution between low rotation and high rotation can be understood in terms of the interference effects discussed in the previous paragraph. At lower rotation, the  $\Delta N^+ = 0$  propensity rule is relaxed, because neither upper nor lower state is in a limiting Hund's case (d), and additional transitions appear.

These decompositions provide a basis for assigning the “other” quantum number - the one not assignable via polarization. Patterns of patterns, or metapatterns, reveal the evolution from Hund's case (b) at low  $N$  toward case (d) at high  $N$ . This evolution is manifest in both the transition intensities and positions. However, because of the rapid  $\ell$ -uncoupling, especially in core-nonpenetrating Rydberg states, as  $N$  increases, the qualitative change in the patterns is particularly abrupt for the lowest rotational levels. This fact, in addition to the absence of combination differences for these most information-rich lowest rotational levels, precludes their unambiguous assignment. Yet, in the rotationless levels of Rydberg states the information about the electronic structure is least contaminated by the coupling between the rotational and electronic motions, and can be obtained directly. Electronic

structure models are particularly sensitive to the rotationless level parameters.

In order to apply polarization measurements, which determine  $J$  directly, to indirectly establish  $N$  in the cases when  $N$  is the pattern-forming quantum number (and the  $2S + 1$   $J$  components of the fine structure are not resolved), one must consider the polarization dependence of the composite spectral features, formed from the transitions between the *unresolved* spin components.

When the spin components are resolved, the  $M$ -dependent part of the transition intensity determines the polarization dependence of the transition intensity for each of the resolved transitions ( $\hbar M$  is the lab-fixed projection of  $\mathbf{J}$ ). For this case, the polarization dependence for the individual components in double resonance spectra has been given by [5] and [3]. At high  $N$ , the transition intensities for individual spin components (the  $2S + 1$   $J$  components belonging to the same value of  $N$ ), as well as their polarization dependence, will not differ among themselves as much as at low  $N$ . Because of approximately the same transition intensity and polarization dependence at high  $N$ , even when the spin components are unresolved to form a composite line, the polarization dependence of the transition intensity for the composite line will be approximately the same as for the individual components. The polarization dependence of the composite line at high  $N$  will resemble that of a singlet  $S = 0$ ,  $\Delta S = 0$ , transition with  $J \approx N$ .

However, at low  $N$  the difference between  $N$  and  $J$  becomes apparent in the transition intensities, with the result that the polarization dependence of the individual components differs. Not only is the polarization-dependent part of each of the unresolved components not equal, but the amplitude factors, in both the lower and upper transition step differ among the components. That means that one has to sum over the intensities (or amplitudes, if an interference between two pathways is possible) of all of the allowed  $J, J', J''$  combinations of an  $N, N', N''$  transition, not only their polarization dependent parts. Bigio and coworkers [4] have used such a procedure in order to understand the body frame transition moment directionality of different spectral features, but their calculation was done only for the case

of linear polarization.

For a rotational assignment procedure, it is most beneficial to use circular polarization, because it has a much more dramatic effect on the transition intensities. Here we give a calculation of the polarization dependence of the transition intensities in a double resonance spectrum for experimental arrangements with both linear and circular polarizations. The result is given for each of the individual components of a transition, as well as for composite lines in  $N \leftarrow N' \leftarrow N''$  transitions. Our analysis assumes that there are no coherences among the states of different  $J'$ , as is the case in our experiment (see the experimental section), but it is straightforward to extend the analysis to the case when these coherences exist using the expressions given in this paper. In addition, we performed polarization measurements in order to make unambiguous low- $N$  assignments of transitions into the Rydberg states of CaF in the  $n^* = 13$  region, and to check those made at intermediate  $N$ .

## 2.3 Calculation

The transition intensity of an unsaturated double resonance transition, with two collinear excitation pulses sufficiently separated in time, denoted here by  $S$ , is given by:

$$S = \sum_{M, M', M''} |\langle \eta, \Lambda, N, S, J, M, p | \mu_{LAB} | \eta', \Lambda', N', S', J', M', p' \rangle|^2 |\langle \eta', \Lambda', N', S', J', M', p' | \mu_{LAB} | \eta'', \Lambda'', N'', S'', J'', M'', p'' \rangle|^2 \quad (2.2)$$

where summation over only one of the lab-fixed projection quantum numbers is independent. In addition to the already introduced quantum numbers,  $\hbar\Lambda$  is the projection of  $\ell$  on the internuclear axis, and  $p$  stands for parity and has value of 0 for (+) and 1 for (-) states.  $\eta$  denotes all quantum numbers not specified explicitly. The transitions, as written here, are between Hund's case (b) basis functions. In order to evaluate expression (2.2), one needs to transform the Hund's case (b) basis functions into the Hund's case (a) basis, where transition dipole matrix elements can be directly evaluated (see, for example [12] and [13]):

$$\langle \eta_a, \Lambda_a, S_a, \Sigma_a, J_a, M_a, \Omega_a | \mu_r | \eta_b, \Lambda_b, S_a, \Sigma_a, J_b, M_b, \Omega_b \rangle = \sum_q (2J_a + 1)^{1/2} (2J_b + 1)^{1/2} \begin{pmatrix} J_b & 1 & J_a \\ -M_b & -r & M_a \end{pmatrix} \begin{pmatrix} J_b & 1 & J_a \\ -\Omega_b & -q & \Omega_a \end{pmatrix} (-1)^{M_a - \Omega_a} \langle \Lambda_a | \mu_q^{(1)} | \Lambda_b \rangle \quad (2.3)$$

$\hbar\Omega$  and  $\hbar\Sigma$  are projections of  $\mathbf{J}$  and  $\mathbf{S}$  on the internuclear axis. Different spherical tensor components of the dipole operator,  $\mu$ , in the body-fixed and lab fixed frames, are denoted by the subscripts  $q$  and  $r$ , respectively. The transformation between the unsymmetrized Hund's case (b) and case (a) bases is given by [14]:

$$|\eta, \Lambda, N, S, J, M\rangle = \sum_{\Sigma, \Omega} (-1)^{N-S+\Omega} (2N+1)^{1/2} \begin{pmatrix} J & S & N \\ \Omega & -\Sigma & -\Lambda \end{pmatrix} |\eta \Lambda S \Sigma J M \Omega\rangle \quad (2.4)$$

Using equations (2.3) and (2.4), the transition dipole matrix elements between the symmetrized Hund's case (b) basis functions become:

$$\begin{aligned} \langle \eta', \Lambda', N', S', J', M', p' | \mu_r | \eta, \Lambda, N, S, J, M, p \rangle &= (-1)^{J+J'+S+1-\Lambda'+M'} \frac{(1 + (-1)^{p+p'+1})}{2(1 + \delta_{\Lambda',0} + \delta_{\Lambda,0} - 2\delta_{\Lambda',0}\delta_{\Lambda,0})^{1/2}} \\ &((2N'+1)(2N+1)(2J'+1)(2J+1))^{1/2} \begin{pmatrix} J & 1 & J' \\ -M & -r & M' \end{pmatrix} \begin{pmatrix} 1 & N & N' \\ \Lambda' - \Lambda & \Lambda & \Lambda' \end{pmatrix} \left\{ \begin{matrix} 1 & N & N' \\ S & J' & J \end{matrix} \right\} \\ \langle \Lambda' | \mu_{\Lambda'-\Lambda} | \Lambda \rangle & \quad (2.5) \end{aligned}$$

where  $q = \Lambda' - \Lambda$  is fixed by the selection of  $\Lambda'$  and  $\Lambda$ . The double resonance transition intensity,  $S$ , can be evaluated by substituting equation (2.5), and a similar expression for the lower transition, into equation (2.2). Then it is possible to separate the double resonance transition intensity into the product of three factors, given by:

$$S = \mathcal{L} \cdot \mathcal{U} \cdot \mathcal{M} \quad (2.6)$$

where  $\mathcal{U}$  is the polarization independent part of the transition intensity for the second transition, and  $\mathcal{L}$  is the polarization independent part of the transition intensity of the first transition.  $\mathcal{U}$  is given by:

$$\mathcal{U} = \frac{(1 + (-1)^{p+p'+1})^2}{4(1 + \delta_{\Lambda',0} + \delta_{\Lambda,0} - 2\delta_{\Lambda',0}\delta_{\Lambda,0})} ((2N' + 1)(2N + 1)(2J' + 1)(2J + 1)) \left( \begin{array}{ccc} 1 & N & N' \\ \Lambda' - \Lambda & \Lambda & \Lambda' \end{array} \right)^2 \left\{ \begin{array}{ccc} 1 & N & N' \\ S & J' & J \end{array} \right\}^2 |\langle \Lambda' | \mu_{\Lambda' - \Lambda} | \Lambda \rangle|^2 \quad (2.7)$$

and  $\mathcal{L}$  can be obtained from equation (2.7) by replacing the primed quantum numbers with double primed, and unprimed ones with primed.  $\mathcal{M}$  is the sum over the  $M, M', M''$  dependent part, and has the following form in the four cases of experimental interest:

$$\mathcal{M}_{\parallel} = \sum_M \left( \begin{array}{ccc} J' & 1 & J \\ -M & 0 & M \end{array} \right)^2 \left( \begin{array}{ccc} J'' & 1 & J' \\ -M & 0 & M \end{array} \right)^2 \quad (2.8)$$

$$\mathcal{M}_{\perp} = \sum_M \frac{1}{2} \left( \begin{array}{ccc} J' & 1 & J \\ -M & 0 & M \end{array} \right)^2 \left( \left( \begin{array}{ccc} J'' & 1 & J' \\ -M+1 & -1 & M \end{array} \right)^2 + \left( \begin{array}{ccc} J'' & 1 & J' \\ -M-1 & 1 & M \end{array} \right)^2 \right) \quad (2.9)$$

$$\mathcal{M}_{\odot\odot} = \sum_M \left( \begin{array}{ccc} J' & 1 & J \\ -M+1 & -1 & M \end{array} \right)^2 \left( \begin{array}{ccc} J'' & 1 & J' \\ -M+2 & -1 & M-1 \end{array} \right)^2 \quad (2.10)$$

$$\mathcal{M}_{\ominus\ominus} = \sum_M \left( \begin{array}{ccc} J' & 1 & J \\ -M+1 & -1 & M \end{array} \right)^2 \left( \begin{array}{ccc} J'' & 1 & J' \\ -M & 1 & M-1 \end{array} \right)^2 \quad (2.11)$$

Subscripts  $\parallel$  and  $\perp$  denote the experimental arrangements with the two excitation steps polarized parallel and perpendicular, respectively. The two polarization arrangements with two excitation steps polarized with the same and opposite helicity are denoted by  $\odot\odot$  and  $\ominus\ominus$ , respectively. Expressions (2.8) - (2.11) can be contracted, following [5], to yield:

$$\mathcal{M} = \sum_{x,y} (-1)^{(J+J'')} (2x+1) \begin{pmatrix} 1 & 1 & x \\ -s_1 & s_2 & y \end{pmatrix}^2 \begin{Bmatrix} 1 & 1 & x \\ J' & J'' & 1 \\ J & J' & 1 \end{Bmatrix} \quad (2.12)$$

where  $x = 0, 1, 2$ .  $s_1$  and  $s_2$  are determined by the polarization arrangement, and  $y$  is fixed by selecting  $s_1$  and  $s_2$ . Expression (2.12) can be written in terms of 6j coefficients, in order to avoid the summation [15, 16, 17, 18, 19]:

$$\mathcal{M}_{\parallel} = (-1)^{J+J''+2J'} (1/3\alpha + 2/3\gamma) \quad (2.13)$$

$$\mathcal{M}_{\perp} = (-1)^{J+J''+2J'} (1/3\alpha - 1/3\gamma) \quad (2.14)$$

$$\mathcal{M}_{\circ\circ} = (-1)^{J+J''+2J'} (1/3\alpha - 1/2\beta + 1/6\gamma) \quad (2.15)$$

$$\mathcal{M}_{\circ\circ} = (-1)^{J+J''+2J'} (1/3\alpha + 1/2\beta + 1/6\gamma) \quad (2.16)$$

where  $\alpha$ ,  $\beta$ , and  $\gamma$  are equal to  $\left\{ \begin{matrix} J' & J'' & 1 \\ 1 & z & J' \end{matrix} \right\} \left\{ \begin{matrix} J & J' & 1 \\ z & 1 & J' \end{matrix} \right\}$ , with  $z = 0, 1, 2$ , respectively. Equations (2.13)-(2.16) are valid for both integer and half-integer values of  $J$ ,  $J'$ , and  $J''$ .

Using equations (2.6), (2.7) and (2.12), transition intensities between Hund's case (b) states can be evaluated, and their polarization dependence becomes apparent. The polarization dependent part of the two-step excitation probability has been tabulated in [5] in terms of  $J$ .

However, in cases when spin fine structure is not resolved, several unresolved transitions form composite lines. These composite lines represent transitions between states with a particular set of  $N$ ,  $N'$  and  $N''$  quantum numbers. In order to evaluate the intensities of the composite lines, one has to sum over all the allowed combinations of  $J$ ,  $J'$  and  $J''$  quantum

numbers, for a fixed combination of  $N$ ,  $N'$  and  $N''$ . If multiple pathways are possible between the initial and the final state, one must first sum over the amplitudes, before squaring to obtain probabilities. When  $J$ -coherences are not formed, as in our experiment (see the experimental section) the summation is done over the intensities, rather than amplitudes. This procedure yields transition intensities in terms of the particular  $N$ ,  $N'$  and  $N''$  combination. These transition intensities depend on the polarization arrangement, but are independent of  $J$ ,  $J'$ ,  $J''$ , and  $\Lambda$ ,  $\Lambda'$  or  $\Lambda''$ .

Although it might be possible to simplify the sum over all the allowed combinations of  $J$ ,  $J'$ , and  $J''$  analytically, we were unable to do so [15, 16, 17, 18, 19], but even if written in a more elegant form, higher- $j$  (e.g. 12j and 15j) symbols are usually numerically evaluated by transforming them into  $6j$  and  $3j$  coefficients, thus further contraction would not simplify the evaluation of the desired transition intensities. However, it is straightforward to evaluate the transition intensities from Eqs. (2.7)-(2.12), or (2.7), (2.8), and (2.13)-(2.16), using a simple computer program.

Furthermore, knowing the transition intensities of the composite lines, we can characterize their polarization dependence. It is useful to form ratios between the transition intensities in different polarization arrangements, for each composite line, as these ratios are more easily experimentally observed than the absolute intensities. The two polarization arrangements that are of primary experimental interest are:

$$\mathcal{R}(N, N', N'')_{\perp\perp} = \frac{S(N, N', N'')_{\perp}}{S(N, N', N'')_{\parallel}} \quad (2.17)$$

$$\mathcal{R}(N, N', N'')_{\circ\circ} = \frac{S(N, N', N'')_{\circ\circ}}{S(N, N', N'')_{\circ\circ}} \quad (2.18)$$

Experimental arrangements that mix linear and circular polarization are irrelevant for the assignment procedure since mixed arrangements would create alignment and probe orientation [20], or vice versa.  $\mathcal{R}(N, N', N'')_{\perp\perp}$  and  $\mathcal{R}(N, N', N'')_{\circ\circ}$  were evaluated for



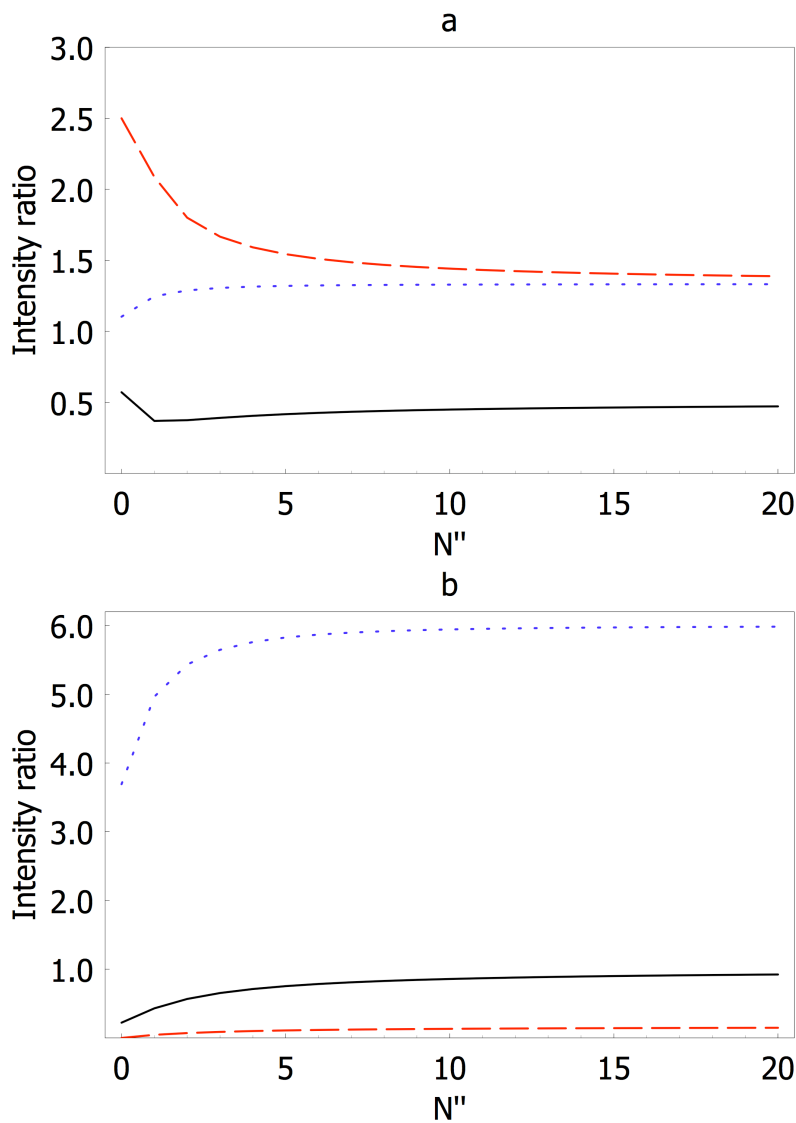


Figure 2.2: Calculated polarization dependence of the double resonance transition intensities of the composite  $N \leftarrow N'' + 1 \leftarrow N''$  lines (R pump). The  $N''$ -dependence of  $\mathcal{R}(N, N', N'')_{\perp}$  and  $\mathcal{R}(N, N', N'')_{\parallel}$  is represented on panels (a) and (b) (see the text for the explanation). The values of the ratios are plotted versus the ground state rotational quantum number,  $N''$ . Note that points with  $N < \Lambda$ ,  $N' < \Lambda'$ , and  $N'' < \Lambda''$  will be absent, as well as Q branches for  $\Lambda = 0$ . P branches are red (dashed line), Q branches are black (solid line) and R branches are blue (dotted line).

${}^2\Sigma^+ \leftarrow {}^2\Sigma^+ \leftarrow {}^2\Sigma^+$  and  ${}^2\Pi^+ \leftarrow {}^2\Sigma^+ \leftarrow {}^2\Sigma^+$  excitation schemes using Mathematica, and are displayed in Figure (2.2) as a function of  $N''$ . The plot is given for the case of an R transition used as the pump. Q or P transitions are less often used as pump transitions, because of possible overlaps between different Q or P transitions. However, since  $\mathcal{R}(N, N', N'')_{\perp}$  and  $\mathcal{R}(N, N', N'')_{\circ\circ}$  are independent of the  $\Lambda, \Lambda', \Lambda''$  combination, the plots are more general. But it should be kept in mind that Q branch transitions do not exist for  $\Sigma^\pm \leftarrow \Sigma^\pm$  transitions, and that points representing the lowest  $N''$  values will be absent for nonexistent levels where  $N'' < \Lambda'', N' < \Lambda'$ , and  $N < \Lambda$ .

## 2.4 Experiment

Our molecular beam double resonance excitation scheme has been described elsewhere [21]. Briefly, following the reaction of  $\text{CHF}_3$ , seeded in He, with the ablation-formed Ca plasma, the pulsed nozzle creates 350  $\mu\text{s}$  long gas pulses at a 20 Hz repetition rate. A 0.5 mm diameter skimmer, placed between the source and detection chambers, and a 3 mm diameter skimmer afterwards, collimate the beam in the excitation region, where it is intersected by pulses from two laser beams, propagating nearly parallel to each other, but at  $90^\circ$  with respect to the molecular beam. Ions formed by autoionization (and forced autoionization) are extracted 200 ns after the excitation pulse by a 250 V/cm electric field. After traveling through the time of flight mass spectrometer, the ions are detected on an MCP detector. After amplification by a low noise voltage amplifier, a 1 GHz LeCroy oscilloscope averages 40 shots.

A Lambda Physik Scanmate 2E dye laser, which provides the photon for the first step in the excitation scheme (pump), is equipped with a  $\beta$ -BBO frequency doubling crystal, and operated with Coumarin 540A laser dye, and is pumped by the third harmonic of the Nd:YAG laser. The excitation from a single rotational level of the  $F' \ ^2\Sigma^+$  state, with unresolved spin components, into the Rydberg states (probe transition) is provided by another dye laser (Lambda Physik Scanmate 2E), pumped by the second harmonic of the same Nd:YAG laser. The frequency of the probe pulse is shifted using a Raman shifter (250 psi  $\text{H}_2$ ; 30 cm path length), and the Stokes shifted IR pulse, used for the probe excitation, is selected using a Pellin-Broca prism. The probe pulse is delayed  $\approx 6$  ns with respect to the pump pulse. A high temperature  $\text{I}_2$  absorption spectrum ( $\approx 100^\circ\text{C}$ ), recorded simultaneously, is used for calibration of the CaF spectra to  $\pm 0.1 \text{ cm}^{-1}$  (etalon was not used). The estimated mode spacing of the dye lasers used in the experiment is  $< 0.0025 \text{ cm}^{-1}$ , smaller than the separation of the spin components in the  $F'$  state ( $\gamma_v = -0.0066 \text{ cm}^{-1}$ , and the separation goes as  $\gamma_v(N' + 1/2)$ ), thus we assumed that no  $J'$ -coherences are formed in the excitation step.

Two calcite Glan-Taylor polarizers, P1 and P2, with extinction ratios  $> 1 : 500$ , and polarization axes set parallel to each other, are inserted in pump and probe beams, respectively. A Soleil-Babinet compensator (SB) is inserted in the pump beam following P1 and set to transmit right circularly polarized (RCP) light. A double Fresnel rhomb (DFR), and a single Fresnel rhomb (SFR), are inserted into the probe beam, following P2. The SFR is kept at a fixed position and DFR is rotated between two positions, switching the input to the SFR between vertical and horizontal polarization, and consequently changing the polarization of the probe beam between RCP and LCP. The frequencies of both pump and probe lasers are fixed on resonance and the signal intensity is measured for 50-100 points with one probe helicity and for another 50-100 points with the other helicity. Often, after another 50-100 points, the probe polarization is rotated again. Since the polarization output of the DFR is a periodic function of the azimuthal angle with a  $90^\circ$  period, in several cases the DFR is rotated to several consecutive positions, separated by  $45^\circ$ , to ensure that the observed intensity changes are not due to the beam deflection.

## 2.5 Results and discussion

Using the described experimental procedure, the polarization dependence of transition intensities of spectral features in  $n^* = 13$ ,  $1 < N' < 11$  double resonance spectra of the Rydberg states of CaF were measured. Figure (2.3) shows one example of the observed dramatic effect of the circular polarization on the relative transition intensities of P and R branches. Such dependence is expected, based on the calculations presented in the previous section. Spectral features for which the change in polarization was below the noise level in the measurement, were assigned as Q branches. Strong polarization dependence, or its absence, was used to make the assignments of all of the low- $N$  spectral features that we were unable to assign otherwise. In addition, previously existing intermediate- and high- $N$  rotational assignments in the  $n^* = 13$  region were verified, and the polarization measurements were used to resolve ambiguities, where they existed. The only cases in which the described experimental method did not yield conclusive assignments were the rare instances of overlapping spectral features. Fits of the assigned spectral features to a long-range ion core multipole model will be discussed elsewhere [22].

Polarization measurements proved indispensable not only for making the assignments at low  $N$ , but also in assigning the components of a particular  $N^+$  cluster. As already described in the introduction, when  $N^+$  becomes the pattern-forming quantum number, the allowed transitions into non-penetrating states will be grouped in clusters of three ( $N - N' = 0, \pm 1$ ). The three transitions in a particular cluster have the same  $N^+$  and appear at similar energy, but they differ in  $N$ , where  $N - N' = 0, \pm 1$ . Although the intensity patterns within the clusters can guide assignments, one cannot rely on the intensities to make the assignments within an  $N^+$  cluster, because of the complex way in which interstate mixing affects the transition intensity. In addition, in the absence of combination differences, it is almost impossible to distinguish between the three  $N$ -components of the  $N^+$  cluster. However, polarization dependence definitively distinguishes between these three transitions.

Polarization dependence represents a convenient tool for distinguishing P, Q, and R

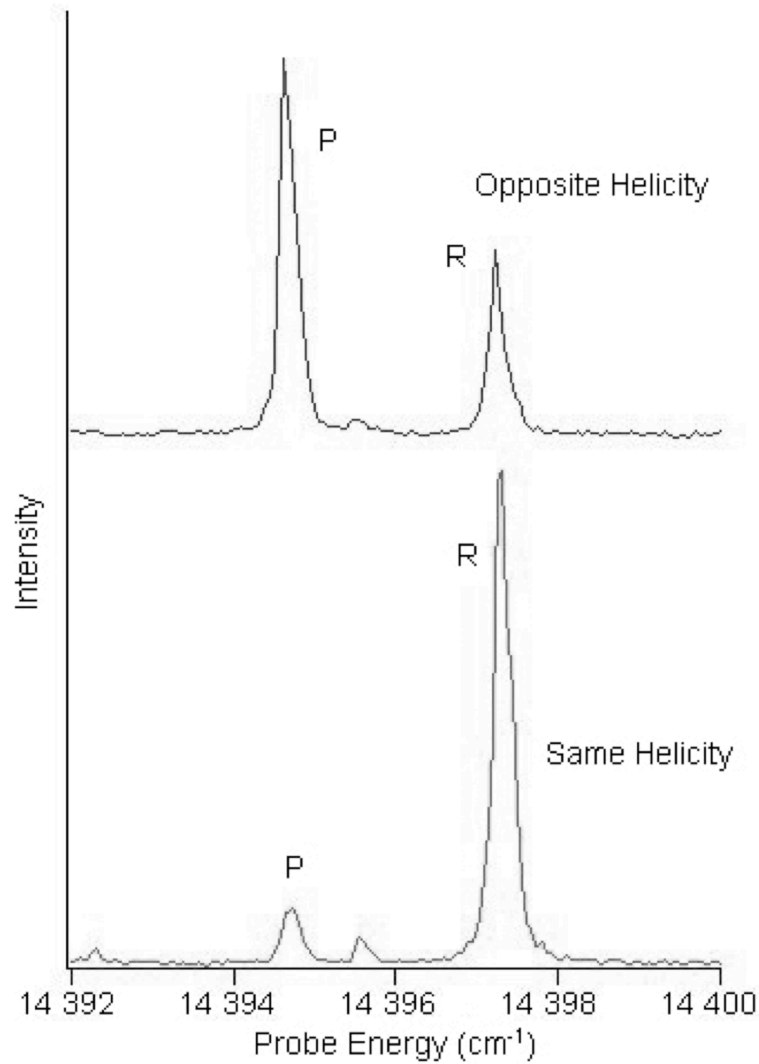


Figure 2.3: Experimentally observed polarization dependence of the intensity of a P(1) and R(1) pair of transitions into a  $^2\Sigma^+$  Rydberg state with R(0) pump pulse. The upper trace is for the case of two photons having the opposite helicity, and the lower is for same helicity. The P transition in the lower trace should be absent and its intensity is due to the imperfect polarization selection.

branches in most multiple-resonance experiments. However, there are cases of experimental interest when the polarization diagnostic is not merely a convenience, but an essential tool for making reliable assignments. Such cases are usually the result of either the absence of combination differences, or the unacceptably large experimental effort required to record them: for assigning Q branches; for assigning lowest- $N$  states where P transitions are absent and patterns broken; for making assignments within  $N^+$  clusters; for making assignments in cases of high density of states; and for assigning high- $N$  states when the transitions into a common level are inconveniently far apart. In each of these cases, the polarization dependence can be used to yield accurate assignments.

The formalism presented here describes how the polarization dependence of transition intensities, which rigorously determine one quantum number, can be used to assign the other quantum number in cases when two rotational/fine structure quantum numbers are needed for the description of the system. In addition, the formalism is presented in such a way that it can be used both for cases when spin fine structure is resolved and unresolved. It is also straightforward to extend the analysis to the cases where more than two photons are involved, or when a static DC field, which has the same matrix elements as the transition dipole matrix elements, is present. In a multiple resonance scheme, a multiplicative factor, like the one given by equation (6), will be needed for each transition, and the necessary modification of  $\mathcal{M}$ , to accommodate more than two photons, is obvious from equations (2.8) - (2.11).  $\mathcal{M}$  can be evaluated by a simple computer calculation.

This formalism is necessary to correctly describe the polarization dependence of the transition intensity at low  $N$ . However, at high  $N$ , when all spin components have approximately the same polarization dependence, simple cartoons, like the ones given in, for example, [23], p. 472, can be used to guide intuition about the polarization dependence of the transition intensity. Linear polarization creates an  $M$ -distribution symmetric around  $M = 0$ , peaked at either low- or high-  $|M|$ , for all three types of branches, as does circular polarization for the Q branches. However, circular polarization creates an  $M$  distribution asymmetric around

$M = 0$  for P and R branches. It follows that the more excitation steps there are, the stronger enhancement of  $M$  selection will be achieved, provided that the electric field polarizations are chosen in such a way that a similarly shaped  $M$  distribution is prepared, or enhanced, in each step. In addition, larger enhancement of  $M$ -selection increases the discrimination between different branches when the spectrum is recorded in different polarization arrangements.



## 2.6 Summary

The polarization dependence of the transition intensity represents a useful diagnostic tool in multiple-resonance spectroscopic experiments. It has been applied in the past to making rotational assignments when, either rigorously or asymptotically, one rotational/fine structure quantum number suffices for the description of the system. Cases when two angular momenta are coupled to make a third angular momentum, and two of these quantum numbers are needed to describe the system, require special attention. This is especially important when the underlying fine structure due to this coupling is not resolved. The polarization dependence of each of the individual fine structure components must be weighted by its transition intensity (or amplitude, if interference between two pathways is possible) before summing, in order to deduce the polarization dependence of the total transition intensity of the composite lines. For the example of the  $2S + 1 J$  components combining to form  $N$ , we present a formalism that enables one to calculate the polarization dependence of the transition intensity of the composite lines in the  $N \leftarrow N' \leftarrow N''$  double resonance transition sequence. We assumed that no  $J$ -coherences are formed, as is the case in our experiment. In addition, the intensities of each of the individual  $2S + 1 J$  components, and their polarization dependences, are given as well. Based on the calculation, we plot the polarization dependence of the double resonance transition intensities for unresolved doublets in the diagnostically relevant polarization arrangements. The results presented in this paper may be straightforwardly extended to experiments with more than two excitation steps, or to experiments with a combination of excitation transitions and the Stark effect, which is essentially a zero frequency transition. The usefulness of the polarization diagnostic has been demonstrated by applying it to assignments of spectral features in  $n^* = 13$ ,  $1 < N' < 11$  double resonance Rydberg spectra of CaF.

## 2.7 Bibliography

- [1] H el ene Lefebvre-Brion and Robert W. Field. *The Spectra and Dynamics of Diatomic Molecules*. Elsevier Academic Press, 2004.
- [2] T. A. W. Wasserman, P. H. Vaccaro, and B. R. Johnson. *J. Chem. Phys.*, 108:7713, 1998.
- [3] R. Zhao, I. M. Konen, and R. N. Zare. *J. Chem. Phys.*, 121:9938, 2004.
- [4] L. Bigio and E. R. Grant. *J. Chem. Phys.*, 87:5589, 1987.
- [5] K. Chen and E. S. Yeung. *J. Chem. Phys.*, 69:43, 1977.
- [6] R. G. Bray and R. M. Hochstrasser. *Mol. Phys.*, 31:1199, 1976.
- [7] W. M. McClain and R. A. Harris. In E. Lim, editor, *Excited States*, number 3, pages 1–56. Academic, New York, 1977.
- [8] C. G. Greene and R. N. Zare. *J. Chem. Phys.*, 78:6741, 1983.
- [9] S. Williams, R. N. Zare, and L. A. Rahn. *J. Chem. Phys.*, 101:1072, 1994.
- [10] D. M. Jonas, X. Yang, and A. M. Wodtke. *J. Chem. Phys.*, 97:2284, 1992.
- [11] Y. Chen. *Spectroscopic studies of highly excited acetylene*. PhD thesis, Massachusetts Institute of Technology, 1988.
- [12] A. Hansson and J. K. G. Watson. *J. Mol. Spec.*, 233:169, 2005.
- [13] J. T. Hougen. The calculation of rotational energy levels and rotational line intensities in diatomic molecules. *National Bureau of Standards monograph*, 115, 1970.
- [14] J. M. Brown and B. J. Howard. *Mol. Phys.*, 31:1517, 1976.

- [15] R. N. Zare. *Angular Momentum*. John Wiley and Sons, 1988.
- [16] A. R. Edmonds. *Angular Momentum in Quantum Mechanics*. Princeton University Press, 1974.
- [17] L. C. Biedenharn, J. D. Louck, and P. A. Carruthers. *Angular Momentum in Quantum Physics*. Addison-Wesley Publishing Company, 1981.
- [18] A. P. Yutsis, I. B. Levinson, and V. V. Vanagas. *Theory of Angular Momentum*. Israel Program for Scientific Translations, 1962.
- [19] D. A. Varshalovich, A. N. Moskalev, and V. K. Khersonskii. *Quantum Theory of Angular Momentum*. World Scientific, 1989.
- [20] K. Blum. *Density Matrix Theory and Applications*. Plenum Press, 1996.
- [21] J. J. Kay, D. S. Byun, J. O. Clevenger, X. Jiang, V. S. Petrović, R. Seiler, J. R. Barchi, A. J. Merer, and R. W. Field. *Can. J. Chem*, 82:791, 2004.
- [22] J. J. Kay, S. L. Coy, V. S. Petrović, B. M. Wong, and R. W. Field. *in preparation*, 2007.
- [23] W. Demtröder. *Laser Spectroscopy*. Springer, 2003.



# Chapter 3

## The Stark effect in Rydberg states of a highly polar diatomic molecule: CaF

### 3.1 Prologue

The text of this chapter was submitted as V. S. Petrović, J. J. Kay, S. L. Coy, and R. W. Field “The Stark effect in Rydberg states of a highly polar diatomic molecule: CaF” to *The Journal of Chemical Physics*. At the time of preparation of this Thesis, reviews recommending publication of somewhat abridged text, and improving its clarity, were received, but the text included in this chapter presents the longer form of the original manuscript. As the text presented here is the first description of the Stark effect in a Rydberg system of a highly polar diatomic molecule at high resolution, the author believes that a gradual introduction of complexity to the interpretation of the Stark effect in Rydberg systems from that of H, Li, and followed by non-polar diatomic molecules, and finally to CaF, is beneficial in the text of this Thesis. The reader is encouraged to consult the abridged version of the text upon its publication in *The Journal of Chemical Physics*.

## 3.2 Introduction

Since its discovery in 1913, the Stark effect has been widely used to probe and exert control over atoms and molecules. The Stark effect in Rydberg states has received especially close attention, due to the exceptionally large transition dipole moments among Rydberg states, especially those belonging to the same  $n^*$ , (which scale approximately  $\propto n^{*2}$ , where  $n^*$  is the effective principal quantum number). Large transition dipole moments make it possible to exert profound external influence over atoms or molecules, even with relatively weak electric fields. Nevertheless, due to the complex patterns of multi-state interactions among Rydberg states, high-resolution spectroscopic studies of the Stark effect in molecular Rydberg states have been limited to only a handful of cases. All of the molecules in which the Stark effect in Rydberg states has been studied have a molecular ion with either a small or zero permanent dipole moment. However, even in the absence of an external electric field the mechanism by which the dipole moment mixes the electron orbital angular momentum quantum number in Rydberg states differs profoundly from the mixing caused by the quadrupole moment and polarizabilities.

For lower- $\ell$  states, core-penetration of the Rydberg electron is the dominant cause of  $\ell$ -mixing: in molecular Rydberg states, not only does the potential energy function experienced by the Rydberg electron differ from the Coulombic potential due to the incomplete shielding of the ion-core, but the non-spherical nature of the ion-core causes  $\ell$ -mixing ( $\ell$  being the orbital angular momentum for the Rydberg electron). For core-nonpenetrating states,  $\ell$ -mixing caused by the ion-core can be understood in terms of the static long-range properties of the ion-core, such as multipole moments and polarizabilities. The interaction selection rules are such that the dipole field of the ion-core causes interaction among states with  $\ell$  differing by one, while the quadrupole field of the ion-core mixes states of  $\ell$  differing by two or zero, see Table 3.1. In CaF, due to the large CaF<sup>+</sup> dipole and quadrupole moments,  $\ell$ -mixing is profound. It is not limited only to  $s - d$  mixing, as in homonuclear molecules, but rather affects all  $\ell \leq 3$  states [1].

Table 3.1: Selection rules for interactions discussed in text. Matrix elements for these types of interactions are nonzero when the conditions from the table are satisfied.

Interaction	$\Delta\ell$	$\Delta N^+$	$\Delta N^a$
Ion-core dipole field operating on Rydberg electron	$\pm 1^b$	$\pm 1$	0
Ion-core quadrupole field operating on Rydberg electron	$0, \pm 2^b$	$0, \pm 2$	0
External homogeneous electric field operating on Rydberg electron	$\pm 1$	0	$0, \pm 1$
External homogeneous electric field operating on the ion-core	0	$\pm 1$	$0, \pm 1$

<sup>a</sup> Electric field polarization can further affect these selection rules.

<sup>b</sup> These matrix elements are zero when  $\Delta n^* = 0$ .

In a non-rotating molecule the information about the different mechanisms of the interaction of the Rydberg electron with the ion-core is not contaminated by rotation-electronic interactions. However, to be able to identify assignment-aiding patterns, spectra usually must be recorded from several rotational levels of an intermediate electronic state. Rotational assignments are then made by identifying pairs of spectral features (combination differences) with the same  $N'$ , but different  $N$  ( $\mathbf{N} = \mathbf{J} - \mathbf{S}$ ; primed values pertain to the intermediate state, unprimed to a Rydberg state). As  $N$  increases, the rotation-electronic interaction ( $\ell$ -uncoupling) results in evolution from Hund's coupling case (b) to Hund's case (d), and the intensity patterns expected for Hund's case (b) are distorted. As a result, combination differences in  $N$  become systematically unobservable. The distortion of the relative intensity patterns from those expected for Hund's case (b) to Hund's case (d) transitions can be understood in terms of the interference effects [2], see Fig 3.1. When the Rydberg state into which a transition is observed is not in the Hund's case (b) limit, we can decompose that state into Hund's case (b) basis states with different values of the  $\Lambda$  quantum number. The transformation between the Hund's case (b)  $|\eta, \ell, \Lambda, N\rangle$  and Hund's case (d)  $|\eta, \ell, N, N^+\rangle$  basis states is given by the following expression:

$$|\eta, \ell, \Lambda, N\rangle = \sum_{N^+} (-1)^{N^+ - \ell + \Lambda} (2N^+ + 1)^{1/2} \begin{pmatrix} N & \ell & N^+ \\ \Lambda & -\Lambda & 0 \end{pmatrix} |\eta, \ell, N, N^+\rangle. \quad (3.1)$$

The low- $n^*$  (and low- $N'$ ) intermediate state through which the Rydberg state is accessed is usually in the Hund's case (a) or (b) limit, and has a definite value of the  $\Lambda'$  quantum number. Since the final Rydberg state is  $\Lambda$ -mixed, transition amplitudes into  $\Lambda = \Lambda'$  and  $\Lambda = \Lambda' \pm 1$  basis states will interfere, resulting in distortion of the relative intensity patterns of Hund's case (b) to Hund's case (b) transitions.

Analysis of the  $\ell$ -uncoupling (caused by the rotation-electronic interaction,  $-B^+(N^\pm L^\mp)$ ) in CaF is further complicated by strong  $\ell$ -mixing (caused by the non-sphericity of the ion-core). Since the intermediate state used in our experiments on CaF is  $\ell'$ -mixed, nonzero transition amplitudes into  $\ell = \ell' \pm 1$  components (optically "bright") of the highly  $\ell$ -mixed final Rydberg state will interfere as well. The effects of both  $\ell$ -mixing and  $\ell$ -uncoupling can result in the disappearance of one member, or a gross distortion, of the expected simple patterns in the spectrum. The distortion is especially strong for the lowest- $N$  rotational levels, where the case (b) to (d) evolution is incomplete, and the rotational spreading of  $N - 1$ ,  $N$ , and  $N + 1$  levels, which is smaller than that at higher  $N$ , results in a higher density of spectral features around integer values of  $n^*$ , where the band origins for the core-nonpenetrating states are located.

We have previously described the use of polarization diagnostics to make  $N$  assignments, even for the lowest- $N$  rotational levels [3]. Here we perform a high-resolution analysis of the Stark effect in the spectrum of the CaF molecule, which has an ion-core,  $\text{CaF}^+$ , with one of the largest permanent dipole moments known in a diatomic molecular ion,  $\approx 9$  D [4] (origin at center of mass of  $\text{CaF}^+$ ).

We describe several stages of the decoupling of the molecular Rydberg electron from the body frame caused by the external electric field. The weak-field Stark effect is employed to gain access to the  $f$ ,  $g$ , and  $h$  states, and to aid the assignment of the actual or nominal value of  $N^+$ , the rotational quantum number of the ion-core ( $\mathbf{N}^+ = \mathbf{N} - \boldsymbol{\ell}$ ), for the lowest- $N$  rotational levels. From the analysis of the lowest- $N$  rotational levels we learn about the interactions of the core-nonpenetrating  $f$ ,  $g$ , and  $h$  states with the lower- $\ell$  core-penetrating



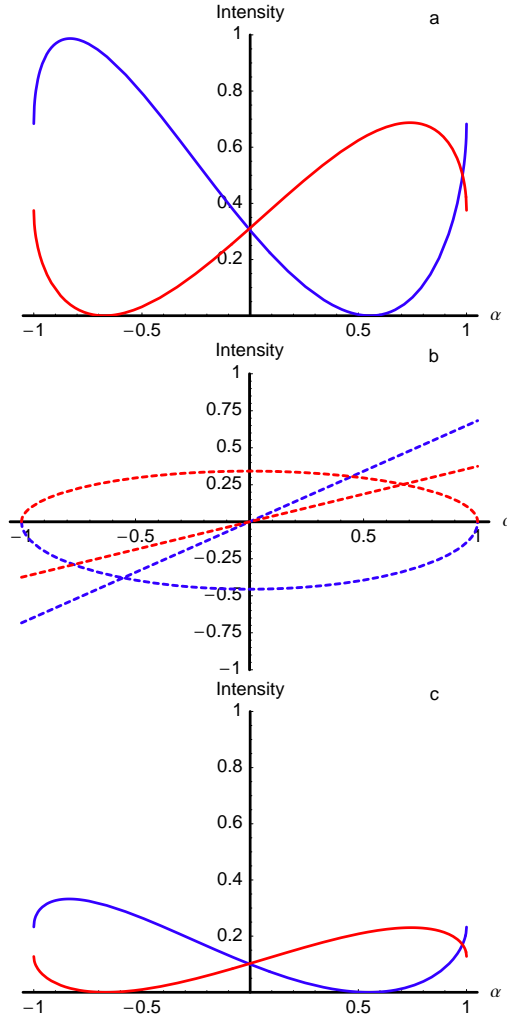


Figure 3.1: Interference effects in the intensity of P (blue) and R (red) branches between a pure Hund's case (b) lower state,  $N' = 3$ , and an upper state that is mixed in this basis. Plotted is the transition intensity (scaled to 1) as a function of the mixing coefficient,  $\alpha$ . In a) the transition is into the states  $\alpha |f, \Sigma^+\rangle + \sqrt{1 - \alpha^2} |f, \Pi^+\rangle$ , from a lower state,  $|d, \Sigma^+\rangle$ . The plot for the case of the  $\alpha |f, \Sigma^+\rangle - \sqrt{1 - \alpha^2} |f, \Pi^+\rangle$  upper state is a mirror image of the plot in a) with the  $y$  axis as the axis of reflection. Plot a) is a square of the sum of  $\Sigma^+$  and  $\Pi^+$  contribution plotted in b), for both P (blue) and R (red) transitions. Distortion of the pattern in a) by  $\ell$ -mixing is shown in c). Here both states involved in the transition are  $\ell$ -mixed in addition to being  $\Lambda$ -mixed, the lower state is  $\eta |p\rangle - \sqrt{1 - \eta^2} |d\rangle$  and the upper state is  $\theta |d\rangle + \sqrt{1 - \theta^2} |f\rangle$ , with  $\eta = 0.5$  and  $\theta = 0.5$ . Both a) and b) plots were produced using the Eq. (5) from [3], but with a correction that  $(1 + \delta_{\Lambda',0} + \delta_{\Lambda,0} - 2\delta_{\Lambda',0}\delta_{\Lambda,0})$  in that equation should appear with the exponent  $\frac{1}{2}$  instead of  $-\frac{1}{2}$ . It was assumed that  $S = 0$ ,  $J = N$ , and  $M_J = 0$  in the plot. The intensities are scaled in the same manner as in a). Since there are no  $\Sigma^-$  states in the CaF Rydberg supercomplex, there are no interferences in the Q branches excited from a  $\Sigma^+$  intermediate state.

states.

Two models, based on experimental data that covers the region surrounding  $n^* = 13$ , have been developed previously to describe the Rydberg states of CaF. A global Multichannel Quantum Defect (MQDT) model was used to fit the states from  $n^* \approx 12 - 18$ ,  $N = 0 - 14$ ,  $v^+ = 1$ ,  $n^* \approx 9 - 10$ ,  $N = 0 - 14$ ,  $v^+ = 2$ , and  $n^* \approx 7$ ,  $N = 3 - 10$ ,  $v^+ = 3$  regions, and generated an  $0 \leq \ell \leq 3$  quantum defect matrix and its derivatives with respect to internuclear distance [5]. A complementary extended long-range model, that included the  $3 \leq \ell \leq 5$ ,  $v^+ = 1$  states from the region of  $13 \leq n^* \leq 17$ , yielded the values for dipole and quadrupole moments, and the isotropic polarizability [6]. The interaction among  $g(-4)$ ,  $f(-3)$  and  $d^2\Sigma^+$  states (here we use Hund's case (d) notation for the first two states:  $\ell(\ell_R)$ , where  $\ell_R = N - N^+$  is the projection of  $\ell$  on the ion-core rotational axis), as uncovered in the analysis of the lowest- $N$  rotational levels presented in this paper, bridges the two models, since in neither of the two previous models are all three of these states ( $g(-4)$ ,  $f(-3)$  and  $d^2\Sigma^+$ ) present together. However, limitations in our fitting capabilities and the current dataset have prevented a global fit involving both sets of data.

### 3.3 Background

In the Rydberg states of the hydrogen atom, accessed from the  $\ell = 0$  ground state through an  $\ell = 1$  intermediate state, an external homogeneous electric field mixes the states of opposite parity in steps of  $\Delta\ell = \pm 1$ , while  $m_\ell$  is conserved, see Fig. 3.2. When Stark mixing between the states that belong to the same  $n$  but different values of  $\ell$  begins, higher- $\ell$  states gain a share of the bright character from the low- $\ell$  states, and a regular-appearing Stark manifold of higher- $\ell$  states appears in the spectrum. The energies of all features in the Stark manifold change linearly with the applied electric field. Once the field is increased above the Inglis-Teller limit,  $E_{Stark} = \frac{1}{3n^5}$  a.u. [7], members of Stark manifolds that belong to different values of  $n$  start to cross. The pure Coulombic potential in the hydrogen atom gives rise to supersymmetry. This symmetry is removed by core-penetration in alkali atoms. In hydrogen, the Runge-Lenz vector ( $\mathbf{A} = \mathbf{p} \times \mathbf{L} - \frac{\mathbf{r}}{r}$ ) commutes with the Hamiltonian and, as a result, the states with different values of the  $n_1$  parabolic quantum number cross instead of undergoing avoided crossings [8]. (The Schrödinger equation for hydrogen atom in an external electric field is separable and analytically soluble in parabolic coordinates. Solutions are expressed in terms of parabolic quantum numbers  $n_1$  and  $n_2$  related by the expression  $n = n_1 + n_2 + |m_\ell| + 1$ ).

In atoms with one electron outside of closed shells, see Fig. 3.3, low- $\ell$  states, which penetrate more deeply into the ion-core, experience a non-Coulombic potential and the electron in these states experiences a phase shift, resulting in distortion of the energy levels from  $IP - \frac{R}{n^2}$  to  $IP - \frac{R}{n^{*2}}$  (in atomic units), where  $n^*$  is the principal quantum number corrected for the quantum defect ( $n^* = n - \delta_\ell$ ),  $R$  is the Rydberg constant, and  $IP$  the ionization potential. As  $\ell$  increases, the inner turning point (defined as  $r$  for which  $V_{eff}(r, \ell) = -\frac{1}{2n^2}$ , in atomic units) of the effective potential ( $V_{eff}(r, \ell) = -\frac{1}{r} + \frac{\ell(\ell+1)}{2r^2}$ , in atomic units) shifts to larger distances from the center of the ion core, and, as a result of this centrifugal barrier, higher- $\ell$  states are less capable of core-penetration. As a result, the quantum defects for the core-nonpenetrating states are close to zero, making them near degenerate. When an

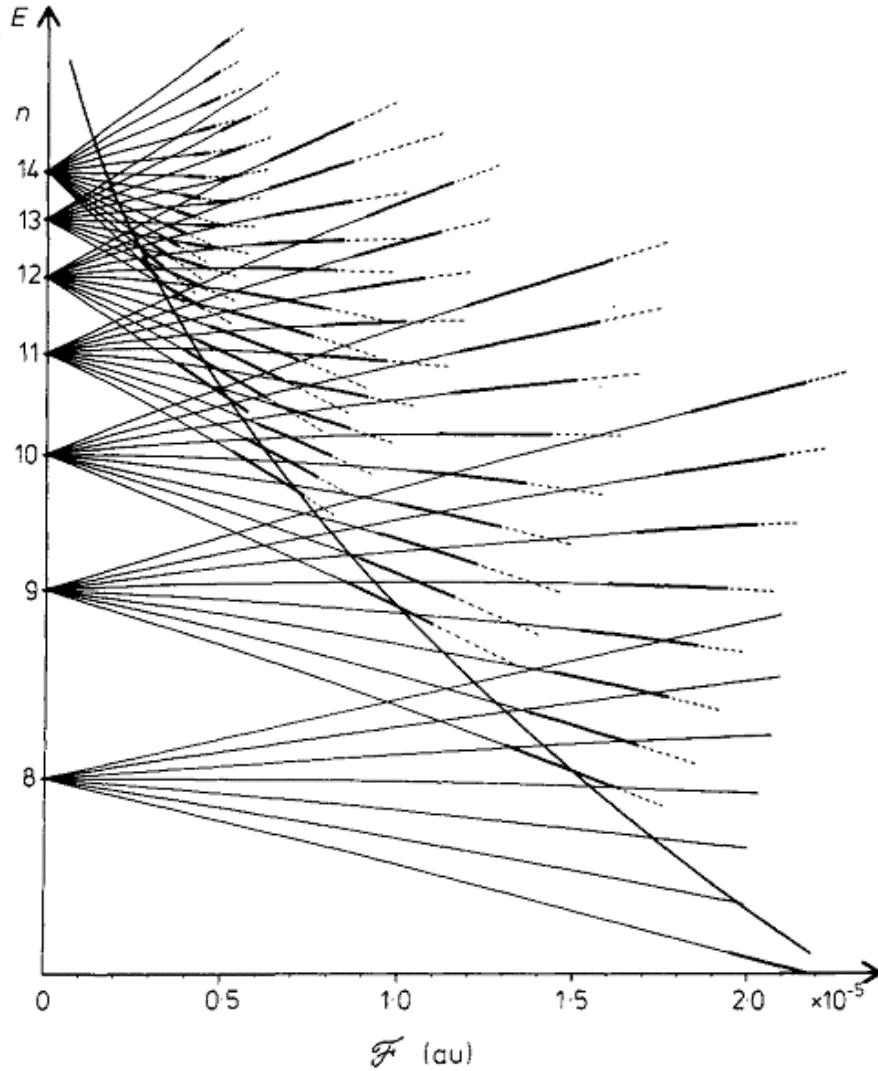


Figure 3.2: Stark effect in the Rydberg states of atomic H,  $m_\ell = 1$ . The external electric field removes the degeneracy between the  $n - |m_\ell|$  states with different values of  $\ell$ , and these states tune linearly with the field. When the field increases above  $E_{Stark} = \frac{1}{3n^5}$  (in atomic units), the states belonging to different  $n$ -manifolds cross. Due to the conservation of the Runge-Lenz vector, which is diagonal in the parabolic basis (in which Schrödinger equation for the hydrogen atom in an external electric field is analytically soluble), the states with different values of the  $n_1$  parabolic quantum number ( $n = n_1 + n_2 + |m_\ell| + 1$ ) cross even though they have same value of  $m_\ell$ . Reprinted with permission, Fig. 5 from E. Luc-Koenig and A. Bachelier in *J. Phys. B* 13, 1743 (1980). Copyright (1980) by the Institute of Physics.

external electric field is applied, the almost-degenerate higher- $\ell$  states mix at low field to form Stark manifolds similar to those in hydrogen, while the states with larger quantum defects initially follow a second-order Stark tuning curve, until they eventually merge with the high- $\ell$  Stark manifold of the same or neighboring  $n^*$  at higher field. One-electron alkali-like systems, unlike hydrogen, have states with nonzero quantum defects, and show  $\Delta n^* = \pm 1$  level-mixing rather than level-crossing above the Inglis-Teller limit, and a series of avoided crossings is formed. In both hydrogenic and alkali cases, destruction of zero-field quantum numbers proceeds in two stages. In the first stage the electric field destroys  $\ell$ , which gets decoupled from electron spin  $s$ , and therefore destroys  $j$ . In the second stage, the principal quantum number ( $n$  or  $n^*$ ) ceases to be a good quantum number. The detailed analysis of the Stark effect in the Rydberg states of alkali atoms is given in [9].

The structure of molecular Rydberg spectra is richer than that of atomic Rydberg spectra due to the vibrational and rotational degrees of freedom, as well as the vibrationally or rotationally modulated non-roundness of the ion core. Core-penetrating states, similarly to the atomic case, have nonzero quantum defects, while the core-nonpenetrating states cluster near integer values of  $n^*$ . However, because of the vibrational and rotational structure, each rotation-vibration state of the ion-core will have a series of Rydberg states converging to it. Each series, associated with a different ionization limit, is characterized by the vibrational and rotational quantum numbers for the ion-core,  $v^+$  and  $N^+$ , respectively.

For atomic hydrogenic Rydberg states, transition dipole moments among the states that belong to the same  $n$  but differ in  $\ell$  by one, scale as  $\langle n, l | er | n, l + 1 \rangle = -\frac{3}{2}ea_0n\sqrt{n^2 - \ell^2}$  [7] and even at intermediate values of  $n$ , are exceptionally large compared to typical permanent molecular dipole moments, see Fig. 3.4. The hydrogenic transition dipole moment for  $13g \leftarrow 13f$  is  $\approx 600$  D, compared to  $\approx 9$  D, the permanent dipole moment for  $\text{CaF}^+$ . The selection rules for the Stark matrix elements, where the external homogeneous electric field interacts with these large intracomplex Rydberg-Rydberg transition dipole moments, are such that the quantum numbers for the Rydberg electron are mixed ( $\Delta\ell = \pm 1$ ,  $\Delta N = 0$ ,

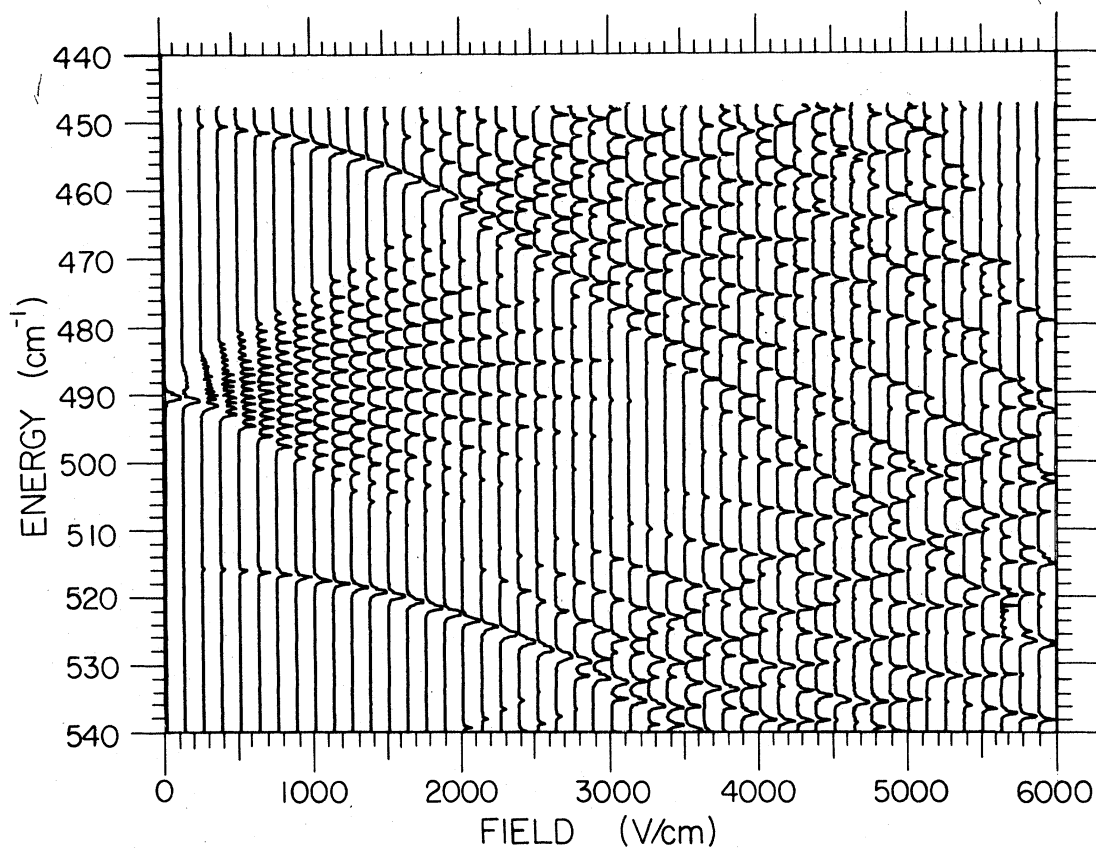


Figure 3.3: Stark effect in  $n^* = 15$ ,  $m_l = 0$ , Rydberg states of atomic Li. In addition to the Stark manifold centered around integer values of  $n^*$ , states with nonzero quantum defects, which tune quadratically with the field, become apparent. Since core-penetration removes the supersymmetry present in hydrogen, the states that belong to neighboring values of  $n^*$  interact above Inglis-Teller limit and undergo avoided crossings. Reprinted with permission, Fig. 7 from M. L. Zimmerman, M. G. Littman, M. M. Kash, and D. Kleppner, published in Phys. Rev. A 20, 1979, 2251. Copyright (1979) by the American Physical Society. [9].

$\pm 1$ ), but those for the ion-core are conserved ( $\Delta N^+ = 0$ ,  $\Delta v^+ = 0$ ), see Table 3.1. Because of the much larger size of the intracomplex Rydberg-Rydberg transition dipole moment relative to the permanent ion-core dipole moment, in the absence of accidental degeneracies among states with different  $N^+$  values, a weak external electric field mixes  $\ell$  and  $N$  for the Rydberg electron, but  $N^+$ -mixing only becomes appreciable at much higher field strengths. Thus two different regimes of the interaction with the external homogeneous electric field can be distinguished. While in atoms the destruction of zero-field quantum numbers by the external electric field proceeds in only two stages (mixing of  $\ell$  and mixing of  $n$ ), the Stark-induced mixing process in molecular Rydberg states exhibits several additional stages. In CaF, for example,  $\ell$ ,  $N$ ,  $N^+$ ,  $n^*$ , and  $v^+$  are sequentially destroyed by the electric field.

How well the different decoupling stages are separated as the electric field is increased, depends on the strength of the electric field, the  $n^*$  region in which the observations are made, and the values of molecular parameters. These molecular parameters include rotational and vibrational constants, and the quantum defects (dependent on the internuclear distance, multipole moments, and polarizabilities). For CaF at  $n^* = 13$ , which we studied, it is possible to observe the different stages of Stark decoupling associated with the  $N^+$ -rotational structure, but not those due to the vibrational structure. When the electric field is applied, core-nonpenetrating states mix first, because of their near-degeneracy.  $\ell$  ceases to be a good quantum number, and  $N$  is destroyed along the way.  $N^+$  is approximately conserved at this stage. Several manifolds of states that display a linear Stark effect appear for each  $N^+$  cluster that possesses bright character. This is a consequence of the intermediate state being  $N^+$ -mixed, since it is not in the Hund's case (d), but rather the Hund's case (b) limit. The existence of several Stark manifolds (associated with different values of  $N^+$ ) is the main difference from the Stark effect in atomic Rydberg states.

As the electric field increases, either  $N^+$  is destroyed, or some low- $\ell$  penetrating states join the high- $\ell$  Stark manifold, since some of the core-penetrating states are accidentally located in the proximity of an integer value of  $n^*$ . As the electric field is increased even further, all

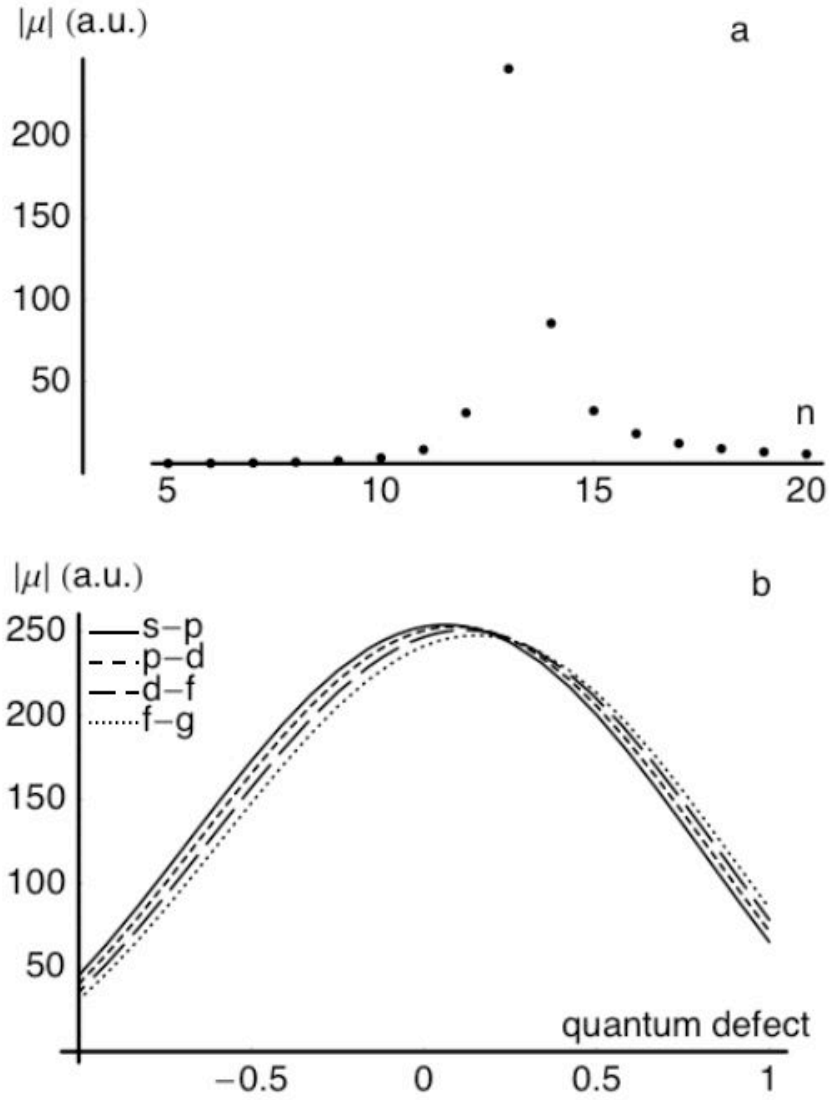


Figure 3.4: Absolute value of the transition dipole moments in which  $\ell$  of the Rydberg electron changes by  $\pm 1$ , in atomic units. Part a) gives the variation of the absolute value of the  $\langle n' = 13, \ell' = 3 | \mu | n, \ell = 4 \rangle$  transition dipole moment with  $n$ , calculated using hydrogenic wavefunctions (for integer values of  $n$ ). b) displays the dependence of the absolute value of the intracomplex (same- $n^*$ ) transition dipole moments on the quantum defect,  $\delta$ , for the  $\langle n^* = 13, \ell' = 0, 1, 2, 3 | \mu | n^* = n' + \delta, \ell = \ell' + 1 \rangle$  transition moment, where  $\delta$  varies between -1 and 1. Nonhydrogenic dipole moments were evaluated using the method described in [10].



of the core-penetrating states must join the Stark manifold before  $N^+$  can be fully mixed. Eventually, the electric field mixes the states that belong to different  $N^+$  clusters, and a hydrogenic Stark manifold associated with a particular  $n^*$  and  $v^+$  is formed.

The effect of an external electric field on both the structure and dynamics of molecular Rydberg states has previously been studied experimentally, and different theoretical descriptions have been developed. In addition to studies at very high  $n^*$ , in the context of ZEKE experiments, various aspects of the Stark effect have been studied at intermediate  $n^*$  in  $\text{H}_2$  [11, 12, 13, 14, 15, 16, 17, 18],  $\text{NO}$  [19, 20, 21, 22],  $\text{Na}_2$  [23, 24, 25, 26],  $\text{H}_3$  [27, 28], and  $\text{Li}_2$  [29, 30]. Unlike these systems,  $\text{CaF}^+$  possesses a large dipole moment which causes profound mixing among the  $\ell \leq 3$  states. It presents an ideal testbed for studying the competition between the mixing caused by the external and internal electric fields. Modeling of the Stark effect in molecular Rydberg states usually relies on an adaptation of Multichannel Quantum Defect Theory to include Stark interactions [13, 24, 20, 25, 19] or effective Hamiltonian matrix diagonalization techniques [19, 27, 28, 16, 11]. When the interaction with the states that belong to a neighboring  $n^*$  value is weak, as is the case at lowest- $N$  core-nonpenetrating states in zero or low external electric field, the  $H_{eff}$  matrix diagonalization method can provide an adequate description [19].

Even though spectral congestion in the already complex spectra of Rydberg states increases when an external electric field is applied, the emergence of Stark manifolds has previously been used for diagnostic purposes [31]. In Ref. [31], core-penetrating and core-nonpenetrating states in  $\text{H}_2$  could be experimentally distinguished when an external electric field is applied. In spectra recorded from an intermediate  $d$  state, an optically bright core-nonpenetrating  $f$  state is located in the vicinity of the higher- $\ell$  cluster, and applying the electric field mixes some bright  $f$  character into the higher- $\ell$  states of the Stark manifold. In contrast, an optically bright core-penetrating  $p$  state at the same field strength and similar  $n^*$  value has no neighboring states with which it can be forced by the Stark field to interact. In addition to distinguishing between field-non-mixed core-penetrating states and the strongly

field-mixed core-nonpenetrating states, a weak electric field can also be used for diagnostic purposes. We applied a weak electric field ( $<100$  V/cm) to access states of higher  $\ell$  ( $\ell \geq 3$ ), which are usually not accessible directly, and to make (or verify) assignments of actual or nominal value of  $N^+$ . In addition, since the Stark effect mixes states of opposite parities, transitions into  $N$  states that are dark at zero field appear when the electric field is applied. This ability to observe a particular state from several values of  $N'$ , is helpful in verifying and extending the zero-field assignments. Assignments made by this method are especially useful for the lowest- $N$  rotational levels.

Lowest- $N$  rotational levels of both core-penetrating and core-nonpenetrating states are described by Hund's case (b). Due to the rotation-electronic interaction, as the rotation increases, evolution towards Hund's case (d) occurs. The evolution into the Hund's case (d) limit at lower- $N$  is achieved much more rapidly for core-nonpenetrating states than for the core-penetrating states. Since the intermediate state, through which the Rydberg state is accessed, is a low-lying Rydberg state, it is in Hund's case (a) or (b). In our experiment, the  $F' \ ^2\Sigma^+$  intermediate state is in Hund's case (b). This means that the transition from  $F' \ ^2\Sigma^+$  into Rydberg states evolves from a (b)  $\leftarrow$  (b) pattern toward that of (d)  $\leftarrow$  (b), as  $N$  increases. The simple patterns expected in a (b)  $\leftarrow$  (b) transition are distorted as the coupling case for the final Rydberg state evolves from (b) to (d). Strong  $\ell$ -mixing caused by the ion-core makes assignment of the patterns even more difficult. The patterns are most distorted at the lowest- $N$  rotational transitions, where the change of the coupling case from (b) to (d) is not yet complete, and the density of states near an integer value of  $n^*$  is larger than at high  $N$ . The lowest- $N$  rotational levels are of greatest value for disentangling the short-range and long-range interactions of the Rydberg electron with the ion-core. The lowest- $N$  levels encode the information free of distortion by the rotation-electronic coupling. We have previously used polarization diagnostics [3] to make  $N$ -assignments in the lowest- $N$  rotational levels. In this paper we describe the application of the Stark effect to access, and assign the actual or nominal value of  $N^+$  quantum number of, the lowest- $N$  rotational levels

of  $f$ ,  $g$ , and  $h$  states, and we characterize the mixing of the core-nonpenetrating states with the core-penetrating states.

Modeling of the Stark effect in Rydberg states requires knowledge of the zero-field quantum defects. We have exploited the extended long-range model [6] to provide a zero-field description of the core-nonpenetrating states. Based on observation of the lowest- $N$  rotational states, we have determined the core-penetrating characters admixed into the  $f$ ,  $g$ , and  $h$  states and, by comparing the experimentally observed Stark effect patterns to the calculated ones, we show that our extended long-range model is valid for higher- $\ell$  states, which had not been explicitly fitted in our determination of the long-range parameters, and which first appear in the spectrum only when the electric field is applied.

## 3.4 Experiment

Our molecular beam double-resonance excitation scheme has been described elsewhere [3] and only the aspects of the experiment pertaining to excitation in the presence of the external electric field (further referred to as  $E_{Stark}$ ) will be given here. Excitation of CaF molecules by two almost collinear laser pulses occurs between two metal meshes  $P_l$  and  $P_u$ , parallel to each other and separated by 1 cm (modification of the R. M. Jordan Co. C-677 model). In the experiment at  $E_{Stark} = 0$ , both  $P_l$  and  $P_u$  were held at the same potential during the excitation (1500 V). The propagation direction of the laser pulses, the direction of the molecular beam, and the direction of  $E_{Stark}$  were mutually perpendicular. In the experiment discussed here, the molecules were excited into an autoionizing state, which is a member of a Rydberg series converging to the  $v^+ = 1$  ionization limit. 200 ns after the excitation, an additional 200 V/cm positive potential (extraction pulse) was applied to  $P_l$  to repel the ions formed by autoionization toward the time-of-flight mass spectrometer. Ions are then detected at a multichannel plate detector. The electric field applied to  $P_l$  and  $P_u$  is controllable to  $\pm 1$  V/cm in our current arrangement. No attempt was made to characterize the stray fields, or the field inhomogeneity, but in the spectral region studied here ( $n^* = 13$ ) electric fields on the order of several volts have a negligible effect compared to the  $0.1 \text{ cm}^{-1}$  resolution of our current experiment.

In the experiment with nonzero  $E_{Stark}$ , the  $P_l$  plate ( $1500 \text{ V} + E_{Stark} \cdot 1 \text{ cm}$ ) was held at a different potential than the  $P_u$  plate (1500 V) during the optical excitation pulses. The range of the values of the applied  $E_{Stark}$  field was 40-180 V/cm, varied in steps of 10 V/cm, and 300 V/cm (in addition to the zero-field conditions described previously). At  $E_{Stark}$  smaller than 40 V/cm, very small changes were observed in the spectrum, and this region of electric field strengths was not systematically studied. In the experiments performed in the presence of the electric field,  $E_{Stark}$  affects the arrival times of the ions, as well as the spread of the arrival times at the detector. Whenever it was necessary, adjustments were made to the ion-optics focusing fields to compensate for this distortion of the signal. No attempt

was made to normalize the relative intensities of the spectra recorded at different values of  $E_{Stark}$ .

Under these conditions, we recorded double resonance spectra in the energy region around the integer value of  $n^* = 13$  for the  $N'$  values of 0, 1, 2, and 3 in the  $F' \ ^2\Sigma^+$  intermediate state (accessed by P(1), R(0), R(1), and R(2) pump transitions from the ground  $X \ ^2\Sigma^+$  state). In our excitation scheme, the spin fine structure doublets are not resolved in the intermediate state, and neither spin fine structure, nor spin-orbit structure are resolved in the Rydberg states in this  $n^*$  region. All CaF spectra were calibrated to  $0.1 \text{ cm}^{-1}$  using high-temperature iodine spectra ( $\approx 100^\circ\text{C}$ ) recorded simultaneously (an extracavity etalon was not used).

Although, in all of the spectra recorded for the purpose of making the assignments, the polarization arrangement was  $pp$ , the effect of the polarization arrangement on the appearance of the Stark spectrum was examined in a subset of spectra by additionally recording spectra in  $ps$ ,  $sp$ ,  $ss$ , RHCP-RHCP-vertical, and RHCP-LHCP-vertical polarization arrangements ( $p$  and  $s$  denote polarization parallel and perpendicular to the direction of the Stark field, respectively, while RHCP and LHCP are right and left hand circularly polarized photons, respectively; the ordering specifies pump photon - probe photon (- Stark field), respectively). Some of the spectra used for monitoring the polarization dependence were recorded at electric field strengths larger than those specified in the previous paragraph ( $E_{Stark}$  up to 350 V/cm).

## 3.5 Calculation

To model the experimentally observed results, an effective Hamiltonian was set up. The calculation was done in  $n^* = 13$  and, since the range of the electric field strengths studied was well below the Inglis-Teller limit ( $\approx 4.6$  kV/cm for this  $n^*$ ), we did not include interactions with the states from the neighboring  $n^*$ . Even in  $n^*=13$ , only the core-penetrating states that are in the neighborhood of integer  $n^*$  (13.19  $\Sigma^+$ , 12.98  $\Pi^\pm$ , 13.14  $\Delta^\pm$ , and 12.88  $\Sigma^+$ ) were included in our calculation, in addition to all of the core-nonpenetrating states ( $3 \leq \ell \leq 12$ ).

The Hamiltonian in the absence of the electric field is given by:

$$H_0 = H_{el} + H_{rot} + H_{SO} \quad (3.2)$$

where, since we did not consider  $v^+$ -changing interactions, the vibrational Hamiltonian is implicitly included in the electronic term by using the ionization potential for  $v^+ = 1$  and  $N^+ = 0$ . We determine the energies of the rotationless core-penetrating states by a fit. Core-penetrating states are well described by Hund's case (b), and we use the case (b) basis in order to implement the fitting procedure.

For core-nonpenetrating states, the  $H_{el}$  was calculated using Watson's long-range expression [32], corrected for the polarizability terms [6]. This approximate expression contains only diagonal matrix elements:

$$H_{el} = IP_{v^+=1} - \frac{R}{n^2} + \frac{2(\mu^2 - Q)(\ell(\ell + 1) - 3\Lambda^2)}{n^3(2\ell + 1)(2\ell + 3)(2\ell - 1)\ell(\ell + 1)} \\ + \alpha \frac{2(\ell(\ell + 1) - 3n^2)}{n^5(2\ell + 3)(2\ell + 1)(2\ell - 1)\ell(\ell + 1)} + \gamma \frac{4(\ell(\ell + 1) - 3n^2)(\ell(\ell + 1) - 3\Lambda^2)}{3n^5(2\ell + 3)^2(2\ell + 1)(2\ell - 1)^2\ell(\ell + 1)} \quad (3.3)$$

where  $IP_{v^+=1} = 47686$  cm $^{-1}$  is the ionization potential for  $v^+ = 1$  [33] and  $n = 13$  in the region studied here.  $\mu$  and  $Q$  are the permanent dipole and quadrupole moments of the CaF $^+$  ion, respectively. The value of  $\mu^2 - Q$  was previously determined by fits [1] and we

used 11.3 a.u.  $\alpha$  is the isotropic polarizability, and we used the value of 15 a.u. previously determined by a fit [6].  $\gamma$  is the anisotropic polarizability, the value of which is difficult to determine by the fit when the separation of the long-range from short-range interactions is incomplete, and we used the value of 5 a.u. [6].

For the core-penetrating states, the value of the matrix elements of  $H_{el}$  were determined by fit rather than from the long-range interaction terms, as described below.

The rotational Hamiltonian is given by:

$$H_{rot} = \sum_{\ell} c_{\ell}^{\ell_1, \Lambda} c_{\ell}^{\ell_2, \Lambda} B^+ [N(N+1) + \ell(\ell+1) - 2\Lambda^2] \quad (3.4)$$

for  $\Delta\Lambda = 0$ , and by

$$H_{rot} = -\sqrt{1 + \delta_{\Lambda_1, 0} + \delta_{\Lambda_2, 0}} \sum_{\ell} c_{\ell}^{\ell_1, \Lambda_1} c_{\ell}^{\ell_2, \Lambda_2} B^+ \sqrt{N(N+1) - \Lambda_1\Lambda_2} \sqrt{\ell(\ell+1) - \Lambda_1\Lambda_2} \quad (3.5)$$

for  $\Delta\Lambda = \pm 1$ .  $B^+ = 0.37 \text{ cm}^{-1}$  is the rotational constant of the  $\text{CaF}^+$  ion [1]. The  $c_{\ell'}^{\ell, \Lambda}$  are the elements of the eigenvector decomposition (admixed  $\ell'$ -amplitude of a nominally  $|\ell, \Lambda\rangle$  state).

The degeneracy between states of the same  $N$  but different  $J$  was removed by adding a small spin-orbit splitting:

$$\Delta E = E(N+1/2) - E(N-1/2) \approx \frac{A\Lambda^2}{N} \left[ 1 - \frac{A\Lambda^2}{2B} \right] \quad (3.6)$$

with  $A = 0.01 \text{ cm}^{-1}$ . The splitting is smaller than our experimental resolution, but removing this degeneracy suppressed non-physical eigenvalues, which resulted from diagonalizing in Mathematica a large-size matrix containing multiple pairs of degenerate entries.

Diagonalization of the Hamiltonian was performed in Mathematica. In the absence of an external electric field, the values of some of the  $c_{\ell'}^{\ell, \Lambda}$  were varied until agreement between

the calculated and the experimentally observed energy values was obtained. In addition, the values of the diagonal matrix elements of  $H_{el}$  for the core-penetrating states were varied as well. The comparison between the calculated and experimentally observed energies was made for a subset of the experimentally observed core-penetrating and core-nonpenetrating states with  $0 \leq N \leq 6$  in  $n^* = 13$ . The fit parameters were varied by hand and the correct matching between the corresponding calculated and observed states was ensured by inspection. In rare instances in which the algorithm for matching the states failed, the state for which the disagreement occurred was removed from the comparison. The sets of computed states of positive and negative Kronig symmetry [34] were compared to the experimental data independently of each other. The fit parameters were varied until the standard deviation in the region of the comparison became smaller than  $0.2 \text{ cm}^{-1}$ . In order to speed up the convergence, as initial values for the  $c_{\ell'}^{\ell, \Lambda=0}$  ( $\ell$  is nominal and  $\ell'$  admixed character), we used a previously available, but unpublished, set of *ab initio* eigenvector decomposition coefficients calculated as in [4, 35]. For  $c_{\ell'}^{\ell, \Lambda=0}$ , mixing of the states with  $\ell \leq 5$  was considered. Our fit was not sensitive to small mixing coefficients for  $c_{\ell'}^{\ell, \Lambda=1}$  and  $c_{\ell'}^{\ell, \Lambda=2}$  when  $\ell > 3$ , and we were only able to determine the mixing coefficients for the  $^2\Sigma^+$  states ( $\Lambda = 0$ ). For  $c_{\ell'}^{\ell, \Lambda=1}$ , only small adjustments were made to the values presented in [5], and no mixing with  $\ell > 3$  states was included. For  $c_{\ell'}^{\ell, \Lambda=2}$  we used the values given in [5], and no mixing with  $\ell > 3$  states was included. We attempted varying  $c_{\ell'}^{\ell, \Lambda=1,2}$  and including the  $\ell = 4$  states, but our fit was not sensitive to these variations. Variation of coefficients for  $c_{\ell'}^{\ell, \Lambda>2}$  was not attempted. The coefficients that were not varied were set to  $\delta_{\ell, \ell'}$ . Since the zero-field Hamiltonian is block-diagonal in Kronig symmetry, the parameters were varied independently in + and - Kronig symmetry blocks. This approach is justified, in part, by the fact that states belonging to higher values of  $v^+$  were not included in the calculation. Higher  $v^+$  interlopers affect the states of positive and negative Kronig symmetry in different ways [1, 5]. Small variations of  $\alpha$ ,  $\gamma$ , and  $\mu^2 - Q$  were attempted, but the best agreement between the calculated and experimentally observed energy values was observed for the values previously reported ([1],



[6]).

Once agreement between experiment and calculation at zero field was optimized, interactions due to the external electric field were included in the Hamiltonian. We made the assumption that, for the range of the electric field strengths used here,  $N^+$ -changing interactions are negligible. When only the  $\ell$ -changing interaction is considered, the Stark matrix element for the electric field oriented along the  $z$  axis is given by (the derivation of this expression will be discussed elsewhere;  $e = 1$  in atomic units):

$$H_{Stark} = eE_{Stark} \sum_{\ell_1, \ell_2} c_{\ell_1}^{\ell', \Lambda_1} c_{\ell_2}^{\ell'', \Lambda_2} (-1)^{N_1 + N_2 + 1/2 + M_J} \left( \frac{1 + (-1)^{p_1 + p_2 + 1}}{2} \right) \langle n, \ell_2 | r | n, \ell_1 \rangle$$

$$\sqrt{1 + \delta_{\Lambda_1, 0} + \delta_{\Lambda_2, 0} - 2\delta_{\Lambda_1, 0}\delta_{\Lambda_2, 0}} \sqrt{(2N_1 + 1)(2N_2 + 1)(2\ell_1 + 1)(2\ell_2 + 1)(2J_1 + 1)(2J_2 + 1)}$$

$$\begin{pmatrix} \ell_2 & 1 & \ell_1 \\ 0 & 0 & 0 \end{pmatrix} \begin{pmatrix} N_1 & N_2 & 1 \\ -\Lambda_1 & \Lambda_2 & \Lambda_1 - \Lambda_2 \end{pmatrix} \begin{pmatrix} \ell_2 & \ell_1 & 1 \\ -\Lambda_2 & \Lambda_1 & \Lambda_2 - \Lambda_1 \end{pmatrix} \begin{pmatrix} 1 & J_1 & J_2 \\ 0 & -M_J & M_J \end{pmatrix} \left\{ \begin{matrix} 1 & J_1 & J_2 \\ \frac{1}{2} & N_2 & N_1 \end{matrix} \right\} \quad (3.7)$$

Transition dipole moments were calculated by numerical integration of hydrogenic wavefunctions. Hydrogenic dipole moments are a good approximation for the core-nonpenetrating states, however, it is likely that the calculated relative intensities were affected by this approximation for transitions between the core-penetrating and core-nonpenetrating states. Since the comparison with experiment was done at low electric field strength and low  $N$  (the states accessed through  $N' = 0, 1, 2,$  and  $3$  intermediate state levels), values of  $N \leq 10$  were considered sufficient for the calculation in the presence of the electric field. The total Hamiltonian, when the external electric field is along the  $z$  axis:

$$H = H_0 + H_{Stark} \quad (3.8)$$

was diagonalized for values of the electric field strength ranging between 0 and 180 V/cm, in steps of 10 V/cm. The Hamiltonian is block-diagonal in  $M_J$ , so all  $M_J$  values accessible in the experiment were treated independently.

In order to compare the calculation to the experiment, a spectrum was calculated from the energy values and eigenvectors obtained by the diagonalization, and convoluted with  $0.1 \text{ cm}^{-1}$  Lorentzian lineshapes. The eigenvectors were used to calculate the transition intensities in the double resonance experiment using the expressions for transition intensities among Hund's case (b) states given in [3], with the correction that  $(1 + \delta_{\Lambda',0} + \delta_{\Lambda,0} - 2\delta_{\Lambda',0}\delta_{\Lambda,0})$  should appear with the exponent  $\frac{1}{2}$  instead of  $-\frac{1}{2}$ . Since the calculation is done for the lowest- $N$  rotational levels, we do not neglect the difference between  $J$  and  $N$  when calculating the transition intensities. The spectrum was calculated for the  $pp$  polarization arrangement.

A simplifying assumption was made for the  $\ell$  character of the intermediate  $F' \ ^2\Sigma^+$  state. It was assumed that this state is composed exclusively of  $p$  and  $d$  characters, in order to avoid having to consider interferences among different transition amplitudes into the Rydberg states (for example, had  $f$  character been included in the intermediate state, then the  $d \leftarrow p$  and  $d \leftarrow f$  transition amplitudes into each Rydberg state would interfere). Similarly, an assumption was made for the ground  $\ ^2\Sigma^+$  state  $\ell$ -characters (to be only  $s$ - $p$ -mixed). No attempt was made to determine the  $\ell$  character of the ground and intermediate states. Instead, since with our assumptions there is no interference between two basis-state transition paths, the intensity of the  $f \leftarrow d \leftarrow p$  transition path relative to that of the  $d \leftarrow p \leftarrow s$  transition path was adjusted by varying only one parameter by hand to get the best agreement with the experimentally observed intensity distribution.

Also, to simplify the calculation, we assumed that all transitions include a change of  $\ell$  for the Rydberg electron. This assumption is not strictly correct for large  $\Delta n^*$  transitions, since for large  $\Delta n^*$  the  $\ell$ -changing transition dipole moment decreases and can become comparable to the permanent dipole moment (see Fig. 3.4). The simplified  $\ell$ -character of the intermediate state, considering only the  $\ell$ -changing transitions, and the use of hydrogenic transition dipole moments, led to occasional disagreements between the calculated and the observed transition intensities.

## 3.6 Results and discussion

### 3.6.1 Stages of decoupling

In the absence of an external electric field, the most suitable representation for a molecular core-nonpenetrating Rydberg state is the Hund's case (d) basis. Each  $\ell$  state is split into  $2 \text{Min}(N, \ell) + 1$  components with different value of  $\ell_R$  ( $\ell_R = N - N^+$ ) due to the coupling of  $\ell$  and  $N^+$  ( $N = \ell + N^+$ ). Each of the  $\ell_R$  components, for a fixed  $N$ , will have a different value of  $N^+$ . When Hund's case (d) is the appropriate coupling case, the energy-level pattern-forming quantum number in the spectrum is  $N^+$ , and the  $N$ -states belonging to the same value of  $N^+$  cluster together in energy.

In the presence of the electric field, interaction among some of the previously uncoupled states is turned on. The Stark effect in molecular Rydberg states has its origin either in the permanent dipole moment of the ion-core or the transition dipole moment. For two Rydberg states belonging to the same- $n^*$  supercomplex, the transition dipole moment scales as  $\langle n, l | er | n, l + 1 \rangle = -\frac{3}{2}ea_0n\sqrt{n^2 - \ell^2}$  [7], and is usually orders of magnitude larger than the permanent dipole moment of the ion-core, even for a highly dipolar ion such as  $\text{CaF}^+$ . When  $n^*$  is sufficiently large, the dominant interaction with the external electric field will thus come from intracomplex ( $\Delta n^* < 1$ ) transition dipole moments. The leading term in the Stark Hamiltonian is given by Eq. 3.7. Selection rules for this type of interaction are  $\Delta \ell = \pm 1$ ,  $\Delta N = 0, \pm 1$ , and  $\Delta N^+ = 0$ , see Table 3.1, and the interaction occurs exclusively within a particular  $N^+$ -cluster. The number of states that belong to a particular  $N^+$ -cluster, among which mixing due to the dominant term in the Stark Hamiltonian can occur is:

$$\sum_{\ell=3}^{n-1} \sum_{N=N^+-\ell}^{N^++\ell} (2\text{Min}(\ell, N) + 1) \quad (3.9)$$

The zero-field structure within a particular  $N^+$  cluster is such that states with higher  $N$  and  $\ell$  are clustered more closely together in energy (the transition toward Hund's case (d)

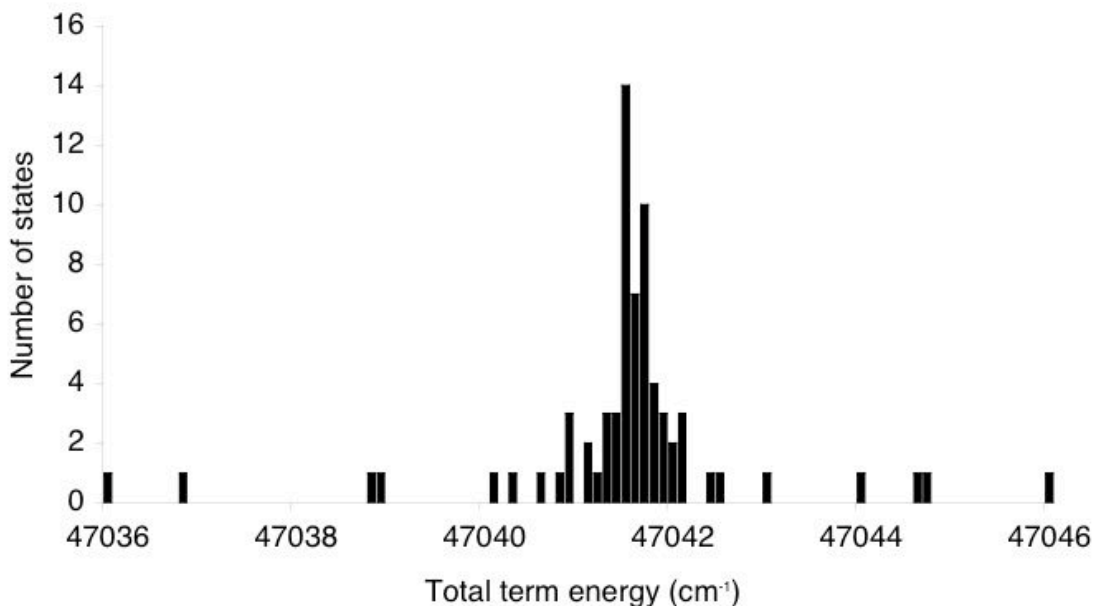


Figure 3.5: Calculated or experimentally observed (where available) energies of all of the the core-nonpenetrating ( $3 \leq \ell \leq 12$ ) states that belong to the  $N^+ = 3$  cluster in  $n^* = 13$ . Most of the states are located near the center of the cluster, especially at higher values of  $\ell$  and  $N$ . Outliers are found among lower- $\ell$ , lower- $N$  states for which the evolution toward Hund's case (d) is not complete, or where core-penetration effects are non negligible.

is complete), while the outliers in energy within the same  $N^+$  are found among the lower- $N$ , lower- $\ell$  states, where the transition toward Hund's case (d) is less complete, see Fig. 3.5. With the resolution available in our experiment, only these low- $N$ , lower- $\ell$  ( $f$ ,  $g$ , and sometimes  $h$ ) outliers are sufficiently separated from the high density of states at the center of the cluster to be assigned. These states contain the most information about the interaction of the core-nonpenetrating states with the core-penetrating states. Because of their low- $N$  character, these outliers will be experimentally accessible when the spectrum is recorded from the lowest- $N$  rotational levels in the intermediate state. In addition, the number of  $\ell_R$  components present at low  $N$  is smaller than at high  $N$ . Thus selecting low  $N$  in the intermediate state helps reduce the number of states accessed at zero field and the number of states that share the bright character at the lowest Stark fields, and low  $N$  provides access to the states most useful in analyzing the interaction with the core-penetrating states.

The appearance of a molecular Rydberg Stark spectrum in a particular  $n^*$  (see Fig. 3.6)

is determined by the amplitudes of  $\ell$ -changing Stark interaction and  $N^+$ -changing Stark interaction relative to the zero-field energy splitting caused by multipole moments, polarizabilities, and rotation. In weak electric fields, unless there is an accidental degeneracy among the states with neighboring  $N^+$  values, the mixing first starts to occur among the states with  $\ell$  differing by  $\pm 1$ , but having the same  $N^+$ . It is only as the field strength increases that the mixing of states belonging to different  $N^+$  complexes starts to occur. In the case of CaF, a manifold of states having different  $\ell$  but the same  $n^*$  and the same  $N^+$  starts to appear around each  $N^+$  that is accessible for a particular choice of pump transition. The relative intensities of each of these  $N^+$ -manifolds will differ from one  $N^+$  value to the next. As the electric field increases, states belonging to two different  $N^+$ -clusters start to interact and manifolds associated with different values of  $N^+$  merge to form a Stark manifold associated with a particular  $n^*$  and  $v^+$ , similar to the atomic case (see Fig. 3.6).

### 3.6.2 Effective Hamiltonian matrix diagonalization

The region of  $n^* = 13$  has previously been studied and most of the  $\ell \leq 3$  and some of the  $\ell > 3$  states have been assigned for the values of the rotational quantum number  $N$  up to 12 [1, 6]. However, most of the rotational assignments for the lowest rotational levels of the core-nonpenetrating states were not previously available. Due to the opposing effects of  $\ell$ -mixing and  $\ell$ -uncoupling, spectral patterns are complex and rotational assignments are problematic, especially for the lowest rotational levels. Assignments additional to those published in [1, 6] have been made using polarization diagnostics described in [3]. Good agreement between the fit described in Section IV and the experimentally observed spectra was critically dependent upon correct assignments of the lowest rotational levels at zero field. These low- $N$  assignments were also a *sine qua non* to making new assignments in the presence of the electric field.

The standard deviation between the fit and the experiment was  $< 0.2 \text{ cm}^{-1}$ . The coefficients in the eigenvector decomposition, for  $\Lambda = 0$  states and  $\ell$  ranging from 0 to 5, that

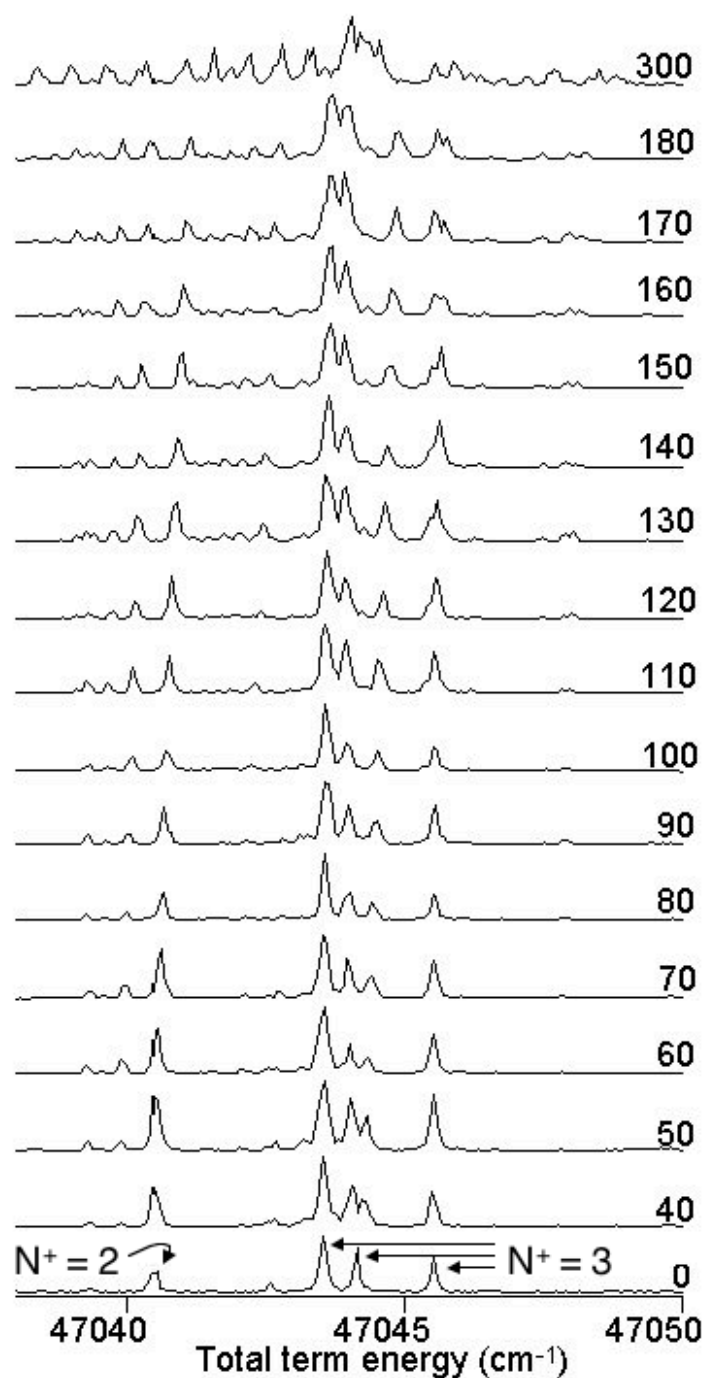


Figure 3.6: Stark effect in the energy region around the integer value of  $n^* = 13$ , experimentally observed in double resonance spectra from the  $N' = 1$  intermediate state, in the  $pp$  polarization arrangement. A weak electric field causes the Stark manifolds associated with different values of  $N^+$  to appear, but as the field increases, these manifolds merge. The electric field in V/cm is given on the right hand side of the plot. The  $N^+$  values of the dominant zero-field bright features are marked on the plot.

Table 3.2: Best fit values for the  $\ell$  mixing coefficients of rotationless  $p, d, f, g,$  and  $h$   ${}^2\Sigma^+$  states. The  $s$   ${}^2\Sigma^+$  basis state was not included in the fit, as it was not located near an integer value of  $n^*$ . Its  $\ell$ -decomposition corresponds to that of [5]. Nonunity in the sum of *squared* mixing coefficients is due to the loss of  $v^+ = 1$  basis state character due to coupling with higher- $v^+$  states.

State	$s$	$p$	$d$	$f$	$g$	$h$	sum
12.88 ${}^2\Sigma^+$	-0.593	-0.805	0.018	0.013	-0.004	0	1.00
13.19 ${}^2\Sigma^+$	0.135	-0.142	0.903	-0.365	0.111	0.026	1.00
$f^2\Sigma^+$	-0.009	0.117	-0.295	-0.821	0.378	-0.093	0.93
$g^2\Sigma^+$	0	-0.017	-0.181	-0.329	-0.850	0.369	1.00
$h^2\Sigma^+$	-0.006	-0.060	-0.161	0.125	0.327	0.921	1.00

gave the best agreement between the fit and the experiment are given in Table 3.2. Of the core-penetrating states included in the fit, the 13.19  ${}^2\Sigma^+$  state was found to be most strongly mixed with the core-nonpenetrating states. Including the 12.88  ${}^2\Sigma^+$  state did not significantly affect the fit. Mixing with states with  $\ell$  higher than 5 was not included in the fit, since states with  $\ell > 5$  have not been experimentally observed at zero field. Only  $v^+ = 1$  states were included in the fit, although interactions with the  $v^+ > 1$  interlopers have been described [5]. A small deviation from unity of the sum of squared mixing coefficients for a particular  $\ell$  was allowed, in order to allow for the losses of  $\ell$ -character due to coupling with states of higher  $v^+$ . Because of the exclusion of mixing with  $\ell > 5$  states, it is possible that the mixing coefficients for  $h$  ( $\ell = 5$ ) states are affected by “edge effects” that result from this  $\ell$ -cutoff. Since our fit was not sensitive to the variation of  $c_{\ell'}^{\ell, \Lambda=1}$  and  $c_{\ell'}^{\ell, \Lambda=2}$ , values from [5] were used, with only a minor modification in the case of  $\Lambda = 1$ .

The mixing coefficients in Table 3.2 indicate a non-negligible core-penetrating character of the  $g(-4)$  state (Hund’s case (d) notation, denoting  $\ell(\ell_R)$ , where  $\ell_R$  is the projection of  $\ell$  on the rotational axis of the ion). The strong interactions among the core-nonpenetrating  $g(-4)$  and  $f(-3)$  states, and a core-penetrating 13.19  ${}^2\Sigma^+$  state, are reflected by the mixing coefficients in Table 3.2. Neither of the two models developed previously to describe the Rydberg states of CaF in this  $n^*$  region includes all three of the states found to interact strongly in this analysis. The interaction of the core-penetrating states ( $\ell = 0, 1,$  and  $2$ )

with the partially penetrating  $f$  states in CaF has previously been modeled using an MQDT fit [33]. That fit has been extended by the addition of higher- $v^+$  interlopers [5]. On the other hand, core-nonpenetrating  $f$ ,  $g$ , and  $h$  states, accessed predominantly at intermediate  $N$  and  $13 \leq n^* \leq 17$  of CaF, have been fitted to a long-range model [6].

The interactions among  $g(-4)$ ,  $f(-3)$ , and  $13.19 \ ^2\Sigma^+$  states are also obvious from the energy and intensity patterns in the observed spectra, plotted in Fig. 3.7. Even though it is impossible to model these three states in isolation from other Rydberg states in their vicinity, it is still obvious that there is a strong interaction among all three of them. The polarization dependence of the transition intensity confirms that all three states involved in this interaction have the same  $N$  value. The usefulness of lower- $N$  rotational assignments in the separation of the short-range and long-range interactions is evident in Fig. 3.7. It is only in the several lowest values of  $N$  that the strong three-state interaction becomes obvious, while, if only  $N > 4$  assignments are considered, this interaction remains too weak to be detected. Our previous fit, described in [6], gave non-physical values for the anisotropic polarizability because the interaction with core-penetrating states was incompletely removed from our long-range model.

Using the coefficients given in Table 3.2, we produced spectra by the method described in Section IV. Figure 3.8 displays the calculated and observed spectra recorded from the  $N = 3$  level in the intermediate state for electric field strengths of 0, 60, 120 and 180 V/cm. Within one spectrum, the quality of agreement between the calculated and experimentally observed transition intensities varied from one  $N^+$  cluster to another. We assumed that the intermediate state is a pure- $\Lambda$  state, but  $\ell$ -mixed. A pure- $\Lambda$ , pure- $\ell$  state in a Hund's case (b) basis, when decomposed in a Hund's case (d) basis, spans either all-even or all-odd  $N^+$ -basis states. However, a pure- $\Lambda$  but mixed- $\ell$  state spans both even and odd values of  $N^+$ . However, since we assumed that the intermediate state contains *only*  $p$  and  $d$  character, this limits the different  $N^+$  basis states present in the intermediate state. The assumption of simplified  $\ell$ -characters in the intermediate state eliminates interferences among the transition



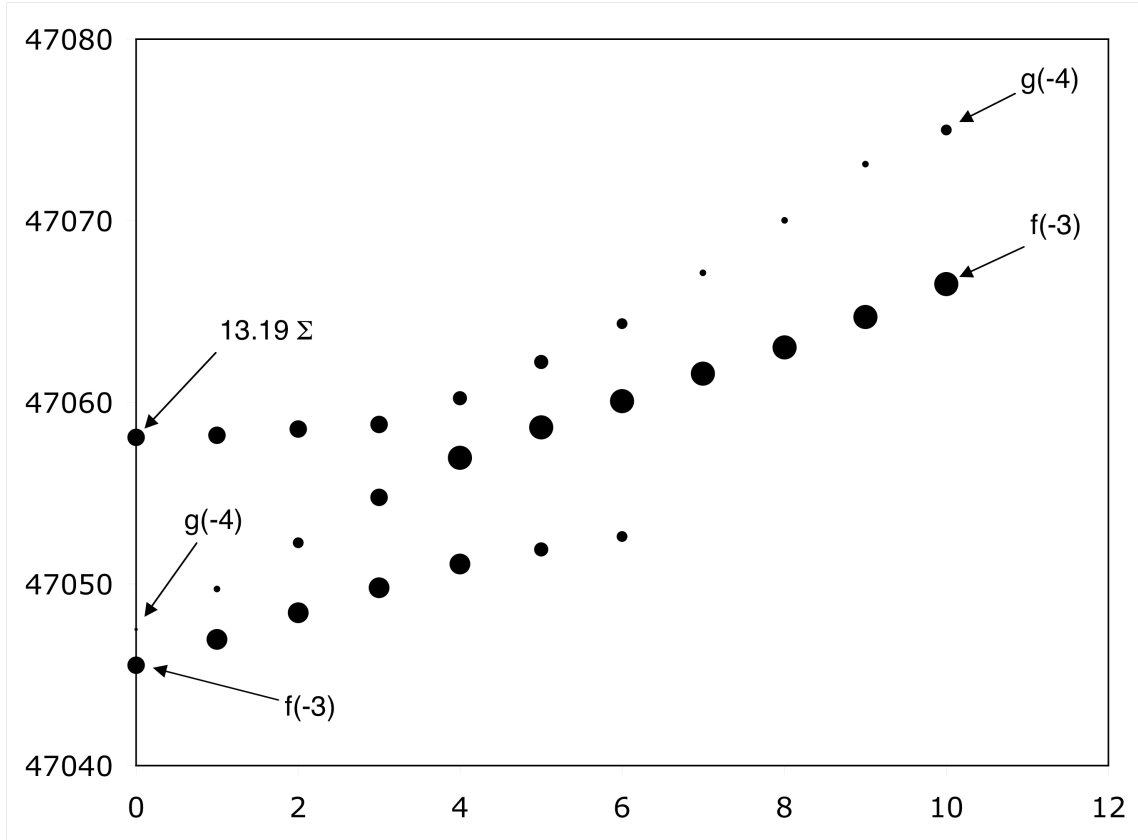


Figure 3.7: Interaction among  $f(-3)$ ,  $g(-4)$ , and  $13.19 \ ^2\Sigma^+$  states. The  $\ell(\ell_R)$  labels at high  $N$  correspond to the assignments in [6]. Marker sizes approximately represent the experimentally observed intensities of the spectral features. The interactions among these three states become apparent only for  $N \leq 4$  rotational levels, and could remain unnoticed if the lowest- $N$  rotational assignments are not available.

amplitudes of the different bright  $\ell$  components, thereby simplifying the intensity patterns in the calculated spectra. We have also assumed that the transition intensity comes exclusively from transition amplitudes in which  $\ell$  changes by  $\pm 1$ . In addition, hydrogenic transition dipole moments were used for both core-nonpenetrating and core-penetrating states. These assumptions result in poorer agreement with the calculated intensities for some of the  $N^+$  clusters. For example, the feature at  $47054.59 \text{ cm}^{-1}$  in Fig. 3.8a belongs to the cluster with the nominal value of  $N^+ = 6$ . The intermediate  $N' = 3$  state in this case contains no  $N^{+'} = 6$  character, because that would require  $f$  character and we have assumed that  $f$  character is negligible in the intermediate state. This absence of  $N^{+'} = 6$  character in the intermediate state results in a weaker transition intensity for this particular feature in the calculated spectrum. Its nonzero intensity comes from small  $N^+ < 6$  character of the  $\ell$ -admixed states in the nominally  $g(-4)$  Rydberg state.

As the electric field is switched on, new states start to appear in both the calculated and experimentally observed spectra. This appearance of new features in the spectrum is due to electric field-induced intensity borrowing from states that have bright character at zero-field. Since the electric field-induced interaction among two states depends on the matrix elements between them and on their energy separation, unless two states that belong to two different values of  $N^+$  are accidentally near-degenerate, the strongest electric field-induced interactions will be among the states that belong to the same  $N^+$  complex. These new features, admixed by the field, are evident in Fig. 3.8b. As the electric field increases, the number of states admixed by the field increases rapidly. In addition to intensity borrowing, the electric field causes energy shifts. Eventually, the electric field becomes strong enough to significantly mix states belonging to different  $N^+$ -clusters, and the agreement with our model worsens compared to that at low field (see Fig. 3.8d).

It is evident from the agreement between the calculated and experimentally observed spectra that modeling the Stark effect in Rydberg states of CaF using an effective Hamiltonian approach is capable of capturing the main features of the low electric field, low- $N$  Stark

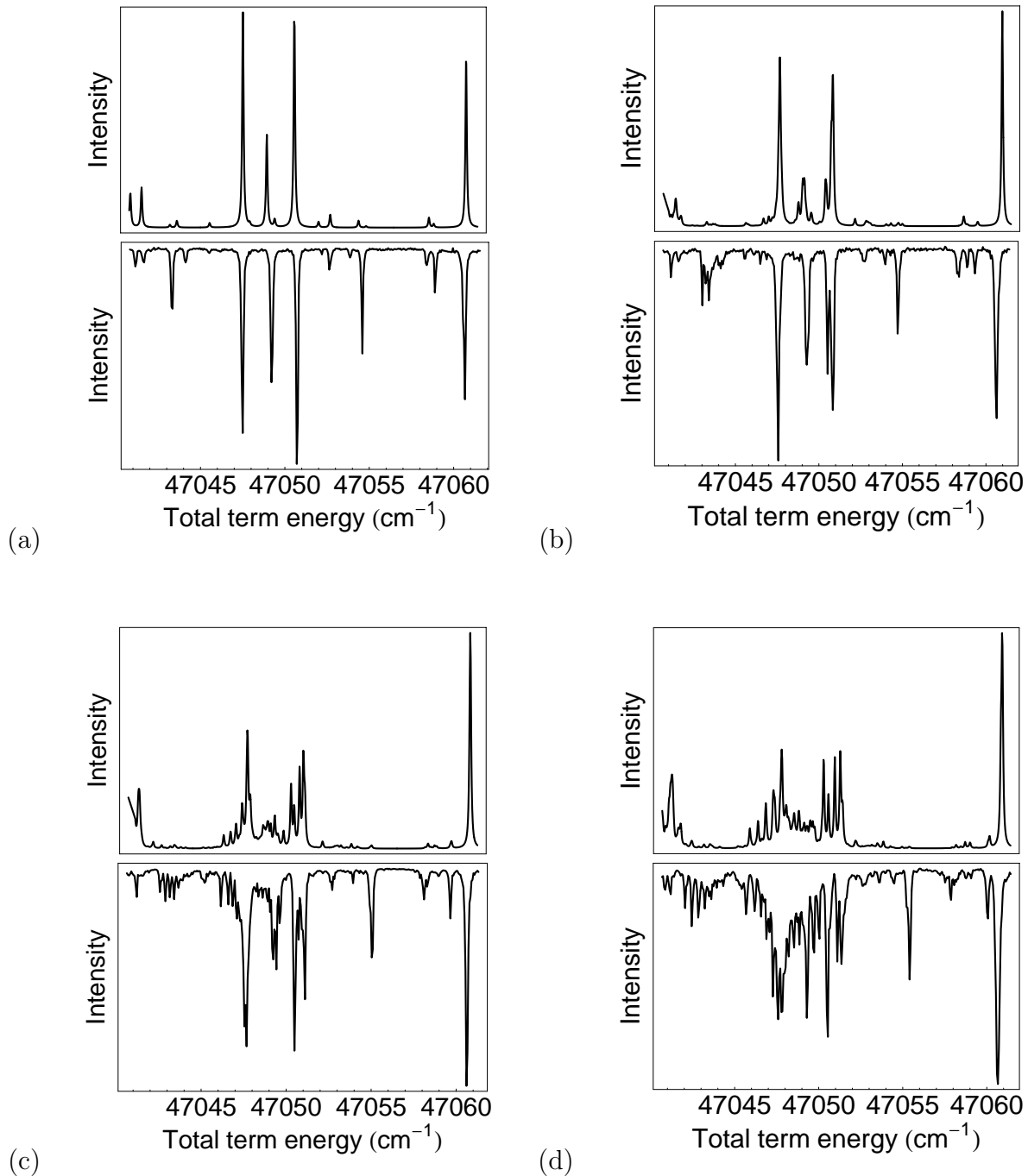


Figure 3.8: Calculated (upper traces) and experimentally observed (lower traces) Stark effect in the double resonance spectra of the Rydberg states of CaF in the vicinity of  $n^* = 13$ . Spectra are accessed through the  $N' = 3$  level of the  $F' \ ^2\Sigma^+$  intermediate state (accessed through an R pump transition from the ground state) in the  $pp$  polarization arrangement. The electric field is 0 V/cm (a), 60 V/cm (b), 120 V/cm (c) and 180 V/cm (d).

effect in molecular Rydberg states. All of the states needed for the long-range description are clustered around integer values of  $n^*$ , requiring inclusion of only a small number of core-penetrating states in the model in order to account for the core-penetration effects. When the electric field is sufficiently weak and  $N$  is sufficiently small, one does not need to include interactions with the neighboring  $n^*$  states. For NO [19], it was reported that there is a negligible difference between the capability of an MQDT model and a matrix diagonalization method (which is more familiar to spectroscopists) to describe the low-field molecular Stark effect. We report here that the same is sufficient for CaF, which, unlike NO, has a molecular ion with a large dipole moment. The main difference between the NO and CaF effective Hamiltonian models is that the penetrating effects in our effective Hamiltonian are included by *ad hoc* parameters determined by the fit. Although the presence of the permanent ion-core dipole moment requires minor changes in the Hamiltonian, the treatment of the Stark effect in Rydberg states by an effective Hamiltonian matrix diagonalization method is the same as in non-dipolar molecules.

### 3.6.3 Assignments

Calculated spectra were used to check the already published assignments, and to make new ones. In order to facilitate the assignment procedure, we prepare stacked spectra at several different values of the electric field. These stacked spectra are prepared by plotting one above another several total term energy spectra originating from successive  $N'$  intermediate levels. In Fig. 3.9 we plot stacked spectra recorded from  $N' = 0, 1, 2,$  and  $3$  at  $0$  and  $70$  V/cm. Since the abscissa is the total term energy, if a particular state is accessed from different intermediate states, this state will appear at the same total term energy in spectra accessed from states with different value of the  $N'$  quantum number. In zero-field spectra, because of the parity alternation as  $(-1)^{N'+\ell}$ , the same state can only appear in two spectra recorded from intermediate state  $N'$  values differing by two. However, since the electric field mixes states of opposite parity, in the presence of the electric field it becomes possible

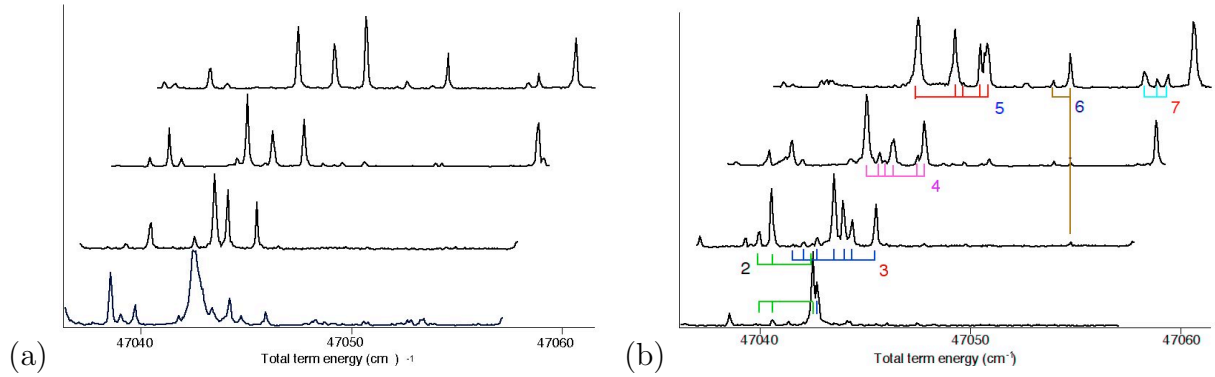


Figure 3.9: Stacked double resonance spectra at 0 V/cm (a) and 70 V/cm (b), recorded from  $N' = 0, 1, 2,$  and  $3$  (bottom to top), in the  $pp$  polarization arrangement. Electric field induced mixing ( $\Delta\ell = \pm 1, \Delta N = 0, \pm 1, \Delta N^+ = 0$ ) results in intensity borrowing and the appearance of new features in the spectrum. Transitions that terminate in different values of  $N^+$  are color-coded according to the value of  $N^+$ , with the corresponding values of  $N^+$  given in the same color on the plot.

for the same Rydberg state to appear in spectra recorded from two consecutive values of  $N'$ . Interpretation of the spectrum recorded from  $N' = 0$  demands special attention. This spectrum is recorded using a P(1) pump transition. The high density of spectral features in the P-branch of the  $F' \ ^2\Sigma^+ \leftarrow X \ ^2\Sigma^+$  transition usually does not permit using P-branches as pump transitions with this particular intermediate state, and only two assignments were made using the spectrum recorded from the  $N' = 0$  state. Both of these assignments have been confirmed in the analysis of the R(0) spectrum recorded at 70 V/cm, where extra transitions induced by the Stark field appear in the spectrum.

When analyzing stacked spectra recorded in the presence of an electric field, we make the assumption that, in the absence of accidental degeneracies,  $N^+$ -intra-cluster mixing is stronger than  $\Delta N^+ = 1$  inter-cluster mixing. This means that the first dark states to obtain intensity by electric field-induced mixing will be the states of the same  $N^+$  as the bright state. Since the transition intensity, when recorded from a particular  $N'$  level, varies from one value of final state  $N^+$  to the next, and also varies within one  $N^+$ -cluster when accessed from a different  $N'$ -level (governed by the decomposition of the lower  $N'$  state in Hund's case (d) basis), there is going to be a particular value of  $N'$  most suitable for accessing each of the

Table 3.3: Assignments of lowest- $N$ , low- $\ell_R$ ,  $f$ -states ( $\text{cm}^{-1}$ ).

N	$f(-3)$	$f(-2)$	$f(-1)$
0	47045.53		
1	47047.77	47044.15	47042.51
2	47050.71	47046.27	47043.52
3	47054.20	47049.20	47045.07
4	47058.49	47052.96	47047.50

Table 3.4: Assignments of lowest- $N$ , low- $\ell_R$ ,  $g$ -states ( $\text{cm}^{-1}$ ).

N	$g(-4)$	$g(-3)$	$g(-2)$	$g(-1)$	$g(0)$
0	47047.50				
1	47050.63		47044.07		
2	47054.59	47049.20	47045.58	47041.94	47040.50
3	47059.18	47053.86	47048.64	47044.12	47041.36
4	47064.34	47058.58	47052.63	47047.38	47043.31

$N^+$  clusters, see Fig. 3.9. If there is an ambiguity whether a particular feature that appears in two spectra recorded from different values of  $N'$  is in fact the same state, the electric field tuning of both spectral features can be compared. Tables 3.3, 3.4, and 3.5, contain the assignments of the  $N \leq 4$  and low- $\ell_R$  levels for  $f$ ,  $g$ , and  $h$  states, made either by the Stark effect, polarization spectroscopy, or previously available [6]. For Stark-based assignments, the value of the zero-field energy is obtained by linear extrapolation of the energy to the zero-field value, unless the same state is accessible at zero-field from a different value of  $N'$ .

Table 3.5: Assignments of lowest- $N$ , low- $\ell_R$ ,  $h$ -states ( $\text{cm}^{-1}$ ).

N	$h(-5)$	$h(-3)$	$h(-1)$
0	47049.79		
1	47053.99	47045.89	
2	47058.89		47042.56
3			47044.56
4			

### 3.6.4 Polarization dependence

Because of their rotational structure and strong  $\ell$ -mixing, even in the absence of the external electric field, zero-field molecular Rydberg spectra will display a polarization dependence of the transition intensities that is different from the atomic case [7]. Because of the polarization dependence of the bright state character, when the Rydberg state spectrum is recorded in the presence of the electric field, the Stark spectrum of each Rydberg state also displays dependence on the polarization arrangement. In the absence of the external electric field, linear polarization can be used to distinguish Q transitions from P and R transitions (at the lowest values of  $N$  it is possible to distinguish P from R, as well). For example, in an  $\omega_1 + \omega_2$  double resonance experiment, with the  $\omega_1$  transition being an R transition, the  $\omega_2$  P or R transition will have stronger intensity when the  $\omega_1$  and  $\omega_2$  photons have parallel polarization than if their relative polarizations are perpendicular. On the other hand, if the  $\omega_1$  transition is R and the  $\omega_2$  transition is Q, the Q transition intensity will be stronger when the relative polarizations of the  $\omega_1$  and  $\omega_2$  photons are perpendicular. Similarly, circular polarization can be used to distinguish all three types of transitions, see Fig. 3.10. Again, if the  $\omega_1$  transition is R, the  $\omega_2$  R transition will have stronger intensity if  $\omega_1$  and  $\omega_2$  photons have the same helicity. If the  $\omega_1$  is an R transition, and  $\omega_2$  a P transition, the transition intensity of  $\omega_2$  will be stronger when  $\omega_1$  and  $\omega_2$  photons have the opposite helicity. The intensity of the  $\omega_2$  Q transition will not differ between RHCP and LHCP polarization of the  $\omega_2$  photon if  $\omega_1$  in this case.

The relative polarizations of the  $\omega_1$  and  $\omega_2$  photons in a double resonance excitation scheme determine the transition intensity into the state with bright character. In each  $N^+$  cluster, in the general case, there might be more than one value of  $N$  with bright-state character. The relative transition intensities for the three possible bright basis states ( $\Delta N = 0, \pm 1$ ) will be polarization-dependent. In the presence of the electric field, the three transition amplitudes ( $\Delta N = 0, \pm 1$ ) will interfere, and the overall appearance of the Stark spectrum will be polarization-dependent. The strength of the coupling caused by the Stark

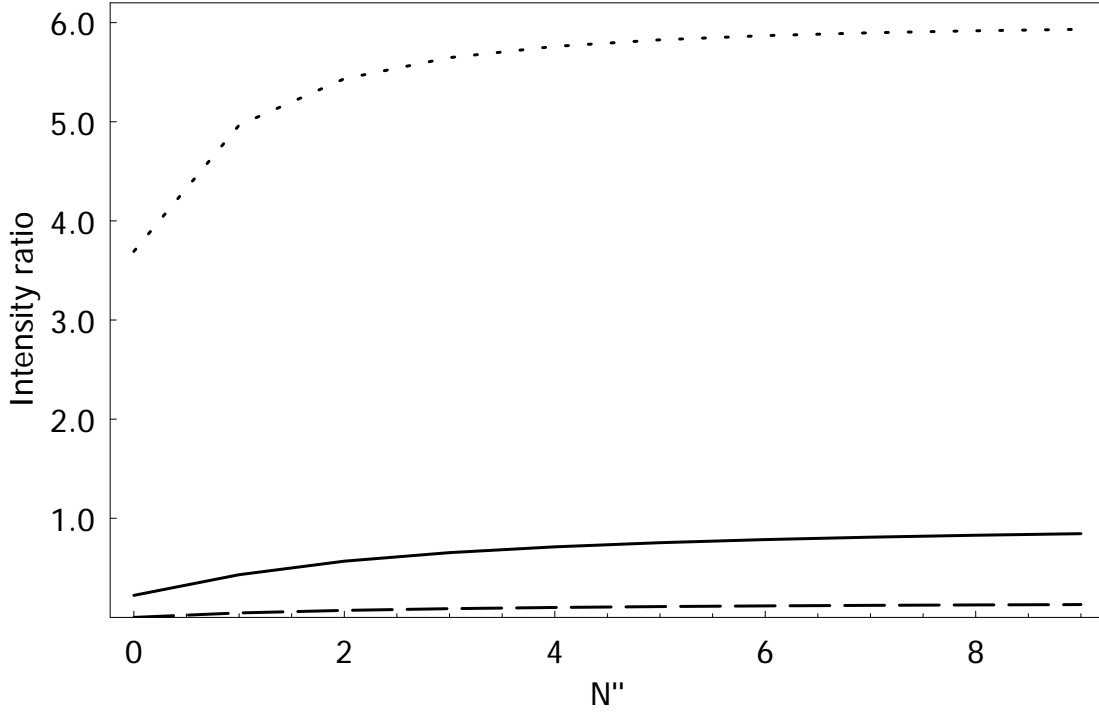


Figure 3.10: Calculated polarization dependence of the double resonance transition intensities of the composite (transition intensities summed over the transitions among the unresolved spin-rotation components)  $N \leftarrow N' = N'' + 1 \leftarrow N''$  lines (R pump), when both photons are circularly polarized. The plots show the  $N''$ -dependence of the ratio of the transition intensity with two photons of the same helicity to that of two photons with opposite helicity ( $N''$  is the ground state rotational quantum number). Note that points with  $N < \Lambda$ ,  $N' < \Lambda'$ , and  $N'' < \Lambda''$  must be absent, as well as Q branches, for  $\Lambda = 0$ . P, Q, and R branches are plotted in dashed, solid, and dotted line, respectively. For more details see [3].



effect is much more strongly dependent on the energy separation among the interacting states than on small variations of the coupling matrix elements with polarization. Therefore the dominant effect of the polarization will come from the relative polarizations of the  $\omega_1$  and  $\omega_2$  photons with respect to each other, and less from the orientation of  $\omega_1$  and  $\omega_2$  photons relative to the Stark field.

As the electric field is increased,  $N$ -mixing increases rapidly, and one would expect that the polarization dependence will be lost when the bright character of the three possible bright paths ( $N - N' = 0, \pm 1$ ) is uniformly distributed among the highly  $N$ -mixed states within one  $N^+$  cluster. In Fig. 3.11 we show a part of a double resonance Stark spectrum around the integer value of  $n^* = 13$ , recorded at 250 V/cm with R(0) pump transition. The two spectra differ in the polarization arrangement (RHCP-RHCP-vertical vs. RHCP-LHCP-vertical polarization arrangement). It is evident that, in this case, even though  $N$  is strongly mixed at 250 V/cm, the bright  $f(-3)$   $N = 0$  state is sufficiently distant from the other states of the  $N^+ = 3$  cluster so that memory that the brightness originates from the  $N = 0$  character is not completely lost in the region of the spectrum around 47045.5  $\text{cm}^{-1}$ . The region of the spectrum in which the intensity is enhanced in the RHCP-LHCP-vertical polarization arrangement is predominantly due to the  $N' - 1$  bright character (for the zero-field spectrum of this region, see the lowest trace in Fig. 3.6).

Thus the polarization dependence of the transition intensity provides insight into the mixing pathways within an  $N^+$  cluster, but it is also possible to use the polarization dependence to observe examples of inter- $N^+$  cluster coupling. Figure 3.12 displays the same region of the spectrum as Fig. 3.11, but this time recorded using linear polarization. The red trace was recorded with the  $pp$  polarization arrangement and the blue trace with the  $ps$  polarization arrangement. Both spectra were recorded with the R(0) pump transition and  $E_{Stark} = 250$  V/cm. The polarization arrangements employed in this experiment are capable of distinguishing Q transitions from P and R transitions. Since most of the bright Q transition character comes from the  $f(-2)$   $N = 1$  state at 47044.15  $\text{cm}^{-1}$ , which is near-degenerate

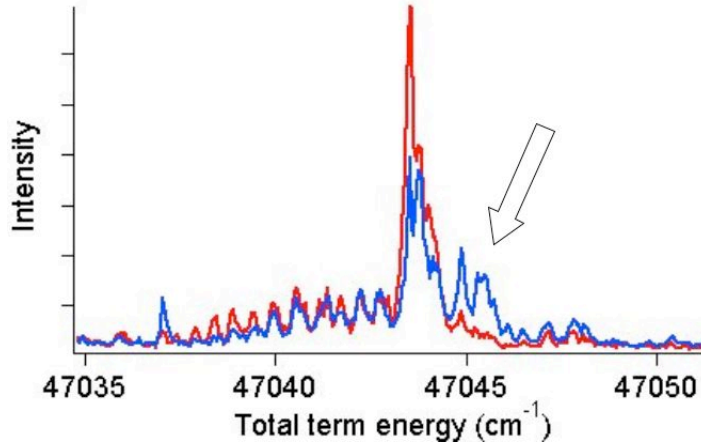


Figure 3.11: Double resonance spectrum of CaF at 250 V/cm in the vicinity of  $n^* = 13$ , recorded from  $N' = 1$  in RHCP-RHCP-vertical (red) and RHCP-LHCP-vertical (blue) arrangements. The arrow identifies the region in the spectrum where the  $N$ -mixing within a particular  $N^+$  cluster due to the external electric field is incomplete, but memory of the polarization dependence is not yet lost.

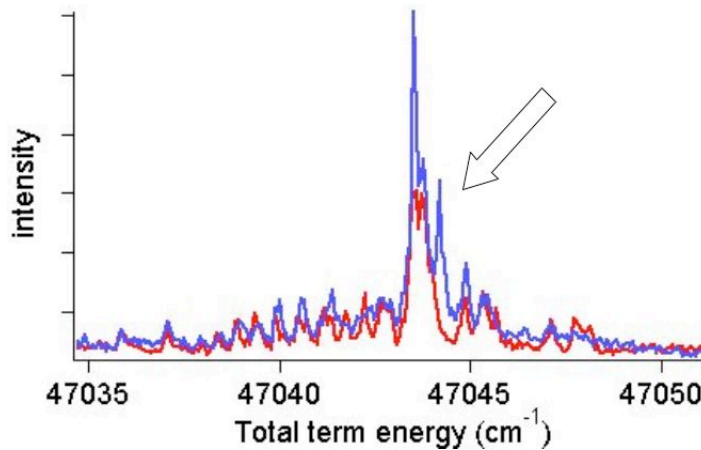


Figure 3.12: Double resonance spectrum of CaF at 250 V/cm in the vicinity of  $n^* = 13$ , recorded from  $N' = 1$  in  $pp$  (red) and  $ps$  (blue) arrangements. The arrow identifies a feature that exhibits a distinct Q-like polarization dependence at 250 V/cm, even though the surrounding features have lost their memory of the polarization dependence due to  $N$ -mixing induced by the field. This polarization behavior, different from other features in the  $N^+ = 3$  cluster at the same electric field amplitude, is explained by an accidental degeneracy between two states that have different values of  $N^+$ .

with many of the states that belong to the  $N^+ = 3$  cluster, it is expected that the  $f(-2)$   $N = 1$  bright state character will be rapidly and uniformly distributed among the states in this  $N^+ = 3$  cluster.

However, it is evident that only one feature in the spectrum in Fig. 3.12, at 47044.21  $\text{cm}^{-1}$ , displays a strong polarization dependence, even at 250 V/cm, and behaves like an almost pure Q transition. This state appears to be mixed with only one state in the  $N^+ = 3$  cluster, but not mixed with any other states in that  $N^+$ -cluster. It is conceivable that this is a result of an accidental degeneracy between two states belonging to different  $N^+$  clusters. In fact, the  $g(-1)$   $N = 3$  state at 47044.12  $\text{cm}^{-1}$  that belongs to  $N^+ = 4$  is almost degenerate with the bright-character bearing  $f(-2)$   $N = 1$  state at 47044.15  $\text{cm}^{-1}$ . The two states, although almost degenerate, cannot interact directly with each other in the presence of the external electric field, but this field can cause them to interact indirectly by coupling each of them to close-lying intermediaries. In cases like this it is difficult to make an unambiguous assignment, because of interferences among the different  $\Delta N = 0, \pm 1$  transition amplitudes. Overall, the polarization dependence of the transition intensity distribution in a Stark spectrum of Rydberg states is useful for making assessments of both  $N^+$  intra- and inter-cluster mixing pathways.

## 3.7 Summary

The ion-core  $N^+$  rotational structure causes the molecular Rydberg electron to decouple from the ion-core due to an external electric field in several stages. The separation of the stages of the decoupling depends on the molecular parameters, the strength of the electric field, and the  $n^*$  value at which the observation is made. We present here an analysis of the Stark effect in CaF in  $n^* = 13$ . In this example it is possible to observe the first stage, in which  $\ell$  and  $N$  become mixed by the electric field, and the second stage, when  $N^+$ -mixing begins.

We used the Stark effect at low electric field ( $< 100$  V/cm), under conditions where  $N^+$  is conserved, to access the lowest rotational levels of  $f$ ,  $g$ , and  $h$  states, and to assign the actual or nominal value of their  $N^+$  quantum numbers. The assignments rely on the large difference in size between the same- $n^*$  transition dipole moment and the ion-core permanent dipole moment. In order to identify possible accidental degeneracies among the states that belong to different  $N^+$ -clusters, we used the dependence of the transition intensities on the relative polarizations of  $\omega_1$  and  $\omega_2$  linearly polarized photons in a double resonance experiment. Spectral features that exhibited polarization dependence distinct from expectations for a particular  $N^+$ -cluster were shown to belong to a different value of the  $N^+$  quantum number. In the example where circularly polarized light was used, the polarization dependence of the transition intensities provided information about the  $N$ -mixing within a particular  $N^+$ -cluster.

An effective Hamiltonian was used to model the experimentally observed Stark effect. If the spectral window of interest is confined to the region of energy around an integer value of  $n^*$ , interactions with states from the neighboring  $n^*$  can be neglected. When this is the case, both effective Hamiltonian matrix diagonalization methods and Multichannel Quantum Defect Theory perform equally well in describing the Stark effect in Rydberg states. The  $\ell$ -decomposition obtained from the fit in this effective Hamiltonian demonstrates the importance of mixing of the core-nonpenetrating  $g(-4)$  state with both an  $f(-3)$  state

and a core-penetrating  $d\ ^2\Sigma^+$  state. It is evident from Fig. 3.7 that this interaction is only discernible for lower- $N$  rotational levels, but could easily be missed when only  $N > 4$  levels are assigned.

In addition to describing the differences between the Stark effect in atomic and molecular Rydberg states, we applied the Stark effect to gain information about the extent of core-penetration of some of the nominally core-nonpenetrating states. The analysis method for the low-field Stark effect on molecular Rydberg states presented here is limited by the 3 GHz experimental resolution in our optical-optical double-resonance experiment. An optical-optical-microwave experimental scheme, which would provide resolution of several hundred kHz, would overcome the resolution limitations, and the analysis of the low-field Stark effect in such an experiment would provide information about considerably higher  $\ell$ -values than presented here.

The analysis of the stages of the decoupling of the Rydberg electron from the body frame by the external electric field in molecular Rydberg states yields information about the gradual destruction of the barriers between different regions of state space. Knowledge of how the structure of the state space depends on the external electric field will be useful for rational design of experimental schemes that seek to control the population flow in state space. For example, since at low electric field all states belonging to a particular  $N^+$ -cluster are weakly coupled to states outside this cluster, it is possible, using a weak pulsed microwave field, to create a wavepacket composed of states with different values of  $\ell$ , but having the same value of the  $N^+$  quantum number. If a series of shaped low-amplitude microwave photons is applied, and the delay between them controlled, it would be possible to channel population into a particular  $\ell$ , while keeping  $N^+$  constant, in a similar manner to the one proposed for alkali-metal atoms [36]. Since the autoionization lifetimes are  $\ell$ -dependent, such a scheme could exert or exploit control over lifetimes as well. Alternatively, instead of controlling the delay among the excitation pulses, varying the amplitude of the external field would permit an adiabatic change of state upon transit through an avoided crossing. Knowing the locations

of avoided crossings among the states associated with different  $N^+$ -clusters, it is possible, by applying a somewhat stronger Stark field than in the first example, to adiabatically drive a  $\Delta N^+ = 1$  process. In such a case, energy is transferred between the Rydberg electron and the ion-core in two steps, since  $\ell$  gets destroyed before the strength of the field sufficient for causing the  $\Delta N^+$  is reached. In both cases polarization can be used to suppress or enhance particular  $\Delta N$  transitions. In both of these two examples, weak-field control schemes rely on knowledge of the state space structure and locations of resonances among the different types of motion, and the propensity rules that govern the strength of interactions.

## 3.8 Bibliography

- [1] C. M. Gittins, N. A. Harris, M. Hui, and R. W. Field. *Can. J. Phys*, 79:247, 2001.
- [2] H el ene Lefebvre-Brion and Robert W. Field. *The Spectra and Dynamics of Diatomic Molecules*. Elsevier Academic Press, 2004.
- [3] V. S. Petrovi c and R. W. Field. *J. Chem. Phys*, 128:014301, 2007.
- [4] S. N. Altunata, S. L. Coy, and R. W. Field. *J. Chem. Phys.*, 123:084318, 2005.
- [5] R. W. Field, C. M. Gittins, N. A. Harris, and Ch. Jungen. *J. Chem. Phys*, 122:184314, 2005.
- [6] J. J. Kay, S. L. Coy, V. S. Petrovi c, B. M. Wong, and R. W. Field. *J. Chem. Phys*, 128:194301, 2008.
- [7] Thomas F. Gallagher. *Rydberg Atoms*. Cambridge University Press, 1994.
- [8] E. Luc-Koenig and A. Bachelier. *J. Phys. B*, 13:1743, 1980.
- [9] M. L. Zimmerman, M. G. Littman, M. M. Kash, and D. Kleppner. *Phys. Rev. A*, 20:2251, 1979.
- [10] A. R. Edmonds, J. Picart, N. Tran Minh, and R. Pullen. *J. Phys. B*, 12:2781, 1979.
- [11] K. Qin, M. Bistransin, and W. L. Glab. *Phys. Rev. A*, 47:4154, 1993.
- [12] G. R. Lloyd, S. R. Procter, E. A. McCormack, and T. P. Softley. *J. Chem. Phys.*, 126:184702, 2007.
- [13] H. H. Fielding and T. P. Softley. *Phys. Rev. A*, 49:969, 1994.

- [14] J. W. Cooper, E. B. Saloman, B. E. Cole, and Shardanand. *Phys. Rev. A*, 28:1832, 1983.
- [15] S. T. Pratt, E. F. McCormack, J. L. Dehmer, and P. M. Dehmer. *Phys. Rev. Lett.*, 68:584, 1992.
- [16] Y. Yamakita, S. R. Procter, A. L. Goodgame, T. P. Softley, and F. Merkt. *J. Chem. Phys.*, 121:1419, 2004.
- [17] W. L. Glab and J. P. Hessler. *Phys. Rev. A*, 42:5486, 1990.
- [18] E. Y. Xu, H. Helm, and R. Kachru. *Phys. Rev. A*, 38:1666, 1988.
- [19] A. L. Goodgame, H. Dickinson, S. R. Mackenzie, and T. P. Softley. *J. Chem. Phys.*, 116:4922, 2002.
- [20] J. B. M. Warntjes, F. Robicheaux, J. M. Bakker, and L. D. Noordam. *J. Chem. Phys.*, 111:2556, 1999.
- [21] T. Kobayashi, J. Geng, and M. Takami. *Chem. Phys. Lett.*, 284:195, 1998.
- [22] N. Nussenzweig and E. E. Eyler. *J. Chem. Phys.*, 101:4617, 1994.
- [23] M. Broyer J. Chevaleyre, C. Bordas and P. Labastie. *Phys. Rev. Lett.*, 57:3027, 1986.
- [24] P. F. Brevet, Ch. Bordas, M. Broyer, G. Jalbert, and P. Labastie. *J. Phys. II France*, 1:875, 1991.
- [25] C. Bordas, P. F. Brevet, M. Broyer, J. Chevaleyre, P. Labastie, and J. P. Perrot. *Phys. Rev. Lett.*, 60:917, 1988.
- [26] G. Jalbert, P. Labastie, P. F. Brevet, C. Bordas, and M. Broyer. *Phys. Rev. A*, 40:784, 1989.
- [27] Ch. Bordas and Hanspeter Helm. *Phys. Rev. A*, 45:387, 1992.



- [28] J. M. Menéndez, I. Martín, and A. M. Velasco. *Phys. Rev. A*, 74:043413, 2006.
- [29] G. R. Janik, O. C. Mullins, C. R. Mahon, and T. F. Gallagher. *Phys. Rev. A*, 35:2345, 1987.
- [30] C. R. Mahon, G. R. Janik, and T. F. Gallagher. *Phys. Rev. A*, 41:3746, 1990.
- [31] A. Osterwalder, R. Seiler, and F. Merkt. *J. Chem. Phys.*, 113:7939, 2000.
- [32] J. K. G. Watson. *Mol. Phys.*, 81:277, 1994.
- [33] Ch. Jungen and A. I. Roche. *Can. J. Phys.*, 79:287, 2001.
- [34] R. de L. Kronig. *Band spectra and molecular structure*. Cambridge University Press, 1930.
- [35] S. N. Altunata, S. L. Coy, and R. W. Field. *J. Chem. Phys.*, 123:084319, 2005.
- [36] H. Wen, C. Rangan, and P. H. Bucksbaum. *Phys. Rev. A*, 68:053405, 2003.



# Chapter 4

## Time domain terahertz spectroscopy for investigation of Rydberg-Rydberg transitions

### 4.1 Introduction

The frequencies of intracomplex Rydberg-Rydberg transitions at intermediate values of  $n^*$  lie between the millimeter wave and far infrared parts of the spectrum. Over the past fifteen years the technology to generate, shape, and coherently detect short THz pulses has been developing rapidly, see [1, 2] and references therein. Time domain THz spectroscopy (TDTS) is applied mostly to studying the dynamics in condensed phase systems. For a recent review see [3] and references therein. However, there has been some effort to use TDTS to study gas phase samples. TDTS has proven especially useful for investigating collisional dynamics at relatively high gas pressures, gaining information from the wings of lineshapes [4], or for learning about adsorption [5], and studying solvation [6]. For other gas-phase applications see [7, 8, 9, 10].

We are interested in using short THz pulses (duration of several ps) to study Rydberg-Rydberg transitions among autoionizing states, in a molecular beam, by recording absorption spectra. In our experimental scheme, the absorption spectrum is obtained from an electric

field transient recorded in transmission, in the time domain. In order to apply this scheme, we built a time domain THz spectrometer, based on the design developed in Keith Nelson's group at MIT. The spectrometer was built with help of Dr. Joshua Vaughan and Dr. Thomas Hornung in 2004, and since then it has gone through numerous modifications.

Our application differs significantly from the usual applications of similar spectrometers. Usually TD-THz spectrometers are designed to operate at 1 kHz or  $\approx 82$  MHz if the amplification stage is not needed, and are used to study mainly condensed-phase samples, where the spectral features are broad. In our case the sample consists of molecules in excited (Rydberg) states, produced at a low repetition rate (20 Hz), in a molecular beam. Molecules excited to Rydberg states are exceptionally strong absorbers of THz radiation, but the absorption features are orders of magnitude sharper (typically hundreds of kHz) than those of condensed-phase samples. Major modifications to the originally built 1 kHz pulse repetition rate THz spectrometers were required, and both the original design and the modifications will be described in this chapter.

After it was built, the THz spectrometer was tested by recording the ground state rotational spectra of small molecules in the gas phase, using static gas cells. After conversion to the low repetition rate, a timing scheme was devised and tested, to ensure that the THz spectrometer can be synchronized with the 20 Hz Nd:YAG-pumped dye laser system, used for the excitation of gas-phase samples into Rydberg states. The THz spectrometer is prepared for being interfaced with the double resonance molecular beam apparatus, and a design has been proposed for the adaptation of the current double resonance molecular beam apparatus, to house both the THz spectrometer, and a Chirped-Pulse mm-Wave spectrometer (to be described in the next chapter). The components for the extension of the chamber, which will house both spectrometers, have been purchased, and modification of the chamber is scheduled after the completion of the experiments which are currently under way.

## 4.2 Generation

In our experimental design (see Fig. 4.1), optical rectification of pulsed broadband near-infrared radiation, centered around 800 nm, was used to generate the radiation in the range of approximately 0.7-2.5 THz. The pulsed NIR radiation, which was to be rectified, was produced by regenerative amplification of the output of Spectra Physics Tsunami laser. The output of the Tsunami, produced at 82 MHz, was amplified with a repetition rate of 1 kHz in a Spectra Physics Spitfire system. In the Spitfire, the pulses were stretched, amplified in Nd:YLF-pumped Ti:sapphire medium (pump laser is a Spectra Physics Evolution), and then compressed to the initial  $\approx 100$  fs duration. Finally, pulses of  $\approx 100$  fs duration, and average power of around 800 mW, output at 1 kHz (or 40 Hz in a modified scheme, described below) were used for optical rectification.

The duration of the pulses output by the Spitfire was measured at one instance during the setting up of the THz spectrometer. In order to measure the pulse duration, a Spitfire pulse was split into two pulses and the autocorrelation between them was recorded by generating the second harmonic in a 4mm-thick BBO crystal. The BBO crystal was followed by a filter that transmitted the second harmonic, but not the fundamental, and the intensity of the second harmonic was recorded using a phase-sensitive detection scheme (described in more detail below) as a function of the delay between the pump and probe pulses. The delay was varied by computer-controlled stepping of an Aerotech Unidex 500 delay stage. A value of  $\approx 140$  fs for the FWHM is measured, which, gives  $\approx 100$  fs ( $\frac{140}{\sqrt{2}}$  fs) for the approximate duration (FWHM) of the pulses produced by our Spitfire laser system.

When the THz spectrometer was operating, the duration of the THz pulses was optimized daily, without recording the autocorrelation scan every time. When the LiNbO<sub>3</sub> crystal, used as the medium for optical rectification in our THz spectrometer, is irradiated with focused ultrashort pulses, the second harmonic is produced in addition to the THz radiation. The intensity of the thus generated second harmonic increases as the pulse duration decreases. Daily, to ensure that the pulse duration was minimized, the position of the motorized hor-

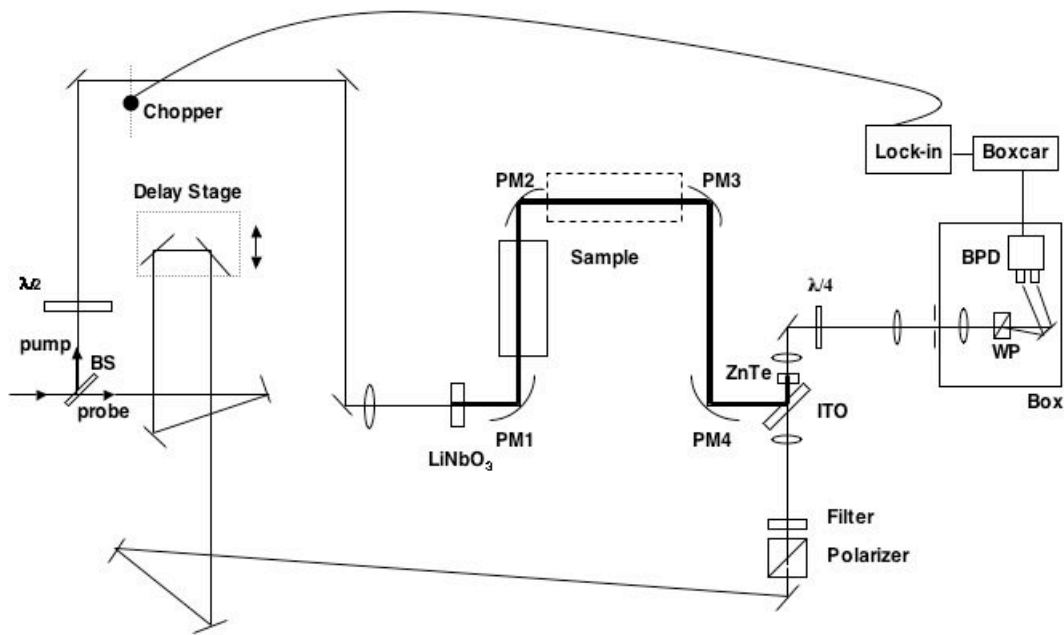


Figure 4.1: Scheme of our 20 Hz THz spectrometer: a  $\approx 100$  fs pulse output by the Spitfire laser at 800 nm is split into pump and probe pulses at the beamsplitter BS. The pump pulse is focused onto a MgO-doped LiNbO<sub>3</sub> crystal to generate THz radiation. The THz pulse (thick line) is collimated and focused twice by four parabolic mirrors (PM1, PM2, PM3, and PM4). The sample cell can be located in either the collimated or focused region of the THz beam. The delay between the pump and probe pulses is varied by stepping a delay stage in the probe beam. Both the probe and THz beams are focused onto ZnTe. ZnTe was used for free space electrooptic sampling. The polarization rotation of the probe pulse is measured using a balanced photodiode pair (BPD) after converting its linear polarization into elliptical (using a quarter waveplate,  $\lambda/4$ ) and spatially separating the two polarization components (in a Wollaston prism WP).

izontal retro-reflector in the Spitfire pulse compressor was varied, as recommended by the Spectra Physics Spitfire Instruction Manual [11] until the intensity of the second harmonic was maximized, by visual inspection on a paper card behind the crystal.

Thus optimized pulses, centered at 800 nm (FWHM in frequency  $\approx 3.7$  THz, assuming a Fourier transform limited pulse), were optically rectified in LiNbO<sub>3</sub> crystals with large nonlinear<sup>†</sup> coefficients, in order to produce the far infrared radiation. Optical rectification is a second order nonlinear process in which polarization  $P$  at frequency  $\Delta\omega$  is generated by mixing two photons at frequencies  $\omega$  and  $\omega + \Delta\omega$  [12, 13]:

$$P_i(\Delta\omega) = \sum_{j,k} \chi_{ijk}^{(2)}(\Delta\omega : \omega + \Delta\omega, -\omega) E_j(\omega + \Delta\omega) E_k^*(\omega), \quad (4.1)$$

where the coefficients  $\chi_{kij}^{(2)}(\Delta\omega : \omega + \Delta\omega, -\omega)$  are defined as (in SI units):

$$\chi_{kij}^{(2)}(\Delta\omega : \omega + \Delta\omega, -\omega) = -\frac{\epsilon_0}{4} n_i^2 n_j^2 r_{ijk}. \quad (4.2)$$

The nonlinear coefficients  $\chi_{ijk}^{(2)}$  with different indices are related among themselves, and the relationships are determined by energy conservation and the symmetry properties of the crystal [12]. Often instead of  $\chi_{ijk}^{(2)}$  coefficients,  $d_{ijk}$  coefficients are used. A discussion of different definitions of nonlinear coefficients, and relationships between them, is given in [14]. LiNbO<sub>3</sub> belongs to the  $3m$  crystallographic point group, in international notation, for which the second order nonlinear coefficients are given by:

$$\begin{pmatrix} 0 & 0 & 0 & 0 & d_{15} & -d_{22} \\ -d_{22} & d_{22} & 0 & d_{15} & 0 & 0 \\ d_{31} & d_{31} & d_{33} & 0 & 0 & 0, \end{pmatrix}$$

where the relationship among different coefficients, following from the crystal symmetry, has been indicated. The abbreviated  $d_{i\alpha}$  notation, commonly used in nonlinear optics, pertains

---

<sup>†</sup>The use of term *nonlinear* in this chapter pertains to a medium capable of producing an output at  $\omega' \notin \{\omega\}$  with input at  $\{\omega\}$ .

to  $d_{ijk}$ , where the index  $\alpha$  takes the values of the matrix elements at the  $jk^{th}$  position in the following matrix:

$$\begin{pmatrix} 1 & 6 & 5 \\ 6 & 2 & 4 \\ 5 & 4 & 3. \end{pmatrix}$$

In optical rectification of ultrashort pulses, the envelopes of the generating pulses  $E_j(\omega + \Delta\omega)$  and  $E_k^*(\omega)$  vary with time. When optical rectification is used to generate short THz pulses, usually both  $E_j(\omega + \Delta\omega)$  and  $E_k^*(\omega)$  photons are derived from the same NIR pulse. The two NIR photons are simultaneous, but because of the large bandwidth of the generating NIR pulse, in general have different frequencies. Because of the focusing of the NIR beam onto the nonlinear crystal, the two pulses have slightly different wavevectors, and both energy and momentum conservation requirements are satisfied. As a result of the time variation of the envelope of the generating pulses, the nonlinear polarization  $P_i(\Delta\omega)$  generated by them also varies with time. Thus, impulsive excitation generates a broadband nonlinear output. In addition to being time dependent, the polarization  $P_i(\Delta\omega)$  moves with the group velocity of the exciting pulses. The radiation, which eventually reaches the detector, results from the interference of the radiation emitted by the oscillating dipoles in the crystal at different positions along the NIR pulse propagation direction.

The phasematching condition:

$$\Delta k = k_{THz} - k_{NIR} - k'_{NIR} = 0 \quad (4.3)$$

determines the coherence length (defined as  $l_c = \frac{2\pi}{\Delta k}$ ) over which THz radiation is generated, before the generating and the generated pulses go out of phase.

In fact, there are several arrangements for generating the short THz pulses using optical rectification with respect to the phasematching condition. If the indices of refraction for the NIR and THz radiation are comparable, the phasematching condition can be satisfied over



Table 4.1: Electro-optic characteristics of ZnTe and LiNbO<sub>3</sub>.

Material	Symmetry	$\lambda$ (nm)	$r_{\alpha,k}$ (pm/V)	$n$
ZnTe	$43m$	800	$r_{41} = 3.9$ [17]	$n = 3.13$ [15]
LiNbO <sub>3</sub>	$3m$	633	(T) $r_{13} = 9.6$ (S) $r_{13} = 8.6$ [18]	$n_o = 2.286$ [18]
			(T) $r_{22} = 6.8$ (S) $r_{22} = 3.4$ [18]	$n_e = 2.150$ [18]
			(T) $r_{33} = 30.9$ (S) $r_{33} = 30.8$ [18]	
			(T) $r_{51} = 32.6$ (S) $r_{51} = 28$ [18]	

larger coherence lengths. Such is the case in ZnTe, where  $n_{NIR}$  and  $n_{THz}$  are comparable (see Tab. 4.1). However, in addition to the phasematching condition, there are several other factors that determine the intensity of the generated THz radiation, and sometimes it is necessary to sacrifice the optimal phasematching arrangement. The Eq. (4.4) gives the dependence of the efficiency of generation of THz radiation as a function of the experimental parameters [15, 16]:

$$\eta_{THz} = \frac{2\omega^2 d_{eff}^2 L^2 I}{\epsilon_0 n_{NIR}^2 n_{THz} c^3} \frac{\sinh^2 \left[ \frac{\alpha_{THz} L}{4} \right]}{\left[ \frac{\alpha_{THz} L}{4} \right]^2} e^{-\alpha_{THz} L/2}, \quad (4.4)$$

where the same notation as in [15] is used. Using the factor of merit (FOM), defined in [15], the efficiency of THz generation in different nonlinear materials can be compared, see Tab. 4.1.

The relationship between the nonlinear coefficients and anharmonicities of the potentials in ferroelectric crystals, responsible for the coupling of the frequencies  $\omega$  and  $\omega + \Delta\omega$ , has been modeled [19]. LiNbO<sub>3</sub> is optically anisotropic and has a relatively large difference between its indices of refraction for THz and NIR radiation (see Table 4.1), but the overall FOM (especially in MgO-doped LiNbO<sub>3</sub>) is larger than in ZnTe, a commonly used crystal for THz generation.

We selected LiNbO<sub>3</sub> as the medium for THz generation in our spectrometer. When the THz and NIR pulses are collinear, and have the same polarization, use is made of the  $r_{33}$  nonlinear coefficient, and the generated THz field is proportional to:

$$P_z(\Delta\omega) = -\frac{\epsilon_0}{4}n_z^4r_{33}E_z(\omega + \Delta\omega)E_z^*(\omega). \quad (4.5)$$

In  $x$ -cut LiNbO<sub>3</sub>, with  $E_z(\omega + \Delta\omega)$  and  $E_z^*(\omega)$  parallel to the optic axis (along  $z$ ), the coherence length is short, and for crystals thicker than several tens of microns, the THz radiation is effectively generated only at the interfaces between the crystal and air. The radiation generated inside the crystal is absent because of destructive interference, as the generating and generated pulses get out of phase. However, because of larger nonlinear coefficients in LiNbO<sub>3</sub>, THz radiation with higher intensity than in ZnTe can be generated.

In our spectrometer, we used an  $x$ -cut LiNbO<sub>3</sub> crystal with the polarization of the NIR pump beam parallel to the optic axis  $z$ . However, it was recently shown by K.-L. Yeh et al. and J. Hebling et al. that it is possible, using excitation pulses with fronts tilted by a dispersive element, to achieve longer effective lengths in a LiNbO<sub>3</sub> crystal [20, 15], and generation of THz radiation at intensity of 5 GW/cm<sup>2</sup> (focused to 0.5 mm × 0.7 mm) was demonstrated in that arrangement. Our THz spectrometer was set up prior to the publication of [20, 15], but the power of the THz radiation generated in our spectrometer already exceeds the power requirement for exciting the Rydberg-Rydberg transitions in an  $n^* \approx 20$  level with a flip angle larger than  $\pi$ .

Alternative non-phased-matched experimental arrangement with a LiNbO<sub>3</sub> medium, in which the THz radiation is generated in a Cherenkov cone [21, 22], was initially attempted, but this arrangement was eventually abandoned in favor of the arrangement in which the THz and NIR beams are collinear. Alignment and maintenance were significantly simpler in the collinear arrangement than in the Cherenkov arrangement. In the Cherenkov arrangement, the angle between the THz and NIR pulses is  $\approx 65^\circ$ , when LiNbO<sub>3</sub> is used. Figure 4.2a shows a THz pulse generated in LiNbO<sub>3</sub> in the Cherenkov arrangement. Figures 4.2b, 4.2c, 4.2d show the THz pulses generated in the perpendicular arrangement with three 0.6 % MgO-doped<sup>†</sup> LiNbO<sub>3</sub> crystals of different thicknesses. Eventually the perpendicular arrangement

---

<sup>†</sup>MgO-doping increases the damage threshold, and enables the use of higher pump intensities.

with 30  $\mu\text{m}$  thick 0.6 % MgO-doped  $\text{LiNbO}_3$  was selected.

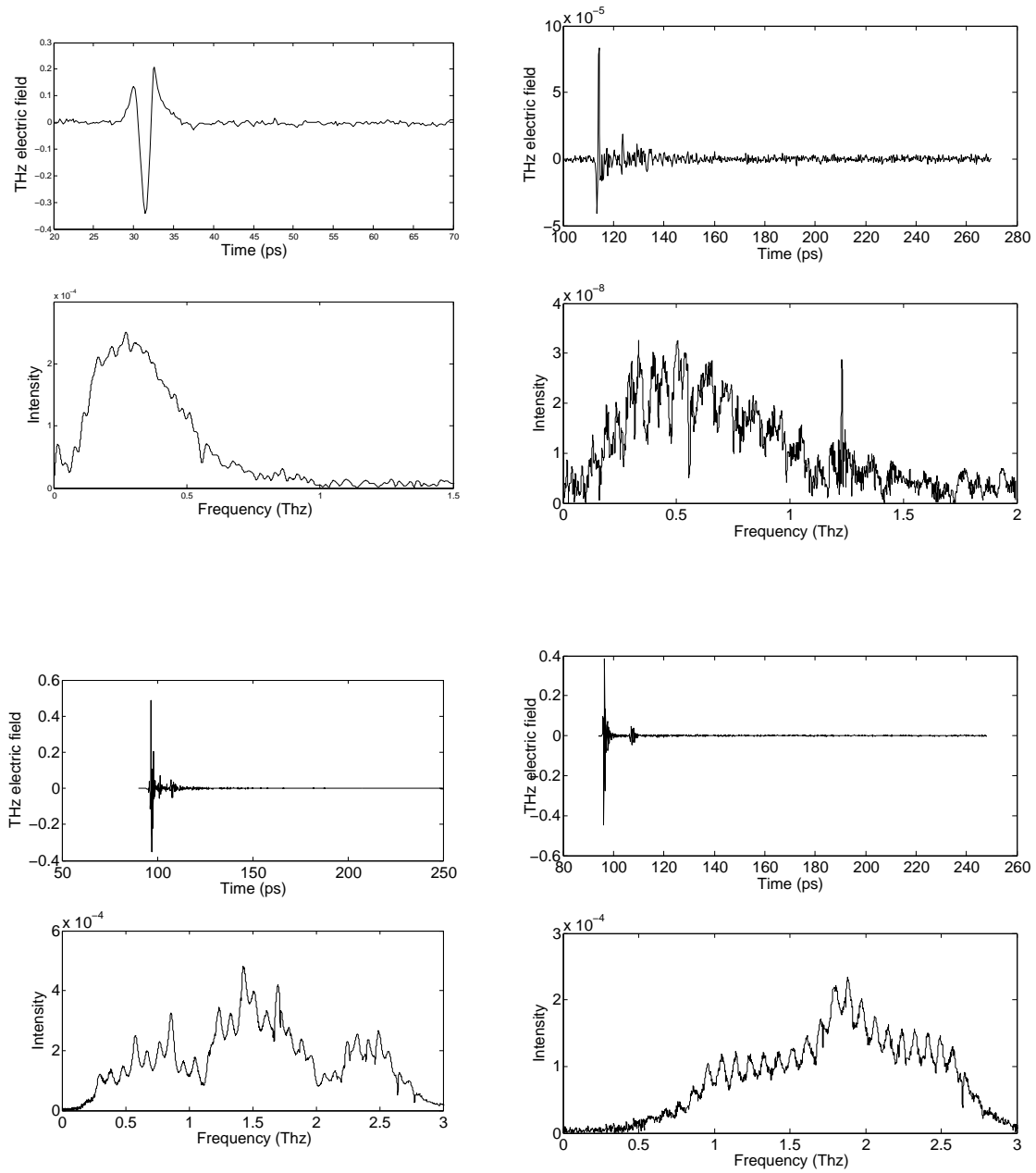


Figure 4.2: Four THz pulses (electric field transients and Fourier transforms), generated under different experimental conditions. Pulse a) was generated in the Cherenkov arrangement, with a  $60 \times 15 \times 25$  mm LiNbO<sub>3</sub> crystal, while b), c), and d) were generated in the perpendicular arrangement, with 2.5 mm, 100  $\mu$ m and 30  $\mu$ m thick 0.6 % MgO-doped LiNbO<sub>3</sub>. The detection scheme changed between recording these spectra (spectra were taken: a), 06/16/04 b) 06/02/05, c) 11/10/06, and d) 01/03/07), and the absolute intensities cannot be directly compared between them. Water absorption was not removed in a) and b).

### 4.3 Propagation of THz pulses

The source of the THz radiation in the LiNbO<sub>3</sub> crystal can be approximated by a point source. A standard arrangement for collecting the divergent THz radiation emitted by what is assumed to be a point source, focusing it first onto the sample, and afterwards focusing it again onto the detector, employs four off-axis parabolic mirrors in a  $4f$  arrangement, see Fig. 4.1. We used four off-axis, gold-coated, parabolic mirrors purchased from Janos Technology. In our spectrometer all of the parabolic mirrors were of 2" diameter, and their focal lengths were  $f_{PM_1} = f_{PM_4} = 10$  cm,  $f_{PM_2} = f_{PM_3} = 20$ cm.

In our TDTTS experiments, we tested both arrangements in which the sample cell was placed in the focused and collimated arms of the spectrometer. For a sample in a gas cell with Si windows mounted at 45° (described below), the arrangement in which the cell was in the collimated arm was preferable. However, for the experiment in which THz radiation will be used to study Rydberg-Rydberg transitions in the molecular beam, the THz radiation must be focused onto the sample. The arrangement with four parabolic mirrors can be used to fulfill both requirements, and we employed it in our spectrometer. The propagation of the THz radiation and the losses on parabolic mirrors with finite aperture size can be modeled, following the method described in [23]. As a result, the  $4f$  arrangement acts as a high frequency filter, as is shown in Fig. 4.3.

Behind the PM<sub>4</sub>, an indium-tin oxide (ITO) coated glass slide (Sigma Aldrich, 8-12 Ω/sq) was placed to reflect the THz beam onto the ZnTe crystal used for detection. The 120-160 nm thick conductive ITO layer reflects the THz beam, but transmits the NIR beam. Thus, use of the ITO-coated glass slide enables focusing both the THz and NIR probe radiation onto the same spot on the ZnTe detector.

Since water absorbs strongly in the THz frequency region [7], an airtight enclosure was built to house the part of the THz spectrometer in which the THz pulses propagate. Usually, after aligning spectrometer, an open container with a dessicant (Drierite) was placed inside the enclosure to absorb the water, the enclosure was sealed with tape, and subsequently

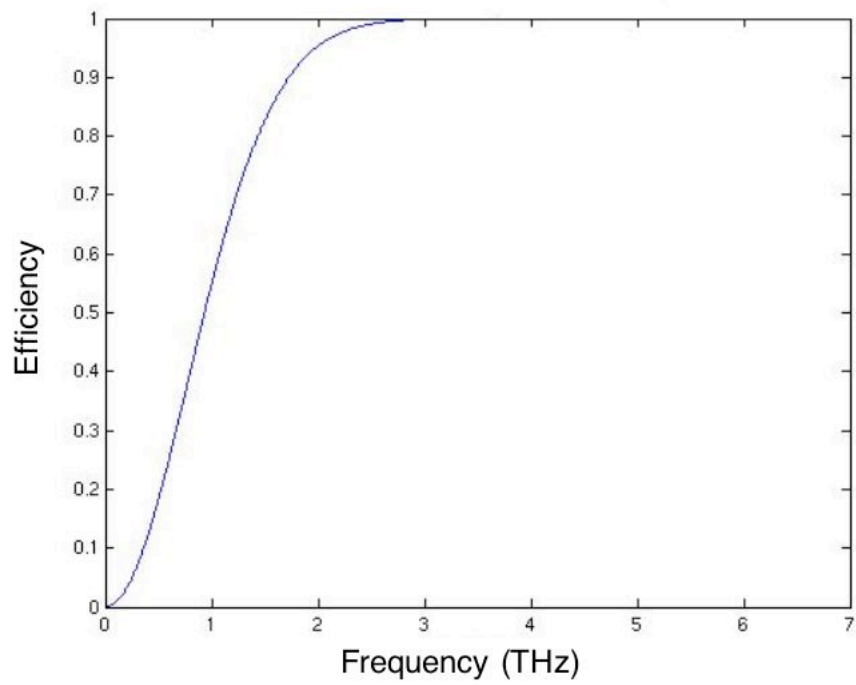


Figure 4.3: Calculated frequency dependence of the filter frequency function due to the finite aperture of the four parabolic mirrors in the  $4f$  arrangement, with  $f_{PM_1} = f_{PM_4} = 10$  cm and  $f_{PM_2} = f_{PM_3} = 20$  cm (see Fig. 4.1).

purged with dry nitrogen. Figure 4.4 is an experimentally recorded spectrum of water lines in the frequency region in which our spectrometer operates. The absorption at the frequencies of the lines in Fig. 4.4 is minimized by the procedure, described above, for removing water vapor from our THz spectrometer.

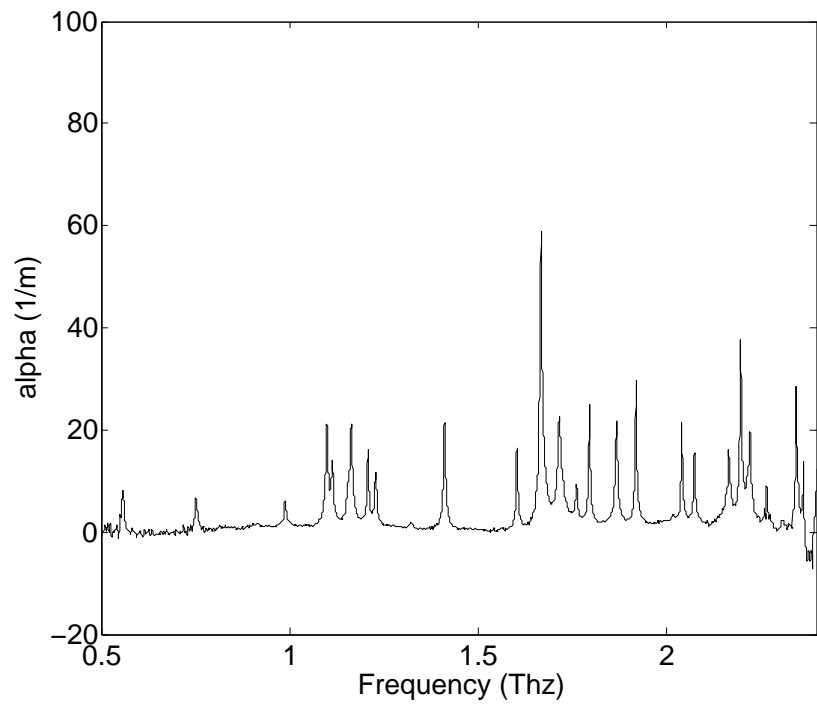


Figure 4.4: Experimentally recorded absorption spectrum of atmospheric water, before the water vapor was removed from the spectrometer by building an enclosure which was dried with a desiccant and purged with  $N_2$ .



## 4.4 Detection

Coherent detection of THz radiation in the time domain usually employs either photoconductive antennas or Free-Space Electro-Optic Sampling (FSEOS) [24, 25]. FSEOS has larger bandwidth than detection by antennas (3 dB for antennas, see [17]), and a detection bandwidth of 70 THz has been demonstrated [26]. FSEOS is based on the second order nonlinear effect (Pockels effect) in which the presence of an external low frequency (or DC) electric field (THz radiation in our case) modifies the index of refraction of the material that exhibits the electrooptic effect [27, 28, 29]. The change of the index of refraction is then measured by detecting the polarization rotation of the probe laser pulse (20 % split off from the Spitfire output at 800 nm).

The most commonly used material for FSEOS is ZnTe [17]. Tables 4.2 and 4.1 summarize the ZnTe characteristics relevant for FSEOS. Due to the comparable indices of refraction, phasematching over lengths of several hundreds of microns is achievable in this material. In addition, due to the symmetry of the  $\bar{4}3m$  crystallographic point group, to which ZnTe belongs, the index of refraction of the crystal is isotropic in the absence of an electric field, and the only nonzero Pockels coefficient is  $r_{41} = r_{52} = r_{63}^\dagger$ . Interpretation of the response of the index of refraction to the applied external electric field is thus straightforward for ZnTe. This crystal is an efficient material for FSEOS near 2 THz, but at higher frequencies the detection efficiency declines because of the presence of a transverse optical phonon resonance at 5.3 THz.

The FSEOS experimental design consists of several elements (see Fig. 4.5). THz and probe beams are focused respectively by an  $f = 10$  cm parabolic mirror and a lens of the same focal length, at the same spot on a 500  $\mu\text{m}$  thick ZnTe crystal (purchased from INGCRYS Laser Systems Ltd.). Because the index of refraction of the ZnTe crystal in the absence of an external electric field is isotropic, when the probe beam is transmitted through it in the

---

<sup>†</sup>Here a similar contraction as in  $d_{ijk}$  to  $d_{i\alpha}$  was used for  $r_{ijk}$ , but the first two indices are contracted to  $r_{\alpha k}$ .

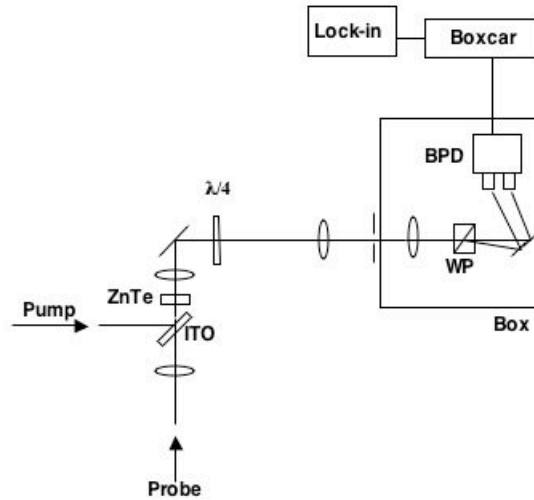


Figure 4.5: Free Space Electro-optic Sampling used to measure  $E_{THz}$  in our THz spectrometer: both the THz and 800 nm probe pulses are focused onto a 500  $\mu\text{m}$  thick ZnTe crystal that has a large electrooptic coefficient, followed by a quarter waveplate ( $\lambda/4$ ) that converts the linear polarization of the probe pulse into an elliptically polarized pulse. The distortion from circular polarization is a measure of  $E_{THz}$ . A Wollaston prism (WP) spatially separates the two polarization components, which are then detected on a balanced photodiode pair (BPD). The signal difference between the two photodiodes, detected in a phase-sensitive scheme using a lock-in amplifier, is proportional to  $E_{THz}$ . A boxcar, acting as a sample-and-hold device, precedes the lock-in amplifier in the low pulse repetition-rate modification of the THz spectrometer.

Table 4.2: Characteristics of materials often used to generate THz radiation. Values are given for 1 THz, except for DAST, for which values are given for 0.8 THz.  $d_{eff}$  is given at 800 nm. All values are for room temperature, except for stoichiometric LiNbO<sub>3</sub> (sLN) at 100 K. The table is reproduced from [15], and for more details refer to this publication.

Material	$d_{eff}$ (pm/V)	$n_{800nm}^{gr}$	$n_{THz}$	$\alpha_{THz}$ (cm <sup>-1</sup> )	FOM (pm <sup>2</sup> cm <sup>2</sup> /V <sup>2</sup> )
CdTe	81.8		3.24	4.8	11
GaAs	65.6	4.18	3.59	0.5	4.21
GaP	24.8	3.67	3.34	0.2	0.72
ZnTe	68.5	3.13	3.17	1.3	7.27
GaSe	28.0	3.13	3.27	0.5	1.18
sLiNbO <sub>3</sub>	168	2.25	4.96	17	18.2
sLN 100 K				4.8	48.6
DAST	615	3.39	2.58	50	41.5

absence of the THz pulse, the polarization of the probe pulse is unchanged. However, when the THz radiation is present, it will, through the electrooptic effect, modify the index of refraction:

$$\begin{aligned}
 \Delta \left( \frac{1}{n^2} \right)_{23} &= \Delta \left( \frac{1}{n^2} \right)_{32} = r_{41} E_1, \\
 \Delta \left( \frac{1}{n^2} \right)_{13} &= \Delta \left( \frac{1}{n^2} \right)_{31} = r_{41} E_2, \\
 \Delta \left( \frac{1}{n^2} \right)_{12} &= \Delta \left( \frac{1}{n^2} \right)_{21} = r_{41} E_3,
 \end{aligned} \tag{4.6}$$

and a phase shift will be introduced between the two polarization components. Here  $E_k$  are the components of  $E_{THz}$ ,  $n$  is the index of refraction, and indices 1, 2, and 3 pertain to the coordinate system associated with the ZnTe crystal axes. The probe beam, after transmission through the crystal, passes through a quarter waveplate ( $\lambda/4$ , Thorlabs WPQ05M-808), after which the beam is elliptically polarized in the general case (or circularly polarized, if no phase shift was introduced by the electrooptic effect). The two polarization components are spatially separated from each other by a 20° Wollaston prism (WP, Thorlabs WP10). The spatial separation of the two orthogonally polarized beams after the Wollaston prism is

sufficient to enable measurement of the intensities of the two polarization components on a large area balanced photodiode pair (BPD, Model 2307 by New Focus) [30, 31]. The polarization optics and the balanced photodiode detector are enclosed in a home-built box that prevents ambient and scattered light from degrading the sensitive balance on the photodiode pair. The probe beam enters the box through a pinhole (300  $\mu\text{m}$  H/P diamond aperture, by Lenox Laser) through which it is focused by an  $f = 20$  cm lens.

Prior to using the New Focus 2307 monolithic balanced photodiode pair, an arrangement with two Thorlabs DET-210 photodiodes was tested. In this arrangement, the difference between the signals on two similar, but independent photodiodes was measured. There were several reasons for selecting the NF 2307 detector, compared to the arrangement with the two DET-210 photodiodes. First, the two independent photodiodes have slightly different responses, and balancing was always imperfect. Second, in the NF 2307, a built-in circuit for subtracting the signals from the two photodiodes minimizes the impedance mismatch. Third, the longer duration of the photodiode response (approximately 2.5  $\mu\text{s}$  FWHM), provided by the NF 2307 balanced pair, was better matched to our detection scheme. The NF 2307 has three gain settings, and  $10^5$  V/A gain was found to be optimal for our case. The duration of the signal with this gain setting (approximately 2.5  $\mu\text{s}$  FWHM) enables gating the central part of the pulse, usually 1  $\mu\text{s}$ , for detection by a boxcar (Stanford Research Systems SR 250). With the two DET-210 photodiodes, the signal was shorter than the shortest available gate setting on our boxcar, and selecting an optimal part of the pulse was not possible.

The boxcar-gated signal is sent to a digital lock-in amplifier (Stanford Research Systems SR830 DSP). The reference frequency for the lock-in amplifier was provided by an optical chopper (Thorlabs MC1000) placed in the pump beam, operating at (500, 20)<sup>†</sup> Hz. In this arrangement, repetition rates of the probe pulse and THz radiation are (1000, 40)<sup>†</sup> and (500, 20)<sup>†</sup>, respectively. Thus, alternate probe pulses are modified by the presence of the THz pulse, see Fig. 4.6. Because of the opposite phase of the reference signal (at (500, 20)<sup>†</sup> Hz)

---

<sup>†</sup>Denoting the high repetition rate and low repetition rate modifications, respectively.

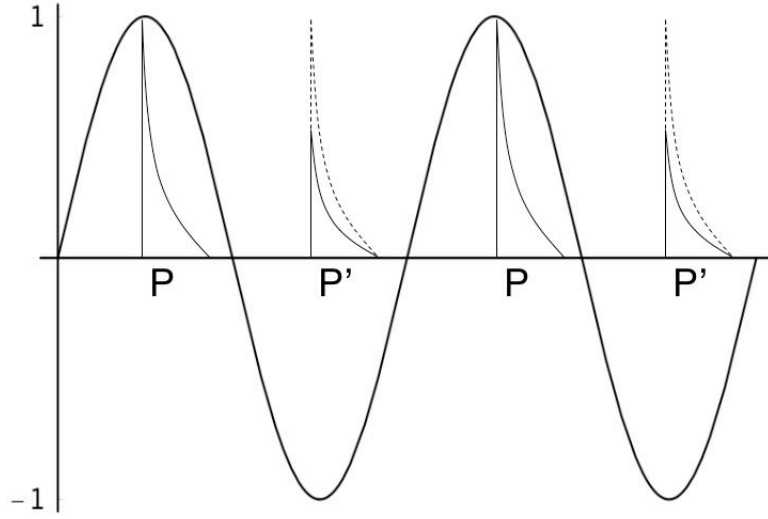


Figure 4.6: Phase sensitive detection: alternate probe pulses ( $P'$ ) are modified in the electrooptic crystal by the presence of the THz pulse (unmodified pulses are labeled by  $P$ ). The signal from the balanced photodiode pair is multiplied by the sinusoidal reference frequency in the lock-in amplifier. The reference frequency has opposite phases between the  $P$  and  $P'$  pulses. The lock-in amplifier thus effectively subtracts the intensities of two successive pulses, and provides a direct measure of  $E_{THz}$ .

between the two consecutive pulses (unmodified,  $P$ , and modified,  $P'$ ), the lock-in amplifier effectively subtracts the intensity of the two successive ( $P$  and  $P'$ ) probe pulses (see Fig 4.6). Such a difference signal is measured, typically with time constant  $T_C = 100 \mu s$  and waiting period  $10T_C$  (when 24 dB/oct slope was used, as recommended by the SR830 Instruction Manual [32]), as a function of the position of the delay stage.

From Eq. (4.6), the largest electrooptic effect in ZnTe is achieved when the wavevectors of the THz and probe pulses are collinear and impinge upon a (110) oriented crystal. When the polarization change introduced by the electrooptic effect is small (as it was for all our experiments), the induced change of the index of refraction is linearly proportional to the external electric field, and the correspondence between the measured signal on balanced photodiodes and the amplitude of the THz field is given by Eq. (4.7) [17]:

$$\Delta I = I_p \frac{\omega n^3 E_{THz} r_{41} L}{2c} (\cos \alpha \sin 2\phi + 2 \sin \alpha \cos 2\phi), \quad (4.7)$$

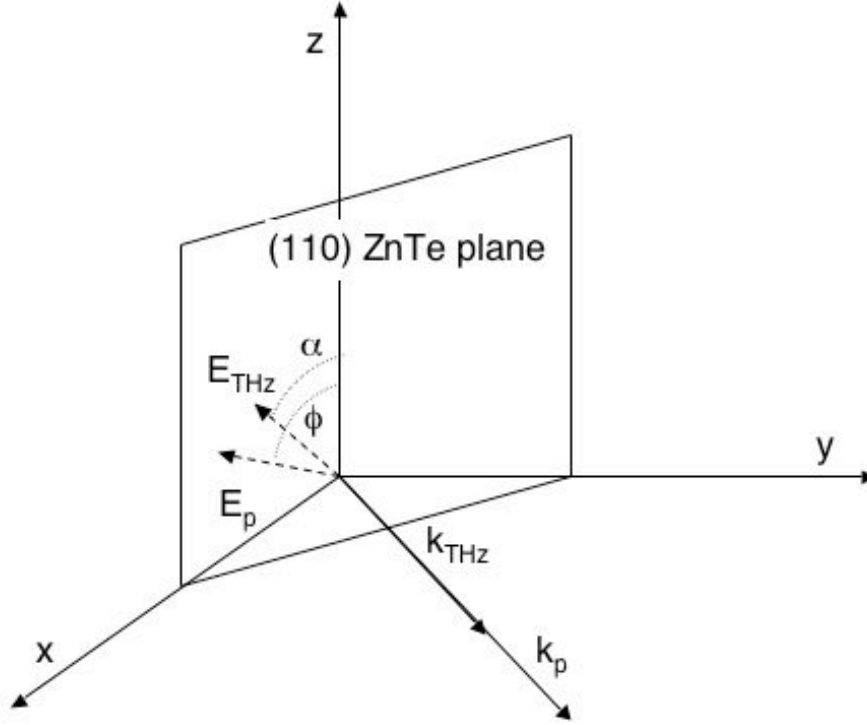


Figure 4.7: The THz and probe beams propagate collinearly ( $k_{THz}$  and  $k_p$ ), impinging on the (110) surface of the ZnTe crystal. The angle that the polarization vectors make relative to the  $z$  axis of the crystal are  $\alpha$  and  $\phi$  for the THz and probe beams, respectively.

where  $I_p$  is the probe intensity,  $n$  is the zero-field index of refraction of ZnTe for 800 nm radiation,  $E_{THz}$  is the amplitude of the THz electric field, and  $c$  is the speed of light. Angles  $\alpha$  and  $\phi$  are defined in Fig. 4.7. Using Eq. (4.7), an estimate of the THz field amplitude in a typical pulse in our spectrometer was made by measuring  $\Delta I$  and  $I_p$ , giving a value of approximately 0.8 kV/cm for the focused THz radiation.

The optimal angle  $\alpha$  between the  $z$  crystal axis and the polarization direction of the THz pulse (see Fig. 4.7) will depend on the relative polarizations of the THz and probe pulses [17]. In our experiment, the polarizations of the THz and probe pulses were parallel to each other ( $\phi = \alpha$ ), and both were vertical. The optimal value for the angle  $\alpha$  was determined experimentally. A curve similar to the one in Fig. 3 in [17] was recorded, measuring the detection efficiency as a function of  $\alpha$ , for the full 360° rotation of the ZnTe crystal, in steps

of  $10^\circ$ , with finer steps in the vicinity of the observed maxima. For each value of the angle  $\alpha$ , the photodiode signal was displayed on an oscilloscope and optimized to compensate for the deflection of the beam caused by rotation of the crystal. After this procedure, the ZnTe crystal was oriented in the position that gave the optimal detection efficiency.

When the amplitude of the THz electric field is measured as a function of time using FSEOS detection scheme, the detected THz electric field amplitude is somewhat distorted from the true value [33, 34]. The distortion of the signal is due to losses from reflection at interfaces in the ZnTe crystal, velocity mismatch between the THz and probe beams in ZnTe, absorption and dispersion in the ZnTe crystal, and the frequency dependence of the  $r_{14}$  [28]. The distortion of the signal can be modeled using Eq. (57) from [34]:

$$f(\Omega) = \int_{-\infty}^{\infty} \frac{\omega^2}{|k'(\omega)|} e^{-2\beta(\omega)l} \chi_{eff}^{(2)}(\omega : \Omega, \omega - \Omega) \frac{e^{i\Delta k_+(\omega, \Omega)} - 1}{i\Delta k_+(\omega, \Omega)} A_{opt}^*(\omega - \omega_0) A_{opt}(\omega - \Omega - \omega_0) d\omega, \quad (4.8)$$

where the same notation as defined in [34] is used.

Using the parameters given in Tables 4.2 and 4.1 for a ZnTe  $500 \mu\text{m}$  crystal, our modeled frequency dependence of the ZnTe detection efficiency is given on Fig. 4.8. The dominant source of distortion in our ZnTe crystal comes from absorption and dispersion inside the crystal, compared to which the other sources of signal distortion are negligible.

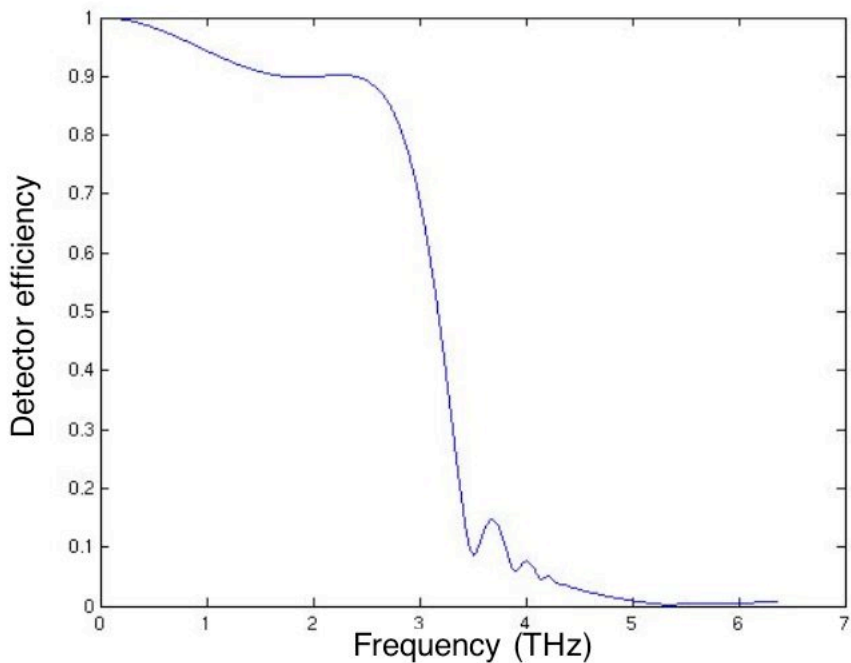


Figure 4.8: Frequency response of a FSEOS detector with a 500  $\mu\text{m}$  thick ZnTe crystal, calculated using Eq. (4.8).

## 4.5 Conversion to 40 Hz operation

THz spectrometers of similar design usually operate at 1 kHz, or at 82 MHz when photoconductive switches, which do not require an amplification stage, are used. In our case, the THz spectrometer was designed in a way that enables it to be interfaced with one or more Nd:YAG-pumped dye lasers, which operate at 20 Hz. The original 1 kHz THz system was modified so that operation at 40 Hz can be achieved. This modification to 40 Hz is required, when interfacing with the 20 Hz dye system, so that alternate THz pulses (produced at 40 Hz) are affected by the sample modification caused by the 20 Hz dye laser pulse. A detection scheme similar to the one shown in Fig. 4.6 then measures the intensity difference between the two successive pulses directly. In order to achieve low-frequency operation of the THz spectrometer, the two Pockels cells in the Spitfire laser were operated at 40 Hz. Ideally, the Spectra Physics Evolution Nd:YLF laser, which pumps the amplifier in the Spitfire would be triggered externally, by a signal synchronized to the Nd:YAG laser. However, since the



Q-switch driver in the Evolution laser did not perform at specifications, external triggering of the Evolution laser introduced a prohibitively large timing jitter. The scheme with external triggering of the Evolution laser was abandoned, and instead, all triggers were derived from the Spitfire signal (see Fig. 4.9). The signal at 40 Hz is provided by downconverting the 1 kHz Evolution trigger to 40 Hz using the Spitfire SDG delay generator, which then triggers the Pockels cells in the Spitfire at 40 Hz. The SDG also triggers the first of the two Stanford Research Systems delay generators (SRS DG 535), which provides a trigger for the optical chopper and for the second SRS DG 535. The second SRS DG 535 converts the input frequency of 40 Hz to 20 Hz. When the delay on at least one of the SRS DG 535 channels is set to exceed the time separation of the triggering pulses, the delay generator acts as a frequency divider, and it was used in this mode in our triggering scheme to provide the frequency downconversion. The second SRS DG 535 provides a trigger for Nd:YAG Q-switch, and a trigger for the Nd:YAG flashlamps almost 50 ms after the Q switch. In this way, the flashlamps are fired before the next Spitfire pulse, without having to trigger the Evolution externally. The timing jitter associated with long delays is thus transferred to triggering the flashlamps, the timing of which is less critical than that of the Q-switch.

In addition to production of THz pulses at 40 Hz, it was also necessary to modify the detection part of the THz apparatus, to accommodate the low duty cycle. Because of a large mismatch between the duration of the signal (slightly under 1  $\mu$ s with NF 2307) and the half-period of the reference frequency for the lock-in amplifier (250 ms at 20 Hz), a boxcar (Stanford Research Systems, SR 250) was introduced between the balanced photodiode detector and the lock-in amplifier. This boxcar was used as a sample-and-hold device, effectively stretching the detected signal over half the period of the lock-in reference frequency, thus increasing the duty cycle.

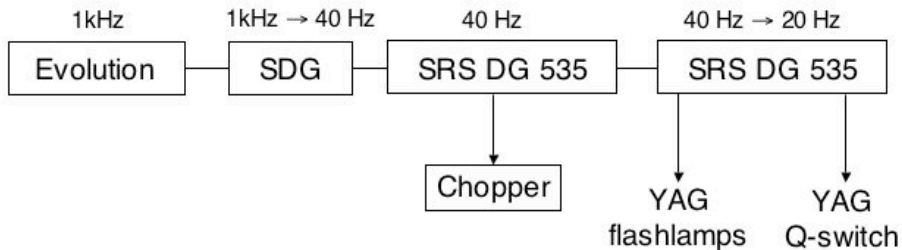


Figure 4.9: Triggering scheme in the 20 Hz THz spectrometer: the Q-switch output signal from the Evolution laser at 1 kHz triggers the Spitfire SDG. The SDG is capable of frequency conversion to 40 Hz. The SDG drives the two Pockels cells in the Spitfire laser at 40 Hz and triggers a Stanford Research Systems Delay Generator, which provides a trigger for the optical chopper and the second Stanford Research Systems Delay Generator. The second SRS DG converts the frequency from 40 Hz to 20 Hz and triggers the Q switch in the Nd:YAG laser. The second SRS DG also provides the trigger for Nd:YAG laser flashlamps, but with almost 50 ms delay, effectively triggering the flashlamps prior to the arrival of the next pulse from the Spitfire laser. Timing jitter associated with long delays is thus transferred to the triggering of the flashlamps, as the experiment is much less sensitive to the timing of the flashlamp firing as it is to that of the Q switch.

## 4.6 Polarization sensitivity

It was noticed that the SNR in the experimentally recorded THz spectra was better when the polarizations of both pump and probe pulses were vertical, making all the necessary changes, than in the case of horizontal polarization. The explanation proposed to explain this effect is that the  $p$ -polarized wave reflecting from a metal surface is more sensitive to the incident angle than the  $s$ -polarized wave. When gold mirrors are used, larger angular sensitivity of the  $p$ -polarized wave resulted in larger polarization noise of the  $p$ -polarized wave caused by vibrations, or any source of fluctuations of the mirror or beam position. Greater angular sensitivity of the  $p$ -polarized pulse, when metallic mirrors are used, can be demonstrated by taking the derivatives with respect to angle of incidence of the  $s$  and  $p$  reflection coefficients for a metal surface given by Eqs. (14.10) in [35].

A gold-coated corner cube retroreflector is mounted on the delay stage in our experiment to reflect the probe beam in a direction parallel to the incoming one. This corner cube retroreflector also affects the polarization of the reflected wave [36, 37, 38]. The polarization

dependence of the reflected wave for a gold-coated corner cube retroreflector was modeled based on the method described in [36]. With a corner-cube retroreflector, there are six possible cases, each with a different polarization dependence. We chose the arrangement that gives the smallest polarization change after the reflection, to minimize the polarization sensitivity to movement of the delay stage.

In addition, we attempted to minimize polarization noise in the detection part of the THz spectrometer. Because of the different reflection coefficients for gold mirrors for the two polarization components, the number of mirrors after the ZnTe crystal was minimized, and dielectric mirrors were used behind the ZnTe crystal.

## 4.7 Spectral content of the pulse

When a 30  $\mu\text{m}$  thick 0.6 % MgO-doped LiNbO<sub>3</sub> crystal was used to generate the THz radiation, frequency content useful for spectroscopic applications between approximately 0.7 and 2.5 THz was produced. When the THz radiation is generated in a thicker crystal, the lower limit can be shifted to lower frequencies. The upper limit is determined by the presence of phonon resonances in the two crystals used respectively for generation and detection). Figure 4.2 shows the experimentally detected transients and the Fourier transforms of four THz pulses generated in different experimental arrangements (Cherenkov arrangement in a  $60 \times 15 \times 25$  mm LiNbO<sub>3</sub> crystal in a), perpendicular arrangement in b), c), and d), with 2500, 100, and 30  $\mu\text{m}$  thick 0.6 % MgO-doped LiNbO<sub>3</sub> crystals, respectively).

Closer inspection of the transients, for example in Fig. 4.2b, shows that in fact two pulses, separated by slightly more than one ps in the first case, are produced in the LiNbO<sub>3</sub> crystal. The two pulses correspond to radiation generated on the back and front surfaces of the LiNbO<sub>3</sub> crystal. Weaker replicas of the original pulse pair are visible at  $\approx 5$  ps and  $\approx 11$  ps. These correspond to reflections in the ITO and ZnTe, respectively. The modulation of the frequency domain spectrum in Fig. 4.2c at  $\approx 0.9$  THz corresponds to the separation of the two pulses in LiNbO<sub>3</sub>, while the modulation at  $\approx 0.08$  THz corresponds to reflections of the THz pulse at the interfaces of the ZnTe detection crystal.

## 4.8 Sample cell

In order to record the rotational spectra of small molecules in the gas phase, two cells were built. The first cell had a length of  $3\frac{3}{4}$ " , and a clear aperture diameter of 1" . The THz pulse entered and left the cell through 7 mm thick high-resistivity (HR) float-zone Si windows (resistivity  $> 10$  k $\Omega$ /cm, purchased from Silicon Quest International), mounted perpendicularly to the THz beam. HR Silicon was used because of the relatively frequency independent index of refraction and absorption coefficient of this material in the THz frequency region [39]. Two fused-silica windows were mounted at  $90^\circ$  to the direction of the THz beam, to enable crossed beam excitation by a dye laser.

The next cell that was built was designed to accommodate collinear UV-THz double-resonance experiments, (see Fig. 4.10). In order to accomplish that, the HR Si windows were mounted at  $45^\circ$  to the direction of the THz beam, and their inner surfaces were polished. Additional fused silica windows were mounted at  $90^\circ$  to the cell axis, see Fig. 4.10. The UV radiation entering through the fused silica window was reflected off the inner surface of the input Si window and propagated through the cell, along the direction of the THz beam. In this design the length of the cell was increased to 18.5 cm, while the clear aperture diameter was 1" .

An improved version of the gas cell has been designed, and is being built at present, with the HR Si windows coated to enhance the UV reflectance. The new cell is also designed with a larger clear aperture diameter of 1.5" .

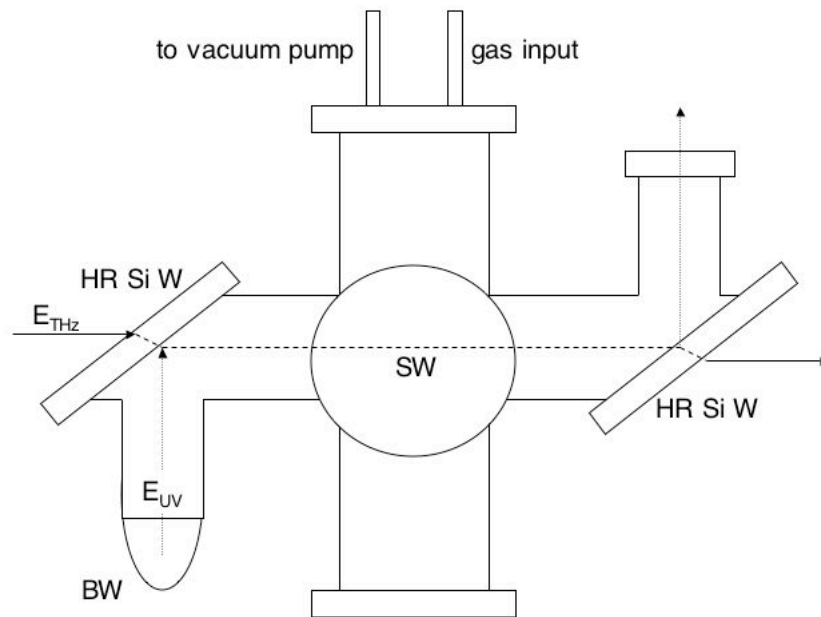


Figure 4.10: Gas cell for UV-THz double resonance experiments: the THz beam enters and exits the cell through a pair of high-resistivity Si windows (HR Si W). The Si surfaces inside the cell are polished so that the UV beam, entering through a perpendicularly mounted Brewster window (BW), is reflected, propagating collinearly with the THz beam through the cell. The fluorescence is collected through a side window (SW).

## 4.9 Attempt to record rotational spectra of small molecules

With useful spectral content between 0.7 and 2.5 THz, we tested our THz spectrometer by recording the ground state rotational spectra of small molecules. Rotational spectra of CH<sub>3</sub>F in a gas cell were previously recorded using TDTS [4]. CH<sub>3</sub>F has a dipole moment strong enough (1.79 D [40]) to enable us to record the rotational spectrum easily (see Table 4.3). CH<sub>3</sub>F is a symmetric rotor with  $B = 25\,536.158$  MHz [41], and the rotational spectrum is simple and well resolved by TDTS. CH<sub>3</sub>F was the first molecule for which we recorded the rotational spectrum using our THz spectrometer (see Fig. 4.11). This spectrum was recorded prior to spectrometer improvements that included the removal of water vapor absorption, minimizing polarization noise, and switching to a thin LiNbO<sub>3</sub> generation crystal.

We have also recorded the ground state rotational spectrum of formaldehyde. Formaldehyde was selected because its low-lying excited electronic state ( $\tilde{A}^1 A_2$ ), easily accessible in the UV, makes it a good candidate for a UV-THz double resonance experiment. Formaldehyde is a near-prolate rotor, with a ground-state dipole moment of 2.33 D along the  $a$  axis, exhibiting  $a$ -type transitions ( $\Delta K_a = 0$ ,  $\Delta K_c = \pm 1$ ) [42]. The rotational constants are given in Table 4.3. In order to record the spectrum, formaldehyde was produced by cracking paraformaldehyde (Sigma-Aldrich), using the method described in [43, 44]. The thus prepared H<sub>2</sub>CO was kept at a temperature of 77 K (cooled by liquid N<sub>2</sub>) until being used in the experiment. All the parts of the apparatus through which the formaldehyde must pass on the way to the gas cell had to be kept dry by being evacuated, as polymerization into paraformaldehyde is catalyzed by water. Figures 4.12a and 4.12b show ground state rotational spectra of formaldehyde at 5.1 Torr and 500 mTorr, respectively. Transition frequencies in the spectrum agree with the Cologne Database for Molecular Spectroscopy [45] with  $\approx 1$  GHz error.

We have also calculated the absorption coefficient and index of refraction of the formaldehyde gas sample, using the expressions given in [4] and [40]. The absorption coefficient  $\alpha$  and dispersion  $\Delta k$  are given by:

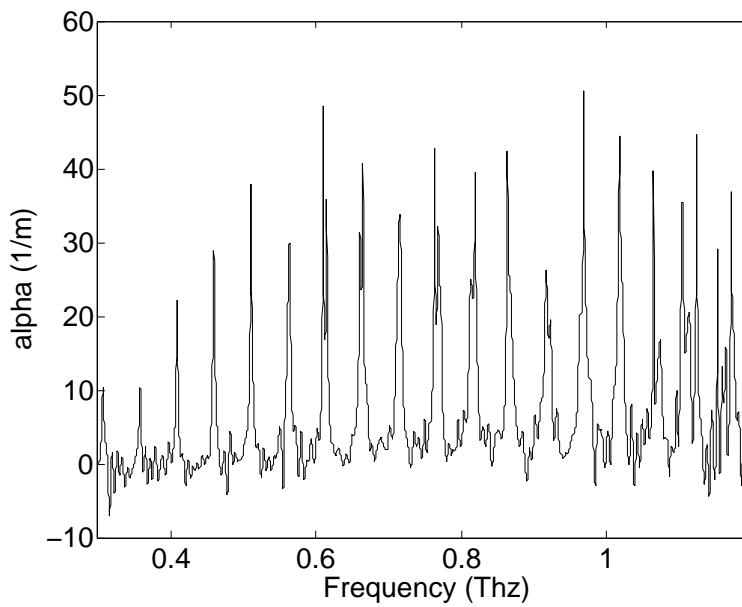
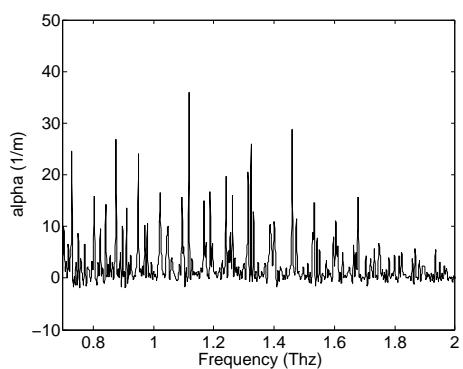


Figure 4.11: Experimentally recorded  $\text{CH}_3\text{F}$  TDTHz spectrum at 100 Torr in an 18.5 cm long gas cell. The spectrum was recorded using a 2.5 mm thick, 0.6 % MgO-doped  $\text{LiNbO}_3$  crystal at 1 kHz, before removal of water vapor absorption, and before numerous improvements to the spectrometer, described in the text, were made. The duration of the electric field transient used to generate the spectrum was  $\approx 160$  ps, respectively.

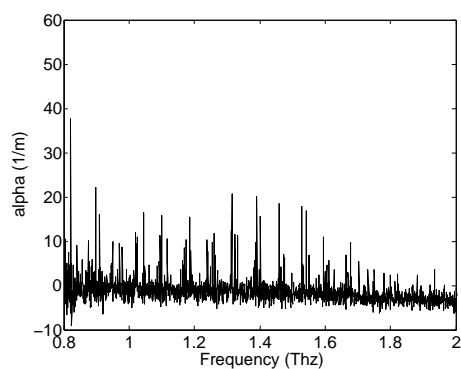


Table 4.3: Rotational constants for molecules studied using TDTTS.

Molecule state	$T_0$ ( $\text{cm}^{-1}$ )	$A$ (MHz)	$B$ (MHz)	$C$ (MHz)	$D_K$ (MHz)	$D_{JK}$ (MHz)	$10^2 D_J$ (MHz)	$\delta_K$ (MHz)	$10^2 \delta_J$ (MHz)
$\text{CH}_3\text{F } \tilde{X}$			25 536.158			0.4390	6.043		
$\text{H}_2\text{CO } \tilde{X}$		281 970.572	38 836.0455	34 002.2034	19.423	1.29050	7.5295	1.02603	1.04567
$\text{H}_2\text{CO } \tilde{A} \nu_4 = 1$	28 312.561	262 377	33 727.0	33 011.41	14.97	1.97	7.76	0.621	6.15



(a)



(b)

Figure 4.12: Experimentally recorded spectra of  $\text{H}_2\text{CO}$  at 5.1 Torr a), and 500 mTorr b). The spectra were recorded at 20 Hz using a  $30 \mu\text{m}$  thick 0.6 % MgO-doped  $\text{LiNbO}_3$  crystal. The transient durations used to generate the Fourier transforms were  $\approx 160$  ps, and  $\approx 900$  ps in a) and b).

$$\alpha = \frac{\pi f_v p \mu_{JK}^2}{18nc\epsilon_0(kT)^2} S(I, K) \sqrt{\frac{ABC\hbar}{\pi kT}} \omega g_\alpha \left(1 - e^{-\frac{\hbar(B+C)(J+1)}{kT}}\right) \left(e^{-\frac{\hbar}{kT} \left[\frac{(B+C)}{2} J(J+1) - \left(A - \frac{(B+C)}{2}\right) K_a^2\right]}\right) \quad (4.9)$$

$$\Delta k = 2 \frac{\pi f_v p \mu_{JK}^2}{18nc\epsilon_0(kT)^2} S(I, K) \sqrt{\frac{ABC\hbar}{\pi kT}} g_K \frac{\omega \omega_{JK}}{\omega_{JK}^2 - \omega^2} \left(1 - e^{-\frac{\hbar(B+C)(J+1)}{kT}}\right) \left(e^{-\frac{\hbar}{kT} \left[\frac{(B+C)}{2} J(J+1) - \left(A - \frac{(B+C)}{2}\right) K_a^2\right]}\right) \quad (4.10)$$

where the notation is defined in [4], and  $S = 3$  for  $K_a$  odd and  $S = 1$  for  $K_a$  even ( $S$  is degeneracy associated with spin inversion). Calculated values of  $\alpha L$  and  $\Delta k L$ , with  $L = 18.5$  cm, for 500 mTorr pressure are given in Figs. 4.13 and 4.14.

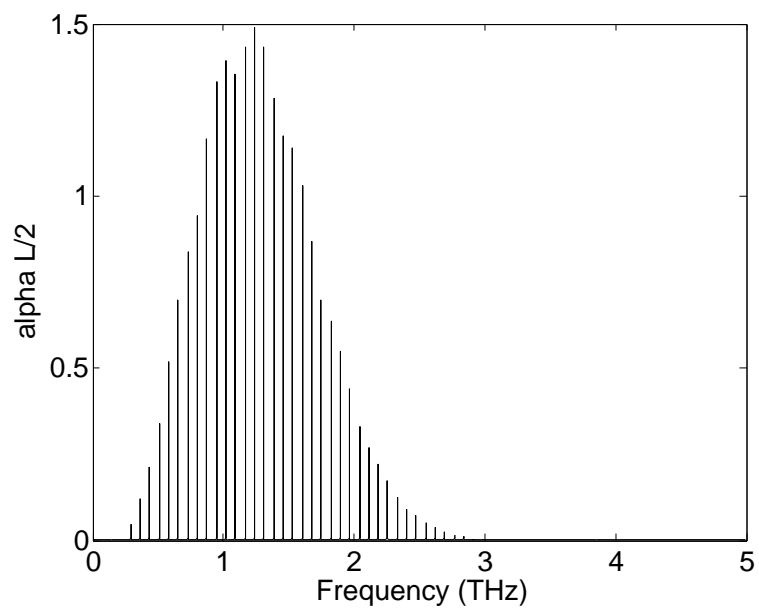


Figure 4.13: Calculated frequency dependence of  $\alpha L/2$  for rotational transitions of  $\text{H}_2\text{CO}$  at 500 mTorr and room temperature.

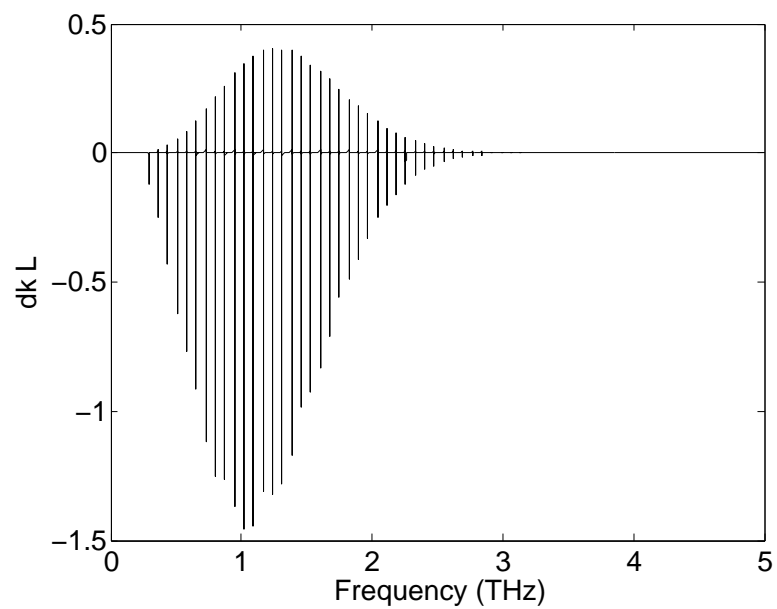


Figure 4.14: Calculated frequency dependence of  $\Delta kL$  for rotational transitions of  $\text{H}_2\text{CO}$  at 500 mTorr and room temperature.

## 4.10 Extraction of molecular parameters

When FSEOS is used for detection, it is the electric field ( $E_{THz}$ ), and not the intensity of the THz pulse that is measured in the experiment. Since both the amplitude and the phase of the  $E_{THz}$  are experimentally determined, it is possible to recover the molecular parameters  $\alpha$  and  $n$  directly, without a Kramers-Kronig analysis. The extraction of  $n$  and  $\alpha$  is based on the transfer function formalism [46, 47, 48], where linear response in the sample is assumed. In this framework, the ratio of  $E_{THz}$  and  $E'_{THz}$ , THz field amplitude after and before the sample, respectively, represents a product of transfer functions through all media and interfaces that constitute the sample.

The transmitted electric field is recorded twice, once with the cell filled with the sample,  $E_{SAMPLE}(t)$ , and once with the empty cell, as a reference,  $E_{REFERENCE}(t)$ . The transients are Fourier transformed into the frequency domain, where the spectral content after the gas cell is related to the spectral content before the gas cell, for both  $E_{SAMPLE}$  and  $E_{REFERENCE}$  pulses, by applying the corresponding transfer functions.

For the sample:

$$E_{SAMPLE}(\omega) = E'_{THz}(\omega)T_{air,Si}(\omega)P_{Si}(\omega, L_{Si})T_{Si,sample}(\omega)P_{sample}(\omega, L)T_{sample,Si}(\omega)P_{Si}(\omega, L_{Si})T_{Si,air}(\omega), \quad (4.11)$$

and for the reference:

$$E_{REFERENCE}(\omega) = E'_{THz}(\omega)T_{air,Si}(\omega)P_{Si}(\omega, L_{Si})T_{Si,reference}(\omega)P_{reference}(\omega, L)T_{reference,Si}(\omega)P_{Si}(\omega, L_{Si})T_{Si,air}(\omega), \quad (4.12)$$

where  $T_{a,b}(\omega)$  are Fresnel coefficients for the interface between the media  $a$  and  $b$ ,  $T_{a,b,\parallel}(\omega) =$

$\frac{2\tilde{n}_a \cos\theta_i}{\tilde{n}_a \cos\theta_t + \tilde{n}_b \cos\theta_i}$  ( $\theta_i$  is the incident angle,  $\theta_t$  is the refracted angle), and  $P_a(\omega, L)$  a transfer function through the medium  $a$  of length  $L$ ,  $P_a(\omega, L) = \exp[-i\frac{\tilde{n}_a \omega d}{c}]$ .  $\tilde{n}_a = n_a - i\kappa_a$  is the complex index of refraction, including both dispersive and absorptive components of the response of the sample, that are determined in the experiment.  $n_a$  is the index of refraction for the material  $a$  and  $\kappa_a$  is related to the absorption coefficient  $\alpha_a$  ( $\alpha_a = \frac{2\omega\kappa_a}{c}$ ). In our experimental design the silicon windows are mounted at a  $45^\circ$  angle to the propagation direction of the THz beam, and the reflections of the THz radiation on the surfaces of the windows are separated in time by  $\approx 160$  ps.

If we neglect the dependence of the Fresnel coefficients  $T_{Si,sample}$  on  $\omega$ , the ratio of the signals for the sample and reference in the frequency domain becomes:

$$\frac{E_{SAMPLE}(\omega)}{E_{REFERENCE}(\omega)} = e^{-\frac{i(\tilde{n}_{sample} - \tilde{n}_{reference})}{c}}, \quad (4.13)$$

and, since in vacuum  $\tilde{n} = 1$ ,

$$\frac{E_{SAMPLE}(\omega)}{E_{REFERENCE}(\omega)} = e^{-\frac{i(n_{sample} - 1 - i\kappa_{sample})}{c}}. \quad (4.14)$$

Thus the  $n$  and  $\alpha$  can be obtained easily from the ratio of the Fourier transforms of the two transients. That neglect of the dependence of  $T_{Si,sample}$  and  $T_{sample,Si}$  on  $\omega$  is justified was confirmed by calculating them with the extracted parameters, and with the parameters calculated using Eq. (4.9) and (4.10). A Matlab code for extracting  $n$  and  $\alpha$  for solid-state samples, based on the algorithm described in [46] and [47], written by Dr. Thomas Hornung, was modified for use with gas-phase samples.

When the molecular parameters  $\alpha$  and  $n$  are extracted using the procedure described above, the separation of the absorptive and dispersive parts of the lineshapes is always imperfect. This results in part from the imperfect knowledge of the zero time for the Fourier transform, in part due to the finite time window for the Fourier transform, and partially because of the absence of absolute calibration of the delay stage. A method for calibration

of the delay stage using an external He-Ne beam has been proposed [49], but has not yet been implemented in our spectrometer. Another solution to the problem of mixing the absorptive and dispersive parts of the lineshapes is a comparison of the experimentally measured transients in time domain to those calculated when the molecular constants are known, as in [4]. However, minimizing the mixing of the absorptive and dispersive parts of the lineshapes, when extracting  $\alpha$  and  $n$  from time domain transients for samples with unknown molecular parameters, remains sub-optimal. This is especially the case for samples with many closely-spaced, sharp absorptive transitions.



## 4.11 UV-THz double resonance experiment

In order to test the interfacing between our time domain THz spectrometer and the 20 Hz dye laser system, a UV-THz double resonance experiment has been designed and attempted. Formaldehyde has a low lying excited electronic state ( $T_0 = 28312.561 \text{ cm}^{-1}$  for the  $4_0^1 \tilde{A}^1 A_2 \leftarrow \tilde{X}^1 A_2$  band), within the frequency range that is easily accessible by the frequency-doubled output (in 37.7°-cut BBO, Spectra Physics) of our Nd:YAG pumped dye laser (operated with LDS 698 laser dye). If the UV radiation provided by this dye laser is resonant with a transition between a particular ground state rotational level ( $J'', K_a'', K_c''$ ) and an excited vibronic state rotational level ( $J', K_a', K_c'$ ), the ( $J'', K_a'', K_c''$ ) level will be depopulated by that transition. If the transition ( $J', K_a', K_c' \leftarrow (J'', K_a'', K_c'')$ ) is close to saturation, the population difference between  $J''$  and  $J'' \pm 1$  created by the UV laser pulse is much larger than the thermal population difference. The lifetime of such a level bleached population difference is estimated to be  $\approx 18 \text{ ns}$  at 500 mTorr ( $\tau = \frac{1}{2\pi p[\text{Torr}]27\text{MHz/Torr}}$ ), using the reported 27 MHz/Torr [50] value for the broadening coefficient for H<sub>2</sub>CO. When a non-thermal population difference between ( $J'', K_a'', K_c''$ ) and ( $J'' \pm 1, K_a'', K_c'' \pm 1$ ) is created, the transition intensity between the  $J''$  and  $J'' \pm 1$  levels is strongly modified, compared to the transition intensities for the sample in thermal equilibrium. The large non-thermal population difference results in a modification of the ground state rotational spectrum, which is expected to be observable using TDTS. The UV-THz double resonance experiment was attempted at H<sub>2</sub>CO pressures below 500 mTorr, to ensure that the on-resonance THz absorption by H<sub>2</sub>CO is not saturated. However, decreasing the pressure below 200 mTorr resulted in very weak THz free induction decay, which was only observable with long delay scans ( $\approx 900 \text{ ps}$ ).

We selected the (12, 3, 9) and (12, 3, 10) pair of ground state rotational levels, unresolved in our experiment, and a pair of unresolved transitions into the excited electronic state (13, 4, 9)  $\leftarrow$  (12, 3, 10) and (13, 4, 10)  $\leftarrow$  (12, 3, 9) in the  $4_0^1 \tilde{A}^1 A_2 \leftarrow \tilde{X}^1 A_2$  band. Since the ground electronic state in CH<sub>2</sub>O is of  $^1 A_1$  symmetry, and the  $\tilde{A}$  is of  $^1 A_2$  symmetry, a

pure electronic transition is forbidden. However, it becomes allowed when accompanied by a  $4_0^1$  vibrational transition (out-of-plane bend is of  $B_1$  symmetry). The modification of the ground state rotational spectrum by the resonant UV transition for this choice of upper and lower states was modeled by Emily Fenn [51].

In order to experimentally locate the mentioned pair of UV transitions, a spectrum was recorded by scanning the UV laser frequency in the range 28320 - 28338  $\text{cm}^{-1}$  and detecting the fluorescence (collected at  $90^\circ$  and focused with an  $f = 7$  cm lens onto the PMT, operated at 800 V, preceded by a filter that blocked the excitation wavelength). A part of the dye laser output was split off before the frequency doubler, and used to record the absorption spectrum of iodine in a cell at  $100^\circ$  C. The iodine spectrum was used for the absolute frequency calibration of the  $\text{H}_2\text{CO}$  spectrum with  $0.03 \text{ cm}^{-1}$  accuracy (an extracavity etalon was used). The experimentally recorded spectrum was, after calibration, compared to one calculated using the package JET/BEAM 95. The calculation was done using the molecular constants for  $\text{H}_2\text{CO}$  published in [42]. The comparison between the predicted and experimentally observed spectra was used to assign the transitions observed in the laser-induced fluorescence spectrum. After making the assignments, the unresolved pair of transitions  $(13, 4, 9) \leftarrow (12, 3, 10)$  and  $(13, 4, 10) \leftarrow (12, 3, 9)$  in the  $4_0^1 \tilde{A} \ ^1A_2 \leftarrow \tilde{X} \ ^1A_2$  band was used in an attempt to observe the UV-THz double resonance spectra.

In the UV-THz double resonance experiment, the sample cell was placed in the collimated arm of the THz spectrometer. Spatial overlap of the UV beam (expanded to  $\approx 5$  mm) and the THz beam was ensured by centering both THz and UV beams on an iris placed in the beam path after the sample cell (the UV beam was centered on the iris with the back window of the cell removed). In addition, both beams were centered on the entrance window as well.

The temporal overlap of the THz and UV pulses was ensured by simultaneously detecting scattered UV and 800 nm pump pulses on a fast photodiode, connected to a 1 GHz oscilloscope. The delay between the two pulses was varied, changing the delay provided by the SDG, with precision of 1 ns. Varying this delay affected the triggering of the Q-switch

in the Nd:YAG laser that pumps the dye laser.

Two detection schemes were attempted. In the first one, independent THz spectra were recorded in the presence and absence of resonant UV radiation. In addition, a reference spectrum with an empty gas cell is recorded. After the transients have been processed to determine  $\alpha$  for the sample in the presence and absence of the resonant UV radiation, the two spectra are compared in order to observe the modification caused by the resonant UV pulse.

The second experimental scheme employs a different repetition rate for the UV and THz beams. UV pulses are produced at 20 Hz, one half of the repetition rate of the THz pulses (40 Hz). Phase sensitive detection with a lock-in amplifier reference frequency at 20 Hz is used to subtract the intensity of two successive pulses, similarly to Fig. 4.6. This way the modification due to the resonant UV transition is recorded directly, in time domain.

Although a strong modification of the ground state rotational spectrum was expected, no effect was observed in either of the two detection schemes. The absence of the expected spectrum modulation was attributed to a Doppler mismatch between the UV and THz pulses. The THz pulse is broadband, and it is absorbed by molecules independently of their translational velocity. However, the UV pulse is narrowband. When an extracavity etalon is used, the bandwidth corresponds to  $\approx 1$  GHz, but for each pulse a particular longitudinal dye laser mode, of only 0.05 GHz linewidth dominates (for a pulse of  $\tau = 7$  ns  $\Delta\nu = \frac{(2\ln 2)^{\frac{1}{2}}}{\pi\tau}$ ). The Doppler width for the UV pulse corresponds approximately to 1 GHz ( $\Delta\nu = \frac{\nu}{c} \left(\frac{2kT\ln 2}{m}\right)^{\frac{1}{2}}$ ), but because of the dye laser mode structure, only  $\approx 1/20^{\text{th}}$  part of the full Doppler lineshape is excited, and the Doppler mismatch decreases the expected signal by a factor of 20, see Fig. 4.15.

Even though the UV-THz experiment on formaldehyde was unsuccessful, a synchronization and triggering scheme between the two laser systems was developed in the process of setting up the UV-THz double resonance experiment. While developing the synchronization scheme, unexpected issues, such as underperformance of the Q-switch driver in the

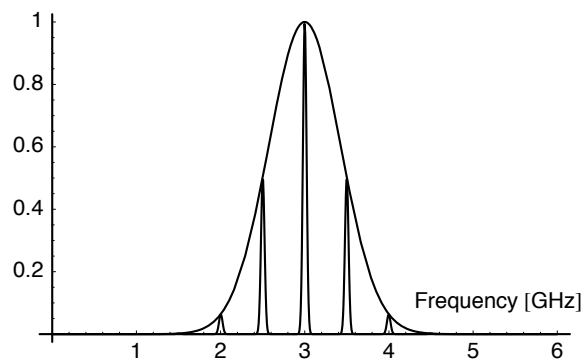


Figure 4.15: The pulse-averaged bandwidth of a dye laser pulse with no extracavity etalon is approximately 1 GHz. However, in each pulse a mode of the 0.05 GHz width is produced.

Spectra Physics Evolution Laser, and false triggers in the Spectra Physics SDG were discovered, and avoided. Since the main obstacle to the UV-THz double resonance experiment on  $\text{H}_2\text{CO}$ , namely the Doppler mismatch, will not be an issue in the molecular beam experiment, and other aspects of the interfacing between the two systems have been verified, it can be concluded that the THz apparatus is ready to be interfaced with the double resonance experiment.

## 4.12 Bibliography

- [1] S. L. Drexheimer, editor. *Terahertz Spectroscopy: Principles and Applications*. CRC Press, 2007.
- [2] B. Ferguson and X.-C. Zhang. *Nat. Materials*, 1:26, 2002.
- [3] C. A. Schmuttenmaer. *Chem. Rev.*, 104:1759, 2004.
- [4] H. Harde, R. A. Cheville, and D. Grischkowsky. *J. Phys. Chem. A*, 101:3646, 1997.
- [5] J. Zhang and D. Grischkowsky. *Opt. Lett.*, 29:1031, 2003.
- [6] B.N. Flanders, X. Shang, N.F. Sherrer, and D. Grischkowsky. *J. Phys. Chem. A*, 103:10054, 1999.
- [7] M. van Exter, Ch. Fattinger, and D. Grischkowsky. *Opt. Lett.*, 14:1128, 1989.
- [8] H. Harde, J. Zhao, M. Wolff, R. A. Cheville, and D. Grischkowsky. *J. Phys. Chem. A*, 105:6038, 2001.
- [9] H. Harde, S. Keiding, and D. Grischkowsky. *Phys. Rev. Lett.*, 66:1834, 1991.
- [10] H. Harde and D. Grischkowsky. *J. Opt. Soc. Am. B*, 8:1642, 1991.
- [11] *Spitfire - User Manual*. Spetra Physics Lasers, 2001.
- [12] Y. R. Shen. *The principles of nonlinear optics*. Wiley-Interscience, 2003.
- [13] D. H. Auston and M. C. Nuss. *IEEE J. Quant. Elec.*, 24:184, 1988.
- [14] G. D. Boyd and D. A. Kleinman. *J. Appl. Phys.*, 39:3597, 1968.

- [15] J. Hebling, K-L. Yeh, M. C. Hoffmann, B. Bartal, and K. A. Nelson. *J. Opt. Soc. Am. B*, 25:B6, 2008.
- [16] R. L. Sutherland. *Handbook of nonlinear optics*. Marcel Dekker, 1996.
- [17] P. C. M. Planken, H.-K. Nienhuys, H. J. Bakker, and T. Wenckenbach. *J. Opt. Soc. Am. B*, 18:313, 2001.
- [18] A. Yariv and P. Yeh. *Photonics: optical electronics in modern communications*. Oxford University Press, 2007.
- [19] D. Ward. *Polaritonics: An intermediate regime between electronics and photonics*. PhD thesis, Massachusetts Institute of Technology, 2005.
- [20] K-L. Yeh, J. Hebling, M. C. Hoffmann, and K. A. Nelson. *Opt. Comm.*, 281:3567, 2008.
- [21] D. H. Auston, K. P. Cheung, J. A. Valdmanis, and D. A. Kleinman. *Phys. Rev. Lett.*, 53:1555, 1984.
- [22] T. E. Stevens, J. K. Wahlstrand, J. Kuhl, and R. Merlin. *Science*, 291:627, 2001.
- [23] J. E. Sipe D. Côté and H. M. van Driel. *J. Opt. Soc. Am. B*, 20:1374, 2003.
- [24] P. Y. Han and X.-C. Zhang. *Meas. Sci. Technol.*, 12:1747, 2001.
- [25] M. C. Beard, G. M. Turner, and C. A. Schmuttenmaer. *J. Phys. Chem. B*, 106:7146, 2002.
- [26] A. Leitenstorfer, S. Hunsche, J. Shah, M. C. Nuss, and W. H. Knox. *Phys. Rev. Lett.*, 82:5140, 1999.
- [27] Q. Wu and X.-C. Zhang. *Appl. Phys. Lett.*, 68:1604, 1996.
- [28] A. Leitenstorfer, S. Hunsche, J. Shah, M. C. Nuss, and W. H. Knox. *Appl. Phys. Lett.*, 74:1516, 1999.

- [29] Q. Wu and X.-C. Zhang. *Appl. Phys. Lett.*, 71:1285, 1997.
- [30] Z. Jiang, F. G. Sun, Q. Chen, and X.-C. Zhang. *Appl. Phys. Lett.*, 74:1191, 1999.
- [31] Y. Li. *Appl. Phys. Lett.*, 88:251108, 2006.
- [32] *Model SR830 DSP lock-in amplifier, User Manual*. Stanford Research Systems, 2004.
- [33] H. J. Bakker, G. C. Cho, H. Kurz, Q. Wu, and X.-C. Zhang. *J. Opt. Soc. Am. B*, 15:1795, 1998.
- [34] G. Gallot and D. Grischkowsky. *J. Opt. Soc. Am. B*, 16:1204, 1999.
- [35] M. Born and E. Wolf. *Principles of optics*. Cambridge University Press, 2005.
- [36] S. E. Segre and V. Zanza. *J. Opt. Soc. Am. A*, 20:1804, 2003.
- [37] M. A. Player. *J. Mod. Opt.*, 35:1813, 1988.
- [38] J. Liu and R. M. A. Azzam. *Appl. Opt.*, 36:1553, 1997.
- [39] J. Dai, J. Zhang, W. Zhang, and D. Grischkowsky. *J. Opt. Soc. Am. B*, 21:1379, 2004.
- [40] C. H. Townes and A. L. Schawlow. *Microwave Spectroscopy*. Dover Publications Inc., 1975.
- [41] T. E. Sullivan and L. Frenkel. *J. Mol. Spec.*, 39:185, 1971.
- [42] D. J. Clouthier and D. A. Ramsay. *Annu. Rev. Phys. Chem.*, 34:31, 1983.
- [43] R. Spence and W. Wild. *J. Chem. Soc.*, page 506, 1935.
- [44] R. Spence and W. Wild. *J. Chem. Soc.*, page 338, 1935.
- [45] Cologne Database for Molecular Spectroscopy.
- [46] L. Duvillaret, F. Garet, and J. L. Coutaz. *IEEE J. Sel. Top. Quant. Elec.*, 2:739, 1996.

- [47] L. Duvillaret, F. Garet, and J. L. Coutaz. *J. Opt. Soc. Am. B*, 17:452, 2000.
- [48] P. U. Jepsen and B. M. Fischer. *Opt. Lett.*, 30:29, 2005.
- [49] J. J. Loparo. *Ultrafast structural fluctuations and rearrangements of water's hydrogen bonded network*. PhD thesis, Massachusetts Institute of Technology, 2006.
- [50] B. J. Orr, J. G. Haub, G. F. Nutt, J. L. Steward, and O. Vozzo. *Chem. Phys. Lett.*, 78:621, 1981.
- [51] E. E. Fenn. B. Sc. Thesis, Massachusetts Institute of Technology, 2006.



# Chapter 5

## Rydberg-Rydberg chirped-pulse microwave spectroscopy

### 5.1 Introduction

Microvawe radiation is an exceptionally useful and widely used means of studying Rydberg states at high resolution. High resolution enables precise determination of atomic and molecular parameters, such as quantum defects, polarizabilities, and multipole moments. In its most often used form, microwave spectroscopy of Rydberg states is coupled with detection by pulsed field ionization (PFI) [1]. Typically, between one and three tunable laser pulses are used to access the launch Rydberg state, from which a microwave transition into another Rydberg state is recorded. After excitation, a delayed pulsed electric field,  $E_I$ , ionizes the excited atoms or molecules. The states owith lower  $n^*$  values<sup>†</sup> require a higher electric field to be field ionized. It is possible to distinguish atoms (or molecules) in different Rydberg states based on the value of  $E_I$  required to induce ionization. If the strength of  $E_I$  is ramped in time, ions from atoms (or molecules) ionized from different Rydberg states are formed at different times, and can be distinguished based on their arrival times to the detector, see Fig. 5.1. If on-resonance microwave radiation, MW, causes a transition between the

---

<sup>†</sup> $n^*$  is the principal quantum number corrected for the quantum defect.

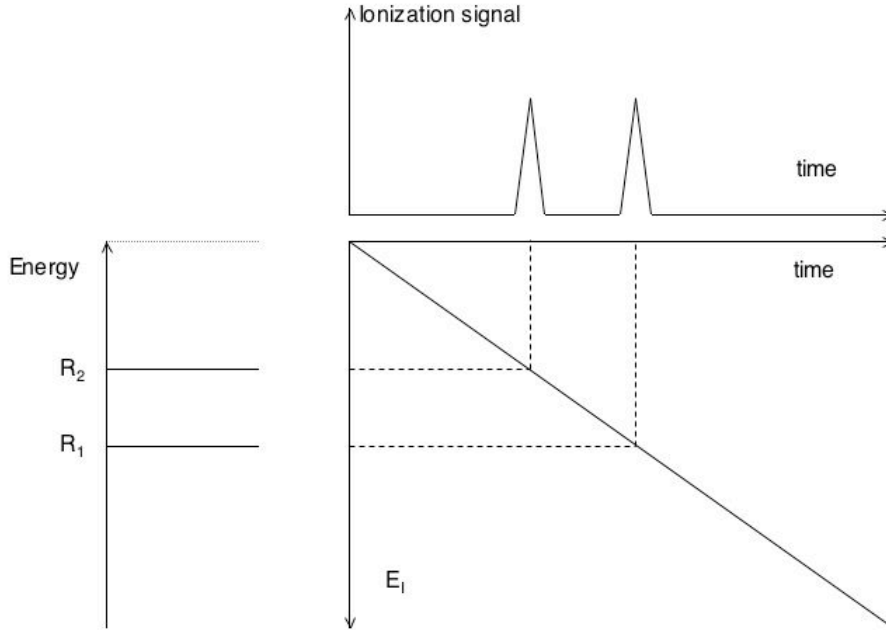


Figure 5.1: When an external electric field,  $E_I$ , which causes ionization, is ramped linearly in time, states with higher energy (and higher  $n^*$ ), such as  $R_2$ , are ionized earlier than states with lower energy, such as  $R_1$ . A time-of-flight mass spectrometer can be used to determine from which state the ionization occurs. The time of flight from the excitation region to the MCP detector is short compared to the time between the two ionization pulses.

Rydberg states  $R_1$  and  $R_2$ , then in the presence of MW the relative population of  $R_1$  and  $R_2$  will be different than without the MW field, see Fig. 5.2. This population difference can easily be observed in a PFI experiment as the number of ions formed from  $R_1$  and  $R_2$  is measured. Thus, the effect of a resonant microwave field can be observed in an ion-detection experiment.

States which belong to the same  $n^*$ , but have a different parabolic quantum number  $n_1^\ddagger$ , ionize at different values of  $E_I$ , as do the states with different  $|m_j|$ . Thus, when  $n^*$  increases, the density of states increases, and at high  $n^*$  it becomes difficult to selectively ionize atoms (or molecules) in closely spaced Rydberg states. In such a case, it is necessary to design shaped pulsed fields. The shape of the ramp is designed taking into account the dynamics

---

<sup>‡</sup>Solutions to the Schrodinger equation for hydrogen atom in presence of external electric field are expressed in terms of parabolic quantum numbers  $n_1$  and  $n_2$ , related by the expression  $n = n_1 + n_2 + |m_\ell| + 1$

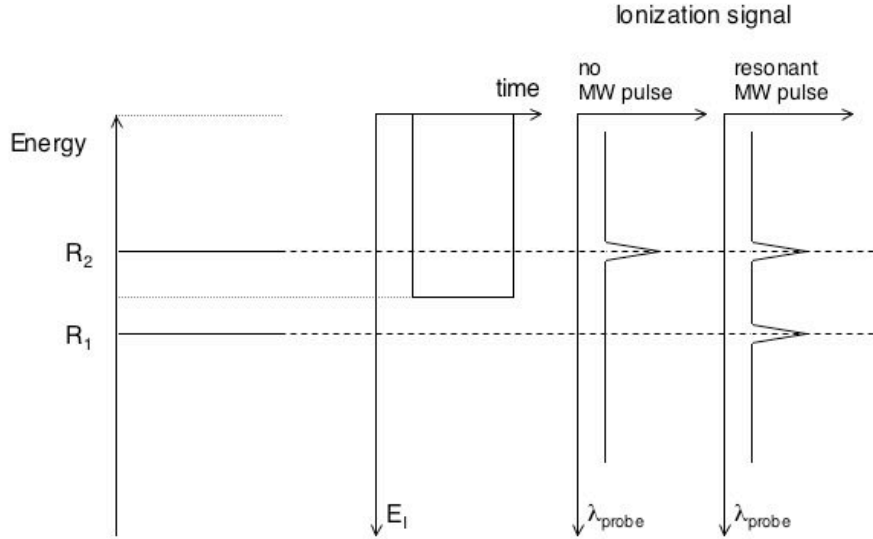


Figure 5.2: In this experiment, a pulsed ionizing electric field,  $E_I$ , has a value sufficient to ionize the higher energy state,  $R_2$ , but not sufficient to ionize the lower energy state,  $R_1$ . When a microwave pulse, resonant with the  $R_2 \leftarrow R_1$  transition, precedes the ionization pulse, ions are detected at laser frequencies resonant with transitions into *both*  $R_2$  and  $R_1$ .

of Stark mixing and ionization, so that the loss in state-selectivity at higher- $n^*$  states is minimized, see [2]. However, at low enough  $n^*$ , it is possible to distinguish between ions formed from two Rydberg states with a simple linearly-increasing pulsed field. Alternatively, at low  $n^*$ , it is possible to use a pulsed ionizing field with a constant value of  $E_I$  after the initial rise time, and adjust that value so that only the higher energy state of the two states connected by a microwave pulse is ionized (see Fig. 5.2). In such a case, ions are formed only in the presence of a resonant microwave pulse (contrast ratio  $> 20$ ).

Ionization-detected microwave spectroscopy has been used extensively to study atomic Rydberg states, for example, see [3], [1], and references therein. Gentile and co-workers studied microwave spectra of Rydberg states of Ca with an accuracy of approximately 1 part in  $10^6$  (in the range between 26.5 and 120 GHz) [4]. F. Merkt and H. Schmutz minimized the sources of line broadening and measured linewidths as narrow as 250 kHz in Ar Rydberg states [5]. Improvements in the resolution of PFI-based MW spectroscopy led to the application of Rydberg state spectroscopy for detection of very weak electric fields (20

$\mu\text{V}/\text{cm}$ ) [6].

All of the described variants of microwave spectroscopy applied to the high resolution study of Rydberg states in molecular beams rely on the detection of ions. However, it is possible to gain the same, and sometimes additional, information by detecting modification of the transmitted microwave field. When the experiment is done in transmission, the main difficulty is the low number density of the excited Rydberg atoms or molecules. We estimate that in our apparatus, we produce  $10^9$  Ca atoms (or  $10^6$  CaF molecules) per quantum state in the  $0.1 \text{ cm}^3$  excitation volume. However, exceptionally large transition dipole moments compensate for the low number density of Rydberg atoms in the molecular beam. The transition dipole moments among the Rydberg states in the same  $n^*$  scale as  $n^2$ , for example, the  $35f \leftarrow 35d$  transition has a transition dipole moment of  $\approx 4700 \text{ D}$ .

The additional information, which cannot reliably be obtained in an ionization-detected experiment without a prohibitively long acquisition time, comes from the relative transition intensities in the spectrum. If it is possible to determine both the transition frequency and relative intensity for a transition among mixed states, then both the energy and the mixing angle between the zero-order states can be determined. In  $\ell$ -mixed Rydberg states, especially the core-nonpenetrating ones, the mixing angles are small, but their precise values are important in separating different mechanisms of interaction between the Rydberg electron and the ion-core. The prospect of being able to use both the frequencies and transition intensities in fit models would result in a breakthrough in our ability to harvest information about  $\ell$ -mixed Rydberg states from a spectrum.

In order to obtain information from a transmission-detected microwave experiment, which cannot be obtained in an ionization-detected experiment, it is necessary to devise a single-shot detection method. When multiple resonance excitation is used to prepare the launch state, shot-to-shot instabilities hamper the relative intensities in a typical spectrum. Single-shot operation is necessary to avoid the difficulties inherent in multiple resonance launch state preparation. The recent development of chirped-pulse microwave spectroscopy (CPMW) by

Brooks Pate, see [7] and references therein, promises a method which can be extended to provide the ability to record microwave spectra of Rydberg states with relative intensities accurate to better than 1 part in  $10^4$ .

In CPMW spectroscopy, a chirped microwave pulse, covering a region up to  $\approx 12$  GHz wide, polarizes the sample, and the free induction decay (FID) is recorded by down-conversion mixing with a local oscillator (a fixed frequency source). The FID is downconverted into the frequency region which can be detected using a fast oscilloscope. The bandwidth of the experiment is limited by the bandwidth of the oscilloscope used in the detection, and can be twice this value if both upper and lower sidebands created by mixing of the signal with the local oscillator are detected. After acquisition and averaging of the signal in the time domain, performed on a digital oscilloscope, a time to frequency Fourier transform is calculated, yielding the frequency-domain absorption spectrum. Since the averaging is performed in the time domain, the method relies on the ability to ensure phase-stability in the generation and detection of the microwave radiation. In this method, the bandwidth of the pulse may be adjusted separately the duration of the pulse, which results in an inverse square root dependence of the signal on the bandwidth, as opposed to a linear decrease with the bandwidth in a pulse with Fourier transform limited bandwidth [8].

Conventional cavity-enhanced microwave spectroscopy, based on the Balle-Flygare design [9, 10, 11], relies on scanning the microwave frequency. At each frequency, a Fabry-Perot cavity has to be tuned into resonance. Even if the procedure is automated, the acquisition times are still much longer than in CPMW. Typically, 10 GHz regions are covered, at a resolution better than 500 kHz. For example, a typical acquisition time for an 11 GHz scan 500 kHz resolution spectrum is  $\approx 14$  hours [12]. Such long scans are not compatible with the stability necessary for relative intensity measurements in a multiple resonance experiment.

However, in CPMW spectroscopy every acquisition event contributes to all of the resolution elements, making the measured relative intensities directly related to the oscillator strengths. In addition, since there are no moving parts in a CPMW spectrometer, the

time that is spent on cavity tuning in conventional microwave spectroscopy, is in CPMW spectroscopy spent on data acquisition. The waiting time is thus decreased, significantly reducing acquisition times. A comparable region of 11 GHz can, with CPMW spectroscopy, be recorded at 500 kHz resolution 40 times faster than by conventional frequency-scanned microwave spectroscopy [7].

CPMW spectroscopy relies on recent developments in microwave technology. State-of-the-art arbitrary waveform generators (AWG) enable typesetting of a microwave waveform with up to 24 Gigasamples/s at present. Additionally, state-of-the-art fast broadband digitizers enable signal detection bandwidth up to 20 GHz. Even though an AWG operates at low frequency range (100 MHz - 2 GHz), their output can be mixed with a fixed frequency source and then up-converted into the desired frequency region in several steps. Active multipliers are commercially available only in the low frequency range, up to somewhat over 100 GHz. However, passive frequency multipliers, which have lower power output than active multipliers, are available for higher frequencies, up to a few THz. The power that can be produced for each multiplication step decreases as the frequency increases.

CPMW pure rotational spectroscopy found an excellent application in studying intramolecular dynamics, such as IVR and isomerization [13]. For typical samples, the permanent electric dipole moments are on the order of 1 D. The microwave power requirement associated with dipole moments of this order of magnitude at present prohibits extension of CPMW spectroscopy to higher frequency ( $> 50$  GHz) studies. However, when CPMW spectroscopy is used to study Rydberg-Rydberg transitions with exceptionally large dipole moments, very low microwave power is needed, and the use of passive multipliers is not an obstacle. Here we describe a modification of the CPMW spectrometer developed in the Pate group, adapted for the study of Rydberg-Rydberg transitions.

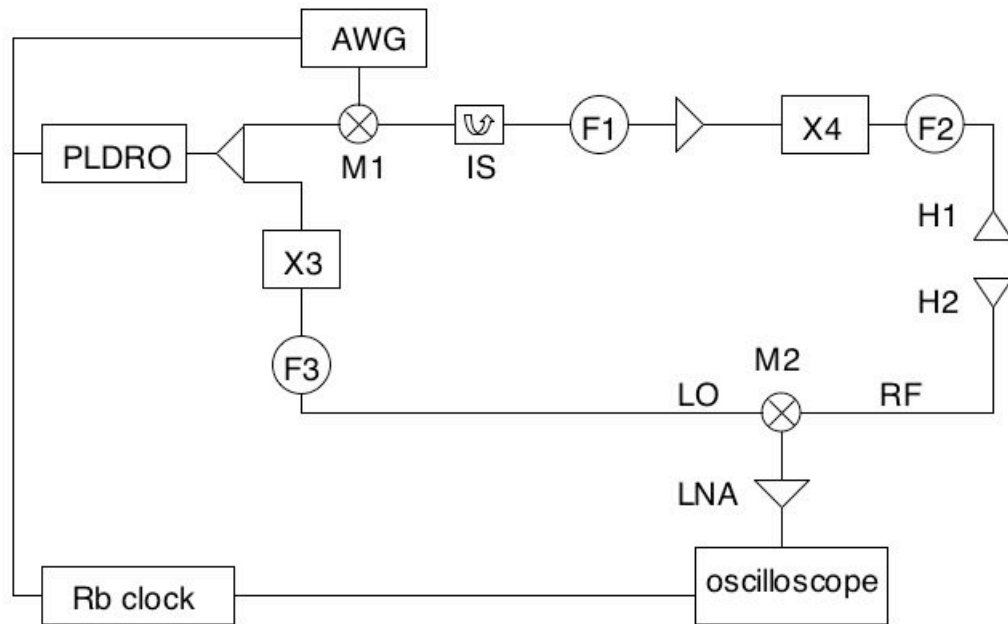


Figure 5.3: 32.5 - 39 GHz chirped pulse microwave spectrometer: AWG is an arbitrary waveform generator, PLDRO is a phase locked dielectric resonator oscillator, M1 is a broadband mixer, IS is an isolator, F1 is a filter, X4 is a frequency quadrupler, X2 is a frequency doubler, H1 and H2 are horn antennas, M2 is a broadband mixer, X3 is a frequency quadrupler, and F3 is a filter. The operation of this spectrometer is discussed in the text.

## 5.2 32.5 - 39 GHz spectrometer

In order to get acquainted with the design and operation of CPMW spectrometers, Barratt Park and Vladimir Petrović visited Professor Brooks Pate's lab at University of Virginia in August 2007. During the visit, a CPMW spectrometer, operating in the frequency range of 32.5 - 39 GHz was set up and tested. A schematic of this spectrometer is shown in Fig. 5.3.

The arbitrary waveform generator (Tektronix AWG7102), operating at 20 Gigasamples/s, produced an output with a linear frequency sweep in the range of 127-1786 MHz. In a 4-12 GHz broadband mixer M1 (Miteq NM0412LW2) the output of the AWG was mixed with the output of a phase-locked dielectric resonator oscillator at 9.9 GHz (PLDRO, Miteq PLDRO-

010-09900-15P). After passing through a 6-18 GHz circulator C (Ditom DMCB018), which prevents reflections from the components downstream from going back into the mixer M1, the radiation passed through the band pass filter F1 (Lorch 3CF7 99001200 S, 9.9 GHz center frequency) which transmits the lower frequency side band. After the filter, the frequency content of the pulse was 8.114-9.773 GHz. This radiation was then amplified in an amplifier, A, (Miteq AFS4-06001200-12-10P-4), with 30 dB gain, to the level of 10 dBm. The pulse was subsequently up-converted in an active frequency quadrupler X4 (Phase One SX40-420). The output was at 32.456-39.092 GHz after this component. A high pass filter F2 (Microwave Circuits H26G4061, 26 GHz) removed the fundamental and lower harmonics. Finally, the microwave radiation in the desired frequency range, and power  $\approx 20$  dBm, was coupled into free space using a 24 dB gain horn (Pasternack Enterprises WR-28-PE9850-20-72875). The microwave pulse, propagating in free space, irradiated the sample. No lenses were used in this experiment. The supersonic molecular beam of the sample was produced using a pulsed solenoid valve (General Valve Series 9). In the experiments performed during the visit to University of Virginia, no skimmers were used, and microwave excitation occurred approximately one inch downstream from the pulsed valve. The microwave beam propagated perpendicularly to the direction of the molecular beam.

The transmitted radiation was collected, together with the free induction decay from the sample, using a 20 dB gain horn antenna. Both emitting and receiving horns were located inside the vacuum chamber, and microwave radiation was coupled into the chamber using microwave feedthroughs (Pasternack Enterprises, part PE9184). The collected microwave radiation was down-converted so that it could be detected directly by a fast oscilloscope. The signal was down-converted by mixing the collected chirped microwave pulse with a local oscillator in a broadband mixer M4 (Miteq TB0440LW1). The local oscillator radiation at fixed frequency was produced by multiplying by three the frequency of the output of the same PLDRO used in the generation arm at 9.9 GHz. This arm of the 9.9 GHz PLDRO was split off using a Wilkinson power divider (Narda 4326.2). Frequency multiplication by three



was performed in an X3 multiplier (Phase One Microwave SX31-320). Subsequently, lower harmonics were removed by the filter F3 (same specifications as F2).

The down-converted signal in the 2.756-9.392 GHz range was then amplified using a 0-12 GHz low-noise amplifier (LNA, Miteq AFS42-01001200-22-10P-42), before being detected using a 12 GHz oscilloscope (Tektronix TDS6124C), with an 8 bit digitizer, and operating at 40 Gigasamples/s. In order to be able to phase-coherently average the detected waveforms in the time domain, the AWG, the PLDRO, and the oscilloscope were locked to a 10 MHz rubidium clock (Stanford Research Systems FS725). The heat generated by all of the microwave components was removed from all active components by home-built water-cooled heat sinks.

The operation of the spectrometer was tested by recording ground state rotational transitions in several small molecules. First, a  $J' = 3 \leftarrow J'' = 2$  transition at 34.489 GHz was recorded in OCS (0.1% OCS, carrier gas was 80 % Ne, 20 % He). OCS has a dipole moment of  $\approx 0.7$  D, which makes the observation of its ground state rotational transitions relatively easy. Two different 1  $\mu$ s long chirped pulses, spanning 10 and 40 MHz, centered around 36.489 GHz were attempted. Figure 5.4 shows the observed transition with the 10 MHz sweep. When the detection conditions were optimized, a real-time (single-shot) signal corresponding to this transition could be observed on screen of the oscilloscope. The ability to observe a real-time signal was of enormous help in enabling optimization of the excitation and detection conditions.

In order to test the resolving power and the dynamic range of the spectrometer, and to optimize the sweep rate, ground state rotational spectra of two other small molecules were recorded in the same frequency region, 32.5-39 GHz. The other two molecules were trifluoropropyne and acetone with dipole moments 2.3 D and 2.6 D, respectively. Both molecules have more than one transition in this frequency range. Figure 5.5 shows the observed K-structure of  $J' = 5 \leftarrow J'' = 4$  and  $J' = 6 \leftarrow J'' = 5$  transitions in trifluoropropyne. The  $J' = 6 \leftarrow J'' = 5$  line of trifluoropropyne was used to measure the dependence of the signal

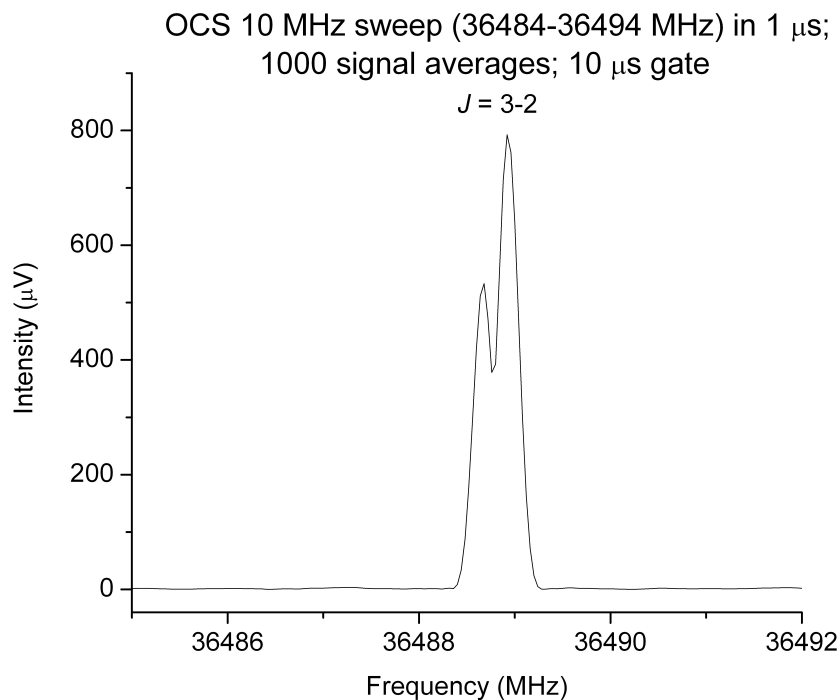


Figure 5.4:  $J = 3 \leftarrow J = 2$  transition in OCS, recorded with a 10 MHz sweep in 1  $\mu\text{s}$ , with 1000 signal averages.

intensity on the sweep rate, see Fig 5.6. The large dipole moment makes trifluoropropyne a good choice of a molecule for optimization of the sweep rate, see Fig. 5.6.

Additionally, the full capability of the CPMW spectrometer to measure relative intensities over a wide dynamic range can be illustrated in the case of acetone. This molecule has several transitions in the frequency range of 30 - 38 GHz, as shown in Figure 5.7. This spectrum was recorded with 10 000 averages, which enabled detection of relatively weak features.

Testing the 32.5 - 39 GHz spectrometer with OCS, trifluoropropyne, and acetone provided an opportunity to examine possible improvements in the spectrometer design. The sensitivity of the coupling of the microwave radiation between the horn antennas and free space, pointed to the necessity of having better control over the locations and tilts of the horns. It was also observed that coupling was improved when both the receiving and emitting horns were of the same type, with the same gain. In addition, it was observed that cables, especially the ones used outside their specified frequency range, contribute to transmission losses. All of

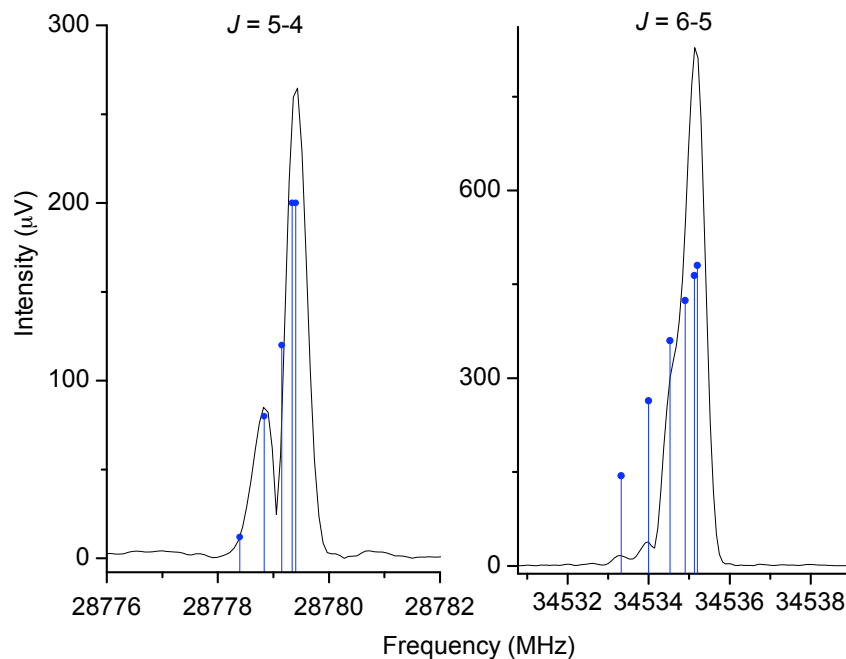


Figure 5.5:  $J = 5 \leftarrow J = 4$  (left) and  $J = 6 \leftarrow J = 5$  (right) transitions in trifluoropropyne, observed with a 6.6 GHz sweep in  $1 \mu\text{s}$ , averaged over 1000 signal pulses.

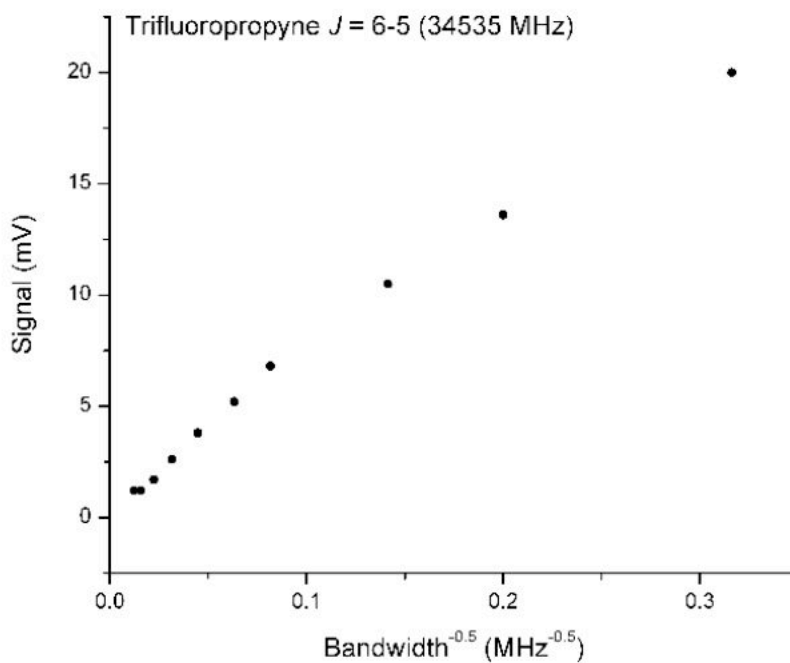


Figure 5.6: Dependence of the CPMW signal intensity on the sweep rate, measured on the  $J = 6 \leftarrow J = 5$  transition in trifluoropropyne at 34.535 GHz.

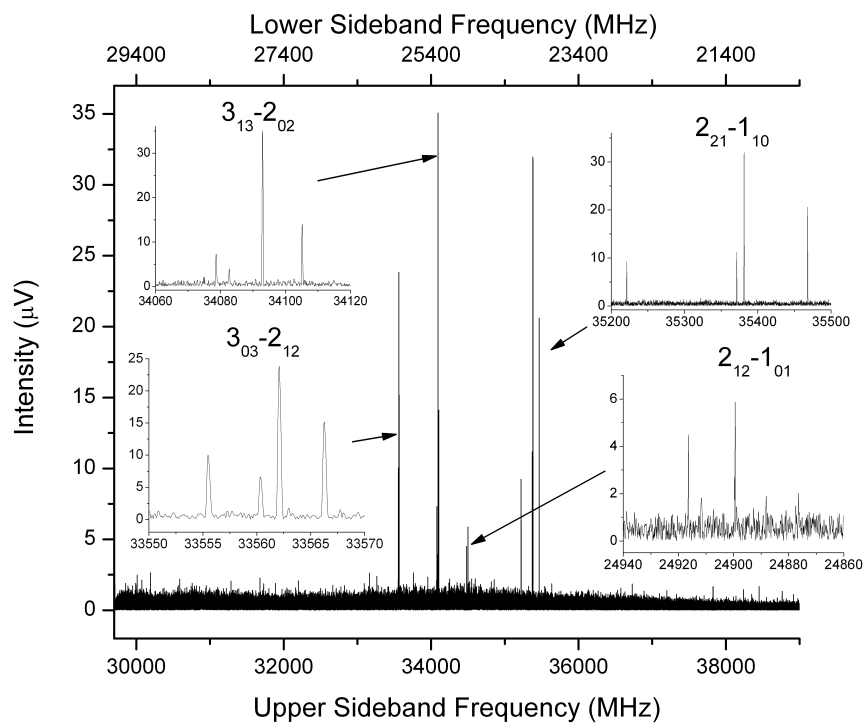


Figure 5.7: 6.6 GHz acetone sweep in  $1 \mu\text{s}$ , averaged over 10000 pulses. Upper and lower sideband frequencies of the downconverted signal are given at the bottom and top of the Figure, respectively.

these observations were taken into account when the next generation of the spectrometer, operating in the range of 69.6 - 84 GHz, was designed and assembled in our lab at MIT.

### 5.3 69.6 - 84 GHz spectrometer

A CPMW spectrometer, operating in the frequency range approximately 69.6 - 84 GHz, has been designed and built in our lab, based on the Pate group CPMW spectrometer design. Justin Neill from Pate group visited in April 2008 to help set up the first generation CPMW spectrometer in our group. The design, testing, and developments to the 69.6 - 84 GHz CPMW Rydberg-Rydberg spectrometer, result from a joint effort of Vladimir Petrović, Barratt Park, Dr. Kirill Kuyanov, Anthony Colombo, and Yan Zhou. A schematic of our spectrometer is shown in Fig. 5.8. A 4.2 Giga-samples/s arbitrary waveform generator, AWG, (Tektronix AWG 710B) produces an output between DC and 2 GHz. The output of AWG is mixed with a fixed frequency of 10.7 GHz, produced by phase locked dielectric resonator oscillator, PLDRO1, (Miteq PLDRO-010-10700-3-8P). The two frequencies are mixed in a broadband mixer M1 (Miteq DM0412LW2). An 8-16 GHz circulator C1 (Hitachi R3113110) prevents reflections from filter F1 from returning to the mixer M1. The pulse is then amplified using an active amplifier A1 (Armatek MH 978141). A band-pass filter (8.7 - 10.5 GHz, Spectrum Microwave C9680-1951-1355) then filters out the higher-frequency band, transmitting a pulse with the frequency content 8.7 - 10.5 GHz. The frequency of this pulse is up-converted twice, first in an active broadband frequency quadrupler X4 (Phase one SX-40-420), and then an active broadband frequency doubler X2 (Phase One SG12-2515). Following the two up-conversion steps, the frequency of the pulse is between 69.6 GHz and 84 GHz. An attenuator T1 with the attenuation range 0-60 dB (Flann Microwave Instruments, Model 2711) is placed after the frequency quadrupler, in order to be able to reduce the microwave field amplitude to the level required for the study of Rydberg states. Microwave radiation is then emitted into free space using a 24 dB gain horn antenna H1 (Pasternack Enterprises WR-28-PE9850-20-72875).

In order to ensure the optimal transmission of the microwave beam between the emitting and receiving horns, H1 and H2, respectively, and focus the microwave beam at the place where it intersects the molecular beam, the alignment of the microwave optics was

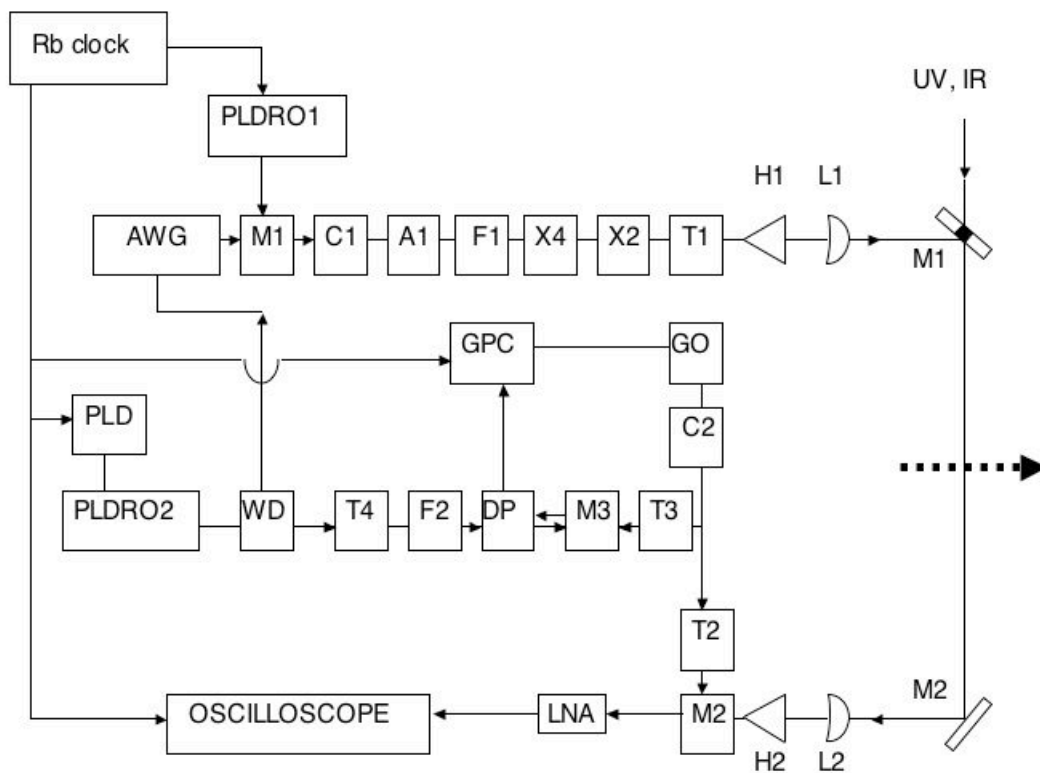


Figure 5.8: 69.6 - 84 GHz chirped pulse microwave spectrometer: AWG is an arbitrary waveform generator, PLD, PLDRO 1 and 2 are phase locked dielectric resonator oscillators, M 1-3 are broadband mixers, C 1 and 2 are isolators, A1 is an amplifier, F 1 and 2 are filters, X4 is a frequency quadrupler, X2 is a frequency doubler, T 1-4 are attenuators, H1 and 2 are horn antennas, L1 and 2 are teflon lenses, M 1 and 2 are mirrors, GO is a Gunn oscillator, GPC is a Gunn phase control unit, DP is a diplexer, LNA is a low noise amplifier, and WD is a Wilkinson power divider. The operation of this spectrometer is discussed in the text.

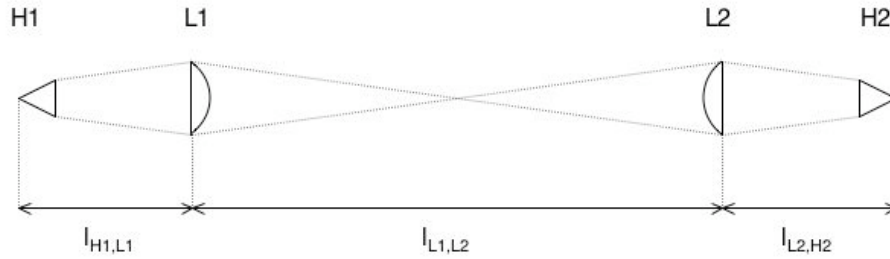


Figure 5.9: In order to optimize the free-space microwave transmission between horns H1 and H2, the optimum distances,  $l_{H1,L1}$ ,  $l_{L1,L2}$ , and  $l_{L2,H2}$ , have been determined in a table-top experiment. A focus located between H1 and H2 is achieved using two tefflon lenses L1 and L2.

done in several stages. Since the microwave beam emitted from a horn antenna is not a Gaussian beam, the optimal distances between the microwave components were determined empirically, in several steps. The optimization involved determining the optimal distances  $l_{H1,L1}$ ,  $l_{L1,L2}$ , and  $l_{L2,H2}$ , in a table-top experiment, see Fig. 5.9. These are, respectively, the distances between the emitting horn, H1, and the first tefflon lens, L1, between the first and second tefflon lens, L1 and L2, and between the second tefflon lens, L2, and the receiving horn, H2. Both tefflon lenses were home built, and had diameter of 219 mm and focal length of 300 mm. The distances  $l_{H1,L1}$ ,  $l_{L1,L2}$ , and  $l_{L2,H2}$  were optimized so that the transmission of the microwave radiation between H1 and H2 was maximized in each step. Subsequently we measured the approximate size of the microwave beam at its focus. This was accomplished by locating an iris at the focus, and closing it until a change in the transmitted signal intensity was observed. The spot size was determined to be approximately 1 square inch. The loss between the horns was  $< 10\%$ .

In the next step, the transmission of the microwave beam through the molecular beam apparatus was optimized. In order to get the microwave beam to propagate colinearly with the two laser beams, we mount a home built aluminum mirror M1 (34.5 cm  $\times$  23 cm) at  $45^\circ$  to the microwave beam. M1 reflects the microwave beam, but it has a  $2 \times 0.5$ " diameter hole in the center, milled at  $45^\circ$  angle to the surface, through which the two laser pulses propagate.



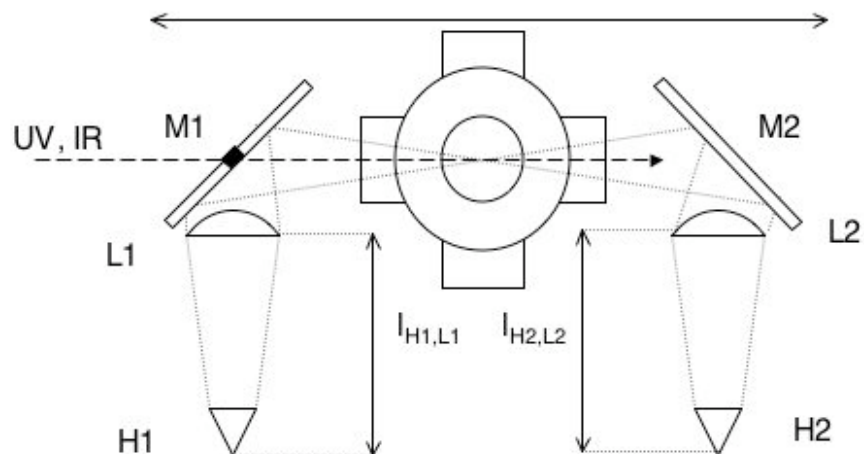


Figure 5.10: Arrangement of the microwave elements used to focus the microwave beam at the spot where it intersects the molecular beam. An aluminum mirror M1, with a  $2 \times 0.5$ " diameter hole in the center, milled at  $45^\circ$  to the surface, is used to combine the microwave beam with the two laser pulses. Labels of the microwave components, and distances between them, are the same as in Fig. 5.9.

Another aluminum mirror, M2, with the same specifications as M1, but without the hole in the center, was placed behind the molecular beam chamber, in a symmetric arrangement, see Fig. 5.10. M2 is followed by another teflon lens, L2. The distances between H1 and L1, L1 and L2, L2 and H2, are the same as determined in the table-top experiment. The focus of the microwave beam is at the position where the microwave beam intersects the molecular beam. When the beam propagates through the chamber, the transmission between H1 and H2 was  $\approx 30\%$  of the table-top value ( $> 90\%$ ).

After propagation through the chamber, the microwave beam is focused by L2 onto the detecting horn H2. The radiation collected in H2 is then down-converted by mixing with a local oscillator at 79.21 GHz (this value can be changed by selecting different settings in the Gunn Oscillator). An attempt was made to use the up-converted output of a Synthesized Signal Generator (2-18 GHz, Hewlett-Packard 8673E), as the local oscillator. Due to the inability to achieve satisfactory phase stability of the synthesizer output, necessary for averaging the microwave waveforms in the time domain, this method was abandoned. In our

current experiment, the local oscillator was provided by a 73-106 GHz Gunn oscillator, GO, (J. E. Carlstrom H129, 80 mW), which produces radiation at the 20<sup>th</sup> harmonic of the input radiation. The input radiation was provided by a 3.96 GHz phase locked dielectric resonant oscillator, PLDRO2, (Microwave Dynamics PLO-2000-03.96). PLDRO2 requires a 90 MHz input, provided by 90 MHz phase locked dielectric oscillator, PLD, (Miteq PLD-10-90-15P). A part of the output of the 3.96 PLDRO2 is split off using a Wilkinson power divider, WD (Anaren 41130), to provide an external clock for the AWG. The other arm of the PLDRO2 output was attenuated with an attenuator T4 (Weinschel Engineering 1-6), and sent through a high pass filter F2 (800 MHz, Mini-Circuits SHP-800) to block the 90 MHz input.

Production of the desired frequency output by the Gunn oscillator, GO, involves several microwave components. A two-port subharmonic downconverter M3 (Pacific Millimeter Products WM) is used to mix the 3.96 GHz input with a subharmonic of the output of the GO, attenuated using an attenuator T3 (Hitachi W 1502). The difference frequency, produced by the mixer M3, is split off using a diplexer DP (Omni Spectra, part number not fully legible). This difference signal, at 10 MHz, is sent to a Gunn phase-lock controller, GPC, which ensures that this 10 MHz difference frequency is locked to the reference at 10 MHz. This reference was provided by the Rubidium clock. The phase lock controller provides the control voltage to the GO. The harmonic is selected by tuning the GO cavity dimensions. The GO is followed by an circulator C2 (Hughes Aircraft Co. 4511GH-1000), which prevents the reflections from the attenuators returning to the GO. A part of the GO output is split off by a directional coupler and sent to T3.

Before a portion of the GO output was sent to the balanced mixer, M2 (Ducommun Technologies FDB-12-01), to be subtracted from the frequency of the microwave radiation collected by H2, it is attenuated to 13 dBm (the power requirement for the LO in the mixer M2) by the attenuator T2 (Hitachi W 0513). The down-converted chirped microwave signal is then sent to a low noise IF preamplifier, LNA (Miteq AMF-5F-0800-1800-14-10P), and detected by a 12 GHz oscilloscope (Tektronix TDS6124C). The heat dissipated by the active

microwave elements was removed either using water-cooled, or fan-cooled, heat sinks.

In order to ensure phase stability between the successive microwave pulses, the PLDRO1, PLD, GPC, and the oscilloscope are locked to a 10 MHz Rb clock (Stanford Research Systems FS725). The triggering sequence starts with the AWG. The AWG produces output at 200 Hz, and because of the upper limit on the number of points in a waveform produced by the AWG, it is not possible to produce 20 Hz output directly with the current typesetting density (which would correspond to a 50 ms long waveform). A marker channel on the AWG provides a trigger to a Delay Generator, DG (Stanford Research Systems, DG 535), which is used in the frequency down-conversion mode. The DG divides the repetition rate of the input trigger, and provides a signal at  $\frac{1}{10}^{th}$  of the input repetition rate. This trigger, with 20 Hz repetition rate, triggers the 12 GHz oscilloscope. However, since the phase stability of the AWG marker channel is superior to that of the signal from the DG, the trigger from the DG is used to indicate to the oscilloscope that it should wait for the trigger from the marker channel from the AWG. In this arrangement, the oscilloscope is effectively triggered by the AWG marker channel, but only when the additional DG trigger immediately precedes the AWG marker channel pulse (effectively triggering the oscilloscope by every tenth AWG trigger pulse).

The operation of the spectrometer was initially tested by recording a  $J' = 6 \leftarrow J'' = 5$  transition in OCS. After optimizing the excitation conditions, principally the overlap of the microwave beam with the molecular beam, on OCS, the spectrometer was used to study Rydberg-Rydberg transitions.

## 5.4 Rydberg-Rydberg transitions in Ca

Molecular Rydberg states are the main target of study of our variant of CPMW spectroscopy. However, our initial attempts to set up a CPMW spectrometer for studying Rydberg-Rydberg transitions employed an atomic sample. This choice was made due to our ability to produce atomic Rydberg states with higher number density and favorable partition function factor in our ablation-based molecular beam apparatus. In our double resonance molecular beam apparatus, normally used for studying Rydberg states of CaF, gas-phase Ca is formed as a side product. Modifications required for switching to production of atomic Ca Rydberg states were straightforward. There are several transitions with frequency 69 - 84 GHz among same- $n^*$  or adjacent- $n^*$  Rydberg states of Ca in the region of moderately high  $n^*$  ( $n^* = 30-40$ ).

The launch state for the microwave experiment was populated in two steps. First, a laser pulse (pump) excited Ca to an intermediate state,  $4s5p\ ^1P(J = 1)$ . Subsequently, another laser pulse (probe) excited Ca to the launch Rydberg state. In order to identify the spectral feature in the double resonance spectrum that corresponds to the launch state, we perform a probe laser frequency calibration. It is inconvenient to use iodine as a calibration standard in this frequency region, as the required  $I_2$  cell temperature is above the limit for our  $I_2$  cell, thus we performed an internal calibration. In a typical double resonance spectrum of Ca in this region, a repeated pattern can usually be observed, see Fig. 5.11. The pattern consists of two stronger lines and several weaker ones. Since the intermediate state is  $4s5p\ ^1P(J = 1)$ , we assume that the two stronger lines are  $4s(n + 1)s\ ^1S(J = 0)$  and  $4snd\ ^1D(J = 2)$ . At lower  $n^*$ , based on NIST tables [14], the  $4s(n + 1)s\ ^1S(J = 0)$  line always appears at somewhat lower energy than the  $4snd\ ^1D(J = 2)$  line. We assumed that this ordering is preserved at higher  $n^*$ , where the values for the  $4s(n + 1)s\ ^1S(J = 0)$  state energies are not reported in [14]. Using this assumption, we identify the higher-energy component in each pair of observed features as the  $4snd\ ^1D(J = 2)$  state. The energy difference scales as  $n^{-3}$ , and we can use the energy intervals to identify the  $n$  value for  $4snd\ ^1D(J = 2)$  states. The

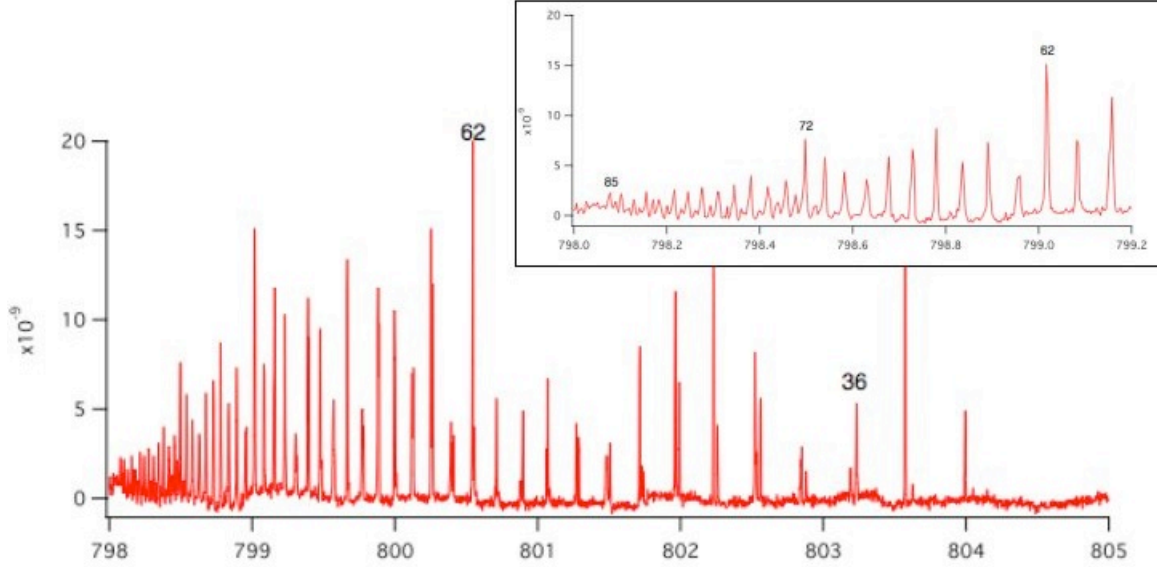


Figure 5.11: Double resonance spectrum of Rydberg states of Ca in the region  $84 \geq n^* \geq 33$ , after compensation of stray homogeneous fields and minimization of inhomogeneous fields in the excitation region. The inset shows the region of  $84 \geq n^* \geq 60$ .

energy intervals between the members of the thus identified  $d$  series are then read off from the spectrum, and compared to the published energy intervals among  $4snd\ ^1D(J=2)$  states [14]. Upon completion of this procedure, the energy differences between the other spectral features observed in the spectrum are compared to the values published in [4]. Observed agreement, within the uncertainty of our laser calibration, confirms our assignments.

Initially, an experiment was attempted to study the  $4s39d\ ^1D(J=2) \leftarrow 4s39p\ ^1P(J=1)$  transition. This transition appears at 77.047 GHz according to the NIST database [14], or at 81.102 GHz according to the measurements by Gentile et al. [4]. At the time when the experiment was first performed, we were unaware of this discrepancy, and we used the value published in [14] to guide our search. The energy levels involved in the experiment are shown in Fig. 5.12 a. When, after numerous attempts under different experimental conditions, the expected FID signal was still not observed, it was suspected that the large transition dipole moments at  $n^* = 39$  make the  $4s39p\ ^1P(J=1)$  and  $4s39d\ ^1D(J=2)$  states more susceptible to external inhomogeneous and uncompensated homogeneous electric fields. We decided to attempt the experiment at lower  $n^*$ , where the achieved level of control over the experimental

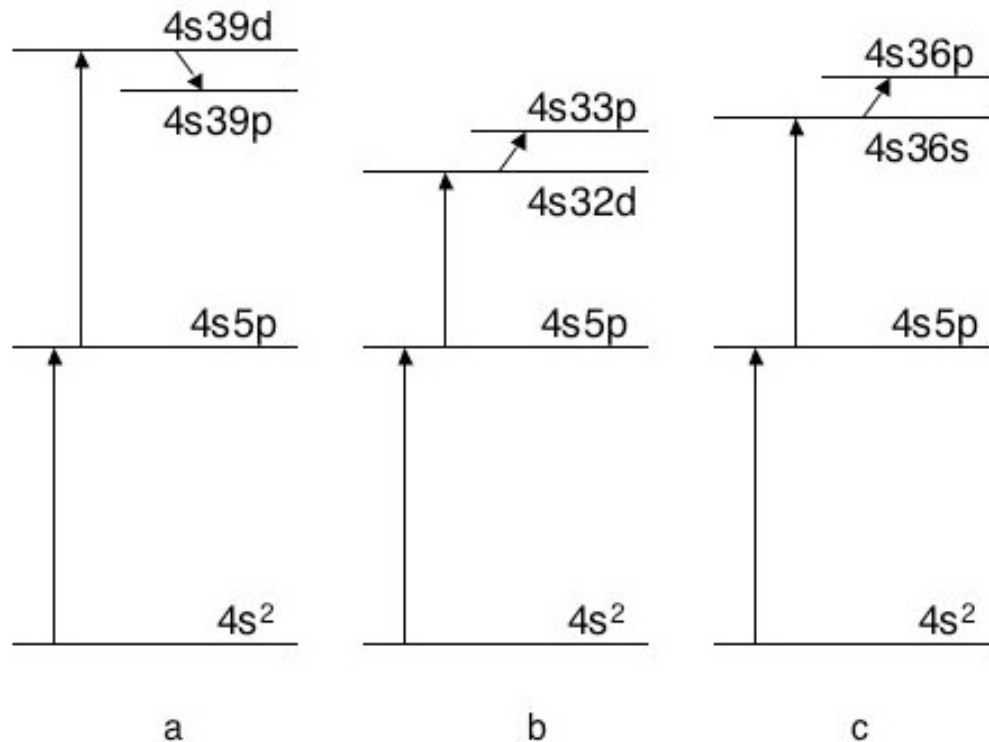


Figure 5.12: Energy level schemes for the three optical-optical-microwave experiments attempted on atomic Ca. The same intermediate state,  $4s5p^1P(J = 1)$  was used in all three cases.

conditions would be more likely to be sufficient. However, in retrospect, since none of our chirped pulses with which excitation was attempted contained the frequency reported in [4], it is likely that the transition was not observed due to absence of resonance, as we were misled by the value reported in [14].

To fulfill the lower- $n^*$  requirement, we made an attempt to observe the  $4s33p^1P(J = 1) \leftarrow 4s32d^1D(J = 2)$  transition, see Fig. 5.12 b. At the time when the experiment was attempted, we were unaware of the discrepancy between the NIST value (75.248 GHz) [14] and the value reported in [4] (70.321 GHz) for the frequency of this transition. In the experiment, the transition was expected at 75.248 GHz. Although we attempted to use numerous chirped microwave pulses covering different frequency regions around 75 GHz,

none of them included the frequency reported in [4]. In retrospect, that is probably the explanation for our inability to observe the  $4s33p\ ^1P(J = 1) \leftarrow 4s32d\ ^1D(J = 2)$  resonance. We have, however, in this experiment, successfully observed the effect of the microwave radiation on the ionization of Ca Rydberg states. The observed effect can be attributed to either non-resonant, or multiphoton, ionization caused by the microwave radiation.

The voltage of the extraction pulse,  $E_I$ , which first ionizes the excited Ca atoms, and then extracts ions towards the MCP detector, was adjusted in such a way that in the absence of the microwave radiation the  $4s33p\ ^1P(J = 1)$  state, but not the  $4s32d\ ^1D(J = 2)$  state, is ionized by  $E_I$ , see Fig. 5.13. However, if the microwave radiation excites the Ca atom above the cutoff for ionization by  $E_I$ , then an increase in the number of ions will be detected in the presence of that microwave radiation. When the microwave field is sufficiently strong, the likelihood of non-resonant and multi-photon ionization increases. The fact that an effect of a microwave pulse with frequency content 73.30 - 73.90 GHz was observed in both  $4s32d\ ^1D(J = 2)$  and  $4s33s\ ^1S(J = 0)$  states, see the lowest trace in Fig. 5.13, points toward non-resonant and multiphoton processes as the explanation of the effect of the microwave radiation on ionization in this case. The absence of an observation of resonance in this experiment was probably due to the actual transition frequency likely being outside the frequency regions of the chirped microwave pulses that were used in the experiment.

Eventually an experiment was attempted to observe the  $4s36p\ ^1P(J = 1) \leftarrow 4s36s\ ^1S(J = 0)$  transition. The energy level diagram for this experiment is shown in Fig. 5.12 c. Similarly to the method described for the  $4s33p\ ^1P(J = 1) \leftarrow 4s32d\ ^1D(J = 2)$  transition, we set up a microwave ionization experiment for  $4s36p\ ^1P(J = 1) \leftarrow 4s36s\ ^1S(J = 0)$  transition. The voltage of the extraction pulse is adjusted in such a way that ionization from  $4s36s\ ^1S(J = 0)$  does not occur in the absence of the microwave radiation, but it does occur from  $4s36p\ ^1P(J = 1)$ . In this case, we used the value of 76.929 GHz for the transition frequency, reported in [4], to guide our search. Upon observation of an ionization signal contingent upon the presence of a microwave pulse covering the 74 - 77.1GHz frequency

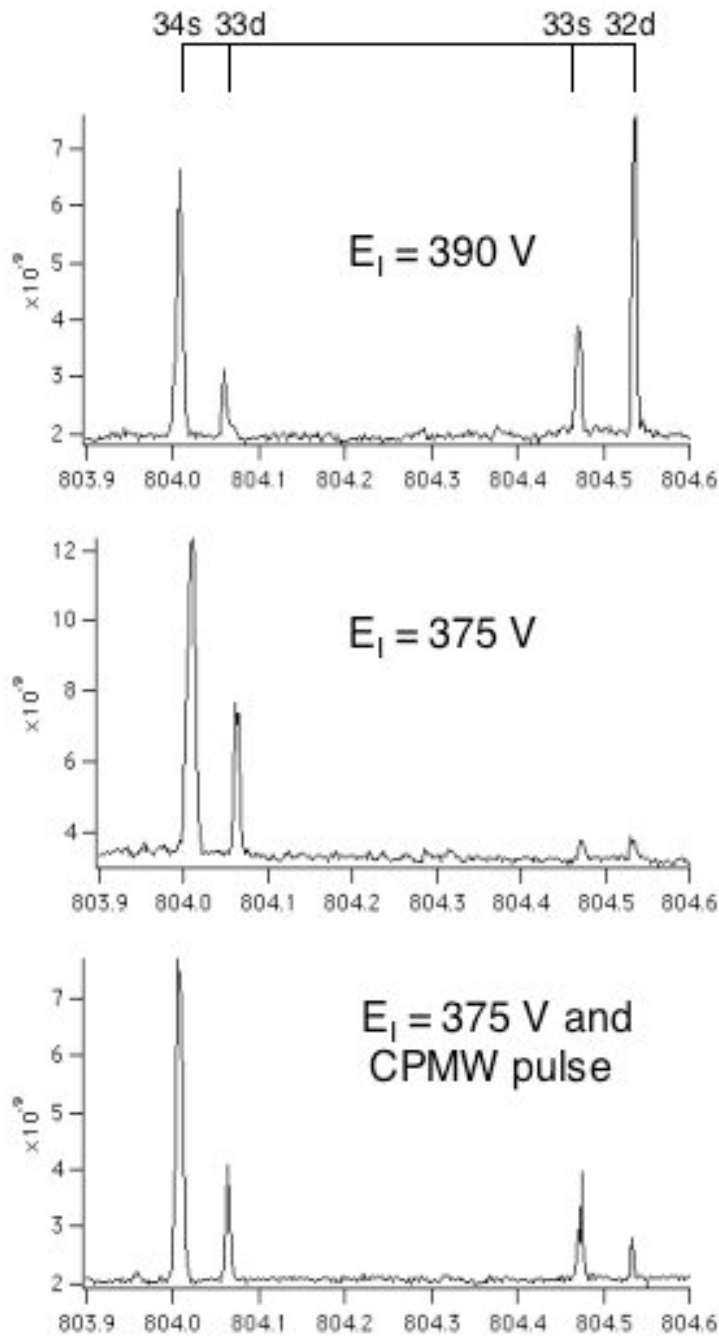


Figure 5.13: Microwave-assisted ionization: when the ionizing electric field strength is 390 V/cm (uppermost trace), it is strong enough to ionize both  $4s32d \ ^1D(J = 2)$  and  $4s33s \ ^1S(J = 0)$  states. However, when the field is decreased to 375 V/cm, neither of these two states are ionized (middle trace), but  $4s33p \ ^1P(J = 1)$  (not a bright state in this spectrum) is ionized. In the presence of a microwave pulse ionization, ionization happens from both of these states (lowermost trace), probably due to non-resonant and multiphoton processes.



region, an experiment was performed to determine whether this signal was due to the  $4s36p$   $^1P(J = 1) \leftarrow 4s36s$   $^1S(J = 0)$  resonance, or some non-resonant, or multiphoton-resonant, process. We divided this frequency region into three parts, and covered them with three separate chirped pulses. A non-resonant ionization signal due to the microwave radiation should be present in all three frequency regions. In fact, when the microwave radiation is strong enough, an ionization signal is observed in all three regions. However, when the microwave radiation is sufficiently attenuated, the ionization signal persists only in one of the three frequency windows. The procedure of dividing the frequency window into three is then repeated, to narrow down the frequency of the resonant transition. Each time the frequency window is narrowed, the sweep rate decreases, and the amplitude of the microwave field had to be attenuated, so that predominantly only the resonant transition is observed. Our search for the frequency of the resonant transition was finally narrowed down to a frequency region 300 MHz wide. To check whether this resonant signal is in fact due to the  $4s36p$   $^1P(J = 1) \leftarrow 4s36s$   $^1S(J = 0)$  resonance, we change  $E_I$  while observing the ionization signal on this resonance. The fact that signal disappears after a small decrease in  $E_I$  points to the conclusion that the transition occurs into a state that lies barely above the ionization cutoff. We therefore concluded that the transition is due to the  $4s36p$   $^1P(J = 1) \leftarrow 4s36s$   $^1S(J = 0)$  resonance.

When the frequency of the resonant transition was narrowed down to 76.78 - 77.08 MHz region, we set up an experiment in which the microwave frequency was scanned in order to locate the resonance frequency more precisely. Such an experiment enables measurement of the transition linewidth. In order to run the experiment in a scanning mode, we used a Synthesized Signal Generator (2-18 GHz, Hewlett-Packard 8673E), instead of the ARB+PLDRO1, to provide the input frequency for up-conversion in the region 9-10 GHz. This frequency was fed into X4, followed by X2, to provide output in the frequency range around 76.929 GHz. Initially, the frequency of the microwave radiation was tuned by hand, while observing the ionization signal. Finding the resonance this way was fairly uncompli-

cated, as the transition was significantly broadened by the strong microwave pulse. A scan over the observed line was then performed under different experimental conditions. The amplitude of the microwave field, as well as the power of the probe laser were varied in order to test for the effects of the excitation conditions on the linewidth. However, the linewidth never became smaller than 65 MHz in these experiments. Several factors which contribute to this broadening will be discussed in the next section.

In the experiment in which the synthesizer was used, the microwave radiation was continuously present. In order to avoid broadening due to the presence of the microwave field at the time of laser excitation, we attempted an experiment in which a pulsed microwave field was used for ionization. Pulsed microwave radiation was produced by mixing a pulsed output from the AWG with the Synthesized Signal Generator output, and then up-converting the frequency with X4 and X2, as described above. Even though only the AWG output is pulsed in this case, both inputs are required for the mixer to produce an output. The microwave pulse was delayed 500 ns with respect to the laser pulse. However, in this experiment the linewidth was still larger than expected, and was never smaller than 25 MHz.

In both experiments, the signal to noise ratio was low. This results partly from the inherent instability of the production of the Rydberg states by double resonance excitation, especially when ablation is the first step of the process. In addition, the frequency instabilities of the microwave synthesizer power output affect both the signal to noise ratio and our ability to correlate the linewidth with the experimental conditions.

## 5.5 Rydberg-Rydberg transitions

Large transition dipole moments ( $\propto n^2$ ), large classical radii ( $\propto n^2$ ), and large polarizabilities ( $\propto n^7$ ) are among the factors that make a cloud of atoms or molecules excited into Rydberg states of even moderately high  $n^*$  (30-40) an entirely different class of sample for study than an ensemble of weak 1 D absorbers. The characteristics which make Rydberg states interesting also make them exquisitely sensitive to the experimental conditions, and the experimental conditions need to be carefully characterized.

While the exceptionally large dipole moments for transitions among Rydberg states result in large transition probabilities, they also render the states involved in transitions susceptible to interaction with exceptionally weak external electric fields (their sensitivity to external magnetic fields is modest). Weak external electric fields can cause frequency shifts, line broadening, and affect the lifetimes (through field-induced mixing with states of different values of the  $\ell$  quantum number, and through the  $\ell$ -dependence of the lifetimes). The relative intensities in a spectrum of moderately high  $n^*$  (30-40) can be significantly altered in the presence of external homogeneous and, especially, inhomogeneous fields, see [5] and references therein. In our experimental apparatus, even when the external electric field between the plates that define the excitation region is nominally zero, there are leakage fields from voltage on other plates that are an essential part of the ion-optics. The discrepancy between the nominal and the actual values of the field can be partially compensated, but even if that is possible, an inhomogeneous field remains. An inhomogeneous electric field can also be a result of the absorber being exposed to a cloud of atoms or molecules excited into Rydberg states, and ions formed by multiphoton excitation at either the first or the second excitation step [5, 6].

The extent to which the expected microwave transition frequency, intensity, and linewidth will be altered with respect to the expected values depends on the excitation conditions, therefore the experimental conditions must be carefully characterized. By recording the frequency of a  $4s36p \ ^1P(J=1) \leftarrow 4s36s \ ^1S(J=0)$  Rydberg-Rydberg transition at several

nominal values of the external field, we found an approximate value,  $E_{min}$ , for the externally applied field at which the microwave transition frequency has an extreme value with respect to changes of the external field, see Fig. 5.14. The value of  $E_{min}$  depends on the voltages on all of the ion-optics plates (in addition to the plates between which the excitation occurs) and has to be re-measured whenever any of these voltages are changed. In our apparatus, in addition to the two plates that define the excitation region, there is another plate 0.27 cm above, which is used for the spatial focusing of the ions ( $E_{SF}$ ). The potential on  $E_{SF}$  is usually different from that of the two plates that define the excitation region. The leakage from  $E_{SF}$  was responsible for the unexpectedly large linewidths, and it was not until the  $E_{SF}$  was set to the same potential as the two plates that define the excitation region that we observed linewidths reduced to 1 MHz, see Fig. 5.15.

The number density of the Rydberg absorbers, and the  $n^*$  principal quantum number in which the experiment is performed, determine whether the effect of dipole-dipole interactions on the dephasing times are relevant on the timescale of the experiment. Collective interactions that result in formation of a plasma from a dense cloud of atoms excited to high- $n^*$  Rydberg states have been described for number densities higher than ours and  $n^*$  higher than ours, see [15] and [16]. When an experiment is performed at  $10^9$  atoms/cm<sup>3</sup> (as we estimate for our excitation conditions), and in the  $n^* = 36$  region, the collective interactions are not relevant on a timescale of one  $\mu$ s.

In the experiment reported in [5], the inhomogeneities of the field due to the leakage field from the MCP, and the nonzero value of the pulsed extraction field to which the potential relaxes between pulses, were characterized and minimized. A resolution of 250 kHz was achieved. However, the authors reported an observation that some transitions, for example  $70p[5/2](J = 2) \leftarrow 64s[3/2](J = 1)$ , still had unexpectedly large linewidths of 8 MHz. These linewidths could not be attributed to the lifetimes of field-free Rydberg states. Rather, they were explained by an inhomogeneous distribution of electric fields in the photoexcitation region, after analyzing several alternative explanations: 1) multiphoton absorption, 2) strong

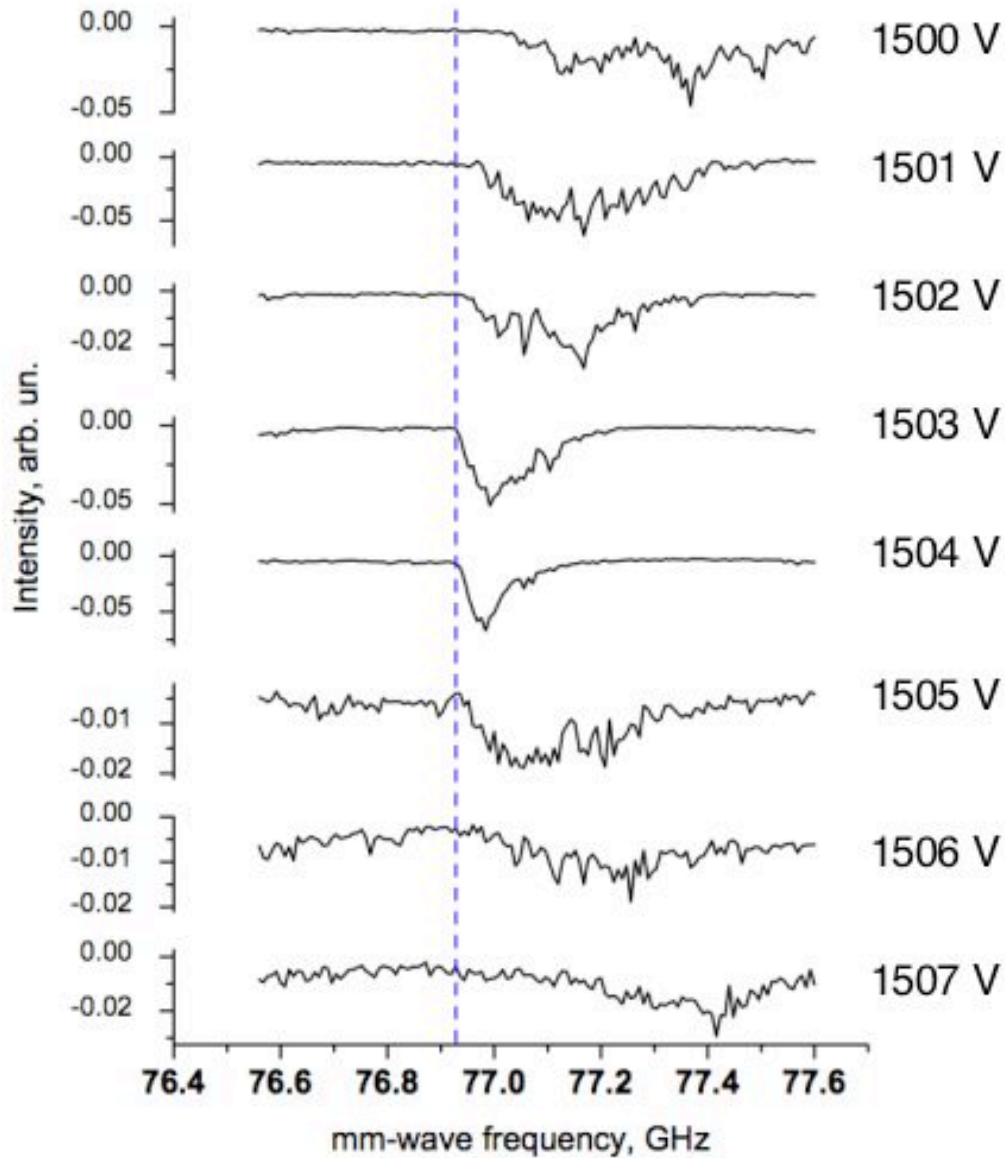


Figure 5.14: The line position and linewidth of the  $4s36p\ ^1P(J = 1) \leftarrow 4s36s\ ^1S(J = 0)$  Rydberg-Rydberg transition dependence on the nominal voltage of one of the plates between which the excitation occurs. The voltage on the other plate is nominally 1500 V. These spectra are recorded prior to balancing out of the stray homogeneous fields and minimization of the inhomogeneous fields between the plates.

Stark shifts of the  $70p[5/2](J = 2)$  state, and 3) dipole-dipole interactions. We attribute the inhomogeneity in the photoexcitation region to the presence of ions. The observation that the lineshape of the transition is asymmetric, with a shoulder on the side toward which the state is shifted by the external field, supports the explanation that involves ions. In this case, there is a distribution of electric field strengths to which absorbers are exposed. A small number of absorbers exposed to a very strong field accounts for the shoulder in the asymmetric lineshape. The observation that the linewidth in the  $4s36p\ ^1P(J = 1) \leftarrow 4s36s\ ^1S(J = 0)$  transition was asymmetric in our experiment as well, points to field inhomogeneity, resulting from the cloud of ions formed by multiphoton absorption of either laser pulse, as the most likely explanation for larger than expected linewidth.

Another significant difference between a typical CPMW experiment with 1 D absorbers, and one with kD absorbers is that the amplitudes of the microwave field required to drive Rydberg-Rydberg transitions will be significantly smaller. The typical output of H1 in our CPMW setup is 30 mW, and the MW pulse power has to be attenuated by several orders of magnitude. The usual interpretation of a CPMW experiment with 1 D absorbers relies on a perturbative approach described in [17], developed for interpretation of scanning Fourier-transform microwave spectroscopy experiments. A non-perturbative approach for propagating either THz or chirped-microwave pulses through a sample of Rydberg absorbers is described in the next chapter. However, if we directly integrate the Bloch equations, using a Mathematica program written by Barratt Park, to make an estimate of the required amplitude of the microwave field to drive a  $\frac{\pi}{2}$ -transition with a 5695.5 D dipole moment (for the  $4s36p\ ^1P(J = 1) \leftarrow 4s36s\ ^1S(J = 0)$  transition, using the constants given in [4] and the method for calculating the dipole moments among non-hydrogenic functions given in [18]), we get 0.346 V/m. If the exciting microwave field is much stronger than the value estimated here, non-resonant ionization, multiphoton processes, and adiabatic ionization become relevant. In addition, the transition linewidth appears to be significantly power broadened, see figure 5.15. Merkt and Schmutz [5] observe that for the  $71p[5/2](J = 2) \leftarrow 64s[3/2](J = 1)$

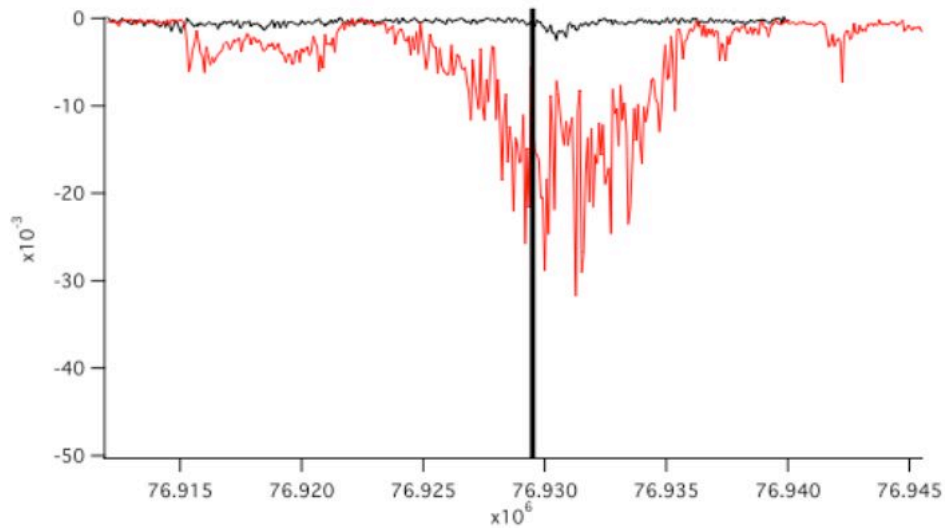


Figure 5.15:  $4s36p^1P(J = 1) \leftarrow 4s36s^1S(J = 0)$  transition in Ca with 60 dB attenuation after H1 (red line) and after a book has been inserted in the microwave beam in addition to 60 dB attenuation (black line). The transition frequency reported in [4] is indicated by a vertical line.

transition, attenuation is needed below the value of the microwave field power measurable by their power meter. In the absence of sufficient attenuation of the microwave beam, the transition was power broadened, although no significant transition frequency shifts were observed.

## 5.6 Conclusion

An optical-optical-microwave triple resonance transition has been demonstrated in order to observe the Ca atom  $4s36p\ ^1P(J=1) \leftarrow 4s36s\ ^1S(J=0)$  transition. The observed linewidth for this transition was 1 MHz, after compensating stray homogeneous and minimizing inhomogeneous external electric fields in our apparatus. Linewidth on the order of 1 MHz means that the lifetimes of the states involved in the transitions are long enough to enable collection of the free induction decay. A potential problem with observation of the FID in the current arrangement might be a much lower number density of the Rydberg absorbers than expected. A larger skimmer, allowing for larger absolute number of absorbers, but smaller number density may be the best path to take. At present, low signal to noise in our ionization detected optical-optical-microwave triple resonance experiment does not allow for a better characterization of the influence of the experimental conditions on the linewidth. This low SNR results, in part, from the frequency instability of the microwave synthesizer currently used in the experiment.

In addition, the FID signal is likely be affected by geometric effects. The sample size is defined by the volume of the intersection between the molecular beam and laser excitation beams. The diameter of this volume is comparable to the microwave wavelength emitted by the sample. It is necessary to model the divergence due to diffraction of the emission from such a sample, in order to know whether a modification to the detection arrangement, possibly by expanding the sample size, is necessary.

Ionization-detected optical-optical-microwave triple resonance provides a good way to optimize the excitation conditions in our experiment. Once the excitation conditions are optimized, and that is currently in progress, then the detection conditions will be optimized. Either of the two steps might require modifications to the currently used molecular beam apparatus.



## 5.7 Bibliography

- [1] Thomas F. Gallagher. *Rydberg Atoms*. Cambridge University Press, 1994.
- [2] U. Hollenstein, R. Seiler, H. Schmutz, M. Andrist, and F. Merkt. *J. Chem. Phys.*, 115:5461, 2001.
- [3] C. Fabre, S. Haroche, and P. Goy. *Phys. Rev. A*, 18:229, 1978.
- [4] T. R. Gentile, B. J. Hughey, D. Kleppner, and T. W. Ducas. *Phys. Rev. A*, 42:440, 1990.
- [5] F. Merkt and H. Schmutz. *J. Chem. Phys.*, 108:10033, 1998.
- [6] A. Osterwalder and F. Merkt. *Phys. Rev. Lett.*, 82:1831, 1999.
- [7] G. G. Brown, B. C. Dian, K. O. Douglass, S. M. Geyer, S. T. Shipman, and B. H. Pate. *Rev. Sci. Instrum.*, 79:053103, 2008.
- [8] J. C. McGurk, T. G. Schmalz, and W. H. Flygare. *J. Chem. Phys.*, 60:4181, 1974.
- [9] T. J. Balle, E. J. Campbell, M. R. Keenan, and W. H. Flygare. *J. Phys. Chem.*, 71:2723, 1979.
- [10] T. J. Balle, E. J. Campbell, M. R. Keenan, and W. H. Flygare. *J. Phys. Chem.*, 72:922, 1980.
- [11] T. J. Balle and W. H. Flygare. *Rev. Sci. Instrum.*, 52:33, 1981.
- [12] R. D. Suenram, J. U. Grabow, A. Zupan, and A. I. Leonov. *Rev. Sci. Instrum.*, 70:2127, 1999.
- [13] B. C. Dian, G. G. Brown, K. O. Douglas, and B. H. Pate. *Science*, 320:924, 2008.

- [14] NIST Atomic Spectra Database.
- [15] W. R. Anderson, M. P. Robinson, J. D. D. Martin, and T. F. Gallagher. *Phys. Rev. A*, 65:063404, 2002.
- [16] W. Li, P. J. Tanner, and T. F. Gallagher. *Phys. Rev. Lett.*, 94:173001, 2005.
- [17] J. C. McGurk, H. Mäder, R. T. Hofmann, T. G. Schmalz, T. G. Schmalz, and W. H. Flygare. *J. Chem. Phys.*, 61:3759, 1974.
- [18] A. R. Edmonds, J. Picart, N. Tran Minh, and R. Pullen. *J. Phys. B*, 12:2781, 1979.

# Chapter 6

## Calculated Pure Electronic spectra of $\ell$ -mixed Rydberg states

### 6.1 Prologue

The following chapter presents work which is still in progress at the time of the submission of this Thesis. Parts of the text presented here will be used in the manuscript by V. S. Petrović, Y. Zhou, S. L. Coy, and R. W. Field, currently in preparation.

## 6.2 Introduction

Electronic spectroscopy of molecular Rydberg states contains detailed information about the electronic structure of the ion-core. It is determined by short range electron-core scattering and by the longer-range interaction of the Rydberg electron with static and dynamic properties of the ion-core. As the electronic orbital angular momentum  $\ell$  increases, the Rydberg electron is increasingly excluded, behind a centrifugal barrier, from the molecular region, forming core-nonpenetrating states. For these states, a long-range model [1], shows that mixing coefficients are directly related to the anisotropy of the ion-core. If mixing coefficients among different Rydberg series are known, then parameters characterizing the ion-core anisotropy, such as multipole moments and polarizability, can be derived from experimental results. These results can be compared with predictions of fully-ab initio calculations [2], and with R-matrix calculations for simpler one-electron effective potentials [3, 4, 5], allowing the refinement of both calculation methods and the computed potentials. For example, deviations from the predicted values for the  $\ell$ -mixing coefficients provide information about the exchange interaction, which occurs through the admixture of penetrating character into nominally core-nonpenetrating states. This type of mixing reveals itself in spectroscopic transition frequencies and intensities, and especially in the relative intensities in polarization-sensitive experiments [6]. However, since Rydberg states are usually experimentally accessed in multiple resonance excitation schemes, subject to pulse-to-pulse fluctuations, relative transition intensities are often insufficiently reliable to determine the mixing coefficients.

Many of these difficulties in obtaining accurate intensities can be avoided when the signal is acquired in the time domain. Although the information content of a spectrum recorded in the frequency domain and in the time domain is equivalent, the principal difference between the two methods is in the way signal is degraded by noise. In an absorption spectrum recorded in the time domain, each acquisition event contributes to the measured transition intensity of each resolution element. In such an experiment, shot-to-shot fluctuations in

populating the launch state do not affect the *relative* transition intensities.

However, as the methods for studying Rydberg states, which rely on selective ionization and ion-detection, are well established for the number densities with which absorbers are typically produced in molecular beams, Rydberg state spectra have never been recorded in transmission. Yet, if a Rydberg state spectrum is recorded among the states close in  $n^*$ , the transition dipole moments are exceptionally large, and can compensate for low number densities in molecular beams. The transition dipole moments scale approximately as  $n^2$ , and thus same- or close- $n^*$  Rydberg-Rydberg spectra offer a possibility of observing Rydberg states in transmission.

Even at moderate  $n^*$ , the transition dipole moments among the same- $n^*$  Rydberg states ( $\mu_{Ryd}$ ) are much larger than the permanent dipole moments of the ion-core ( $\mu_{core}$ ), even for highly polar ion-cores. As a result, an external electric field, either DC or time-dependent, exerts a  $\frac{\mu_{Ryd}}{\mu_{core}}2$  times stronger torque on the Rydberg electron, than on the ion-core. Thus, either in the Stark effect, or in a transition, the interactions with the applies field that cause a change in the quantum numbers for the Rydberg electron ( $\Delta\ell = \pm 1$ ,  $\Delta N = 0, \pm 1$ ) are dominant. These transitions conserve the rotational and vibrational quantum numbers of the ion-core,  $N^+$  and  $v^+$ , respectively. Rotational and vibrational transitions of the ion-core become *de facto* forbidden and transitions of the Rydberg electron dominate the spectrum, resulting in, effectively, a *pure electronic spectrum*.

A pure electronic spectrum with accurate relative transition intensities can be recorded in the time domain using either time domain THz spectroscopy (TDTS), or chirped-pulse microwave spectroscopy (CPMW). TDTS covers a region of approximately 0.5 - 3 THz, while in CPMW spectroscopy, 24 GHz wide regions<sup>†</sup> with up to  $\approx 300$  GHz upper limit, can be obtained an a single shot.

Here we present a method that can be used to predict pure electronic spectra recorded in the time domain using either TDTS or CPMW spectroscopy. In the example shown here,

---

<sup>†</sup>This bandwidth corresponds to twice the bandwidth of the available oscilloscope.

Rydberg-Rydberg spectra are calculated when the  $\ell$ -mixing coefficients are known, but it is straightforward to go into the opposite direction and recover the  $\ell$ -mixing coefficients from the measured relative transition intensities. The calculation is based on the propagation of an electromagnetic pulse through a sample of Rydberg absorbers by solving coupled Liouville-Helmholtz equations, using a finite difference approach. In an experiment where strong absorbers interact with a broadband EM pulse, the relative transition intensities will depart from those expected based on the squares of the dipole moments and the envelope of the EM pulse. The main reason for this departure is the additional non-resonant interaction with the EM pulse. In addition, for a sample of strong absorbers, such as Rydberg molecules, the possibility of optical thickness of the sample might skew the transition intensities, even in the weak-field limit. The method presented here gives the relative intensities in a Rydberg-Rydberg spectrum, accounting for both of these problems. For the example of the Rydberg states of CaF, we calculate some examples of pure electronic spectra, and discuss the type of diagnostic information that would be obtained in an experiment for several choices of the launch state. We show how, for a particular choice of the launch state, the effect of the ion-core dipole moment can manifest itself in the transition intensities in a way that permits its measurement separately from the quadrupole moment.

### 6.3 Calculation

The field-free Hamiltonian, used to describe the Rydberg states of CaF in the region of  $n^* = 13$ , was described elsewhere [7], and only the most important aspects will be briefly revisited here. The effective Hamiltonian, which is set up in the Hund's case (b) basis, relies on the Watson's long-range model [8], corrected by addition of polarizability terms [1]. At zero field the effective Hamiltonian includes the core-nonpenetrating  $f$ ,  $g$ , and  $h$  states, and the core-penetrating states that are located in the vicinity of the  $n^* = 13$  integer value (13.19  $\Sigma^+$ , 12.98  $\Pi^\pm$ , 13.14  $\Delta^\pm$ , and 12.88  $\Sigma^+$ ). In the presence of an external electric field, values of  $6 \leq \ell \leq 12$  are allowed to be mixed in. Only the states belonging to  $v^+ = 1$  are included in the model. The rotationless energies of the core-penetrating states are determined by a fit. The implementation of the fitting procedure is straightforward in the Hund's case (b) basis. The  $\ell$ -mixing coefficients among the  $1 \leq \ell \leq 5$   $^2\Sigma^+$  states were determined using by this, while the mixing coefficients published in [9] were used for the  $\Pi^\pm$  and  $\Delta^\pm$  states. The energies for the  $0 \leq N \leq 6$  in  $n^* = 13$  states, which were observed in the double resonance spectrum, were used in the fit. No attempt was made to use the relative transition intensities in the fitting procedure, as the relative intensities are not measured with sufficient precision in our double resonance spectrum. The standard deviation of the fit was  $0.2 \text{ cm}^{-1}$ .

In order to solve the time-dependent Schrödinger equation in Liouville form

$$i\hbar \frac{d\rho}{dt} = [H, \rho], \quad (6.1)$$

we first set up the time-dependent Hamiltonian. Relaxation was not included in the model, as the relaxation was slow compared to the FID acquisition times in the calculation. In the presence of an electromagnetic pulse,  $E(t)$ , the Hamiltonian is given by

$$H = H_0 + H'(t) = \sum_i |i\rangle \varepsilon_i \langle i| - \sum_{i,l} \mu_{il} E(t) |i\rangle \langle l|, \quad (6.2)$$

where  $\varepsilon_i$  is the energy of  $i^{\text{th}}$  state,  $\mu_{il}$  is the projection of the dipole moment between  $i^{\text{th}}$

state and  $l^{th}$  state onto the polarization direction of the EM pulse. A set of the transition dipole moments used to set up the field-dependent Hamiltonian was the same as used to model the Stark effect in  $n^* = 13$  of CaF, described in detail in [7]. However, to implement a numerical procedure to solve Eq. (6.1), the Hamiltonian was truncated, so that only the states connected directly to the launch state are included. In addition, only the final states,  $|f\rangle$ , with dipole moments,  $\mu_{i,f}$ , larger than  $\frac{1}{20}$  of the largest dipole moment in the set, where  $|l\rangle$  is the launch state, were retained in the calculation. Since we are interested in the response of the system under the weak-field conditions, the fact that no multiple step processes are allowed in the model does not affect the result.

After solving Eq. (6.1) numerically in Mathematica, the polarization of the sample, given by

$$P = N \langle \mu \rangle = N \sum_{m,n} \rho_{mn} \mu_{nm}, \quad (6.3)$$

produces the response from the system, which is proportional to  $\frac{\partial^2 P}{\partial t^2}$ .  $N$  in the Eq. (6.3) is the number density of the Rydberg absorbers, assumed to be  $10^{10} \frac{\text{molecules}}{\text{cm}^3}$ . Typically  $10^9 \frac{\text{molecules}}{\text{cm}^3}$  are produced in our experiment, but in order to speed up the calculation by reducing the FID collection time, we selected higher number density of excited molecules. This is not a problem, as under typical experimental conditions the FID collection time would be longer than selected in the calculation.

To propagate the EM pulse through the sample, the Helmholtz equation

$$\nabla^2 E - \frac{1}{c^2} \frac{\partial^2}{\partial t^2} E = \mu_0 \frac{\partial^2}{\partial t^2} P \quad (6.4)$$

is solved numerically on a grid. The EM field radiated by the sample at the  $i^{th}$  step on the grid is used to correct the electric field amplitude on the  $(i + 1)^{th}$  step. When the electric field radiated by the sample is not negligible compared to the amplitude of the excitation field, several iterations are needed to solve self-consistently for  $E$  on a particular grid-step.



An increase in the number of iterations for each spatial position increases the computation time. When the electric field radiated by the sample becomes comparable to the amplitude of the excitation field, the computation procedure diverges. The solution to the Eq. (6.4) is coupled to the solution of Eq. (6.1), so that Eq. (6.1) is solved at each spatial position along the direction of the EM pulse propagation. The thickness of the sample layer was typically chosen to be between 1 and 3 mm in the calculations.

We simulate two kinds of Rydberg-Rydberg spectrum acquisition experiments. In the first experiment, a broadband EM pulse in the frequency region typical for time domain THz spectroscopy, but modified as described later in the text, polarizes the sample. In the second experiment, the sample polarization is created by a pulse chirped over a relatively narrow frequency range in the millimeter wave region. The two cases require somewhat different numerical treatments, as the TD-THz and CPMW pulses differ significantly in their duration and frequency content.

In the case of the chirped microwave pulse, a 30 ns pulse with an amplitude of 2.5 V/m linearly chirped between 56 and 80 GHz, was used in the calculation. For the THz pulse, we use a typical THz pulse generated in our THz spectrometer based on optical rectification in LiNbO<sub>3</sub>. The frequency content of such a pulse is approximately 0.5 - 3 THz (the content of the pulse extends to higher frequency, but the efficiency of our ZnTe-based detector decreases rapidly beyond 3 THz), and the pulse amplitude is  $\approx 1$  kV/cm. For the calculation, we used the value of 0.1 kV/cm for the THz field peak amplitude. A pulse in this frequency range would drive the same- $n^*$  Rydberg-Rydberg transitions at  $n^*$ , lower than  $n^* = 13$ . Instead of setting up another effective Hamiltonian for the lower  $n^*$  region, it was less difficult to use the already existing effective Hamiltonian for the  $n^* = 13$  region, and to use a model THz pulse, obtained by contracting the frequency span of the THz pulse by a factor of 10 (the frequency separation among the states belonging to the same  $n^*$  scales as  $n^{-3}$ , so the factor of 10 in frequency shifts the  $n^*$  region from 13 to 6).

After the EM pulse propagates through the sample, the free induction decay, with dura-

tion of 1.40 ns<sup>†</sup> or 90 ns in case of the THz or CPMW excitation, respectively, is collected and Fourier transformed. This procedure is repeated for  $J = N + \frac{1}{2}$  and  $J = N - \frac{1}{2}$  for a particular value of  $N$  accessible from the launch state, and for all values of  $M_J$  in each of the spin components. As  $N$  increases, the transition dipole moments for  $\Delta J \neq \Delta N$  transitions decrease relative to those for which  $\Delta J = \Delta N$ . As a result  $\Delta J \neq \Delta N$  transitions are completely absent from our truncated Hamiltonian, and the transitions into the two spin components can be treated independently. The frequency domain spectra for both values of  $J$  and all values of  $M_J$  accessible from the launch state are summed. Before summing, they are multiplied by the coefficients proportional to the double-resonance transition intensities that correspond to the excitation probability of each  $(J, M_J)$  state. These coefficients are given by Eq. (7) in [6].

---

<sup>†</sup>A factor of 10 comes from the frequency contraction, so the FID collection time corresponds to 140 ps for the  $n^{*'}$  region.

## 6.4 Results and discussion

As  $N^+$  is conserved in pure electronic transitions, a choice between a pure- $N^+$  and an  $N^+$ -mixed launch state profoundly affects the complexity of the observed Rydberg-Rydberg spectrum. In addition, the diagnostic information encoded in such a spectrum will also depend on the *a priori* knowable character of the launch state. Typically, as the rotational quantum number  $N$  increases, the rotation-electronic term in the Hamiltonian decouples the Rydberg electron from the ion-core [10]. The appropriate coupling case evolves as  $N$  increases from Hund's case (a) or (b) toward Hund's case (d). The Hund's case (d) basis functions are characterized by separate quantum numbers for the ion-core and Rydberg electron,  $N^+$  and  $\ell$ , respectively. Thus, a launch state in the Hund's case (d) basis has a pure  $N^+$  character, while a launch state in the Hund's case (b) basis is  $N^+$ -mixed. As the  $\ell$ -conserving rotation-electronic term in the Hamiltonian connects basis states of the same parity, a launch state in Hund's case (b) is composed of states with  $N^+$  differing in steps of two (parity in the Hund's case (d) basis is given by  $(-1)^{N^++\ell}$ ). Thus, in the absence of  $\ell$ -mixing, from a Hund's case (d) launch state characterized by a single value of the  $N^+$  quantum number, only one value of  $N^+$  can be accessed in a pure electronic spectrum. In the absence of  $\ell$ -mixing, from a launch state in the Hund's case (b) basis, several values of  $N^+$  (all even or all odd) can be reached.

The anisotropy of the ion-core leads to  $\ell$ -mixing, and the  $\ell$ -mixing in turn causes  $N^+$ -mixing. The selection rules for dipole-induced mixing are  $\Delta\ell = \pm 1$ ,  $\Delta N^+ = \pm 1$ , while for quadrupole and lowest-order polarizability induced mixing, the selection rules are  $\Delta\ell = 0, \pm 2$ ,  $\Delta N^+ = 0, \pm 2$ . Since quadrupole and lowest-order polarizability cause mixing among the states with  $N^+$  differing in steps of 2, as does the rotation-electronic coupling term in the Hamiltonian, quadrupole and polarizability terms will only cause redistribution of transition intensities in a Rydberg-Rydberg spectrum among the states already mixed by the rotation-electronic coupling. An ion-core dipole, on the other hand, admixes the values of  $N^+$  not initially admixed by either the quadrupole, polarizability, or rotational-electronic

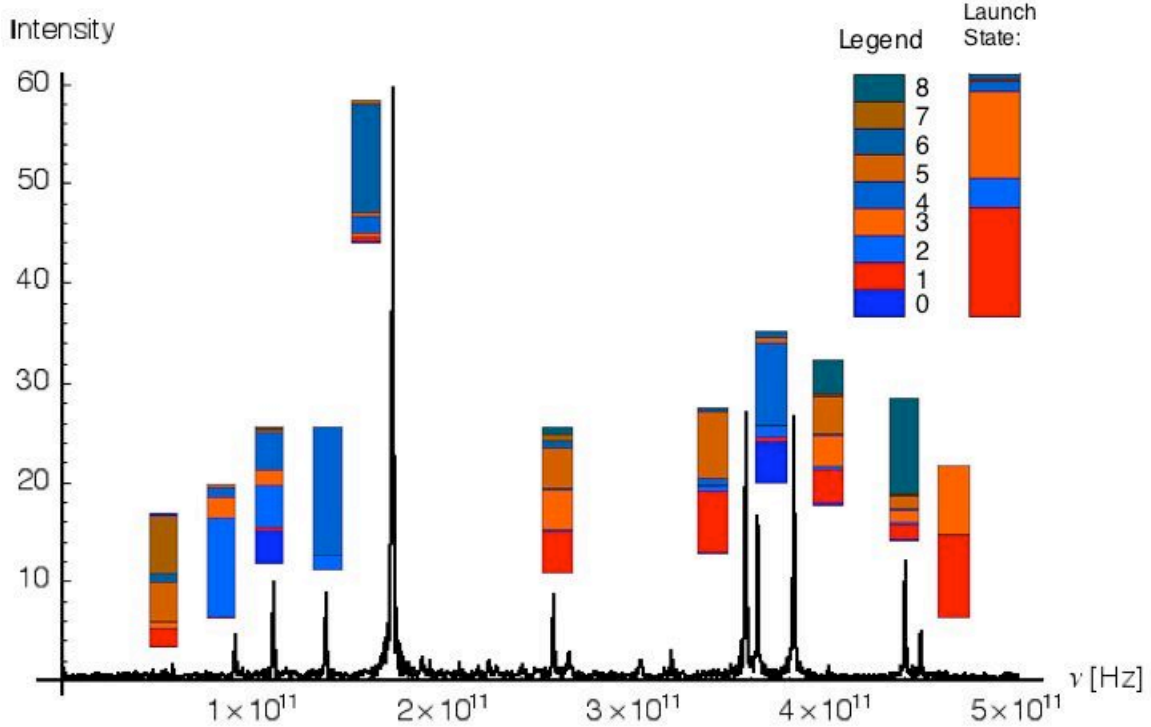


Figure 6.1: Simulated pure electronic Rydberg-Rydberg spectrum of CaF, acquired using time domain THz spectroscopy. The launch state was a strongly  $\ell$ -mixed,  $N^+$ -mixed,  $f(-3)$ ,  $N = 2$  state. The  $N^+$  characters of each feature observed in the spectrum, and those of the launch state, are represented by the color coding of each bar next to the corresponding spectral feature. Even values of  $N^+$  are represented by shades of blue and odd values of  $N^+$  by shades of red.

interactions.

If a state with dipole-admixed values of  $N^+$  is used as a launch state when recording a Rydberg-Rydberg spectrum, the values of  $N^+$  contained in the launch state will light up in a Rydberg-Rydberg spectrum and both even and odd values of  $N^+$  will be accessed. Figure 6.1 shows a spectrum recorded from a strongly  $\ell$ -mixed,  $N^+$ -mixed launch state, which has both even and odd values of  $N^+$  in its character. It is observable that states that contain wide range of both even and odd values of  $N^+$  are accessed in this type of Rydberg-Rydberg spectrum, even though  $N^+$  is conserved in the Rydberg-Rydberg transitions.

As  $N$  increases, the evolution toward the Hund's case (d) basis becomes more complete,

and  $N^+$  becomes a good quantum number. For a fixed value of  $\ell$  and a fixed value of  $N$ , states with a higher value of the  $\Lambda$  quantum number (or a higher value of the  $\ell_R$  quantum number in Hund's case (d) notation) will be less mixed, as they, tend to penetrate the ion-core more weakly. Also, the  $\Lambda = 0$  components of the nominally core-nonpenetrating states, which have the strongest core-penetrating character for a given value of  $\ell$ , do not exist for negative Kronig symmetry [11]. This means that states of negative Kronig symmetry will have smaller admixed core-penetrating character, and will be of purer  $N^+$  character. Figure 6.2 shows a chirped-pulse millimeter wave spectrum recorded from a launch state with higher values of  $N$  and  $\ell_R$  quantum numbers than those for the spectrum shown in the Fig. 6.1. The dipole-mixing and core-penetrating character of the launch state in the Fig. 6.2 example are therefore less pronounced than in the Fig. 6.1 example. As a chirped-pulse microwave spectrum probes a lower frequency region than the time-domain THz spectrum, CPMW spectroscopy is more suited for recording transitions into the restricted set of states that have the same *nominal* value of the  $N^+$  quantum number. These transitions typically occur at lower frequency than the transitions among the states belonging to different  $N^+$  clusters<sup>†</sup>.

In addition to the already described diagnostic information contained in Rydberg-Rydberg spectra, the dependence of the relative polarizations of the photons in each successive excitation step in a multiple resonance experiment can be used. Polarization dependence provides the information about the value of the rotational quantum number  $N$  of the target state, as described in [6]. Also, when combined with the high resolution of the chirped-pulse microwave technique, the Stark effect can be used to gain access to the states with higher values of the  $\ell$  quantum number, thus providing information about the value of the  $N^+$  quantum number in the same manner as described in [7], but at higher resolution than possible by the optical-optical double resonance method.

For the purpose of disentangling the different mechanisms of the interaction among the

---

<sup>†</sup>Energy separation among the states *within* a particular  $N^+$ -cluster is determined by the magnitude of the electron-core interactions, while the energy separation *between* the states belonging to different  $N^+$ -clusters by the rotational constant, as  $2BN^+$ .

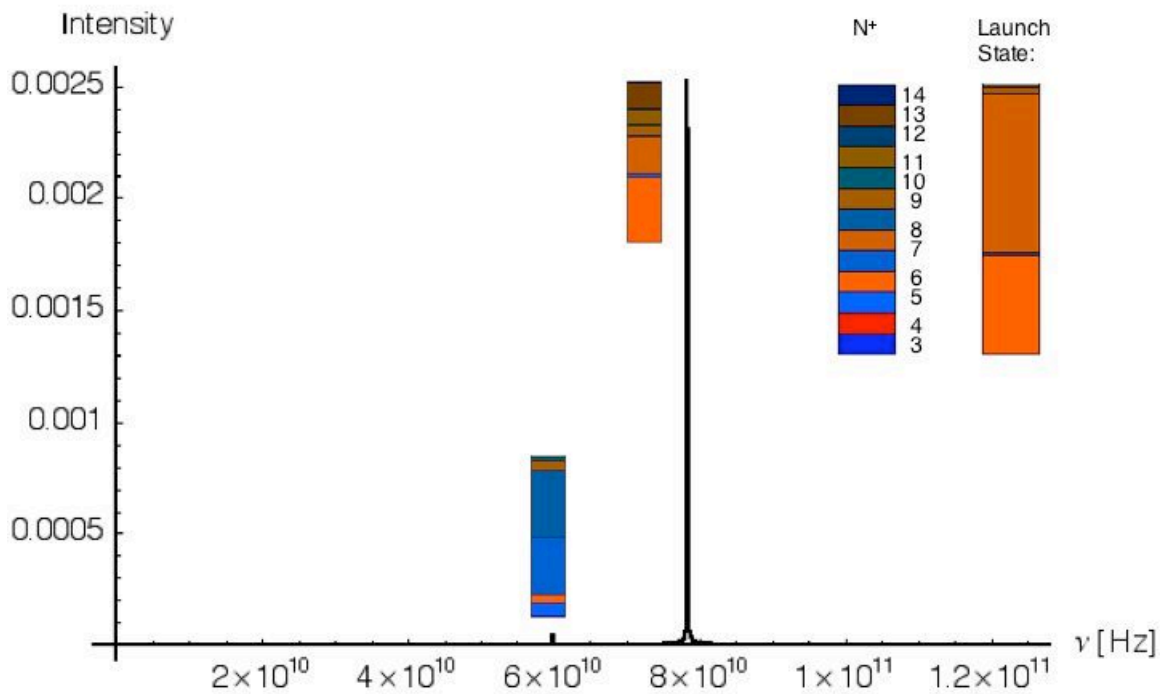


Figure 6.2: Simulated pure electronic Rydberg-Rydberg spectrum of CaF, acquired using the chirped-pulse microwave spectroscopy. The launch state was  $f(3)$ ,  $N = 9$ . The  $N^+$  characters of each feature observed in the spectrum and of the launch state, are represented by the color coding of each bar next to the corresponding spectral feature. Even values of  $N^+$  are represented by shades of red and odd values of  $N^+$  by shades of blue.

Rydberg electron and the ion-core using the information encoded in the relative transition intensities, the Rydberg-Rydberg spectrum should be recorded in the weak-field limit. As the amplitude of the EM excitation pulse increases, the values of the Rabi frequency for different transitions will vary widely. As a result, their relative transition intensities will be distorted from the pattern expected in the weak-field limit. In addition, as the EM amplitude is increased, the probability of multiphoton processes, especially multiphoton ionization of the Rydberg states, increases. However, even in the weak-field limit, due to the broadband character of the EM pulses used for the excitation, non-resonant interactions between the sample and the EM pulse cannot be neglected. Also, in a sample with exceptionally strong absorbers, even in the weak-field limit, reabsorption along the EM pulse propagation direction alters the intensities from what would be expected for optically thin samples. In order to predict the relative transition intensities in a spectrum, it is necessary to propagate the EM pulse through the sample, instead of basing the prediction of relative transition intensities solely on the squared transition dipole moments and the amplitude of the EM pulse.

## 6.5 Summary

Diagnostic information encoded in the relative transition intensities in a Rydberg-Rydberg spectrum depends on the strength of the  $\ell$ - and  $N^+$ -mixing in the launch state. If the goal is to obtain the information about the long-range interactions between the Rydberg electron and the ion-core, a pure- $\ell$ , pure- $N^+$ , launch state should be selected. A CPMW spectrum recorded from such a launch state terminates in states that have the same value of the  $N^+$  quantum number as the launch state. The states accessed in such a CPMW Rydberg-Rydberg spectrum belong to  $N^+$ -clusters with the same  $N^+$  value as the launch state, but they have  $\ell$  quantum numbers differing by one from the launch state ( $g \leftarrow f$  in the example in Fig. 6.1). The energy separations among the states belonging to the same value of the  $N^+$  quantum number, in the limit when  $N^+$  is a good quantum number, is determined by the long-range interactions between the Rydberg electron and the ion-core. Thus the information about the long-range interaction between the Rydberg electron and the ion-core is directly obtained from a CPMW Rydberg-Rydberg spectrum launched from a pure- $\ell$ , pure- $N^+$  state. The choice of a pure- $N^+$  launch state is easily achievable at high  $N$ . Such a choice leads to a simplified pure electronic spectrum, which will be particularly useful in analyzing the spectra of more complex Rydberg systems than that of CaF.

On the other hand, when a spectrum is recorded from a strongly  $\ell$ - and  $N^+$ -mixed launch state, states that are not expected to be accessed in the absence of dipole-mixing will appear in the spectrum. If the character of the launch state is not known, the complexity of a Rydberg-Rydberg spectrum recorded from such a state provides qualitative information about whether the launch state is  $N^+$ - and  $\ell$ -mixed, or not. This can be used indirectly, to determine the  $\Lambda$  quantum number of the launch state if it is unknown (Kronig symmetry is easily determined using polarization diagnostics [6]). If an assignment does exist for the launch state, then the distortion of the relative transition intensities from those expected for the case with only even-step  $\ell$ -mixing is informative. The relative transition intensities in such a spectrum provide direct information about the core-penetration and dipole-admixed



character. Time domain THz and chirped-pulse microwave spectroscopic methods provide complementary information about the interaction between the Rydberg electron and the ion-core.

## 6.6 Bibliography

- [1] J. J. Kay, S. L. Coy, V. S. Petrović, B. M. Wong, and R. W. Field. *J. Chem. Phys.*, 128:194301, 2008.
- [2] B. M. Wong, S. L. Coy, J. J. Kay, and R. W. Field. *work in progress*.
- [3] S. N. Altunata, S. L. Coy, and R. W. Field. *J. Chem. Phys.*, 122:184314, 2005.
- [4] S. N. Altunata, S. L. Coy, and R. W. Field. *J. Chem. Phys.*, 123:084318, 2005.
- [5] B. M. Wong, S. N. Altunata, and R. W. Field. *J. Chem. Phys.*, 124:014106, 2006.
- [6] V. S. Petrović and R. W. Field. *J. Chem. Phys.*, 128:014301, 2007.
- [7] V. S. Petrović, J. J. Kay, S. L. Coy, and R. W. Field. *J. Chem. Phys.*, *submitted*, 2008.
- [8] J. K. G. Watson. *Mol. Phys.*, 81:277, 1994.
- [9] R. W. Field, C. M. Gittins, N. A. Harris, and Ch. Jungen. *J. Chem. Phys.*, 122:184314, 2005.
- [10] Hélène Lefebvre-Brion and Robert W. Field. *The Spectra and Dynamics of Diatomic Molecules*. Elsevier Academic Press, 2004.
- [11] R. de L. Kronig. *Band spectra and molecular structure*. Cambridge University Press, 1930.

# Chapter 7

## Appendix

## 7.1 Multipole expansion of the Hamiltonian

If the interaction of the Rydberg electron with the ion-core can be described using a long-range model, the electronic term in the Hamiltonian can be expanded using a multipole expansion (in atomic units):

$$\begin{aligned}
 H_{el} &= \sum_{core} \frac{e_{Ryd} e_{core}}{|r - r_{core}|} \\
 &= \sum_{core, \ell} e_{Ryd} e_{core} \frac{r_{core}^\ell}{r_{Ryd}^{\ell+1}} P_\ell(\cos \Theta_{Ryd, core}), \tag{7.1}
 \end{aligned}$$

where the summation is done over the core electrons.  $e_{Ryd}$  and  $e_{core}$  are the charges of the Rydberg and core electrons,  $-e$ , where  $e = 1$  *a.u.* is the signless elementary charge.  $P_\ell$  is the Legendre polynomial of the  $\ell^{th}$  order, and  $\Theta_{Ryd, core}$  is the angle between vectors pointing to the Rydberg electron and each core electron. If only the first two terms, corresponding to the interaction of the Rydberg electron with the dipole and quadrupole of the ion-core, are retained in the expansion, we have:

$$\begin{aligned}
 H_{el} &= \sum_{core} e_{Ryd} e_{core} \frac{r_{core}}{r_{Ryd}^2} P_1(\cos \Theta_{Ryd, core}) \\
 &+ \sum_{core} e_{Ryd} e_{core} \frac{r_{core}^2}{r_{Ryd}^3} P_2(\cos \Theta_{Ryd, core}). \tag{7.2}
 \end{aligned}$$

Using Eq (3.85) from [1], Eq. 7.2 can be rewritten:

$$\begin{aligned}
 &= \sum_{core} e_{Ryd} e_{core} \frac{r_{core}}{r_{Ryd}^2} \frac{4\pi}{3} \sum_{q=-1}^1 Y_{1,q}^*(\theta_{Ryd}, \phi_{Ryd}) Y_{1,q}(\theta_{core}, \phi_{core}) \\
 &+ \sum_{core} e_{Ryd} e_{core} \frac{r_{core}^2}{r_{Ryd}^3} \frac{4\pi}{5} \sum_{q'=-2}^2 Y_{2,q'}^*(\theta_{Ryd}, \phi_{Ryd}) Y_{2,q'}(\theta_{core}, \phi_{core}), \tag{7.3}
 \end{aligned}$$

where the  $Y_{L,M}$  are spherical harmonics, and  $\theta$  and  $\phi$  are Euler angles ( $\theta_i$  is the angle between  $r_i$  and  $z$ , and  $\phi_i$  is the angle between the projection of  $r_i$  on the  $xy$  plane and the  $x$  axis), with subscripts indicating whether the coordinate belongs to the Rydberg electron or the core electrons. For a cylindrically symmetric charge distribution, Eq. 7.3 simplifies to:

$$\begin{aligned}
&= \sum_{core} e_{Ryd} e_{core} \frac{r_{core}}{r_{Ryd}^2} \frac{4\pi}{3} Y_{1,0}(\theta_{Ryd}, \phi_{Ryd}) Y_{1,0}(\theta_{core}, \phi_{core}) \\
&+ \sum_{core} e_{Ryd} e_{core} \frac{r_{core}^2}{r_{Ryd}^3} \frac{4\pi}{5} Y_{2,0}(\theta_{Ryd}, \phi_{Ryd}) Y_{2,0}(\theta_{core}, \phi_{core}) \\
&= \sqrt{\frac{4\pi}{3}} e_{Ryd} \frac{1}{r_{Ryd}^2} Y_{1,0}(\theta_{Ryd}, \phi_{Ryd}) \mu_0^{(1)} \\
&+ \sqrt{\frac{4\pi}{5}} e_{Ryd} \frac{1}{r_{Ryd}^3} Y_{2,0}(\theta_{Ryd}, \phi_{Ryd}) Q_0^{(2)}, \tag{7.4}
\end{aligned}$$

where

$$\mu_0^{(1)} \equiv \sum_{core} e_{core} r_{core} Y_{1,0}(\theta_{core}, \phi_{core}), \tag{7.5}$$

and

$$Q_0^{(2)} \equiv \sum_{core} e_{core} r_{core}^2 Y_{2,0}(\theta_{core}, \phi_{core}), \tag{7.6}$$

are the dipole and quadrupole moments of the ion-core, respectively.

The coordinates  $\theta_{Ryd}$ ,  $\theta_{core}$ ,  $\phi_{Ryd}$ , and  $\phi_{core}$  are defined in the molecular frame. In order to evaluate the matrix elements of the electronic Hamiltonian in Hund's (d) basis, we need to transform the operator into the lab frame. The rotation,  $R$ , transforms a spherical harmonic expressed in the molecular frame into a superposition of lab-frame spherical harmonics, and the transformation coefficients are expressed in terms of the rotation matrices  $D$ . Using Eq. (3.87) from [1] we can write:

$$\begin{aligned}
Y_{LM'}(\theta_{LAB}, \phi_{LAB}) &= RY_{LM'}(\theta_{MOLECULE}, \phi_{MOLECULE}) \\
&= \sum_M D_{MM'}^L(\phi, \theta, \chi) Y_{LM}(\theta_{MOLECULE}, \phi_{MOLECULE}). \quad (7.7)
\end{aligned}$$

The new angles,  $\theta$  and  $\phi$ , are now expressed in the lab frame. When  $M' = 0$ , as it is in Eq. (7.4), we have:

$$\begin{aligned}
D_{M,0}^L(\phi, \theta, \chi) &= \sqrt{\frac{4\pi}{2L+1}} Y_{LM}^*(\theta, \phi) \\
&= \sqrt{\frac{4\pi}{2L+1}} (-1)^M Y_{L-M}(\theta, \phi). \quad (7.8)
\end{aligned}$$

The operator  $H_{el}$  now becomes:

$$\begin{aligned}
&= \frac{4\pi}{3} e_{Ryd} \mu_0^{(1)} \frac{1}{r_{Ryd}^2} \sum_M (-1)^M Y_{1,-M}(\theta, \phi) Y_{1,M}(\theta_{Ryd}, \phi_{Ryd}) \\
&+ \frac{4\pi}{5} e_{Ryd} Q_0^{(2)} \frac{1}{r_{Ryd}^3} \sum_{M'} (-1)^{M'} Y_{2,-M'}(\theta, \phi) Y_{2,M'}(\theta_{Ryd}, \phi_{Ryd}), \quad (7.9)
\end{aligned}$$

where the first term can be written as  $H_{dipole}$  and the second  $H_{quadrupole}$ , for short. In order to evaluate the matrix elements of the electronic Hamiltonian in Hund's case (d) basis, we need to separate the coordinates in the wavefunction  $|\psi\rangle$ , where  $|\psi\rangle = |\psi_{Ryd}\rangle |\psi_{nucl}\rangle |\psi_{core}\rangle$ . Throughout the derivation, we will assume that  $L_{core} = 0$ , and that the only net nonzero orbital angular momentum is that of the Rydberg electron, so that  $L = \ell$ . Since  $\vec{N} = \vec{R} + \vec{\ell}$ , we have:

$$|NR\ell M_N\rangle = \sum_{M_R, M_\ell} \langle RM_R | \langle \ell M_\ell | NR\ell M_N \rangle |RM_R\rangle | \ell M_\ell \rangle, \quad (7.10)$$

and therefore:

$$|\psi\rangle = |\psi_{core}\rangle |vRn\ell NM_N\rangle = |\psi_{core}\rangle \sum_{M_R, M_\ell} \langle RM_R \ell M_\ell | NR \ell M_N \rangle |vRM_R\rangle |n\ell M_\ell\rangle. \quad (7.11)$$

Only the derivation of matrix elements of the dipole term will be given here. The derivation of the matrix elements of quadrupole term can be done in an analogous way, and is given in [2]. The electronic Hamiltonian matrix elements derived here can be augmented as described in [3] and [4] to account for polarizability and higher order terms. Throughout this appendix, hydrogenic radial wavefunctions are used.  $\langle v'R'n'\ell'N'M'_N | H_{dipole} | vRn\ell NM_N \rangle$  becomes:

$$\begin{aligned} \langle v'R'n'\ell'N'M'_N | H_{dipole} | vRn\ell NM_N \rangle &= \frac{4\pi}{3} e_{Ryd} \langle n'\ell' | \frac{1}{r_{Ryd}^2} | n\ell \rangle \langle v'R' | \mu_0^{(1)} | vR \rangle \\ &\sum_{M', M_R, M_\ell, M'_R, M'_\ell} (-1)^M \langle RM_R \ell M_\ell | NM_N \rangle \langle R'M'_R \ell' M'_\ell | N'M'_N \rangle \\ &\langle R'M'_R | Y_{1,-M}(\theta, \phi) | RM_R \rangle \langle \ell' M'_\ell | Y_{1,M}(\theta_{Ryd}, \phi_{Ryd}) | \ell M_\ell \rangle, \end{aligned} \quad (7.12)$$

which can be rewritten as:

$$\begin{aligned} &\langle v'R'n'\ell'N'M'_N | H_{dipole} | vRn\ell NM_N \rangle = \\ &e_{Ryd} \langle n'\ell' | \frac{1}{r_{Ryd}^2} | n\ell \rangle \langle v'R' | \mu_0^{(1)} | vR \rangle [(2R+1)(2R'+1)(2\ell+1)(2\ell'+1)(2N+1)(2N'+1)]^{1/2} \\ &\begin{pmatrix} R' & 1 & R \\ 0 & 0 & 0 \end{pmatrix} \begin{pmatrix} \ell' & 1 & \ell \\ 0 & 0 & 0 \end{pmatrix} \sum_{M', M_R, M_\ell, M'_R, M'_\ell} (-1)^{M'_N + M_N - M} \\ &\begin{pmatrix} R' & R & 1 \\ -M'_R & M_R & M \end{pmatrix} \begin{pmatrix} \ell & \ell' & 1 \\ -M_\ell & -M'_\ell & -M \end{pmatrix} \begin{pmatrix} R & N & \ell \\ -M_R & M_N & M_\ell \end{pmatrix} \begin{pmatrix} \ell' & N' & R' \\ M'_\ell & -M'_N & M'_R \end{pmatrix} \end{aligned} \quad (7.13)$$

and, finally, the sum over the product of  $3j$  coefficients can be reduced to a  $6j$  coefficient, using Eq. (4.12) from [1], giving:

$$\begin{aligned}
& \langle v' R' n' \ell' N' M'_N | H_{dipole} | v R n \ell N M_N \rangle = \\
& e_{Ryd} \langle n' \ell' | \frac{1}{r_{Ryd}^2} | n \ell \rangle \langle v' R' | \mu_0^{(1)} | v R \rangle [(2R+1)(2R'+1)(2\ell+1)(2\ell'+1)]^{1/2} \\
& (-1)^{R+R'+N} \begin{pmatrix} R' & 2 & R \\ 0 & 0 & 0 \end{pmatrix} \begin{pmatrix} \ell' & 2 & \ell \\ 0 & 0 & 0 \end{pmatrix} \left\{ \begin{matrix} N & R' & \ell' \\ 2 & \ell & R \end{matrix} \right\}. \tag{7.14}
\end{aligned}$$

The analogous expression for the interaction between the Rydberg electron and the quadrupole moment of the ion core is:

$$\begin{aligned}
& \langle v' R' n' \ell' N' M'_N | H_{quadrupole} | v R n \ell N M_N \rangle = \\
& e_{Ryd} \langle n' \ell' | \frac{1}{r_{Ryd}^3} | n \ell \rangle \langle v' R' | Q_0^{(2)} | v R \rangle [(2R+1)(2R'+1)(2\ell+1)(2\ell'+1)]^{1/2} \\
& (-1)^{R+R'+N} \begin{pmatrix} R' & 1 & R \\ 0 & 0 & 0 \end{pmatrix} \begin{pmatrix} \ell' & 1 & \ell \\ 0 & 0 & 0 \end{pmatrix} \left\{ \begin{matrix} N & R' & \ell' \\ 1 & \ell & R \end{matrix} \right\}. \tag{7.15}
\end{aligned}$$



## 7.2 Matrix elements in the Hund's case (d) basis for the Stark effect arising from Rydberg-Rydberg electric dipole transition moments

To evaluate the matrix elements of  $H_{Stark} = -\vec{\mu} \cdot \vec{E}_{Stark}$  in the Hund's case (d) basis, where  $\vec{E}_{Stark} = E_{Stark} \vec{e}$  is the electric field vector with amplitude  $E_{Stark}$  and direction along the unit vector  $\vec{e}$ , we first expand the dot product:

$$\vec{\mu} \cdot \vec{e} = -\sqrt{3} [\mu^{(1)} \otimes e^{(1)}]_0^{(0)} = -\sqrt{3} \sum_M \langle 1M1 - M | 00 \rangle \mu_M^{(1)} e_{-M}^{(1)}, \quad (7.16)$$

where the notation for tensors is analogous to that of [1]. We select the direction of the external electric field to be along  $Z$  in the laboratory frame. Then the only component of  $\vec{e}$  is along  $e_0^{(1)}$ . Therefore:

$$H_{Stark} = \sqrt{3} \langle 1010 | 00 \rangle E_{Stark} \mu_0^{(1)} e_0^{(1)}. \quad (7.17)$$

Since  $\mu_0^{(1)}$  has two components, one due to the permanent dipole moment of the ion-core, and the other one due to the electric dipole transition moment among the Rydberg states, it can be written as:

$$\mu_0^{(1)} = \mu_{0,ion}^{(1)} + \mu_{0,Rydb}^{(1)}, \quad (7.18)$$

and the Stark Hamiltonian will have two terms:

$$H_{Stark} = H_{Stark,ion} + H_{Stark,Rydb}. \quad (7.19)$$

First we evaluate the term in the Hamiltonian due to the Rydberg-Rydberg transition moment, while the term due to the permanent dipole moment will be derived in the next section. The Rydberg-Rydberg transition moment involves the coordinates for the Rydberg

electron:

$$\mu_{0,Rydb}^{(1)} = e\sqrt{\frac{4\pi}{3}}r_{Rydb}Y_{1,0}(\theta_{Rydb}, \phi_{Rydb}), \quad (7.20)$$

where  $Y_{1,0}(\theta_{Rydb}, \phi_{Rydb})$  is expressed in the lab frame. Since  $\langle 1010|00\rangle = -\frac{1}{\sqrt{3}}$ , and  $|e_0^{(1)}| = 1$ ,  $H_{Stark,Rydb}$  becomes:

$$H_{Stark,Rydb} = -E_{Stark}e\sqrt{\frac{4\pi}{3}}r_{Rydb}Y_{1,0}(\theta_{Rydb}, \phi_{Rydb}). \quad (7.21)$$

We now evaluate the matrix elements in the Hund's case (d) basis, with basis functions defined by Eq. (7.10). The Stark matrix element due to the transition dipole moment can be rewritten as (where the integration is carried out over  $d\Omega(\theta, \phi, \chi)$ ):

$$\begin{aligned} & \langle v'R'n'\ell'N'M'_N | H_{Stark,Rydb} | vRn\ell NM_N \rangle = \\ & -E_{Stark}e\sqrt{\frac{4\pi}{3}} \sum_{M_R, M_\ell, M_{\ell'}} \langle n', \ell' | r_{Rydb} | n, \ell \rangle \langle v'R|vR \rangle \int Y_{\ell', M_{\ell'}}^* Y_{1,0} Y_{\ell, M_\ell} d\Omega \\ & \langle RM_R \ell M_\ell | NM_N \rangle \langle RM_R \ell' M_{\ell'} | N' M'_N \rangle \delta_{RR'} \delta_{M_R, M'_R}. \end{aligned} \quad (7.22)$$

Using Eq. (3.115) from [1], Eq. 7.22 can be rewritten as:

$$\begin{aligned} & \langle v'R'n'\ell'N'M'_N | H_{Stark,Rydb} | vRn\ell NM_N \rangle = \\ & -E_{Stark}e\sqrt{\frac{4\pi}{3}} \langle n', \ell' | r_{Rydb} | n, \ell \rangle \langle v'R|vR \rangle \left[ \frac{3(2\ell+1)}{4\pi(2\ell'+1)} \right]^{1/2} \langle \ell M_\ell 10 | \ell' M_{\ell'} \rangle \langle \ell 0 10 | \ell' 0 \rangle \\ & \sum_{M_R, M_\ell, M_{\ell'}} \langle RM_R \ell M_\ell | NM_N \rangle \langle RM_R \ell' M_{\ell'} | N' M'_N \rangle. \end{aligned} \quad (7.23)$$

equation 7.23 can be rewritten using  $3j$  coefficients as:

$$\begin{aligned}
& \langle v'R'n'\ell'N'M'_N | H_{Stark,Rydb} | vRn\ell NM_N \rangle = \\
& -E_{Stark} e[(2\ell+1)(2\ell'+1)(2N+1)(2N'+1)]^{1/2} \langle n', \ell' | r_{Rydb} | n, \ell \rangle \langle v'R | vR \rangle \\
& \sum_{M_R, M_\ell, M_{\ell'}} (-1)^{M_N + M'_N + M'_\ell - 1} \\
& \begin{pmatrix} R & \ell & N \\ M_R & M_\ell & -M_N \end{pmatrix} \begin{pmatrix} R & \ell' & N' \\ M_R & M'_\ell & -M'_N \end{pmatrix} \begin{pmatrix} \ell & 1 & \ell' \\ M_\ell & 0 & -M'_\ell \end{pmatrix} \begin{pmatrix} \ell & 1 & \ell' \\ 0 & 0 & 0 \end{pmatrix}. \quad (7.24)
\end{aligned}$$

From the properties of  $3j$  coefficients it follows that  $M_\ell = M'_\ell$ . In that case, it follows that  $M_N = M'_N$ . Since  $M_\ell = M_N - M_R$ , and we are not summing over  $M_N$ , the Eq. 7.24 can be rearranged using Eq. (4.12) from [1] to give:

$$\begin{aligned}
& \langle v'R'n'\ell'N'M'_N | H_{Stark,Rydb} | vRn\ell NM_N \rangle = \\
& (-1)^{M_N - R + 1} E_{Stark} e[(2\ell+1)(2\ell'+1)(2N+1)(2N'+1)]^{1/2} \langle n', \ell' | r_{Rydb} | n, \ell \rangle \langle v'R | vR \rangle \\
& \begin{pmatrix} \ell' & 1 & \ell \\ 0 & 0 & 0 \end{pmatrix} \begin{pmatrix} N & N' & 1 \\ M_N & -M_N & 0 \end{pmatrix} \left\{ \begin{matrix} N & N' & 1 \\ \ell' & \ell & R \end{matrix} \right\}. \quad (7.25)
\end{aligned}$$

### 7.3 Matrix elements in the Hund's case (d) basis for the Stark effect due to the permanent dipole moment of the ion-core

In the case of the permanent dipole moment,  $\mu_{0,ion}^{(1)}$  in Eq. (7.18), the operator must be transformed from the molecular frame into the laboratory frame. Transformation of a spherical harmonic between the lab and molecular coordinate systems is given by:

$${}^{LAB}Y_{1,M''} = \sum_M (-1)^{M''-M} D_{-M-M''}^1 {}^{MOLECULE}Y_{1M}. \quad (7.26)$$

In our case  $M'' = 0$ :

$${}^{LAB}Y_{1,0} = \sum_M (-1)^{-M} D_{-M0}^1 {}^{MOLECULE}Y_{1M}. \quad (7.27)$$

Therefore the term in the Stark effect Hamiltonian due to the permanent dipole moment of the ion-core,  $\mu_{0,Rydb}^{(1)}$ , is:

$$H_{Stark,ion} = -E_{Stark} \frac{4\pi}{3} \sum_{core} e_{core} r_{core} \sum_M (-1)^{-M} Y_{1,-M}^*(\theta, \phi) Y_{1,M}(\theta_{core}, \phi_{core}). \quad (7.28)$$

When matrix elements of this term are evaluated in the Hund's case (d) basis, we get:

$$\begin{aligned} & \langle v' R' n' \ell' N' M'_N | H_{Stark,ion} | v R n \ell N M_N \rangle = \\ & -E_{Stark} \frac{4\pi}{3} \sum_{M, M_R, M'_R, M_\ell, M'_\ell} (-1)^{-M} \langle R M_R \ell M_\ell | N M_N \rangle \langle R' M'_R \ell' M'_\ell | N' M'_N \rangle \langle R' M'_R | Y_{1,M} | R M_R \rangle \\ & \sum_{core} \langle \psi'_{core} | \langle v' R' | e_{core} r_{core} Y_{1,M}(\theta_{core}, \phi_{core}) | v, R \rangle | \psi_{core} \rangle \langle \ell' M'_\ell | \ell M_\ell \rangle \langle n' \ell' | n \ell \rangle. \end{aligned} \quad (7.29)$$

The term

$$\sum_{core} \langle \psi'_{core} | \langle v' R' | e_{core} r_{core} Y_{1,M}(\theta_{core}, \phi_{core}) | v, R \rangle | \psi_{core} \rangle = \sqrt{\frac{3}{4\pi}} \mu_z \quad (7.30)$$

in Eq. 7.29 is the permanent dipole moment of the ion-core. In a diatomic molecule the dipole moment must lie along the  $z$  axis and  $M$  is 0. The Stark effect matrix element then becomes:

$$\begin{aligned} & \langle v' R' n' \ell' N' M'_N | H_{Stark,ion} | v R n \ell N M_N \rangle = \\ & -E_{Stark} \sqrt{\frac{4\pi}{3}} \sum_{M_R, M_{R'}, M_\ell} \langle R M_R \ell M_\ell | N M_N \rangle \langle R' M'_{R'} \ell M_\ell | N' M'_N \rangle \\ & \int d\Omega Y_{R' M'_{R'}}^* Y_{1,0} Y_{R, M_R} \mu_z \delta_{\ell, \ell'} \delta_{n, n'} \delta_{M_\ell, M'_\ell}. \end{aligned} \quad (7.31)$$

It can be rearranged into

$$\begin{aligned} & \langle v' R' n' \ell' N' M'_N | H_{Stark,ion} | v R n \ell N M_N \rangle = \\ & -E_{Stark} \mu_z [(2R+1)(2R'+1)(2N+1)(2N'+1)]^{1/2} \begin{pmatrix} R & 1 & R' \\ 0 & 0 & 0 \end{pmatrix} \\ & \sum_{M_R, M_{R'}, M_\ell} (-1)^{R+R'+M'_N+M_N+M'_R} \delta_{\ell, \ell'} \delta_{n, n'} \delta_{M_\ell, M'_\ell} \\ & \begin{pmatrix} R & \ell & N \\ M_R & M_\ell & -M_N \end{pmatrix} \begin{pmatrix} R' & \ell & N' \\ M'_{R'} & M_\ell & -M'_N \end{pmatrix} \begin{pmatrix} R & 1 & R' \\ M_R & 0 & -M'_R \end{pmatrix}. \end{aligned} \quad (7.32)$$

It follows from the last  $3j$  coefficient that  $M'_R = M_R$ , and thus  $M'_N = M_N$ . The sum over  $3j$  coefficients can be transformed into a  $6j$  coefficient, and the matrix element becomes:

$$\begin{aligned}
& \langle v'R'n'\ell'N'M'_N | H_{Stark,ion} | vRn\ell NM_N \rangle = \\
& -E_{Stark\mu_z} [(2R+1)(2R'+1)(2N+1)(2N'+1)]^{1/2} \begin{pmatrix} R' & 1 & R \\ 0 & 0 & 0 \end{pmatrix} \\
& (-1)^{M_N+N+N'-\ell+1} \left\{ \begin{matrix} N' & 1 & N \\ R & \ell & R' \end{matrix} \right\} \begin{pmatrix} N' & 1 & N \\ -M'_N & 0 & M_N \end{pmatrix} \delta_{\ell,\ell'} \delta_{n,n'} \delta_{M_\ell,M'_\ell}. \quad (7.33)
\end{aligned}$$

## 7.4 Hamiltonian expressed in the Hund's case (d) basis set

Combining the matrix elements from Eqs. (7.14), (7.15), (7.25), and (7.33), the Hund's case (d) Hamiltonian can be written as:

$$\begin{aligned}
& \langle v'R'n'\ell'N'M'_N | H | vRn\ell NM_N \rangle = \\
& -\frac{1}{2n^2} + BR(R+1)\delta_{RR'}\delta_{nn'} + E_{vib} \\
& -e \langle n'\ell' | r^{-2} | n\ell \rangle \langle v'R' | \mu_0^{(1)} | vR \rangle [(2R+1)(2R'+1)(2\ell+1)(2\ell'+1)]^{1/2} \\
& (-1)^{R+R'+N} \begin{pmatrix} R' & 1 & R \\ 0 & 0 & 0 \end{pmatrix} \begin{pmatrix} \ell' & 1 & \ell \\ 0 & 0 & 0 \end{pmatrix} \begin{Bmatrix} N & R' & \ell' \\ 1 & \ell & R \end{Bmatrix} \\
& -e \langle n'\ell' | r^{-3} | n\ell \rangle \langle v'R' | Q_0^{(2)} | vR \rangle [(2R+1)(2R'+1)(2\ell+1)(2\ell'+1)]^{1/2} \\
& (-1)^{R+R'+N} \begin{pmatrix} R' & 2 & R \\ 0 & 0 & 0 \end{pmatrix} \begin{pmatrix} \ell' & 2 & \ell \\ 0 & 0 & 0 \end{pmatrix} \begin{Bmatrix} N & R' & \ell' \\ 2 & \ell & R \end{Bmatrix} \\
& +e \langle n', \ell' | r | n, \ell \rangle \langle v'R | vR \rangle E_{Stark} [(2\ell+1)(2\ell'+1)(2N+1)(2N'+1)]^{1/2} \\
& (-1)^{M_N-R+1} \begin{pmatrix} \ell' & 1 & \ell \\ 0 & 0 & 0 \end{pmatrix} \begin{pmatrix} N & N' & 1 \\ M_N & -M_N & 0 \end{pmatrix} \begin{Bmatrix} N & N' & 1 \\ \ell' & \ell & R \end{Bmatrix} \\
& -E_{Stark}\mu_z [(2R+1)(2R'+1)(2\ell+1)(2\ell'+1)]^{1/2} \delta_{\ell,\ell'}\delta_{n,n'}\delta_{M_\ell,M'_\ell} \\
& (-1)^{M_N+N+N'-\ell+1} \begin{pmatrix} R' & 1 & R \\ 0 & 0 & 0 \end{pmatrix} \begin{pmatrix} N' & 1 & N \\ -M'_N & 0 & M_N \end{pmatrix} \begin{Bmatrix} N' & 1 & N \\ R & \ell & R' \end{Bmatrix} \quad (7.34)
\end{aligned}$$

## 7.5 Stark effect matrix elements expressed in the Hund's case (b) basis set

The Stark matrix element in the Hund's case (b) basis set can be derived by rearranging the term derived for Hund's case (d), given in Eq. (7.25), or it can be derived from Eq. (3) in [5], by replacing the  $\langle \Lambda_a | \mu_q^{(1)} | \Lambda_b \rangle$  term with the Rydberg-Rydberg transition dipole moment. The latter procedure is shorter, and will be employed here.

We need to evaluate  $\langle \eta', \ell' \Lambda' | \mu_q | \eta, \ell \Lambda \rangle$ , where

$$|\eta, \ell, \Lambda\rangle = \sum_{\ell} c_{\ell} F_{\ell} Y_{\ell, \Lambda}, \quad (7.35)$$

and

$$\mu_q = er \sqrt{\frac{4\pi}{3}} Y_{1,q}. \quad (7.36)$$

$F_{\ell}$  is the radial wavefunction, and  $c_{\ell}$  are the amplitudes in the  $\ell$ -decomposition for an  $\ell$ -mixed state. It follows that:

$$\langle \eta', \ell', \Lambda' | \mu_q | \eta, \ell, \Lambda \rangle = e \sqrt{\frac{4\pi}{3}} \sum_{\ell, \ell'} c_{\ell} c_{\ell'}^* \int F'_{\ell'} r F_{\ell} dr \int d\Omega(\theta, \phi) Y_{\ell', \Lambda'}^* Y_{1,q} Y_{\ell, \Lambda}. \quad (7.37)$$

Using Eq. (3.119) and Eq. (1.56) from [1], and integrating over  $\theta$  and  $\phi$  (but not  $\chi$ ), we can write:

$$\langle \eta', \ell', \Lambda' | \mu_q | \eta, \ell, \Lambda \rangle = e \sum_{\ell, \ell'} c_{\ell} c_{\ell'}^* \langle n' \ell' | r | n, \ell \rangle (-1)^{\Lambda'} [(2\ell + 1)(2\ell' + 1)]^{1/2} \begin{pmatrix} \ell & 1 & \ell' \\ 0 & 0 & 0 \end{pmatrix} \begin{pmatrix} \ell & 1 & \ell' \\ \Lambda & q & -\Lambda' \end{pmatrix} \quad (7.38)$$

When Eq. (7.38) is substituted into Eq. 2.5, we get the Hund's case (b) expression for the



Stark effect matrix element given in Eq. 3.7.

## 7.6 Bibliography

- [1] R. N. Zare. *Angular Momentum*. John Wiley and Sons, 1988.
- [2] E. E. Eyler and F. M. Pipkin. *Phys. Rev. A*, 27:246, 1983.
- [3] J. K. G. Watson. *Mol. Phys.*, 81:277, 1994.
- [4] J. J. Kay, S. L. Coy, V. S. Petrović, B. M. Wong, and R. W. Field. *J. Chem. Phys.*, 128:194301, 2008.
- [5] V. S. Petrović and R. W. Field. *J. Chem. Phys.*, 128:014301, 2007.



## Curriculum Vitae

BIRTH DATE: October 28, 1978

EDUCATION: University of Belgrade, Serbia, Sc. B. (2002); Massachusetts Institute of Technology, Ph.D. expected December 2008.

AWARDS AND HONORARY SOCIETIES: Dragomir Nicolitch Trust Scholarship (2005-2008); Serbian Chemical Society Award (2003); Pavle Savić Award (Valedictorian), University of Belgrade (2003); Karadjordjevic Foundation Fellowship (2002); Serbian National Art and Science Foundation Fellowship (1994-2002).

## PUBLICATIONS AND PRESENTATIONS:

V. S. Petrović. "Toward pure electronic spectroscopy." Modern Optics and Spectroscopy Seminar, Massachusetts Institute of Technology (2008)

V. S. Petrović, Y. Zhou, S. L. Coy, and R. W. Field. "Calculated Pure Electronic spectra of  $\ell$ -mixed Rydberg states.", in preparation

V. S. Petrović, J. J. Kay, S. L. Coy, and R. W. Field. "Stark Effect in  $n^* = 13$  of Rydberg States of CaF." Journal of Chemical Physics, submitted (2008)

V. S. Petrović and R. W. Field. "Stark effect in Rydberg States of CaF." 63<sup>rd</sup> International Symposium on Molecular Spectroscopy, Ohio State University, Columbus (2008)

V. S. Petrović and R. W. Field. "Toward pure electronic spectroscopy." 235<sup>th</sup> American Chemical Society Spring Meeting, New Orleans (2008)

J. J. Kay, S. L. Coy, V. S. Petrović, B. M. Wong, and R. W. Field. "Separation of long-range and short-range interactions in Rydberg states of diatomic molecules." Journal of Chemical Physics 128, 194301 (2008)

V. S. Petrović and R. W. Field. "Polarization dependence of the transition intensity in double resonance experiments; Unresolved spin doublets." Journal of Chemical Physics 128, 014301 (2007)

V. S. Petrović, E. E. Fenn and R. W. Field. "Assignment methods for Rydberg states of CaF." 62<sup>nd</sup> International Symposium on Molecular Spectroscopy, Ohio State University, Columbus (2007)

J. J. Kay, D. S. Byun, J. O. Clevenger, X. Jiang, V. S. Petrović, R. Seiler, J. R. Barchi, A. J. Merer, and R. W. Field. "'Spectrum-only' assignment of core-penetrating and core-nonpenetrating Rydberg states of calcium monofluoride." Canadian Journal of Chemistry 82, 791 (2004)

V. S. Petrović, E. E. Fenn and R. W. Field. "Assignment methods for high- $N$  Rydberg states of CaF." 61<sup>st</sup> International Symposium on Molecular Spectroscopy, Ohio State University, Columbus (2006)